213

Topics in Current Chemistry

Springer

Berlin
Heidelberg
New York
Barcelona
Hong Kong
London
Milan
Paris
Singapore
Tokyo

Transition Metal and Rare Earth Compounds

Excited States, Transitions, Interactions I

Volume Editor: Hartmut Yersin

With contributions by
K. L. Bray, M. Glasbeek, H. Kunkely, A. Vogler

Springer

The series *Topics in Current Chemistry* presents critical reviews of the present and future trends in modern chemical research. The scope of coverage includes all areas of chemical science including the interfaces with related disciplines such as biology, medicine and materials science. The goal of each thematic volume is to give the nonspecialist reader, whether at the university or in industry, a comprehensive overview of an area where new insights are emerging that are of interest to a larger scientific audience.

As a rule, contributions are specially commissioned. The editors and publishers will, however, always be pleased to receive suggestions and supplementary information. Papers are accepted for *Topics in Current Chemistry* in English.

In references *Topics in Current Chemistry* is abbreviated Top. Curr. Chem. and is cited as a journal.

Springer WWW home page: http://www.springer.de
Visit the TCC home page at http:/link.springer.de/series/tcc/
or http://link.springer-ny.com/series/tcc/

ISSN 0340-1022
ISBN 3-540-67986-3
Springer-Verlag Berlin Heidelberg New York

Library of Congress Catalog Card Number 74-644622

Springer-Verlag Berlin Heidelberg New York
a member of BertelsmannSpringer Science+Business Media GmbH

Printed in Germany

Cover design: Friedhelm Steinen-Broo, Barcelona; MEDIO, Berlin
Typesetting: Fotosatz-Service Köhler GmbH, 97084 Würzburg

SPIN: 10706755 02/3020 ra - 5 4 3 2 1 0 - Printed on acid-free paper

Volume Editor

Prof. Dr. Hartmut Yersin
Institut für Physikalische und Theoretische Chemie
Universität Regensburg
Universitätsstraße 31
93053 Regensburg, Germany
E-mail: hartmut.yersin@chemie.uni-regensburg.de

Editorial Board

Prof. Dr. Armin de Meijere
Institut für Organische Chemie
der Georg-August-Universität
Tammannstraße 2
37077 Göttingen, Germany
E-mail: ameijer1@uni-goettingen.de

Prof. Dr. Horst Kessler
Institut für Organische Chemie
TU München
Lichtenbergstraße 4
85747 Garching, Germany
E-mail: kessler@ch.tum.de

Prof. Steven V. Ley
University Chemical Laboratory
Lensfield Road
Cambridge CB2 1EW, Great Britain
E-mail: svl1000@cus.cam.ac.uk

Prof. Dr. Joachim Thiem
Institut für Organische Chemie
Universität Hamburg
Martin-Luther-King-Platz 6
20146 Hamburg, Germany
E-mail: thiem@chemie.uni-hamburg.de

Prof. Dr. Fritz Vögtle
Kekulé-Institut für Organische Chemie
und Biochemie der Universität Bonn
Gerhard-Domagk-Straße 1
53121 Bonn, Germany
E-mail: voegtle@uni-bonn.de

Prof. Kendall N. Houk
Department of Chemistry and Biochemistry
University of California
405 Hilgard Avenue
Los Angeles, CA 90024-1589, USA
E-mail: houk@chem.ucla.edu

Prof. Jean-Marie Lehn
Institut de Chimie
Université de Strasbourg
1 rue Blaise Pascal, B.P.Z 296/R8
67008 Strasbourg Cedex, France
E-mail: lehn@chimie.u-strasbg.fr

Prof. Stuart L. Schreiber
Chemical Laboratories
Harvard University
12 Oxford Street
Cambridge, MA 02138-2902, USA
E-mail: sls@slsiris.harvard.edu

Prof. Barry M. Trost
Department of Chemistry
Stanford University
Stanford, CA 94305-5080, USA
E-mail: bmtrost@leland.stanford.edu

Prof. Hisashi Yamamoto
School of Engineering
Nagoya University
Chikusa, Nagoya 464-01, Japan
E-mail: j45988a@nucc.cc.nagoya-u.ac.jp

Topics in Current Chemistry Now Also Available Electronically

For all customers with a standing order for Topics in Current Chemistry we offer the electronic form via LINK free of charge. Please contact your librarian who can receive a password for free access to the full articles by registration at:

http://link.springer.de/orders/index.htm

If you do not have a standing order you can nevertheless browse through the table of contents of the volumes and the abstracts of each article at:

http://link.springer.de/series/tcc

There you will also find information about the

- Editorial Board
- Aims and Scope
- Instructions for Authors

Preface

For a long time, the properties of transition metal and rare earth compounds have fascinated chemists and physicists from a scientific view-point, and more recently also their enormous potential as new materials has been explored. Applications in different fields have already been realized or are under current investigation, for example, new laser materials, IR to visible upconversion systems, compounds for photolithographic processes, systems involving photoredox processes for solar energy conversion, new photovoltaic devices, chemical sensors, biosensors, electroluminescent devices (OLEDs) for flat panel display systems, supramolecular devices with wide-range definable photophysical properties, materials for energy harvesting, optical information and storage systems, etc. Metal complexes are also highly important in biology and medicine. Most of the applications mentioned are directly related to the properties of the electronic ground state and the lower-lying excited states. Metal complexes with organic ligands or organometallic compounds exhibit outstanding features as compared to purely organic molecules. For instance, metal compounds can often be prepared and applied in different oxidation states. Furthermore, various types of low-lying electronic excitations can be induced by a suitable choice of ligands, for example, such as metal-centered transitions (MC, e.g. d-d* transition), ligand-centered (LC, e.g. π-π^*), metal-to-ligand-charge transfer (MLCT, e.g. d-π^*), intra-ligand-charge-transfer (ILCT) transitions, etc. In particular, the orbitals involved in the resulting lowest excited states determine the photophysical and photochemical properties and thus the specific use of the compound. It is of further interest that the lowest excited electronic states can be shifted over the large energy range from the U.V. to the I.R. by chemical variation of the ligands and/or the central metal ion. Moreover, these excited states have mostly spin-multiplicities different from those of the electronic ground states. In contrast to organic molecules, spin-orbit coupling induced by the metal center is of crucial importance for the splitting and the population and decay dynamics of these multiplets as well as for transition probalities. In summary, it is of outstanding importance that this class of compounds provides the possibility of tuning excited state properties by chemical variation. Thus, compounds with user-defined excited state properties can be prepared.

In view of the fascinating potential of these compounds, it is of great interest to develop a deeper understanding of their photophysical properties. In this volume, leading scientists present modern research trends in comprehensive reviews which not only provide a deep insight into the specific subjects, but are also written in a style that enables researchers from related fields and graduate students to follow the interesting subjects. In particular, in the present volume Kevin L. Bray presents effects that are observed under the application of high pressure. Max Glasbeek introduces us to optically detected magnetic resonance (ODMR) techniques as applied to transition metal complexes and Arnd Vogler and Horst Kunkely give a summary concerning the diversity of excited states as found in various compounds. In a companion volume (Topics in Current Chemistry 214, in press) Daniel R. Gamelin and Hans U. Güdel review upconversion processes in luminescent transition metal and rare earth systems. Mark J. Riley relates geometric and electronic properties of copper(II) compounds. Finally, Hartmut Yersin and Dirk Donges explain on the basis of case studies, the ways in which photophysical properties of organometallic and related compounds depend on the metal character of the low-lying electronic states and how these properties can be tuned by chemical variation.

I hope that the contributions in the present and in the subsequent volume demonstrate the attractiveness and the enormous potential of metal compounds and that a more detailed understanding of the photophysical properties will open pathways to new developments.

Regensburg, Germany
October 2000

Hartmut Yersin

Contents

Contents of Volume 191

Electronic and Vibronic Spectra of Transition Metal Complexes II

Volume Editor: Hartmut Yersin

ISBN 3-540-62922-X

Spectroscopy of the Spin Sublevels of Transition Metal Complexes
T. Azumi, H. Miki

Magnetic and Spectroscopic Properties of $Os_2(O_2CR)_4Cl_2$. Evidence for $a^3(\delta^*\pi^*)$ Ground State
V. M. Miskowski, H. B. Gray

Luminescence and Absorption Studies of Transition Metal Ions in Host Crystals, Pure Crystals and Surface Environments
H. H. Patterson

Angular Overlap Model Applied to Transition Metal Complexes and d^N-Ions in Oxide Host Lattices
T. Schönherr

Characterization of Excited Electronic and Vibronic States of Platinum Metal Compounds with Chelate Ligands by Highly Frequency-Resolved and Time-Resolved Spectra
H. Yersin, W. Humbs, J. Strasser

Contents of Volume 214

Transition Metal and Rare Earth Compounds

Excited States, Transitions, Interactions II

Volume Editor: Hartmut Yersin

ISBN 3-540-67976-6

Upconversion Process in Transition Metal and Rare Earth Metal Systems
D. R. Gamelin, H. U. Güdel

Geometric and Electronic Information from the Spectroscopy of Six-Coordinate Copper(II) Compounds
M. J. Riley

Low-Lying Electronic States and Photophysical Properties of Organometallic Pd(II) and Pt(II) Compounds. Modern Research Trends Presented in Detailed Case Studies.
H. Yersin, D. Donges

High Pressure Probes of Electronic Structure and Luminescence Properties of Transition Metal and Lanthanide Systems

Kevin L. Bray

Department of Chemistry, Washington State University, Pullman, WA 99164-4630 USA
E-mail: kbray@wsu.edu

Recent work has demonstrated that unique insight into the electronic structure and optical properties of solid state transition metal and lanthanide systems is achievable through high pressure studies. In this review, we present selected examples that illustrate the advances in understanding possible from high pressure luminescence experiments. The ability of pressure to continuously vary energy level structure and coordination environment is emphasized and related to variations in luminescence properties. Pressure is shown to influence luminescence properties through crystal field, covalency, and spin-orbit coupling effects. The effect of pressure on luminescence energy, intensity, and decay properties will be considered. Additional phenomena to be discussed include electronic crossovers, vibrational coupling, admixing of electronic states, energy transfer and site selective spectroscopy. High pressure luminescence properties of transition metal and lanthanide ions in crystalline solids, metal complexes, and glasses will be reviewed.

Keywords. Pressure, Luminescence, Crystal field, Energy transfer

Topics in Current Chemistry, Vol. 213

1
Introduction

The ability to predict and control the luminescence properties of transition metal and lanthanide systems has long been an objective of the optical materials community. Solid state lasers, solar energy conversion, optical sensing, optical data storage, and phosphors are examples of areas where precise control over the wavelength, lineshape, and efficiency of luminescence is essential for optimizing performance and extending the range of applications. Luminescence properties of transition metal and lanthanide ions are ultimately controlled by the chemical and physical interactions they experience in a given material. The most important interactions occur in the nearest neighbor coordination shell where factors such as bond lengths, bond angles, coordination number, and covalency determine the energy, mixing, and splittings of the electronic states involved in luminescence. Secondary effects associated with more distant neighbors are also frequently important and depend on the system in which a luminescent ion is found. When transition metal and lanthanide ions are incorporated as dopants in crystalline or amorphous solids, ligands in the first coordination shell are strongly bonded to second nearest neighbors. As a result, the spatial distribution and electronic interactions of ligands in the first coordination shell are constrained. In molecular inorganic or organometallic complexes, intramolecular interactions normally dominate intermolecular interactions and the influence of atoms outside the first coordination shell occurs secondarily through ligand-ligand interactions or chelation effects.

The design of luminescent materials for new and more exacting applications requires a systematic understanding of the relationship between the bonding environment of transition metal and lanthanide centers and absorption and emission properties. The customary approach for investigating the relationship between bonding environment and optical properties is through variations of chemical composition. By changing chemical composition, it is possible to systematically vary the local bonding environment of luminescent centers and gain information useful in developing a predictive capability. Examples of this approach include luminescence studies of a given metal ion as a dopant in a series of host lattices or of complexes of a given metal ion with a series of ligands.

In this review, we present an alternative approach to gaining structure-bonding-property information for luminescent transition metal and lanthanide ions in solids and complexes. The approach is based on using hydrostatic pressure to systematically influence the bonding environment of luminescent centers. We will show that with pressure it is possible to directly influence the bonding interactions that are responsible for determining the luminescence properties of the electronic states of transition metal and lanthanide ions. By correlating pressure-induced changes in electronic states, structure, and bonding with pressure-induced changes in luminescence properties, we create new opportunities for generalizing the behavior of transition metal and lanthanide ions.

High pressure studies are complementary to the conventional chemical composition approach and offer several potential advantages. First, with high pressure we can continuously vary structure, coordination environment, and luminescence properties. Variations in chemical composition, on the contrary, lead to discrete changes. The continuous tuning capability of pressure provides new opportunities for correlating structure, bonding, and luminescence properties. The finer resolution offered by high pressure is particularly important at conditions such as electronic crossovers or phase transitions where optical properties vary abruptly. Second, with high pressure we have the ability to study a given chemical composition over a wide range of structure and bonding conditions. As a result, the need to synthesize a range of host lattice compositions or complexes with a variety of ligands is minimized. Complications such as differences in impurities or defects that may accompany a series of systems are also avoided. Third, high pressure provides the potential for achieving structures, molecular configurations, phases and electronic states that are not achievable through other means. Variations in pressure alter the relative thermodynamic stability of different states of a system and offer the possibility of creating new states with new properties. Finally, high pressure often allows us to resolve overlapping or competing excited state processes. Frequently several optical processes and/or electronic states contribute to ambient pressure luminescence properties. Since competing effects are typically perturbed to differing extents by pressure, it becomes possible to stabilize one effect relative to others. Characterization of dominant effects at high pressure, followed by back-extrapolation to ambient pressure, frequently leads to new understanding of ambient pressure luminescence properties.

High pressure and variable chemical composition studies share the goal of striving to identify the chemical and physical factors necessary for controlling optical properties. The ultimate objective is to progress toward the rational design of new materials with new ambient pressure properties. The following review attempts to illustrate the unique insight into luminescence properties achievable through high pressure studies. We restrict our attention to the luminescence properties of transition metal and lanthanide ions in insulating inorganic solids and metal complexes. The effects of pressure on the luminescence properties of pure organic systems [1–18], inorganic systems that do not contain transition metal or lanthanide ions [19–25], semiconductors [26–38], and liquid phase systems [39–50], as well as related techniques such as uniaxial stress [51–54] and shockwaves [55, 56], will not be discussed. We begin by describing the methods of high pressure luminescence spectroscopy and the phenomenological effects of pressure on basic luminescence properties. We then present several examples from the recent literature that illustrate the range of phenomena observable at high pressure and conclude with a few remarks concerning the future.

2
Methods of High Pressure Luminescence

Studies of material properties as a function of pressure have received less attention historically than studies as a function of temperature. As a result, most investigators have a more intuitive sense of the effect of temperature on materials and routinely consider temperature-dependent experiments during the course of their work. This state of affairs is unfortunate because pressure is an equally valuable variable that not only complements temperature, but also provides an opportunity to gain insight not attainable through temperature studies. Whereas temperature studies are valuable probes of competing states and processes that are separated by an energy barrier, pressure can alter the heights of energy barriers and is much more likely to stabilize new states and phases.

The underutilization of high pressure methods is partly due to the perception that the laboratory facilities and procedures needed to create high pressure conditions are cumbersome and time consuming. Contrary to this perception, the tremendous advances that have been made in high pressure experimentation over the past decade have greatly increased the accessibility of high pressure methods to the scientific community and have prompted growing interest in research at high pressure conditions. The range of experiments that can now be conducted as a function of pressure includes [57–60] X-ray diffraction, Brillouin scattering, EXAFS, optical absorption, luminescence, non-linear spectroscopy, Raman scattering, NMR, and conductivity. High pressure experiments can also be completed at both low and high temperature.

In this section, we present basic aspects of modern high pressure experimentation. We begin with a few introductory comments about pressure, its effect on materials, and the range of pressure normally needed for studying solids. We continue by discussing the diamond anvil cell technique used by many groups to generate high pressure in the laboratory and conclude with a discussion of luminescence experiments at high pressure.

2.1
High Pressure as an Experimental Variable

High pressure has traditionally been viewed as a macroscopic, thermodynamic experimental variable. Classic applications of pressure have involved equation of state studies of liquids and solids and measurements of the variation of physical properties as a function of pressure [57, 59–66]. The basic effect of pressure on a system is a consequence of the thermodynamic stability requirements of the second law [67] and can be expressed most generally as

$$\left(\frac{\partial V}{\partial P}\right)_{\mathrm{T}} < 0 \tag{1}$$

Equation (1) indicates that, in order to comply with the second law, the volume of a material must decrease upon isothermal compression. The precise manner, however, in which a material reduces its volume in response to an applied pressure is unspecified by the second law and requires consideration on a molecular level. Molecular attributes such as bond angles, bond lengths, covalency, coordination number, and intermolecular forces can be influenced by pressure. Since these attributes are responsible for defining chemical, electrical, optical, and magnetic properties, pressure is a potentially powerful probe of the properties of materials.

When considering the potential effect of pressure on a system, it is useful to recognize the magnitude of pressure required to significantly alter molecular and bulk properties. The isothermal compressibility, κ (or its reciprocal K, the bulk modulus) (Eq. 2), gives an indication of the sensitivity of a system to pressure:

$$\kappa = -\frac{1}{V}\left(\frac{\partial V}{\partial P}\right)_{\mathrm{T}} = \frac{1}{K} \tag{2}$$

Systems with large compressibilities ("soft" or "highly compressible" systems) exhibit large volume decreases per unit applied pressure and as a result are expected to show significant changes in properties with pressure. Pressures of a few bars, for example, can significantly alter the behavior of gases. Condensed phases experience much stronger intermolecular interactions and are much less compressible. As a result, pressures in the kbar and even mbar range are generally required to measurably perturb the properties of solids and liquids.

Our focus in this review is on the luminescence behavior of solid state lanthanide and transition metal systems over a pressure range extending up to ~300 kbar. Since this magnitude of pressure is well beyond everyday experience, it is beneficial to consider how these pressures compare to those encountered in the physical world. Table 1 presents selected examples from a more comprehensive compilation presented by Jayaraman [68]. The pressures in Table 1 range from 10^{-19} bar in outer space to 10^{11} bar at the center of the sun. The unit of pressure of relevance to this review is the kbar. From Table 1, we see that 1 kbar corresponds approximately to the pressure at the deepest point in the ocean. A pressure of 50 kbar would result if one were to invert the Eiffel tower and place it on

Table 1. Pressures encountered in several physical situations

Situation	Approximate pressure (bar)
Pressure in outer space	10^{-19}
High vacuum chamber	10^{-14}
Sound waves	10^{-10}-10^{-4}
Inside light bulb	10^{-1}
Sea level	1
Engine cylinder	10
Charged scuba tank	100
Marianas Trench (37,800 ft)	1000
Freezing of H_2O at 100 °C	3×10^4
Center of Earth	6×10^6
Center of Jupiter	10^8
Center of Sun	10^{11}

a 12 cm square plate [69]. Static pressures well above 1 Mbar have been achieved and are routinely used in many laboratories [57–60, 70–73].

2.2
Diamond Anvil Cell

The generation of high pressure in the laboratory is typically accomplished by placing a sample between opposing anvils and forcing the anvils together to produce pressure. The strength of the anvil material ultimately determines the maximum attainable pressure. In the early days, large hydraulic presses based on diametrically opposed hardened steel or carbide anvils were used in high pressure research. Over the years, several revisions occurred which led to the development of devices based on multiple anvil and toroidal geometries. These devices are capable of generating ~ 300 kbar and continue to be widely used today [59, 60, 74].

A new era of high pressure research began with the advent of the diamond anvil cell [57–60, 68, 75, 76]. The use of diamond as an anvil material has two important advantages over steel or carbide anvils. First, diamond is the hardest known substance and is capable of reaching higher pressures than steel or carbide anvils. Second, diamond is optically transparent and therefore permits a wider range of experimental probes at high pressure. Photon spectroscopies, in particular, become possible in diamond anvil cells. Although diamond anvil cells were recognized to be versatile devices for generating pressure, they were not widely used initially because of the difficulty in accurately determining the pressure exerted on a sample. It was not until the development of the ruby fluorescence pressure calibration method (see Sect. 2.2.1) in the 1970s that the diamond anvil cell became the leading device for generating static high pressures.

A schematic depiction of a diamond anvil cell is shown in Fig. 1. The principle of operation of the cell is straightforward [77]. A sample is placed between the two parallel diamonds. By moving the diamonds together, a force is trans-

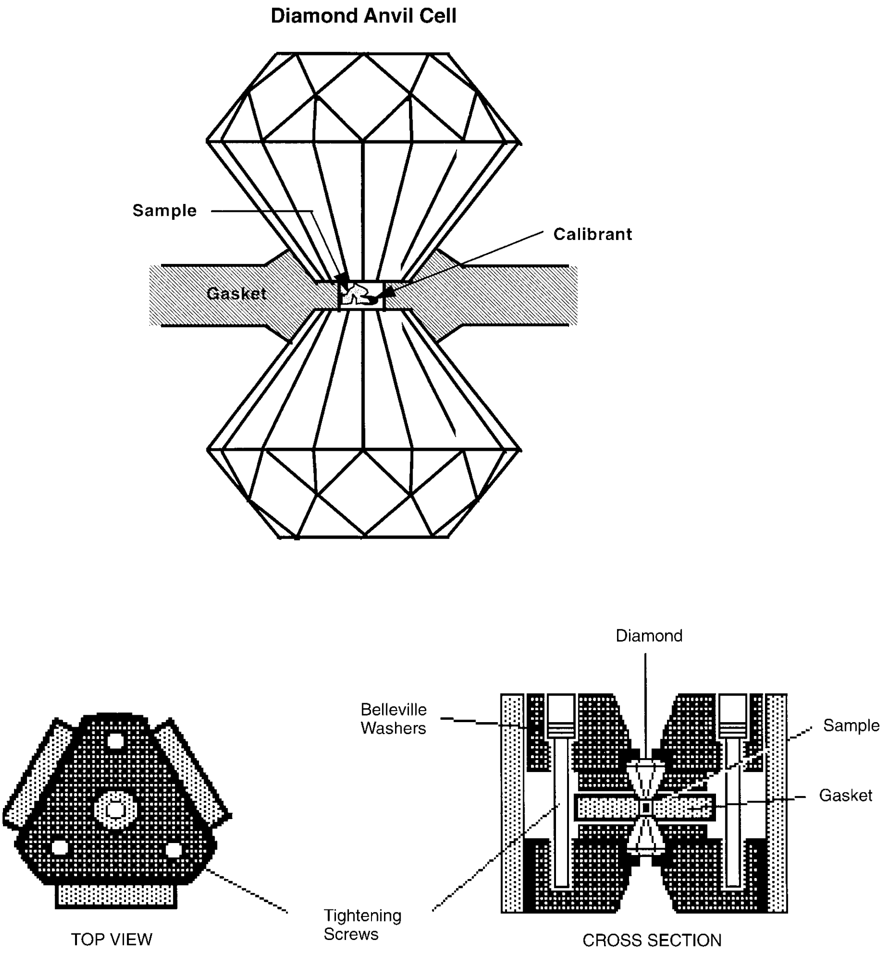

Fig. 1. Schematic depiction of a diamond anvil cell. The *upper half* shows an enlargement of the opposed diamond anvils that are used to generate pressure. The sample is placed in the central hole of the metal gasket along with a pressure transmitting fluid and a pressure calibrant. The *lower half* of the figure illustrates one method for applying mechanical force to the diamonds. The resulting translational force leads to a reduction in sample volume and a consequent increase in sample pressure

mitted to the sample and the sample pressure increases. The metal gasket [78] contains the sample radially to prevent it from extruding outward. A hole drilled in the center of the gasket defines the sample chamber. Along with the sample, a pressure calibrant and a transparent pressure transmitting fluid (not shown) are placed in the gasket hole. The fluid fills up the free volume of the hole and flows as the diamonds are moved together to insure a uniform pressure throughout the sample chamber. The diamonds are mounted on hardened steel or carbide platens that are incorporated into a mechanical force generating system. Several force generating mechanisms are currently in use [76]. In the modified Merrill-

Bassett [79] design used in our laboratory (lower part of Fig. 1), the platens are countersunk into the triangular halves of the cell proper and three screws are used to translate the halves of the cell. As the halves move together, the distance between the diamonds decreases and the sample pressure increases as a result of the consequent reduction of sample volume. Three guide plates attached to the lower half of the cell provide translational stability and aid in maintaining the parallel alignment of the flat, load bearing surfaces of the diamond (culets). Diamond alignment is critical because, although diamond is strong, it is susceptible to cleavage failure in the presence of shear stresses.

The diamond anvils are typically gemstone quality and weigh about 0.2 carat. Since pressure is simply force per unit area and the upper force limit is determined by the strength limits of the components of the cell, the diameter of the diamond culet ultimately determines the maximum achievable pressure. No definitive relationship between the culet diameter and maximum pressure is available, but with a well-designed cell one can typically expect to reach pressures of 100 kbar with 700 μm culets, 500 kbar with 400 μm culets, and 1 Mbar with 200 μm culets [77]. Bevelled diamonds are recommended for pressures above 1 Mbar [77, 80–82]. Sapphire [83, 84] and cubic zirconia [85] are less expensive alternatives to diamond, but are not as strong and can be used only to ~100 and ~30 kbar, respectively.

2.2.1
Pressure Calibration

The determination of the pressure inside the diamond anvil cell requires a calibrated standard. The most commonly used standard is the R-line ($^2E \rightarrow {}^4A_2$) emission from ruby. The wavelengths of the ruby R_1 and R_2 lines have been accurately calibrated as a function of pressure using fixed point standards [86] and the measured lattice constant of NaCl in conjunction with the Decker equation of state [87–89]. The shift rate of the lower energy R_1 line is normally used to calibrate pressure. The room temperature R_1 shift rate is linear up to 200 kbar (0.365 Å/kbar (–0.759 cm^{-1}/kbar)) [87]. Above 200 kbar, the shift becomes non-linear and has been quantified empirically [90–93]. The currently accepted R_1 line wavelength calibration is valid up to 800 kbar and can be expressed [91] by

$$\Delta\lambda = \lambda_0 \left[\left[\left(\frac{B}{A} \right) P + 1 \right]^{\frac{1}{B}} - 1 \right] \tag{3}$$

where A = 19.040 kbar, B = 7.665, $\lambda_0 = 6942$ Å and $\Delta\lambda = \lambda(P) - \lambda_0$. The pressure shift of ruby has also been determined at low [94, 95] and high [94–96] temperature.

Other fluorescent pressure sensors have also been suggested, but are used less frequently than ruby. Wavelength calibrations with pressure have been reported for alexandrite [97, 98], Sm^{2+}: $Y_3Al_5O_{12}$ (YAG) [99–101], Sm^{2+}: MFCl (M = Ba, Sr) [102, 103], Sm^{2+}: SrB_4O_7 [104, 105], Eu^{3+}: YAG [106], Tm^{3+}: YAG [107], Nd^{3+}: $YAlO_3$ [108], and V^{2+}: MgO [109]. Fluorescence lifetime calibrations have also been reported for ruby [110–112], Cr^{3+}:YAG [113], alexandrite [114, 115], and Sm^{2+}: MFCl (M = Sr, Ca) [116].

Calibrations based on techniques other than fluorescence are also available. Lattice parameter calibrations from pressure dependent X-ray experiments have been reported for several systems. The most commonly used X-ray standards include MCl (M = Na, K, Cs) [89], Au [117, 118], W [119], and Cu [120]. Spectral shifts of Raman lines in N_2 [121] and diamond [122] have also been calibrated as a function of pressure.

2.2.2
Pressure Transmitting Media

The pressure transmitting medium plays a critical role in the success of diamond anvil cell pressure experiments. The function of the medium is to insure a homogeneous pressure distribution in the sample chamber by flowing or deforming in response to the forces created as the diamonds are moved closer together. Pressure gradients and shear stresses need to be avoided because they can alter the physical state of a sample independent of any hydrostatic pressure effects. Pressure transmitting media can be soft solids, liquids, or gases at ambient pressure. Liquid media can readily distribute force and eliminate pressure gradients by flowing. When gases are used, they are normally introduced into the diamond cell in liquid form at low temperature and pressurized sufficiently to maintain the liquid state upon warming to room temperature. Fluidity of a liquid or liquefied gas medium is maintained with increasing pressure until solidification due to glassification or crystallization occurs. Once solidification occurs, a medium possesses mechanical strength and can support pressure gradients. The yield strength of a solidified medium represents the maximum supportable pressure gradient. Since most solidified materials have high yield strengths, most substances become unsuitable as pressure media upon solidification. Solids (whether at ambient pressure or formed at high pressure) with low yield strengths, however, may be suitable as pressure transmitting media because they deform easily and lead to only small pressure gradients. When used with samples that have small compressibility factors (Eq. 2), solid media provide conditions that are nearly hydrostatic.

The process of identifying potential pressure transmitting media is largely empirical [123]. Cryogenic gases such as Ar, Ne, N_2, He, and Xe provide hydrostatic or nearly hydrostatic conditions at room temperature and are essential for work above about ~300 kbar [70, 76, 124]. The main drawbacks for cryogenic gases are the need to load them remotely into a cryogenically cooled cell and their tendency to escape from the sample chamber because of their low viscosity. Low volatility liquid media are much more convenient to work with, but have lower hydrostatic pressure limits. A 4:1 mixture by volume of methanol and ethanol is the most widely used pressure medium and provides hydrostatic conditions at room temperature up to its glass transition at 104 kbar [123, 125]. It is only weakly non-hydrostatic above the glass transition up to ~200 kbar and becomes severely non-hydrostatic at higher pressure. Addition of a small amount of water to the mixture (16:3:1 methanol:ethanol:water) has been reported to extend the hydrostatic limit to ~140 kbar [126]. Other liquids that have been suggested include simple alkanes [125, 127], mineral oil [123], poly(chlorotrifluoroethylene) [128], and silicone oil [129]. We have recently completed experiments on $[(CH_3)_3SiO]_2Si(CH_3)_2$ and have shown that it remains nearly hydrostatic up to ~300 kbar. Solid media are the simplest to use, but are also the least hydrostatic. Alkali halides are the most commonly used solid media [125].

Much less is known about the low temperature hydrostatic limits of pressure media. The flow and deformation properties of cryogenic gas and solid media are likely not significantly altered at low temperature. Low temperature can, however, be expected to promote solidification and lower the hydrostatic limit of liquid media. Few quantitative studies of this effect have been reported [70, 124]. In practice, most investigators indirectly assess the onset of non-hydrostatic stresses at low temperature and limit experiments to P, T conditions that are sufficiently hydrostatic for their purposes. The linewidth of fluorescence lines or X-ray diffraction peaks of the pressure calibrant used in an experiment provide a qualitative measure of hydrostaticity. Non-hydrostatic stresses lead to inhomogeneous broadening and an increase in linewidth. A discontinuous increase in linewidth with pressure is an indication that solidification of a liquid pressure medium has occurred and that significant non-hydrostatic stresses are present.

2.3
Luminescence

The diamond anvil cell can normally be readily adapted to standard luminescence systems. The presence of the diamond windows and the small sample sizes are the two important considerations not encountered in standard luminescence experiments. The sample dimensions in diamond anvil experiments are typically 100 × 100 × 50 µm and in many samples of interest to this review the emitting transition metal and lanthanide ions are present at low concentrations. As a result, luminescence signals tend to be weak, data acquisition times are increased, and alignment requirements of the optical system are more stringent. Laser excitation sources are required for experiments involving $d \rightarrow d$ or $f \rightarrow f$ excitation of transition metal and lanthanide ion dopants in host lattices. The higher oscillator strengths of $f \rightarrow d$ and charge transfer transitions may permit excitation of some systems or complexes with conventional lamp sources.

The diamond anvils used in a high pressure luminescence experiment need to be carefully selected to avoid unwanted diamond fluorescence. Diamond anvils are normally natural, rather than synthetic, and contain impurities that produce fluorescence [130, 131]. Nitrogen-related defects are the most abundant fluorescent impurities in diamond and give emission in the visible and infrared that can overlap the fluorescence from the sample [132, 133]. It is possible to select anvils that do not fluoresce and these should be used in luminescence experiments. Low fluorescence diamonds are also essential for high pressure Raman experiments. Care must also be exercised when using diamonds in pulsed laser experiments. The high peak powers encountered in pulsed lasers can damage the culet and table surfaces of the diamond anvils and lead to catastrophic failure. To our knowledge, the pulsed laser damage thresholds of diamond for the most commonly used pulsed laser excitation wavelengths have not been quantified. It is therefore recommended to use the minimum power necessary to complete an experiment when using pulsed laser excitation.

3
High Pressure Luminescence Phenomena

The ability of pressure to alter the coordination environment of luminescence centers in solids or complexes provides an opportunity to understand better the relationship of local structure and bonding to electronic energy levels and optical properties. One objective of high pressure luminescence studies is to gain new insight into the fundamental chemical and physical factors necessary for achieving user-designed optical properties in new materials. This objective benefits not only practical applications, but also allows us to understand better the ability of luminescence centers to function as probes of chemical and physical phenomena. Progress toward this goal requires elucidation of the fundamental effects of pressure on the behavior of luminescence centers. In this section, we discuss the fundamental effects of pressure on luminescence centers. We begin with a qualitative discussion of the effect of pressure on luminescence transitions in the context of a single configurational coordinate mode. We continue by discussing more specifically how pressure influences luminescence energies and lifetimes. We consider d → d, f → f, f → d, and charge transfer transitions of transition metals and rare earths in solids and complexes. We then discuss pressure induced electronic crossovers and the effect of pressure on energy transfer processes. The section includes several theoretical and experimental examples from the recent literature.

3.1
Pressure and the Configuration Coordinate Model

A single configuration coordinate model with linear electron-phonon coupling [134, 135] is appropriate for the analysis of most high pressure luminescence experiments. A depiction of the single configuration coordinate model is shown in Fig. 2 a. The ground and excited electronic states involved in a luminescence process are shown. The model is based on harmonic potential wells with equal force constants for both electronic states and includes vibrational sublevels separated by a phonon frequency $\hbar\omega$. The model assumes coupling of the luminescent center to a single, totally symmetric vibrational mode. The other key parameters in the model are E_0, the zero phonon energy, and S, the Huang-Rhys factor. The value of S is a measure of the strength of coupling of the luminescent center to the surrounding lattice. S ranges from values close to zero for f → f transitions of lanthanides to values of 4 or 5 for spin allowed d → d transitions of transition metals. The value of S is an important factor in determining the lineshape of a luminescence transitions (Fig. 2 b).

In the context of the single configuration coordinate model, pressure can potentially influence E_0, S, and $\hbar\omega$. Changes in E_0 lead to shifts of electronic energy

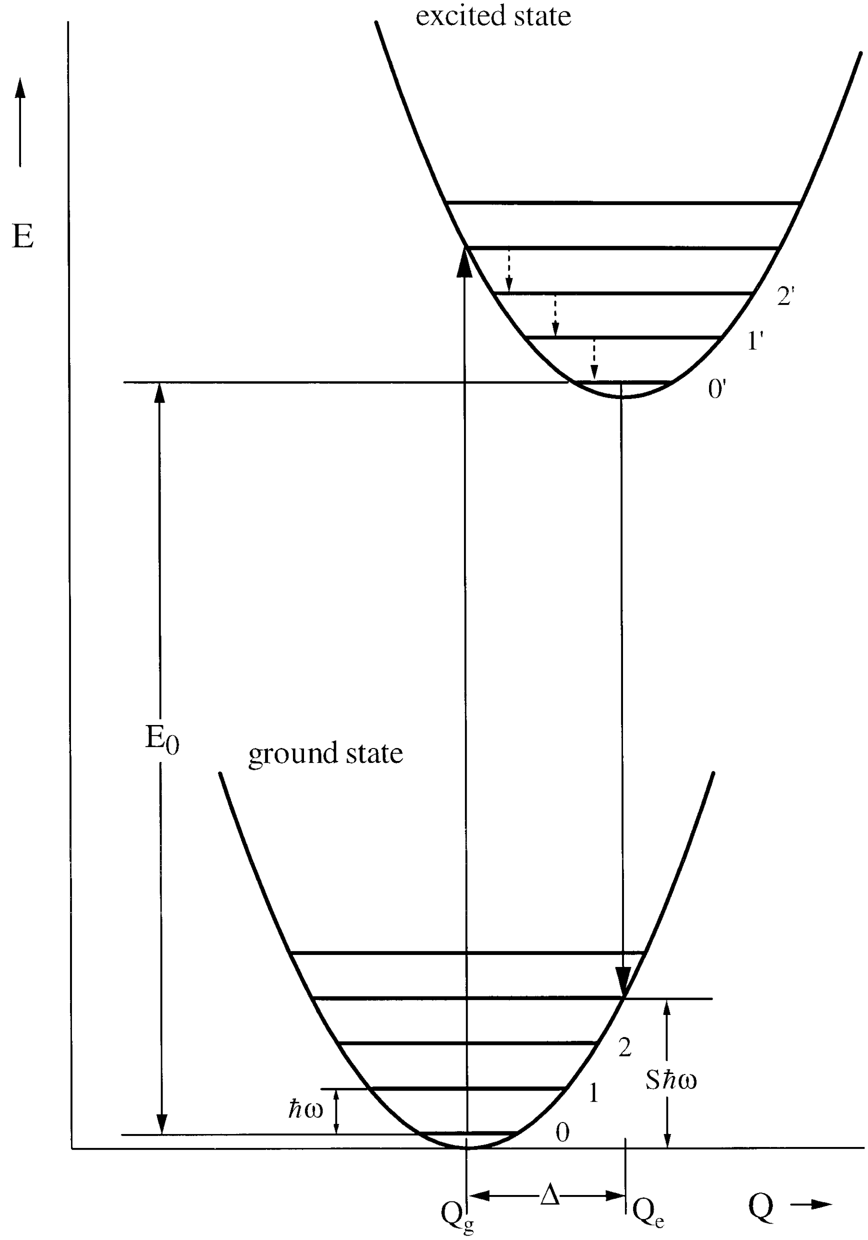

Fig. 2a. The single configuration coordinate model of luminescence centers. The energies of the ground and excited states of a luminescence transition are shown as a function of a totally symmetric configuration coordinate Q. 0, 1, 2 … and 0′, 1′, 2′, … denote vibrational sub-levels corresponding to a single coupling mode with energy $\hbar\omega$. E_0 denotes the zero phonon energy and S the Huang-Rhys factor of the transition. Solid and dashed arrows represent radiative and non-radiative processes, respectively.

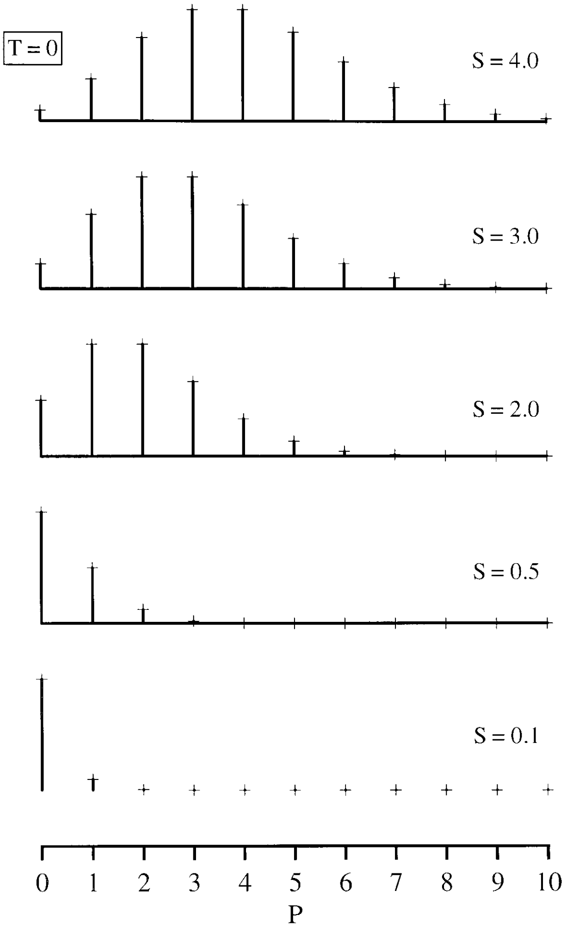

Fig. 2 b. Calculated influence of S on the lineshape of a luminescence transition at T = 0 K. Intensity (*vertical lines capped with* "+") as a function of energy relative to the zero phonon energy is shown. P represents energy in multiples of the coupling phonon energy $\hbar\omega$ shown in Fig. 2a. P = 0 corresponds to the zero phonon energy. In the weak coupling limit (small S), most luminescence intensity occurs in the zero phonon line and sharp luminescence spectra result. Upon increasing coupling strength of the luminescence center to the lattice, S increases and luminescence intensity is progressively distributed into the (Stokes) sideband to produce a broad luminescence band

states with pressure. Depending on the nature of the electronic states, shifts of absorption and luminescence transitions to higher (blue shifts) or lower (red shifts) energy can occur with pressure. Changes in S reflect changes in the strength of lattice coupling of the luminescent center in the excited state relative to the ground state with pressure. Experimentally, changes in S are observed as changes in linewidth with pressure. The linewidth is also influenced by changes in phonon frequency with pressure. The variation of phonon frequency with pressure is normally quantified by the mode Grüneisen parameter γ:

$$\gamma = -\frac{V}{\omega}\left(\frac{\partial\omega}{\partial V}\right)_T \tag{4}$$

Phonon frequencies normally increase slightly with pressure so that small positive values for γ are normally observed.

Unambiguous quantification of the pressure variation of single configuration coordinate model parameters is complicated by the fact that all of the parameters can vary simultaneously. Changes in luminescence energy can be accurately measured with pressure and, in the case of narrow transition metal or lanthanide transitions, the zero phonon energy E_0 can be readily determined as a function of pressure. The pressure variation of the peak maximum of broad luminescence bands can also normally be accurately measured, but determination of the zero phonon energy of broad bands requires information about the variations of S and $\hbar\omega$. The pressure variation of phonon energies can be measured directly in Raman or IR experiments. Relating phonon energies to the configuration coordinate model, however, is difficult because the model is based on coupling of the luminescent center to the lattice through an idealized totally symmetric mode that represents an undetermined average of all modes that couple to the center. The case of low concentration transition metal and lanthanide dopants presents the additional difficulty of needing local, rather than lattice, mode information. Mode coupling information can be obtained from the well-resolved phonon sidebands of narrowline spectra, but is frequently obscured in broadband spectra.

Once a plausible identification of an average coupling mode energy is made, further determination of S still requires experimental linewidth data. Spectral linewidths can be accurately determined as a function of pressure, but are subject to some difficulties in interpretation because inhomogeneous broadening effects contribute to the experimental linewidth. Multisite behavior is one source of inhomogeneous broadening. Multiple bonding environments are easily distinguished for systems with narrow line spectra, but are difficult to detect in broadband spectra. Strain broadening and pressure inhomogeneities are additional sources of inhomogeneous broadening in high pressure experiments. Pressure inhomogeneities are spatial variations in pressure that can occur in a sample chamber. When present, pressure inhomogeneities lead to slightly different emission energies from sample pieces located at different positions in the sample chamber. Since the measured spectrum normally represents a superposition of all sample pieces, an inhomogeneously broadened linewidth results. The pressure gradients associated with inhomogeneities also introduce uniaxial and higher order strain effects that can influence spectral lineshapes independently of any hydrostatic pressure effects. The existence of pressure-related inhomogeneous broadening effects has been recognized previously, but is only now beginning to be appreciated seriously [55, 123, 133, 136]. Inhomogeneous broadening also complicates using the temperature dependence of linewidth as additional data for determining S and $\hbar\omega$. The uncertainties in establishing the pressure dependence of S and $\hbar\omega$ has limited application of the configuration coordinate model to approximate forms.

3.2
Energies of Electronic States

The ability of pressure to systematically vary the energies of electronic states is one of the unique attributes of using pressure to probe the luminescence properties of transition metal and lanthanide systems. Variations in bond lengths and bond angles with pressure influence electronic energies. The magnitude of pressure-induced effects is directly related to the stiffness of a material and the nature of the electronic state. Materials with high bulk moduli (Eq. 2) are difficult to compress, exhibit small volume changes per unit applied pressure, and generally show small pressure shifts of electronic energy states in comparison to systems with low bulk moduli.

The nature of an electronic state is important because it determines the interaction of the state with the surrounding lattice. States that interact strongly with the lattice are affected more significantly by pressure than states that interact weakly. Valence d orbital states of transition metals, for example, are more spatially extended than f orbital states of lanthanides and are consequently influenced to a greater degree by pressure. When considering the effect of pressure on luminescence transitions, we need to consider the extent to which the strength of lattice interaction changes as we go from the excited state to the ground state. Significant pressure effects are anticipated when the strength of interaction of the excited state with the lattice differs appreciably from that of the ground state. In transition metal systems, we expect large pressure shifts for d → d transitions in which the d orbital occupancy changes. Spin flip d → d transitions, on the contrary, involve ground and excited states with the same d orbital occupancy and a similar strength of interaction with the lattice. Consequently, spin flip transitions are expected to show small shifts with pressure. The shielded nature of f orbitals leads to weak interactions of f electronic states with the lattice and to small anticipated effects of pressure on f → f transitions of lanthanide ions regardless of f orbital occupancy. In contrast, f → d transitions include one configuration that interacts strongly with the lattice and one that interacts weakly. Large pressure shifts are expected as a result. Charge transfer transitions of transition metal or lanthanide ions in solids or complexes can involve a significant redistribution of electron density and are also expected to exhibit significant pressure shifts.

Theoretical models of the effects of pressure on electronic energy states need to consider pressure-induced changes in nearest neighbor coordination environment, covalency, orbital overlap, secondary interactions with more distant neighbors in the lattice, and overall lattice structure. Inorganic systems containing stoichiometric amounts of transition metal and lanthanide ions are amenable to modern synchrotron X-ray high pressure structure methods. These methods can provide valuable structural data for modeling electronic properties.

Many of the systems of interest to the optical materials community, however, are based on host lattices that contain non-stoichiometric, doping (~ 1 % or less) concentrations of transition metal or lanthanide ions. The low concentrations preclude the use of X-ray methods to obtain local structural information as a function of pressure. When dopants enter into a lattice, they introduce a local perturbation to the lattice structure and occupy sites that are structurally distorted relative to the lattice. Since these perturbations can have a significant effect on optical properties, it is important to understand them and their variation with pressure. In large samples, local structural information can in principle be obtained through EXAFS (Extended X-ray Absorption Fine Structure). EXAFS experiments on the small samples required for high pressure are much more difficult and are only now becoming feasible for ideal systems [57, 59]. Using EXAFS to distinguish local features of dopants, relative to lattice features, is not currently possible. Structure measurements of organometallic complexes provide the additional complication of needing to distinguish light elements such as C and N in the sample from the diamond.

As a result of the difficulties in obtaining local structural information, theoretical models are generally based on approximations and tested indirectly through optical or vibrational spectroscopy. The simplest theoretical treatments are based on isotropic compression. Isotropic compression models are scaling models that assume no changes in bond angles and preservation of local symmetry. Dopant ions are presumed to behave identically with the lattice ion for which they substitute. Pressure effects are attributed solely to symmetric bond compression and are scaled to changes in pressure or volume as dictated by the bulk modulus or equation of state of the host lattice. Metal ions in complexes can be treated in a similar fashion. When equations of state are unavailable, a physically plausible form is normally assumed and used to model spectroscopic data. A higher level of consideration is to assume symmetric compression using a local dopant compressibility that differs from that of the host lattice. These models attempt to account for the fact that the interaction of a dopant with a host lattice differs from that of the ion for which the dopant substitutes. Similarly, in complexes, a local central metal ion compressibility that differs from the crystal lattice compressibility can be used. The highest level of consideration includes local structural distortions of the dopant relative to the symmetry of the host lattice and directional asymmetries in compressibility. No studies currently available provide sufficient data to justify treatment at this level.

In the following sections, we consider theoretical and experimental aspects of the influence of pressure on electronic energies. We emphasize the two major effects, covalency and crystal field strength, that are responsible for determining electronic energies in transition metal and lanthanide systems. For convenience of discussion, we choose to treat covalency and crystal field effects separately and to describe each effect with an independent set of theoretical parameters. We note, however, that the separation of covalency and crystal field effects is only approximate and that each effect influences the parameter values of the other effect to some extent in most systems. Our discussion will focus on experimental variations of covalency (B, C and F_k) and crystal field strength (Dq, B_{kq}) parameters with pressure and the predictions of the theoretical models that have been proposed to explain the variations.

3.2.1
$d \rightarrow d$ Luminescence Transitions

3.2.1.1
Covalency Effects

3.2.1.1.1
Recent Experimental Results

Nearest neighbor covalency effects in transition metal systems are normally described by the two Racah parameters B and C. Qualitatively, reductions in B and C are predicted to occur with pressure due to enhancements in covalency expected from increased metal-ligand orbital overlap as the nearest neighbor bond length decreases. In order to assess the effect of pressure on B and C, the effect of pressure on Dq needs to be known or transitions whose energies are independent or approximately independent of Dq need to be considered. The effect of pressure on Dq will be considered below and can be determined experimentally. If suitable spectroscopic data in absorption and/or emission is available, it is therefore possible to determine the effect of pressure on B and C.

Experimental consideration of the effect of pressure on B and C has focused on the R line ($^2E \rightarrow {}^4A_2$) emission of Cr^{3+} in ruby because of the availability of extensive ruby R line pressure calibration data (see Sect. 2.2.1). In regular octahedral symmetry, over the range of values $1.5 < Dq/B < 3.5$ and $3 < C/B < 5$ normally encountered for Cr^{3+}, the energy of the $^2E \rightarrow {}^4A_2$ transition is given approximately by [134]

$$E(^2E) = 3.05\,C + 7.90\,B - 1.80\left(\frac{B^2}{Dq}\right) \tag{5}$$

Although there is some variation in the literature [93, 144, 145], the ambient pressure parameter values for ruby are generally taken to be B ~650 cm^{-1}, C ~3200 cm^{-1}, and Dq ~1810 cm^{-1} [134, 146, 147]. From Eq. (5), we therefore see that the Dq dependent contribution accounts for less than 3% of the ^2E energy at ambient pressure and that, to a reasonable approximation, the ^2E energy is determined by B and C at ambient pressure. Since Dq increases with pressure (see below), the approximation remains valid at high pressure.

At room temperature, the ruby R line shift is linear up to ~200 kbar with a slope of 0.365 Å/kbar (–0.759 cm^{-1}/kbar) (Sect. 2.2.1). Data analysis is generally based on the assumption of variable B and a constant B/C ratio with pressure. In the case of ruby, analysis of the R line red shift and other spectral transitions as a function of pressure has led to an estimated decrease in B in the range ~0.02–0.1 cm^{-1}/kbar depending on the pressure range considered, approximations employed, and the number of transitions included in the analysis [93, 145–147]. R line emission from Cr^{3+} has also been measured in alexandrite and several garnets (Table 2). Although the variation of B with pressure for these systems has not been directly reported, the observed ^2E shift rates are similar to ruby and suggest comparably small decreases in B. A similar decrease in B (–0.068 cm^{-1}/kbar) was reported for Cr^{3+} in uvarovite garnet ($Ca_3Cr_2Si_3O_{12}$) by

Table 2. R_1 line shifts (nm or cm^{-1}) with pressure of Cr^{3+} in several host lattices and complexes

Host lattice or complex	$\Delta\lambda_{R_1}\left(\frac{nm}{kbar}\right)$	$\Delta E_{R_1}\left(\frac{cm^{-1}}{kbar}\right)$	Pressure range (kbar)	T (K)	Ref.
$BeAl_2O_4$	0.0292		0–500	273	[97] [a]
	0.027		0–40	300	[98]
		–0.062	0–70	300	[137]
		–0.062	0–120	77, 300	[138]
Al_2O_3 [b]	0.0365	–0.754	0–195	298	[87]
	0.0365		0–200	RT	[92]
		–0.759	0–100	299	[96]
$La_3Lu_2Ga_3O_{12}$		–0.8	~100–152	RT	[139]
$Y_3Al_5O_{12}$		–0.8	0–240	RT	[113]
	0.0377		0–120	RT	[140]
$Gd_3Ga_5O_{12}$		–0.65	~25–110	300	[141]
$Gd_3Sc_2Ga_3O_{12}$		–0.65	~60–120	300	[141]
Cs_2NaYCl_6		–3.77	~85–115	86	[142]
$[Cr(H_2NC(O)NH_2)_6](ClO_4)_3$		–5.5	0–23	120	[143]

RT = Room Temperature.

[a] [97] also reports a quadratic correction (1.3×10^{-5} $cm^{-1}/kbar^2$).

[b] See Sect. 2.2.1 for non-linear corrections above ~200 kbar.

Abu-Eid on the basis of $^4A_2 \rightarrow {}^4T_2, {}^4T_1$ absorption spectra as a function of pressure [148].

Table 2 also contains data for one non-oxide host lattice and one Cr^{3+} complex. The much larger ^2E shifts observed in these three systems is a consequence of the highly compressible nature of halide lattices and molecular complexes relative to oxide lattices. The bulk modulus of Cs_2NaYCl_6 (~495 kbar [142]) is about five times smaller than that of ruby (2530 kbar [149, 150]) and is primarily responsible for the difference in shift rate. A similar explanation holds for the Cr^{3+} complex. When normalized to compressibility, therefore, the variation in B for all of the systems in Table 2 is comparable.

Other evidence of weak variations of B with pressure is found in absorption and emission studies of d^5 (Mn^{2+}, Fe^{3+}) and d^2 (Cr^{4+}, Mn^{5+}) systems. In high spin octahedral d^5 systems, the energy of two visible absorption transitions are independent of Dq:

$$\begin{aligned} E(^6A_{1g} &\rightarrow {}^4A_{1g}, {}^4E(^4G)) = 10B + 5C \\ E(^6A_{1g} &\rightarrow {}^4E_{1g}(^4D)) = 17B + 5C \end{aligned} \qquad (6)$$

Smith and Langer [151] found a –1.8 cm^{-1}/kbar shift up to 112 kbar for the $^6A_{1g} \rightarrow {}^4A_{1g}, {}^4E_g$ (^4G) transition of Mn^{2+} in $Mn_3Al_2Si_3O_{12}$ and attributed it to a 0.06 cm^{-1}/kbar decrease in B. High spin Mn^{2+} has also been studied in the chalcogenide phosphor systems ZnS, ZnSe, and ZnTe [152–156]. Mayrhofer et al. [152], for example, observed shifts of –10.5 cm^{-1}/kbar and –14.5 cm^{-1}/kbar up to 100 kbar for the $^6A_{1g} \rightarrow {}^4A_{1g}, {}^4E_g$ (^4G), and $^6A_{1g} \rightarrow {}^4E_g$ (^4D) absorption bands, respectively, of Mn^{2+}:ZnS and concluded that B decreased by ~0.34 cm^{-1}/kbar. Similar behavior has been observed for Fe^{3+} in $Ca_3Fe_2Si_3O_{12}$ [148].

Tetrahedral d^2 ion systems have been recently studied by Shen et al. [157, 158]. Depending on the crystal field strength, $^3T_2 \rightarrow {}^3A_2$ or $^1E \rightarrow {}^3A_2$ emission can occur in d^2 systems. The energy of the intraconfigurational spin flip $^1E \rightarrow {}^3A_2$ transition is given approximately by [159]

$$E(^1E \rightarrow {}^3A_2) = 8B + 2C - \frac{6B^2}{10Dq} \tag{7}$$

As in the case of the $^2E \rightarrow {}^4A_2$ emission of Cr^{3+}, a weak dependence on Dq is expected. The spectroscopy of d^2 ions is complicated by distortions from regular tetrahedral symmetry that influence electronic energies and alter the prediction of Eq. (7). In Mn^{5+}:Y_2SiO_5, Shen et al. reported that distortion effects were unimportant above ~100 kbar and that the $^1E \rightarrow {}^3A_2$ luminescence energy was constant within experimental uncertainty in the absence of site distortion effects [158]. A similarly weak dependence of the $^1E \rightarrow {}^3A_2$ luminescence energy was observed in Cr^{4+}: $Y_3Al_5O_{12}$ at high pressure after an electronic crossover of the $^3T_2$ and ^1E states was induced [157]. The weak shift observed for the ^1E emission indicates only small changes in B with pressure in the d^2 systems.

3.2.1.1.2
Quantitative Considerations

Munro's early semi-empirical treatment [146] of the R line shift in ruby with pressure was an isotropic compression model based on a central field covalency mechanism [160]. According to central field covalency, reduced nearest neighbor bond lengths with pressure lead to greater penetration of ligand lone pair electrons into the metal ion valence shell and increased screening of the valence electrons from the nucleus. The net result is a reduction in the effective nuclear charge and an expansion of the valence shell. In his model, Munro proposed that the effect of pressure could be simulated by scaling the force laws that govern interelectronic repulsion and electron-nucleus attraction. Munro scaled the squared electronic charge (e^2) and the nuclear charge number (Z) according to

$$\begin{aligned} e^2 &\rightarrow \Lambda(P)e^2 \\ Z &\rightarrow \frac{\Omega(P)}{\Lambda(P)} Z \end{aligned} \tag{8}$$

where $\Lambda(P) = 1 + \delta\Lambda P$, $\Omega(P) = 1 + \delta\Omega P$, and $\delta\Lambda$ and $\delta\Omega$ are adjustable parameters. These equations were used to scale Dq, B, and C to model the effect of pressure on the energies of the R lines and other electronic transitions of ruby. The predicted variation of B from Munro's theory was given by $B = B_0\Lambda(P)\Omega(P)$ where $B_0 = 680$ cm^{-1} is the ambient pressure value. By fitting the pressure shifts of several transitions, Munro predicted a linear variation of B (−0.0204 cm^{-1}/kbar) and constant B/C ratio as a function of pressure.

Eggert et al. [90] modified Munro's approach by scaling through volume, rather than pressure. They proposed $\Lambda(P) = 1 + \delta\Lambda dV$, $\Omega(P) = 1 + \delta\Omega dV$, with

$$dV = \frac{V(P) - V_0}{V(P)} \tag{9}$$

and used the Birch-Murnaghan equation of state for ruby [150, 161] to relate pressure to volume. With their approach, Eggert et al. were able to maintain a two parameter model and extend its range of validity to 1560 kbar for the R line shifts using the optimized values $\delta\Lambda = 0.129$ and $\delta\Omega = -0.051$. Eggert et al. did not directly report the variation of B with pressure, but their results can be used to deduce a non-linear decrease in B with positive curvature and an initial slope of -0.019 cm^{-1}/kbar.

Ma et al. [147, 162, 163] argued that pressure-induced covalency effects can be understood in terms of the radial expansion of the valence electron wavefunctions as the nearest neighbor bond length decreases with pressure. They considered an isotropic compression model based on the scaling of the Slater integrals F^k upon which B and C are defined ($B = F^2/49 - 5F^4/441$, $C = 35F^4/441$) in terms of a function of the ratio of the nearest neighbor bond lengths at high pressure (R_p) and ambient pressure (R_0). The nearest neighbor bond length ratio was assumed to be equal to the cube root of the unit cell volume ratio Vp/V_0 of ruby as a function of pressure and was obtained from the equation of state of ruby [164]. By expressing the R line energy in terms of the scaled Slater integrals, Ma et al. were able to reproduce the ruby R line red shift data up to 1700 kbar using a model with only two parameters. The approach of Ma et al. predicted a non-linear decrease in B and a constant B/C ratio with pressure. The decrease in B was most pronounced at low pressure (initial slope ~ -0.042 cm^{-1}/kbar) and became more gradual with increasing pressure. The model of Ma et al. also suggested an underlying physical basis for the empirical equation proposed by Mao and Bell (Eq. 3). Ma et al. also successfully applied their model to the R line transitions of Cr^{3+}:MgO and obtained a nearly linear decrease in B up to 140 kbar (~ -0.032 cm^{-1}/kbar) [165].

Zhao et al. [144, 166] proposed an approach based on symmetry restricted covalency [167]. Symmetry restricted covalency attributes covalency effects to the delocalization of d electron density onto ligand orbitals through σ and π molecular orbital formation between metal d orbitals and ligand s, p, and/or d orbitals [168]. The formation of molecular orbitals occurs between metal d orbitals and ligand orbitals of the same symmetry and varies with the coordination environment. The delocalization of d electron density that occurs upon molecular orbital formation leads to a reduction in the Racah B and C parameter values from the free ion values B_0 and C_0. The reduction can be expressed by

$$\begin{aligned} B &= N^4 B_0 \\ C &= N^4 C_0 \end{aligned} \tag{10}$$

where the covalency reduction factor N is a measure of the extent of metal-ligand orbital mixing (including σ and π bonding contributions) and is obtained empirically. In their original paper [144], Zhao et al. do not directly report the variation of B with pressure for ruby. They do, however, report the variation of the R-line splitting and observe excellent agreement with experiment.

Zheng [169, 170] used an approach based on Zhao's model and scaled the covalency reduction factor through the equation of state of ruby. Zheng proposed

$$B(P) = B_0 f_{\mathrm{n}} \left[1 + \left(\frac{d \ln f}{d \ln R} \right) \left(\frac{d Ln R}{dP} \right) P \right] \tag{11}$$

where f is the same as N^4 in Zhao's model (Eq. 10), $f_n = 0.8677$ is the value of f at ambient pressure, B_0 is the free ion value, and R is the nearest neighbor bond length. Zheng assumed that variations in R with pressure scaled with $V^{1/3}$ where the unit cell volume V is obtained from the equation of state of ruby. Zheng used Eq. (11) to fit the ruby R-line pressure shift data and obtained a –0.062 $\mathrm{cm^{-1}}$/kbar change in B with pressure. Zheng also applied his model to the R line shifts of Cr^{3+}:$Y_3Al_5O_{12}$ [140], Cr^{3+}:$Gd_3Ga_5O_{12}$ [141], and Cr^{3+}:$Gd_3Sc_2Ga_3O_{12}$ [141], and found that B changed at a rate of –0.065 $\mathrm{cm^{-1}}$/kbar, –0.068 $\mathrm{cm^{-1}}$/kbar, and –0.068 $\mathrm{cm^{-1}}$/kbar in the three systems, respectively. Zheng et al. [171] similarly considered the $^3A_2 \rightarrow {}^3T_1, {}^3T_2$ absorption transitions of NiO and reported essentially no change in B with pressure (–0.0029 $\mathrm{cm^{-1}}$/kbar).

In a later paper [166], Zhao extended his model for ruby to include off-center site displacements of Cr^{3+}. The model accounts for the fact that Cr^{3+} does not substitute exactly into Al^{3+} sites, but rather is displaced along the trigonal axis. Zhao quantitatively included the position of Cr^{3+} relative to an Al^{3+} lattice site as a function of pressure in his model and re-evaluated the R-line shift data up to 1650 kbar. Zhao's extended model predicted a –0.0489 $\mathrm{cm^{-1}}$/kbar change in B with pressure up to 400 kbar and a constant value ($B = 784\ \mathrm{cm^{-1}}$) above 400 kbar.

3.2.1.2
Crystal Field Effects

3.2.1.2.1
Recent Experimental Results

The preceding section has shown that pressure leads to a small decrease in the Racah parameter B of transition metal systems. The small change in B indicates that pressure only weakly increases bonding covalency in transition metal systems. As a result, the energies of electronic transitions that depend primarily on covalency effects are expected to exhibit weak shifts to lower energy with pressure.

In this section we discuss electronic transitions with energies that depend primarily on the crystal field strength parameter Dq. Consideration of a simple point charge model of crystal field effects leads one to expect significant changes in Dq with pressure. In the case of an octahedral distribution of point ligands each with charge –Ze located at a distance R from a central transition metal ion (Fig. 3), the crystal field strength parameter is given by [134, 172]

$$Dq = \frac{Ze^2}{6R^5} \left\langle r^4 \right\rangle_{\mathrm{d}} \tag{12}$$

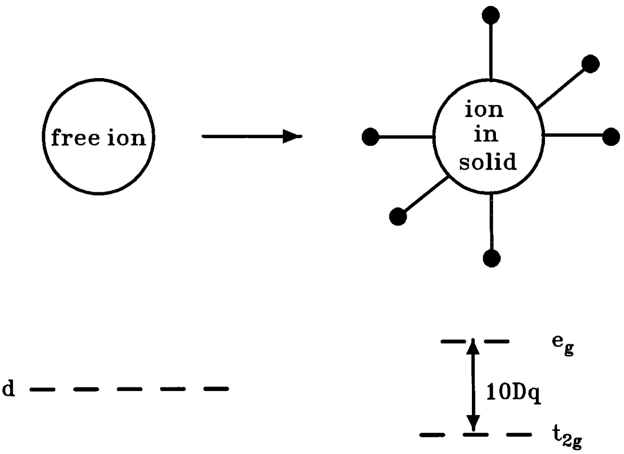

Fig. 3. Schematic depiction of the octahedral point charge crystal field model. In the free ion, the set of five d orbitals is degenerate. When the ion is placed in a solid and bonds to six nearest neighbor ligands arranged in an octahedral geometry, the d orbitals split into e_g (d_{z^2}, $d_{z^2-y^2}$) and t_{2g} (d_{xy}, d_{xy}, d_{yz}) subsets separated by an energy 10Dq

Equation (12) predicts a strong sensitivity of Dq to nearest neighbor bond length. Since pressure directly influences the nearest neighbor bond length, we expect significant changes in crystal field strength with pressure.

Most recent experimental studies of the effect of pressure on crystal field strength have considered the $^4T_2 \rightarrow {}^4A_2$ luminescence transition of Cr^{3+} because the zero phonon energy difference between the $^4T_2$ and $^4A_2$ states is simply 10 Dq. Table 3 summarizes recent high pressure studies of crystal field strength in Cr^{3+} systems. The table reports the variation of the energy of the $^4T_2$ level relative to the $^4A_2$ level as determined from absorption, luminescence, or luminescence excitation spectroscopy as a function of pressure. The reported shift rates for the $^4T_2 \leftrightarrow {}^4A_2$ transition correspond to peak maxima, rather than zero phonon energies, and range from 8.4 to 35 cm^{-1}/kbar. Similar to the $^2E \rightarrow {}^4A_2$ transition, we observe larger shifts for the more compressible (lower bulk moduli) halides and complexes than for the stiffer oxide materials. A comparison of Tables 2 and 3 reveals that the shift of the $^4T_2$ state is an order of magnitude greater than the shift of the ^2E state with pressure for chemically similar systems.

The most comprehensive experimental study of the effect of pressure on crystal field effects in a Cr^{3+} system was reported by Duclos et al. [145] who completed a luminescence excitation study of ruby up to 350 kbar. They recorded the $^4A_2 \rightarrow {}^4T_2$ and $^4A_2 \rightarrow {}^4T_1$ transitions in excitation while monitoring the $^2E \rightarrow {}^4A_2$ emission. A noteworthy feature of the study was the inclusion of vibronic coupling effects in the crystal field analysis. The vast majority of previous high pressure studies assumed the validity of the Tanabe-Sugano (pure electronic) model [179] without modification. Duclos et al. considered the effect of pressure on bandshapes and determined variations in zero phonon energies of the $^4T_2$ and $^4T_1$ levels with pressure using the configuration coordinate model of Struck and Fonger [135]. Using the zero phonon ^2E, $^4T_2$, and $^4T_1$ energies obtained from

Table 3. Pressure shift (cm^{-1}/kbar) of the $^4T_2 \leftrightarrow {}^4A_2$ transition of Cr^{3+} in several host lattices and complexes

Host lattice or complex	$\Delta E \left(\frac{cm^{-1}}{kbar}\right)$	Experiment[a]	Pressure range (kbar)	T (K)	Ref.
$La_3Lu_2Ga_3O_{12}$	10	L	0–~110	RT	[139]
$Y_3Al_5O_{12}$	9	L	0–40	RT	[140]
$Gd_3Sc_2Ga_3O_{12}$	~10	L	0–~40	300	[141]
$Gd_3Ga_5O_{12}$	~10	L	0–~20	300	[141]
Al_2O_3	8.4	LE	0–350	RT	[145]
$KZnF_3$	17.9	L	0–80	300	[173]
	16.7	L	0–50	90	[173]
$Na_3In_2Li_3F_{12}$	14.8	L	0–90	300	[174]
K_2NaGaF_6	18.0	L	0–61	RT	[175]
K_2NaScF_6	17.6	L	0–70	RT	[176]
Cs_2NaYCl_6	25.7	L	0–~70	RT	[142]
$(NH_4)_3CrF_6$	~ 9	L	0–71	22	[177]
$[LCr(OH)_3CrL](ClO_4)_3$[b]	35	A	0–48	RT	[178]
$[(NH_3)_5Cr(OH)Cr(NH_3)_5]Cl_5 \cdot H_2O$	21	A	0–50	RT	[178]

RT = Room Temperature.

[a] L = Luminescence; A = Absorption; LE = Luminescence excitation of $^2E \rightarrow {}^4A_2$ emission.

[b] L = 1,4,7-trimethyl-1,4,7-triazacyclononane.

their lineshape analysis, Duclos et al. determined the variations of Dq (1673 cm^{-1} + 0.84 P(kbar)), B (468 cm^{-1} – 0.11 P(kbar)), and C (3402 cm^{-1} + 0.08 P(kbar)) with pressure. Their ability to obtain data for the $^4T_1$ level permitted independent determination of C and allowed them to show that the B/C ratio decreases with pressure. This finding indicates for the first time that the assumption of a constant B/C ratio commonly used in high pressure studies may not be valid.

The effect of pressure on crystal field strength in several Mn^{2+} systems has also been reported. The electronic structure of Mn^{2+} is convenient for the determination of crystal field strength because Dq and B can be determined independently (see Sect. 3.2.1.1 for a discussion of B). Once the variation of B is known, the energies of transitions from the $^6A_1$ ground state to any of the $^4T_1(^4G)$, $^4T_2(^4G)$, or $^4T_2(^4D)$ excited states can be used to determine the effect of pressure on Dq. Increases in Dq with pressure of 0.89 cm^{-1}/kbar and 1.45 cm^{-1}/kbar have been reported for Mn^{2+} in ZnS [152] and ZnTe [180], respectively.

3.2.1.2.2
Quantitative Considerations

Quantitative treatments of the effect of pressure on crystal field strength can be approached through Eq. (13):

$$\frac{dDq}{dP} = \left(\frac{dDq}{dR}\right)\left(\frac{dR}{dP}\right) \tag{13}$$

Equation (13) indicates that an understanding of the variation of crystal field strength with pressure requires knowledge of the variation of Dq with the nearest neighbor bond length R and the variation of R with P. Much of the theoretical work has been directed at these two quantities.

The simplest description of the effect of pressure on crystal field strength assumes that the variation of Dq with R is given by the point charge model (Eq. 12) and that the variation of R with P can be directly obtained from the volume of the host lattice through its equation of state. According to this approach, the predicted effect of pressure on crystal field strength is given by

$$\frac{Dq(P)}{Dq_0} = \left(\frac{R_0}{R(P)}\right)^5 = \left(\frac{V_0}{V(P)}\right)^{\frac{5}{3}} \tag{14}$$

where the subscript "0" denotes a quantity at ambient pressure and V(P) is obtained from the equation of state. Equation (14) can also be inverted to obtain a prediction of the effect of pressure on the volume of the host lattice from spectroscopic data when the equation of state is unknown. This approach has been widely used in geophysics and has been discussed in detail by Burns [172, 181].

Several studies have focused on whether the R^{-5} distance dependence assumed in the point charge model is accurate and on the validity of the assumption that the local structural changes in the vicinity of a dopant ion can be described by the equation of state for the host lattice. Since the two effects are difficult to separate experimentally, most studies have probed one assumption and assumed that the other is valid. Often the conclusions that are drawn are ambiguous. Duclos et al. [145], for example, found that an R^{-5} dependence overestimated the measured increase in Dq with pressure in their study of ruby when they assumed the validity of the ruby equation of state. An $R^{-4.5}$ dependence was found to represent the data better. They found equally good agreement, however, when they retained the R^{-5} dependence and assumed that the local bulk modulus (Eq. 2) in the vicinity of Cr^{3+} was 26% higher than that of the Al_2O_3 lattice. They argued that a higher local bulk modulus was physically reasonable since the radius of Cr^{3+} (0.615 Å) is larger than that of the Al^{3+} (0.53 Å) ion for which it substitutes.

The studies of ruby by Zhao [166], Zhao et al. [144], Munro [146], Ma et al. [147, 162, 163], and Eggert et al. [90] assumed the validity of the bulk crystal equation of state and obtained good agreement with the R-line shift data in their models. Zheng [169, 170], on the contrary, assumed the validity of the R^{-5} dependence of Dq and obtained good agreement with experimental R line shift data when using local bulk moduli of Cr^{3+} in $Y_3Al_5O_{12}$, $Gd_3Ga_5O_{12}$, and $Gd_3Sc_2Ga_3O_{12}$ that were higher by a factor of ~1.7 than expected from the host lattice equation of state.

At ambient pressure, Marco de Lucas et al. [182] and Rodriquez and Moreno [183] have considered the effect of nearest neighbor bond length on Dq in a series of octahedral Mn^{2+} fluoride systems (Mn^{2+}:$RbCdF_3$, Mn^{2+}:$RbCaF_3$, Mn^{2+}:$CsCaF_3$, $RbMnF_3$, Mn^{2+}:$KMgF_3$, Mn^{2+}:$KZnF_3$ and Mn^{2+}:$KMnF_3$). The systems were selected because they are among the few for which accurate nearest neighbor distances are available. The Mn-F distances in these systems range from 2.070 Å to 2.155 Å. Since the local Mn-F distance is known directly over a series of systems with the same structure type and local coordination geometry, the distance dependence of Dq can be obtained without consideration of the local bulk modulus. Using the zero phonon line of the $^4T_{1g} \leftrightarrow {}^4A_{1g}$ transition to determine Dq, an $R^{-4.7}$ dependence was found.

Marco de Lucas et al. [182] and Moreno et al. [184] further considered the distance dependence of the Huang-Rhys factor S and Stokes shift in general terms and derived a relationship that could be used to predict the variation of either quantity with nearest neighbor distance. Their model predicts that the magnitude of the Grüneisen parameter (Eq. 4) and the power dependence of the variation of Dq with R ultimately determines whether S and the Stokes shift increase or decrease with nearest neighbor distance in a given chromophore. Although these predictions have not yet been directly tested with pressure, they have important implications for high pressure studies.

Dolan et al. [176] and Rinzler et al. [142] presented a semi-empirical approach based on a single configuration coordinate model (see Sect. 3.1) for separating the effects of local compressibility and crystal field strength on pressure-induced changes in the $^4T_2$ energy of Cr^{3+} in several fluoride elpasolite systems. Their approach is based on an empirical form, motivated by the Born-Mayer potential, for the local compressibility $\kappa(P)$:

$$\kappa(P) = -\frac{1}{V}\left(\frac{dV}{dP}\right)_T = -\frac{3}{R_e}\left(\frac{dR_e}{dP}\right)_T = \kappa_0 \exp(-\alpha P) \tag{15}$$

where R_e is the Cr^{3+}-ligand distance in the relaxed excited state and κ_0 and α are adjustable parameters. They continued by assuming a general power law dependence form for the crystal field strength:

$$E({}^4T_{2g} \rightarrow {}^4A_g) = 10Dq_e\alpha(R_e)^{-n} \tag{16}$$

where Dq_e refers to the excited state crystal field strength of Cr^{3+} and is obtained from the peak maximum of the $^4T_{2g} \rightarrow {}^4A_g$ emission band. In this model, the pressure-induced shift of the $^4T_{2g} \rightarrow {}^4A_g$ emission band is governed by n, κ_0 and α through

$$\frac{dE({}^4T_{2g} \rightarrow {}^4A_g)}{dP} \alpha - \frac{n}{R_e^{n+1}}\frac{dR_e}{dP}$$

$$\frac{1}{E({}^4T_{2g} \rightarrow {}^4A_g)}\frac{dE({}^4T_{2g} \rightarrow {}^4A_g)}{dP} = \frac{d\ln(E({}^4T_{2g} \rightarrow {}^4A_g))}{dP} = \frac{n}{3}\kappa(P)$$

$$= \frac{n}{3}\kappa_0 \exp(-\alpha P)$$

Integration gives

$$\ln\left(\frac{E({}^4T_{2g} \rightarrow {}^4A_g)}{E({}^4T_{2g} \rightarrow {}^4A_g)_0}\right) = \frac{n\kappa_0}{3\alpha}[1 - \exp(-\alpha P)] \tag{17}$$

where $E({}^4T_{2g} \rightarrow {}^4Ag)_0$ is the emission maximum at ambient pressure.

Dolan et al. [176] and Rinzler et al. [142] used Eq. (17) to fit the $^4T_{2g} \rightarrow {}^4A_g$ emission energy as a function of pressure to obtain values for $n\kappa_0$, α, and E_0 for

Table 4. Parameter values obtained from fits of Eq. (17) to experimental peak energies of the $^4T_2 \rightarrow {}^4A_2$ luminescence transition of Cr^{3+} as a function of pressure in three host lattices

Host lattice	$n\kappa_0$	α	E_0	n
K_2NaGaF_6	0.00633	0.01184	13155	4.53
K_2NaScF_6	0.00443	0.00263	12830	4.66
Cs_2NaYCl_6	0.01235	0.01281	10076	6.13

the three elpasolite systems listed in Table 4. The coupling of n and κ_0 in this approach captures the essence of the difficulty in separating the effects of local compressibility and the distance dependence of Dq. Dolan et al. [176] proposed that the value of n could be obtained independently from a single configuration coordinate model. Under the assumption of linear coupling to a totally symmetric vibrational mode, the Cr^{3+}-ligand distance R_i is simply $Q_i/\sqrt{6}$ where Q is the configuration coordinate and i = g or e denotes the ground or excited state, respectively. The crystal field strength Dq_i is therefore proportional to Q_i^{-n}. As a result, the energy of the $^4T_2$ state and its variation with Q_i can be written

$$
\begin{aligned}
E(^4T_{2g}) &= 10\,Dq_i\,\alpha\,10\,Q_i^{-n} \\
\frac{dE(^4T_{2g})}{dQ_i} &\quad \alpha - \frac{10n}{Q_i} Q_i^{-n} \\
&= -\frac{10n}{Q_i} Dq_i \\
&= -\frac{10n}{\sqrt{6}R_i} Dq_i
\end{aligned}
\tag{18}
$$

where $10\,Dq_g$ and $10\,Dq_e$ represent the $^4T_2$ peak maximum energy in absorption and emission, respectively.

We see from this model that the crystal field strength determines the horizontal displacement $\Delta = Q_e - Q_g$ of the $^4T_2$ excited state minimum and the Stokes shift $2S\,\hbar\omega$ between the $^4T_2$ absorption and emission maxima. Dolan et al. [176] recognized that the Stokes shift was related to the variation of $E(^4T_2)$ with Q at Q_g through [135]

$$
\left.\frac{dE(^4T_2)}{dQ}\right|_{Q=Q_g} = -M\omega^2\Delta = -M\omega^2\left(\frac{2\hbar S}{M\omega}\right)^{\frac{1}{2}} \tag{19}
$$

where M is the mass of a single halide ligand ion and R_g is assumed to equal the sum of the ionic radii of Cr^{3+} and the halide ligand. Eqations (18) and (19) may be combined to obtain an expression for n:

$$
n = \left[\frac{6\,MR_g^2\,\hbar\omega^3 S}{50\,Dq_g^2}\right]^{\frac{1}{2}} \tag{20}
$$

Dolan et al. [176] and Rinzler et al. [142] used ambient pressure Stokes shift and vibrational frequency data and Eq. (20) to evaluate n for the three elpasolites listed in Table 4. The values of n are seen to deviate appreciably from 5. Other features of the method developed by Dolan et al. [176] and Rinzler et al. [142] include analysis of vibrational mode frequencies and thermal quenching effects as a function of pressure.

3.2.2
f → f Luminescence Transitions

The underlying phenomena associated with the energies of f → f transitions in lanthanides are similar to those described above for d → d transitions in transition metal systems. The principal difference between f orbitals and d orbitals is the restricted spatial extent of the former. The 4f orbitals of lanthanides are shielded by 4d orbitals and interact only weakly with surrounding ligands. As a result, f → f transitions are less sensitive to pressure than d → d transitions.

Covalency and crystal field effects in lanthanide systems are normally described by the Slater parameters F_k ($k = 2, 4, 6$) and the crystal field parameters B_{kq} (k, q depend on the symmetry of the lanthanide bonding environment). In contrast to transition metal systems, covalency and crystal field effects are coupled in lanthanide systems and cannot be considered separately through judicious selection of optical transitions. As a result, the covalency and crystal field parameters are obtained simultaneously during an analysis of crystal field transitions as a function of pressure. Analysis of crystal field energies involves a determination of $^{2S+1}L_J$ multiplet barycenter (free ion) energies in an intermediate coupling scheme followed by perturbations of these energies by a crystal field. The barycenter energies are quantified through the F_k covalency parameters and the spin-orbit coupling constant ζ. F_k and ζ experience a decrease from their free ion values through the nephelauxetic effect when a lanthanide ion is placed in a chemical environment. The crystal field perturbations are quantified by the B_{kq} parameters. Several discussions and examples of the methods used to analyze crystal field energies of lanthanide systems at ambient pressure are available [134, 185, 186]. In the following discussion, we consider recent work on the effect of pressure on covalency and crystal field effects in lanthanide systems. Bond length reductions induced by pressure can be expected to enhance both nephelauxetic and crystal field effects.

3.2.2.1
Covalency Effects

Several studies of the variation of the Slater covalency parameters and spin-orbit coupling constant with pressure have appeared in the last decade and are summarized in Tables 5–7. The values in Tables 5 and 6 were obtained from an optimization of multiplet barycenter energies during a complete analysis of crystal field energies as a function of pressure for the listed systems. The reported values indicate that the variations of F_k and ζ_{4f} with pressure are generally small. The parameters are universally observed to decrease with pressure and are consistent with increased nearest neighbor bonding covalency at high pressure.

Theoretical modeling of the effect of pressure on nearest neighbor covalency in lanthanide systems has focused on the central field covalency and symmetry restricted covalency models (see Sect. 3.2.1.1) [144, 167, 191, 192]. In the central

Table 5. Ambient pressure values of the Slater covalency parameters F_k and spin-orbit coupling constant ζ for several lanthanides in various host lattices

Lanthanide	Host lattice	F_2 (cm^{-1})	F_4 (cm^{-1})	F_6 (cm^{-1})	ζ_{4f} (cm^{-1})	Ref.
Pr^{3+}	$LaCl_3$	304.4	45.47	4.41	749.2	[187]
	$LaCl_3$	304.0	46.07	4.47	746.3	[188]
	$PrCl_3$	314.3	36.87	5.07	749.1	[188]
	LaOCl	299.1	46.00	4.48	742.2	[189]
Nd^{3+}	$LaCl_3$	319.7	47.9	4.83	876.2	[188]
	$NdCl_3$	319.2	48.0	4.82	872.3	[188]
Eu^{3+}	LaOBr	385.0	[a]	[a]	1357.5	[190]
	LaOBr	395.8	57.6		1373	[191]
	LaOCl	384.3	[a]	[a]	1349.5	[190]
	LaOCl	393	57.45	[b]	1364	[192]
	GdOCl	351.3	[c]	[c]	1336.3	[193]
	La_2O_2S	395.6	54.6	6.0	1333.1	[194]
	Gd_2O_2S	350.2			1331.0	[195]
	Y_2O_2S	349.9			1329.8	[196]
Sm^{2+}	BaFCl	332.0	[a]	[a]	1058	[190]
	SrFCl	330.7	[a]	[a]	1057	[190]
	CaFCl	328.8	[a]	[a]	1055	[190]

[a] The hydrogenic ratios $F_4/F_2 = 0.138$ and $F_6/F_2 = 0.0151$ were assumed.

[b] The hydrogenic ratio $F_4/F_6 = 9.139$ was assumed.

[c] The ratios $F_4/F_2 = 0.1484$ and $F_6/F_2 = 0.0161$ were assumed.

field covalency model, covalency is attributed to spherically symmetric penetration of ligand electron density into the 4f valence shell. The penetration leads to additional screening of the 4f valence electrons from the nuclear charge and enhanced covalency through the consequent radial expansion of the 4f orbitals. Quantitatively, the expansion of 4f electron density is achieved by scaling the effective nuclear charge Z_{eff} through an expansion factor $\kappa < 1$ according to $Z_{eff} = \kappa Z^0_{eff}$ where Z^0_{eff} is the free ion value. Incorporation of Z_{eff} instead of Z^0_{eff} in the 4f radial wavefunction leads to $F_k = \kappa F^0_k$ and $\zeta_{4f} = \kappa^3 \zeta^0_{4f}$ where the superscript denotes the free ion value. The predicted relative changes in F_k and ζ_{4f} according to this model are

$$\frac{\Delta F_k}{F_k} = \frac{\Delta\kappa}{\kappa} \quad \text{and} \quad \frac{\Delta\zeta_{4f}}{\zeta_{4f}} = 3\,\frac{\Delta\kappa}{\kappa} \tag{21}$$

The central field covalency model predicts that the spin-orbit coupling constant is three times more sensitive to increased covalency than the interelectronic repulsion parameter F_k.

The symmetry restricted covalency model attributes covalency to bonding interactions and molecular orbital formation between ligand orbitals and the 4f valence orbitals. The participation of free ion 4f orbitals φ_m in molecular orbital formation leads to 4f radial expansion and enhanced covalency. Molecular orbital formation is directional (non-spherical) and is determined by the symmetry of the ligand distribution around the lanthanide. The lanthanide centered mole-

Table 6. High pressure values of the Slater covalency parameters F_k and spin-orbit coupling constant ζ for the systems listed in Table 5. The table entries correspond to values obtained at the maximum pressure (P_{max}) of each study. Linear variations between ambient pressure and P_{max} were reported for all parameters

Lanthanide	Host Lattice	F_2 (cm^{-1})	F_4 (cm^{-1})	F_6 (cm^{-1})	ζ_{4f} (cm^{-1})	P_{max} (kbar)	Ref.
Pr^{3+}	$LaCl_3$	300.8	45.20	4.38	746.7	80	[187]
	$LaCl_3$	300.7	45.71	4.43	742.9	80	[188]
	$PrCl_3$	308.0	36.78	4.87	745.1	80	[188]
	LaOCl	294.6	45.54	4.46	734.8	160	[189]
Nd^{3+}	$LaCl_3$	317.5	47.7	4.80	872.3	80	[188]
	$NdCl_3$	316.9	47.8	4.80	869.6	80	[188]
Eu^{3+}	LaOBr	382.6	[a]	[a]	1340	130	[190]
	LaOBr	389.5	57.2		1354	130	[191]
	LaOCl	382.2	[a]	[a]	1336	130	[190]
	LaOCl	388.3	57.15	[b]	1351	100	[192]
	GdOCl	349.9	[c]	[c]	1330.3	100	[193]
	La_2O_2S	394.1	54.39	5.98	1330.2	130	[194]
	Gd_2O_2S	348.5			1328.5	150	[195]
	Y_2O_2S	348.4			1327.4	130	[196]
Sm^{2+}	BaFCl	327.9	[a]	[a]	1053	80	[190]
	SrFCl	326.8	[a]	[a]	1051.5	80	[190]
	CaFCl	325.0	[a]	[a]	1052	80	[190]

[a] The hydrogenic ratios $F_4/F_2 = 0.138$ and $F_6/F_2 = 0.0151$ were assumed at all pressures.
[b] The hydrogenic ratio $F_4/F_6 = 9.139$ was assumed at all pressures.
[c] The ratios $F_4/F_2 = 0.1484$ and $F_6/F_2 = 0.0161$ were assumed at all pressures.

cular orbitals formed by the symmetry adapted free ion 4f orbitals φ_Γ can be written

$$\varphi'_\Gamma = N_\Gamma \left(\varphi_\Gamma - \sum_\tau \lambda_{\Gamma\tau}\chi_\tau\right) \tag{22}$$

where Γ denotes an irreducible representation of the point group defined by the local ligand symmetry, τ indexes the ligand orbitals χ, $\lambda_{\Gamma\tau}$ is a coefficient that describes the mixing of φ_Γ with χ_τ, and N_Γ is a normalization constant. In the limit of weak bonding, the 4f orbital will dominate the lanthanide centered molecular orbital and we can write

$$\varphi'_\Gamma = N_\Gamma \varphi_\Gamma \approx N\varphi_\Gamma \tag{23}$$

where the normalization constants for the different 4f orbitals are assumed to be approximately equal. Since $N<1$, we see that Eq. (23) is tantamount to an expansion of the symmetry adapted free ion 4f orbitals. When Eq. (23) is used to determine F_k and ζ_{4f}, we find

$$F_k = N^4 F_k^0 \quad \text{and} \quad \zeta_{4f} = N^2 \zeta_{4f}^0 \tag{24}$$

and

$$\frac{\Delta F_k}{F_k} = 4\frac{\Delta N}{N} \quad \text{and} \quad \frac{\Delta \zeta_{4f}}{\zeta_{4f}} = 2\frac{\Delta N}{N} \tag{25}$$

Table 7. Relative changes in the Slater covalency parameter F_2 and spin-orbit coupling constant ζ between ambient pressure and P_{max} for the systems listed in Tables 5 and 6. The value of P_{max} is given in Table 6 for each system. $(\Delta F_2)_{P_{max}} = F_2(P_{max}) - F_2(P_0)$ and $(\Delta\zeta_{4f})_{P_{max}} = \zeta_{4f}(P_{max}) - \zeta_{4f}(P_0)$ where P_0 refers to ambient pressure. The ratio of the relative changes of the two parameters is defined as the ratio of column 3 to column 4 and is used to evaluate theoretical covalency models in the text

Lanthanide	Host lattice	$10^2 \cdot \frac{(\Delta F_2)_{P_{max}}}{F_2(P_0)}$	$10^2 \cdot \frac{(\Delta\zeta_{4f})_{P_{max}}}{\zeta_{4f}(P_0)}$	Ratio	Ref.
Pr^{3+}	$LaCl_3$	-1.18	-0.33	3.6	[187]
	$LaCl_3$	-1.09	-0.46	2.4	[188]
	$PrCl_3$	-2.00	-0.53	3.8	[188]
	LaOCl	-1.51	-1.00	1.51	[189]
Nd^{3+}	$LaCl_3$	-0.69	-0.45	1.5	[188]
	$NdCl_3$	-0.72	-0.31	2.3	[188]
Eu^{3+}	LaOBr	-0.62	-1.29	0.48	[190]
	LaOBr	-1.59	-1.38	1.15	[191]
	LaOCl	-0.55	-1.00	0.55	[190]
	LaOCl	-1.20	-0.95	1.3	[192]
	GdOCl	-0.40	-0.45	0.88	[193]
	La_2O_2S	-0.38	-0.22	1.7	[194]
	Gd_2O_2S	-0.49	-0.19	2.6	[195]
	Y_2O_2S	-0.43	-0.18	2.4	[196]
Sm^{2+}	BaFCl	-1.24	-0.47	2.6	[190]
	SrFCl	-1.18	-0.52	2.3	[190]
	CaFCl	-1.16	-0.28	4.1	[190]

The symmetry restricted covalency model therefore predicts that the interelectronic repulsion parameters F_k will be more sensitive to increased covalency than the spin orbit coupling constant ζ_{4f}.

In order to evaluate the applicability of the two covalency models, we have included relative changes in F_2, ζ_{4f}, and their ratio in Table 7. The values listed correspond to the total observed change at the highest pressure for which data are available for each system. The central field covalency and symmetry restricted covalency models predict ratios of 0.33 and 2.0, respectively. From Table 7, we see that Eu^{3+}:LaOBr and Eu^{3+}:LaOCl most closely agree with the prediction of the central field covalency model. This is a reasonable result given the small size of Eu^{3+} relative to the La^{3+} ion that it replaces in the lattice and the ionic nature of oxide and halide ligands. Under these conditions, the 4f orbitals of Eu^{3+} would be less extended spatially relative to the ligands and would experience weak directional interactions, consistent with the spherical nature of central field covalency. In Eu^{3+}: Y_2O_2S, on the other hand, Eu^{3+} is large relative to its lattice site and is in the presence of a covalent sulfide ligand. Under these conditions, we expect stronger Eu^{3+}-ligand overlap and increased directional character in the local bonding. This is consistent with the closer agreement of Eu^{3+}: Y_2O_2S to the symmetry restricted covalency model.

The Sm^{2+} systems listed in Table 7 are all in much better agreement with the symmetry restricted covalency model than the central field covalency model. The greater directionality in bonding suggested by the Sm^{2+} results is consistent with the greater expected spatial extent of 4f orbitals in Sm^{2+} relative to trivalent lanthanides. The largest ratio occurs in Sm^{2+}:CaFCl, the system with the smallest cation site for Sm^{2+}. The data for Nd^{3+} and Pr^{3+} are also better described by the symmetry restricted covalency model. This finding may be a consequence of the greater spatial extent of 4f orbitals in the lighter lanthanides. The central field covalency model may become increasingly valid as we move across the lanthanide series due to the lanthanide contraction effect.

Shen and Holzapfel [190] and Wang and Bulou [191, 192] have considered a covalency model that combines the central field and symmetry restricted covalency models. The approach incorporates the effects of nuclear screening and hybridization of ligand orbitals with 4f orbitals. When the radial 4f wavefunctions of the central field covalency model (instead of the free ion 4f wavefunctions) are used in the formation of lanthanide centered molecular orbitals, we obtain

$$F_k = N^4 \kappa F_k^0 \quad \text{and} \quad \zeta_{4f} = N^2 \kappa^3 \zeta_{4f}^0 \tag{26}$$

which lead to

$$\frac{\Delta F_k}{F_k} = \frac{\Delta \kappa}{\kappa} + 4\frac{\Delta N}{N} \quad \text{and} \quad \frac{\Delta \zeta_{4f}}{\zeta_{4f}} = 3\frac{\Delta \kappa}{\kappa} + 2\frac{\Delta N}{N} \tag{27}$$

The combined model allows for concerted effects of the two covalency models and provides a simple way of rationalizing ratios between 0.33 and 2.0 in Table 7.

Shen and Holzapfel [190] also considered the effect of lanthanide-ligand distance on covalency across series of isostructural Eu^{3+} and Sm^{2+} host lattices at ambient pressure. Shen and Holzapfel [190] reported the variation of F_2 and ζ_{4f} with the average nearest neighbor distance for Eu^{3+} in LaOX (X = Cl, Br, I), LnOX (Ln = Y, Gd; X = Cl, Br) and Ln_2O_2S (Ln = Y, La, Gd, Lu) as well as for Sm^{2+} in MFCl (M = Ca, Sr, Ba). Their results are summarized in Figs. 4 and 5. Average distances were computed using crystallographic data for the host lattices without considering local distortion effects. Linear decreases in F_2 and ζ_{4f} with decreasing distance were observed.

Shen and Holzapfel [190] further compared the distance dependence of F_2 and ζ_{4f} across a series of host lattices with the distance dependence obtained from high pressure studies in the systems Sm^{2+}:MFCl (M = Ca, Sr, Ba). The Sm^{2+} coordination polyhedron in MFCl consists of five Cl^- and four F^- ligands (Fig. 6). Shen et al. [197] determined the variation of bond angles and bond lengths of BaFCl as a function of pressure in a synchrotron X-ray study and obtained the results shown in Fig. 7. Estimated results for SrFCl based on a simple scaling through the ambient pressure lattice parameters are also shown as dashed lines. The bond lengths shown in Fig. 7 were used to calculate the average nearest neighbor bond length $\bar{R}$ for Sm^{2+} in BaFCl and SrFCl as a function of pressure in Fig. 4 and Fig. 5. Similar determinations were made for Sm^{2+}:CaFCl and Eu^{3+}:LaOCl.

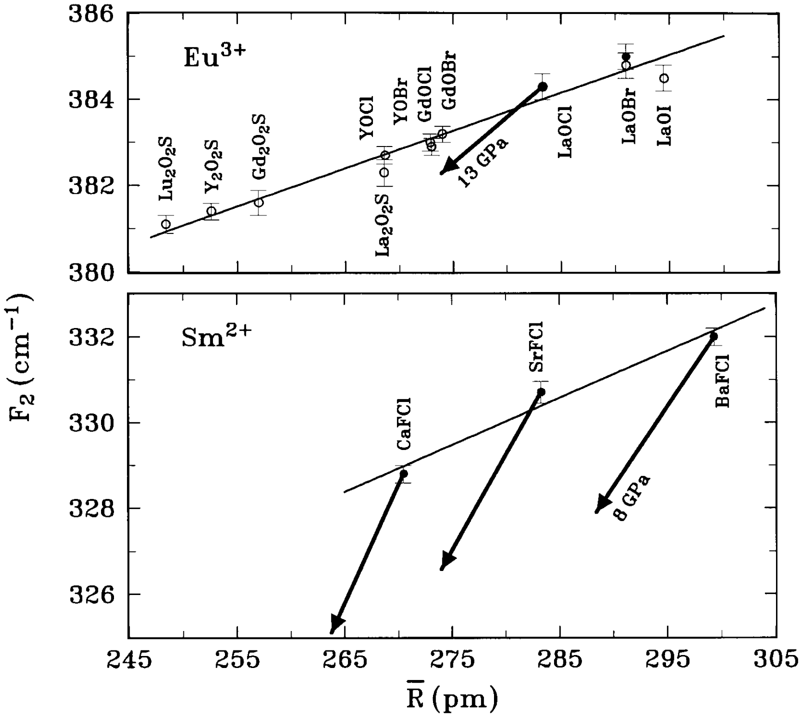

Fig. 4. Variation of the Slater covalency parameter F_2 of Eu^{3+} and Sm^{2+} as a function of average nearest neighbor bond length $\bar{R}$. The data points represent values in different host lattices. *Solid arrows* show the variation of F_2 with pressure

A comparison of the distance dependence of F_2 and ζ_{4f} obtained from host lattice and high pressure studies is included in Figs. 4 and 5. We see from the figures that the distance dependence obtained from the pressure study is more pronounced. Shen and Holzapfel attributed the difference in distance dependence to pressure-induced distortions in the local coordination environment of Sm^{2+}. We consider local distortions in more detail below in our discussion of lanthanide crystal field parameters.

3.2.2.2
Crystal Field Effects

Crystal field interactions in lanthanide systems are treated in the weak field limit and are normally expressed by the one-electron crystal field Hamiltonian H_{CF} given by

$$H_{CF} = \sum_{k,q} B_{kq}(r)\, C_{kq}(\theta, \phi) \qquad (28)$$

where the permitted values of k and q are determined by the local symmetry of the lanthanide bonding environment, $B_{kq}(r)$ are radial crystal field parameters,

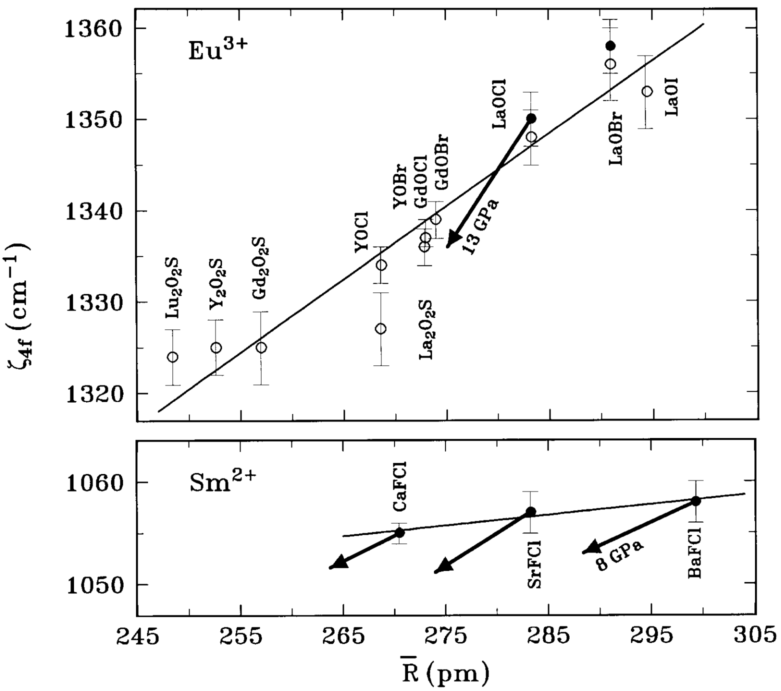

Fig. 5. Variation of the spin-orbit coupling constant ζ_{4f} of Eu^{3+} and Sm^{2+} as a function of average nearest neighbor bond length $\bar{R}$. The data points represent values in different host lattices. *Solid arrows* show the variation of ζ_{4f} with pressure

and $C_{kq}(\theta, \phi)$ are angular factors [134, 179, 185]. In application, the $C_{kq}(\theta, \phi)$ can be evaluated exactly from knowledge of the ligand positions. Exact determination of the $B_{kq}(r)$ parameters requires knowledge of the lanthanide 4f radial wavefunctions in the crystal bonding environment. These wavefunctions are generally unknown and simple predictions based on the free ion 4f wavefunctions do not adequately reproduce experimental energy level data. As a result, the $B_{kq}(r)$ are normally obtained empirically through fits to experimental data.

Several studies of the effect of pressure on the radial B_{kq} crystal field parameters have been reported. Lanthanide oxyhalides (REOX; RE = La, Gd, Y; X = Cl, Br) doped with Eu^{3+} have been extensively studied. The REOX lattices are isostructural and incorporate Eu^{3+} in bonding sites with C_{4v} symmetry. In the oxybromides, Eu^{3+} is coordinated to four oxygens and four bromides. The RE-O bond lengths (~2.3–2.4 Å) are significantly shorter than the RE-Br bond lengths (~3.2–3.3 Å). A fifth, more distant bromide (~3.5–3.9 Å) is located on the C_4 axis [191]. Eu^{3+} in the oxychlorides is coordinated similarly (RE-O ~2.3–2.4 Å, RE-Cl ~3.0–3.2 Å), but differs with respect to the position of the fifth chloride. The smaller size of the chlorides allows the fifth, axial chloride to approach more closely Eu^{3+} and enter the coordination sphere at a distance of ~3.0–3.2 Å [192].

Table 8 summarizes the variation of the B_{kq} crystal field parameters with pressure in several Eu^{3+}-doped REOX systems. The crystal field parameters were

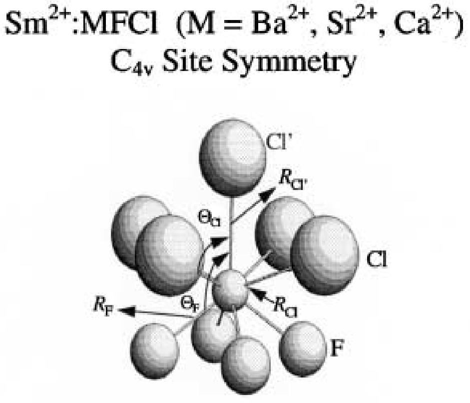

Host Lattice	R_{Cl} (Å)	Θ_{Cl}	$R_{Cl'}$ (Å)	R_F (Å)	Θ_F
BaFCl	3.286	71.0	3.196	2.494	124.0
SrFCl	3.112	69.6	3.072	2.362	124.2
CaFCl	2.963	68.3	3.048	2.387	124.5

Fig. 6. Coordination polyhedron of the Sm^{2+} site in MFCl host lattices. The listed bond lengths and bond angles correspond to the M^{2+} site in undoped MFCl crystals

obtained by measuring fluorescence energies of several $^5D_{0-2} \rightarrow {}^7F_{0-4}$ transitions of Eu^{3+} as a function of pressure. The fluorescence energies were used to establish the energies of the ^5D_J and ^7F_J crystal field states relative to the $^7F_0$ ground state. These energies were fit to obtain the values of B_{kq}. The crystal field strength parameter S is also listed. S is a parameter originally proposed to provide a measure of average crystal field strength and is given by [198]

$$S = \left[\frac{1}{3} \sum_k \frac{1}{2k+1} \left(B_{k0}^2 + 2 \sum_{q>0} |B_{kq}|^2 \right) \right]^{\frac{1}{2}} \tag{29}$$

Table 8. Effect of pressure on the crystal field parameters B_{kq} (cm^{-1}) for Eu^{3+} in several lanthanide oxyhalide systems. S (cm^{-1}) is an average crystal field strength parameter (see text). P denotes pressure in kbar and P_{max} represents the maximum pressure achieved in each study. The linear shifts given in the table are good approximations of data given in graphical or tabular form in the original references

Host	B_{20}	B_{40}	B_{44}	B_{60}	B_{64}	S	P_{max}	Ref.
LaOCl	−1347 + 2.16P	−476 − 0.99P	1051 − 0.71P	913 + 0.71P	282 + 0.29P	486.4 − 0.40P	136	[199]
GdOCl	−946 + 1.85P	−685 − 0.73P	887 − 0.18P	1039 + 1.85P	386 + 0.17P	413 − 0.10P	100	[193]
GdOBr	−1091 + 0.98P	−984 + 1.73P	860 + 0.16P	890 + 1.99P	387 − 0.61P	445 − 0.18P	120	[200]
LaOBr	1517 − 3.48P	509 + 0.76P	1100 + 0.28P	1083 − 0.83P	127 − 0.08P	538 − 0.59P	120	[191]

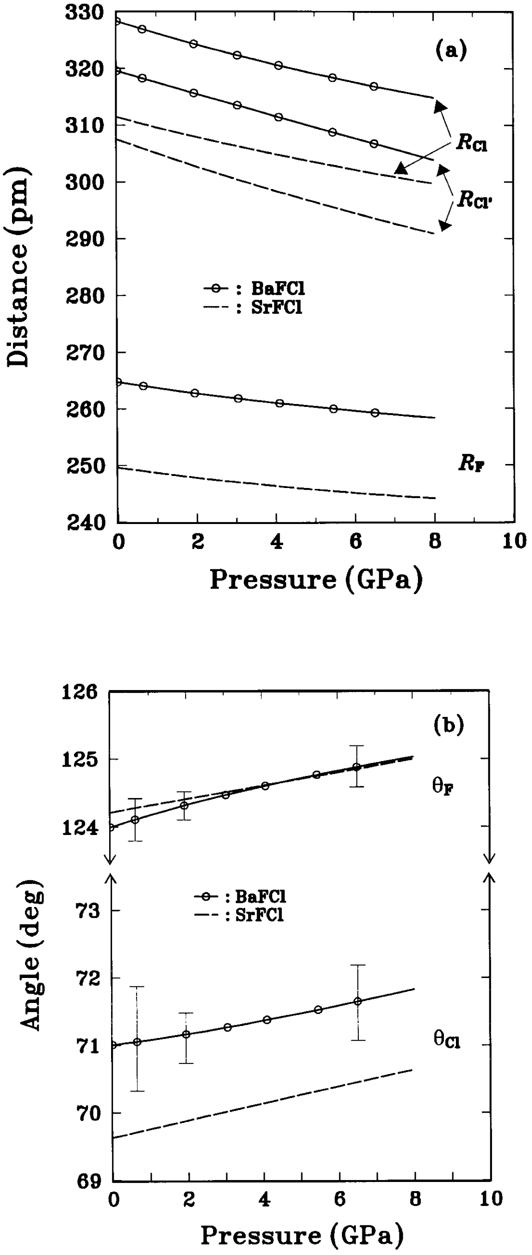

Fig. 7 a, b. Variation of: **a** bond lengths; **b** bond angles of the M^{2+} site in MFCl (M = Ba, Sr) with pressure. See Fig. 6 for an illustration of the M^{2+} coordination polyhedron and definitions of R_{Cl}, $R_{Cl'}$, R_F, θ_{Cl}, and θ_F

Since S is independent of symmetry, it provides a way to compare the crystal field strength of a lanthanide ion in different host lattices.

In the oxyhalides, B_{40}, B_{44}, B_{60}, and B_{64} account for the cubic crystal field strength, and B_{20} accounts for the tetragonal field. The data in Table 8 indicate that the magnitude of B_{20} decreases with pressure in the four listed oxyhalides. This suggests that the distortion from cubic symmetry decreases with pressure. A possible explanation is that local compression of the four oxygen and four non-axial halide ligands closes the coordination shell of Eu^{3+} and partially screens the influence of the fifth, axial halide so that the local coordination approaches regular cubic symmetry. The decrease in average crystal field strength with pressure is consistent with this explanation. As in the case of transition metal ions, decreases in nearest neighbor distances are expected to increase crystal field strength. A decreased crystal field strength in the presence of reduced bond lengths implies a decrease in the effective ligand charge or a reduction in coordination number with pressure. Enhanced screening of a ninth coordinating ligand would consequently contribute to a decrease in crystal field strength. The ambient pressure crystal field strength data are also consistent with the explanation. As we move across the series LaOBr-GdOBr-YOBr, we observe an increase in the RE-Br (axial) bond length, decreases in the RE-O and other RE-Br bond lengths, and a decrease in average crystal field strength [191].

Table 9 includes crystal field parameter data for the lanthanide oxysulfides (RE_2O_2S; RE = Y, La, Gd). The Eu^{3+} site in the lanthanide oxysulfides has C_{3v} symmetry with Eu^{3+} coordinated to three sulfur and four oxygen ligands [194]. The local environment can be viewed as hexagonal prismatic with three sulfur ligands located on the upper hexagonal face, three oxygen ligands located on the lower hexagonal face and staggered relative to the sulfur ligands, and a fourth, slightly more distant oxygen located below the lower hexagonal face and on the C_3 symmetry axis. The lanthanide ion is located below center in the hexagonal prism with all RE-O bonds being shorter than the RE-S bonds.

Table 9. Effect of pressure on the crystal field parameters B_{kq} (cm^{-1}) for Eu^{3+} in several lanthanide oxysulfide systems. S (cm^{-1}) is an average crystal field strength parameter (see text). P denotes pressure in kbar and P_{max} represents the maximum pressure achieved in each study. The linear shifts given in the table are good approximations of data given in graphical or tabular form in the original references

Host	B_{20}	B_{40}	B_{43}	B_{60}	B_{63}	B_{66}	S	P_{max}	Ref.
Y_2O_2S	117−0.74P	692+0.18P	1107+1.15P	491+0.35P	−335−0.14P	461+0.49P	461+0.49P	100	[194]
	125−0.86P							42	[201]
	118−0.78P	798−0.63P	1121+1.32P	576+0.38P	−276+0.19P	414+1.02P	373+0.32P	130	[196]
La_2O_2S	58−0.15P	762−0.27P	922+1.51P	452+0.80P	−182−0.25P	369+0.48P	314+0.38P	130	[194]
Gd_2O_2S	166−0.83P	869+1.08P	1048+0.45P	368+0.48P	−376+0.10P	448+1.20P	364+0.27P	148	[195]

In trigonal symmetry, B_{20} and B_{66} reflect the deviation from cubic symmetry. B_{20} decreased and B_{66} increased with pressure and consequently no clear trend in the net trigonal field was observed in the oxysulfides. The overall coordination environment is likely preserved with pressure and the primary influence of pressure is probably symmetric compression of all seven coordinating ligands. Unlike the oxyhalides, all seven ligands are in close proximity to Eu^{3+}. As a result, a change in coordination number is unlikely. The increase in average crystal field strength with pressure is consistent with this viewpoint.

Crystal field parameter variations with pressure have also been reported for $Na_5Eu(MO_4)_4$ (M = Mo, W) [202], Tb^{3+}:YAG [203], Pr^{3+}:$LaCl_3$ [187, 188], $PrCl_3$ [188], $Nd^{3+}LaCl_3$ [188], $NdCl_3$ [188], Pr^{3+}:$LaOCl_3$ [189], and Sm^{2+}:MFCl (M = Ca, Sr, Ba) [103, 204]. The effect of pressure on higher order two-electron correlation crystal field effects has also been reported for Sm^{2+}:MFCl [205] and Nd^{3+}:$LaCl_3$ [206].

Attempts to model quantitatively the variation of crystal field parameters with pressure have focused on a superposition model [207, 208] description of the local coordination environment. The objective of the superposition model is to relate the radial B_{kq} crystal field parameters to nearest neighbor bond lengths. In the superposition model, the crystal field experienced by a lanthanide ion is given by a sum of contributions from ligands in the nearest-neighbor coordination shell. Each ligand is assumed to perturb the lanthanide f orbital energies independently of other ligands with the combined effect of all ligands constituting the overall crystal field. Ligand-ligand interactions are neglected. In the superposition model, the contributions from individual ligands are further resolved into distinct physical and geometric factors and these are related to the crystal field parameters through

$$B_{\mathrm{kq}} = \sum_{\mathrm{L}} \overline{B_{\mathrm{k}}}(R_{\mathrm{L}})\, K_{\mathrm{kq}}(L) \tag{30}$$

where the sum is over all ligands L, R_L is the bond length to ligand L, $\bar{B}_{\mathrm{k}}(R_{\mathrm{L}})$ is the intrinsic crystal field parameter, and $K_{kq}(L)$ is a geometric coordination factor. The $K_{kq}(L)$ factors depend only on the angular positions of the nearest neighbor ligands and can be determined exactly from crystallographic data. The intrinsic parameters depend only on the chemical identity of the ligand and R_L. The intrinsic parameters account for electrostatic (point charge, charge penetration) and contact (exchange, ligand overlap, covalency) interactions between individual ligands and the central lanthanide ion.

In the point charge model, the distance dependence of the intrinsic parameters is given by the proportionality

$$\overline{B_{\mathrm{k}}}(R) \propto \frac{1}{R^{k+1}} \tag{31}$$

In practice, the point charge model is not strictly adhered to and a power law form

$$\overline{B_{\mathrm{k}}}(R) = \overline{B_{\mathrm{k}}}(R_0)\left(\frac{R_0}{R}\right)^{t_{\mathrm{k}}} \tag{32}$$

is adopted where R_0 is the ambient pressure nearest neighbor bond length and t_k is an adjustable power law exponent.

Application of the superposition model to high pressure crystal field data is best suited to stoichiometric lanthanide systems or systems in which the ionic radius of the lanthanide dopant closely matches that of the lattice cation it replaces. Such systems simplify the determination of the pressure dependence of R and permit us to use host lattice bond lengths as a function of pressure. Tröster et al. [188] measured the crystal structure and crystal field energies of $PrCl_3$ as a function of pressure and analyzed the results using the superposition model. They obtained $\bar{B}_6(R)$ = 282 cm^{-1} and $t_6 = 5$. Concentration quenching limited the number of observable crystal field transitions and precluded unambiguous experimental determination of the B_{4q} parameters. Tröster et al. [188] also considered $NdCl_3$, a system isostructural to $PrCl_3$ in which a large number of crystal field levels is observable. By assuming that the pressure dependence of the crystal structure of $NdCl_3$ scaled with that of $PrCl_3$, they obtained $\bar{B}_4(R)$ = 242 cm^{-1}, $\bar{B}_6(R)$ = 288 cm^{-1}, $t_4 = 6$, and $t_6 = 5$. The results for both systems indicate deviations from the point charge model.

Shen and Holzapfel [103] applied the superposition model to Sm^{2+}:SrFCl. Since the ionic radii of Sm^{2+} (1.32 Å) and Sr^{2+} (1.31 Å) are nearly identical [209], Sm^{2+} is expected to enter the lattice with no local structural perturbation. Shen and Holzapfel assumed that the pressure dependence of the structure of SrFCl scaled directly from the measured dependence of isostructural BaFCl and used the experimental ^5D_J and ^7F_J crystal field energies of Sm^{2+}:SrFCl to obtain $\bar{B}_4(R)$ and $\bar{B}_6(R)$ for both the Cl^- and F^- ligands as a function of nearest neighbor distance by systematically increasing pressure. The results are shown as open symbols in Figs. 8 and 9. A numerical fit using the power law form in Eq. (32) (not shown) [103] revealed a stronger distance dependence for the Cl^- ligand ($t_4 = 14$, $t_6 = 10$) than for the F^- ligand ($t_4 = 5.8$, $t_6 = 4.6$).

Figures 8 and 9 also show an attempt to model the distance dependence of the intrinsic crystal field parameters $\bar{B}_4$ and $\bar{B}_6$ using an ab initio approach. The approach is based on relating the intrinsic parameters to the one-electron 4f orbital energies through [207]

$$\overline{B_k} = \frac{(2k+1)}{\left[(2l+1)\begin{pmatrix} l & l & l \\ 0 & 0 & 0 \end{pmatrix}\right]} \sum_{m=-l}^{l} (-1)^m \begin{pmatrix} l & l & k \\ -m & m & 0 \end{pmatrix} \overline{\varepsilon_m} \qquad (33)$$

where $l = 3$ and $m = -3, -2, \ldots 2, 3$ are the 4f orbital angular momentum quantum numbers and $\overline{\varepsilon_m}$ are the one-electron 4f energies upon combination of the free ion 4f wavefunctions with ligand s and p orbital wavefunctions to form molecular orbitals. The energies $\overline{\varepsilon_m}$ include electrostatic (point-charge, charge penetration) and contact (exchange, ligand overlap, and covalency) contributions. The details of the calculation are discussed by Shen and Bray [210]. We see that the ab initio model underestimates the data for the chloride ligand and overestimates the data for the fluoride ligand. Shen and Bray [210] have proposed that interactions between chloride and fluoride ligands, an effect not in-

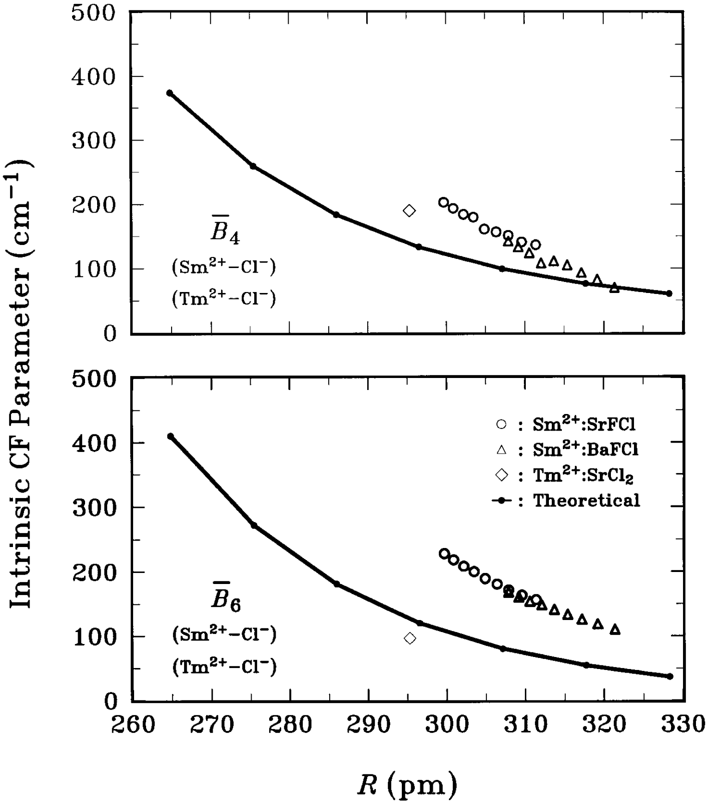

Fig. 8. Experimental (*open symbols*) and calculated (*closed symbols*) values of the intrinsic crystal field parameters $\bar{B}_4$ and $\bar{B}_6$ of the Sm^{2+}-Cl$^-$ pair in Sm^{2+}:SrFCl as a function of Sm^{2+}-Cl$^-$ bond length. The experimental bond length was varied with pressure and determined from high pressure X-ray diffraction data. The calculated curve was obtained from an ab initio calculation based on Eq. (33) [210]

cluded in the superposition model, are responsible for the difference between the calculation and experimental data.

Application of the superposition model to high pressure crystal field effects in arbitrary lanthanide doped systems is complicated by the local structural distortions that arise from the size mismatch between lanthanide dopants and lattice cations. When a lanthanide dopant differs in size from the lattice cation for which it substitutes, the lattice responds locally through distortions of nearest neighbor bond angles and bond lengths. These distortions are difficult to detect and quantify using experimental structural probes, but are readily apparent in optical spectra because of the accompanying reduction in symmetry. The inability to know precisely the extent of local distortions, however, makes it difficult to predict the values of crystal field parameters at ambient and high pressure using geometric models.

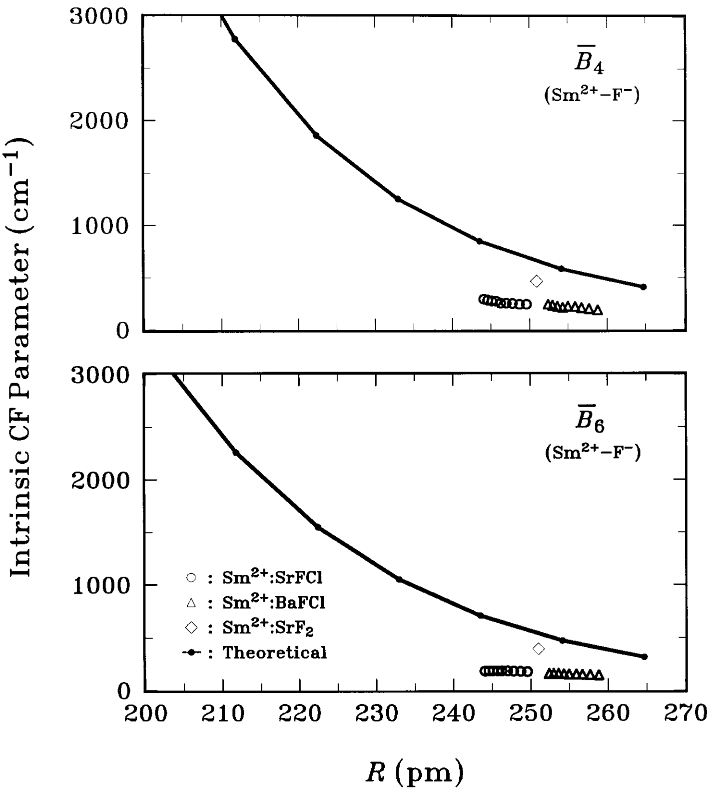

Fig. 9. Experimental (*open symbols*) and calculated (*closed symbols*) values of the intrinsic crystal field parameters $\bar{B}_4$ and $\bar{B}_6$ of the Sm^{2+}-Cl$^-$ pair in Sm^{2+}:SrFCl as a function of Sm^{2+}-Cl$^-$ bond length. The experimental bond length was varied with pressure and determined from high pressure X-ray diffraction data. The calculated curve was obtained from an ab initio calculation based on Eq. (33) [210]

Gregorian et al. [187] have reported the only model to date that attempts to account for the effect of local distortions on the high pressure behavior of lanthanide crystal field parameters. Their model was developed in a study of Pr^{3+} emission in RECl$_3$ (RE = La^{3+}, Pr^{3+}, Nd^{3+}, Gd^{3+}) lattices. The RE^{3+} bonding environment in these systems is a nine coordinate tricapped trigonal prism with six equivalent axial and three equivalent equatorial nearest neighbor ligands. The Pr^{3+} emission spectrum was measured in each system at ambient pressure. In addition, high pressure emission spectra and X-ray diffraction measurements of Pr^{3+}:LaCl$_3$ were reported. The X-ray measurements provided axial and equatorial La-Cl bond length variations as a function of pressure.

The premise of the distortion model of Gregorian et al. [187] is that there is a one-to-one relation between the PrCl$_9$ coordination polyhedron and the 4f electronic barycenter energies of Pr^{3+}. As a result, equivalence of barycenter energies of Pr^{3+} in various isostructural host lattices at different pressures indicates equivalence of coordination environment. By using $PrCl_3$ as an undistorted reference system for Pr^{3+}:$LaCl_3$, Gregorian et al. found that the multiplet barycenter energies of Pr^{3+}:$LaCl_3$ at 10 kbar were very similar to those of $PrCl_3$ at ambient pressure and concluded that the coordination environment of Pr^{3+} in $LaCl_3$ at 10 kbar was equivalent to that of Pr^{3+} in $PrCl_3$ at ambient pressure. Since the axial and equatorial bond lengths of $PrCl_3$ at ambient pressure and $LaCl_3$ at 10 kbar were known, Gregorian et al. were able to estimate the local distortion of the Pr^{3+} site relative to the La^{3+} site in $LaCl_3$ at 10 kbar. They found essentially no distortion in the equatorial ligand distance and a ~1.3% expansion of the axial ligand distance of the Pr^{3+} site in $LaCl_3$ at 10 kbar relative to the Pr^{3+} site in $PrCl_3$ at ambient pressure. They continued by assuming a constant distortion of the Pr^{3+} site with pressure, correcting the experimental axial and equatorial La-Cl bond lengths for the distortion and computing the intrinsic crystal field parameters $\bar{B}_4(R)$ and $\bar{B}_6(R)$. In addition to predicting the pressure dependence of the crystal field parameters, the model of Gregorian et al. [187], in conjunction with high pressure luminescence data, more generally provides a method for estimating local distortions associated with lanthanide dopants in host lattices. Since its introduction, the model has subsequently been used to analyze the distance dependence of the crystal field parameters of Nd^{3+}:$LaCl_3$ [188], Sm^{2+}:CaFCl [204], and Sm^{2+}:BaFCl [103] as a function of pressure.

3.2.3

d → f Luminescence Transitions

d → f emission (formally $4f^{n-1}5d \rightarrow 4f^n$ emission) occurs in many Ce^{3+} ($4f^1$) systems because of the absence of high energy 4f states and in divalent lanthanide systems (Sm^{2+}, Eu^{2+}) when the $4f^{n-1}5d$ excited configuration is comparable in energy to the first excited state of the $4f^n$ ground configuration. d → f transitions are parity allowed and produce intense, broad luminescence bands at energies ranging from the UV to the IR, depending on the system. The difference in spatial extent of the 5d and 4f orbitals is responsible for the broad luminescence bands and further suggests that large pressure effects should be observed for d → f transitions. Specifically, the energy of the emitting 5d state is expected to be highly sensitive to pressure while the energy of the terminal 4f state is expected to be only weakly dependent on pressure.

The emitting 5d state is the lowest energy state of the crystal field split 5d manifold. Its shift direction and magnitude with pressure will depend on the variation of both the crystal field strength and the 5d barycenter energy. As in the 3d systems described previously (see Sect. 3.2.1.2), an increase in crystal field strength can be expected with pressure. As a result, the total splitting of the 5d manifold is expected to increase with pressure. The 5d barycenter energy is controlled by covalency through the nephelauxetic effect, an effect that is enhanced by the bond compression associated with pressure. The higher covalency produced by pressure is expected to lead to a reduction in the 5d barycenter energy. We therefore find that both the increase in crystal field strength and enhancement of covalency with pressure contribute to a red shift for the emitting 5d state in a 5d → 4f transition.

Only a few high pressure studies of d → f emission in divalent lanthanide systems have been reported. The early study by Tyner and Drickamer [211] remains one of the most comprehensive. They considered the $4f^65d \rightarrow 4f^7$ emission of Eu^{2+} in $CaAl_2O_4$, $SrAl_2O_4$, $CaBPO_5$, $SrBPO_5$, $Ca_2P_2O_7$, and Ba_2SiO_4 at pressures up to ~ 100 kbar and observed red shifts ranging from ~ 7 cm^{-1}/kbar to ~ 37 cm^{-1}/kbar for the peak of the d → f emission band. They also considered the effect of pressure on thermal quenching and emission lineshape. Yoo et al. [212] stabilized d → f emission above 45 kbar at 30 K (see Sect. 3.4.2 for a discussion of $4f^{n-1}5d$-$4f^n$ electronic crossovers) in Sm^{2+}: SrF_2 and reported a red shift rate for the emission of 14.9 cm^{-1}/kbar. Similarly, we recently stabilized d → f emission in Sm^{2+}: SrFCl above ~ 160 kbar at room temperature and observed a red shift of ~ 10 cm^{-1}/kbar.

Chen et al. [213] have reported a blue shift for the $4f^55d$ state of Sm^{2+} in $CsSmI_3$. The system is known to exhibit $4f^55d \rightarrow 4f^6$ emission at ambient pressure. At 164 kbar, they observed new emission features at 14,583 cm^{-1} and 13,795 cm^{-1} and assigned them to $^5D_0 \rightarrow {}^7F_0$ and $^5D_0 \rightarrow {}^7F_2$ emission. They argued that the appearance of the new features was a consequence of a blue shift of the $4f^55d$ state and stabilization of the $^5D_0(4f^6)$ state as the first excited state in an electronic crossover process.

In our opinion, several aspects of the report by Chen et al. need to be considered before accepting their conclusion that the $4f^55d$ state shifts blue with pressure. First, the new features reported by Chen et al. are strongly overlapped by intense fluorescence from the ruby calibrant in their experiment and correspond closely to previously reported satellite peaks of ruby. Second, the new features are considerably broader than typical 4f → 4f transitions of lanthanides. Third, Chen et al. did not systematically measure the pressure shift of the $4f^55d$ state, but rather measured spectra at ambient pressure (probably in the absence of ruby) and 164 kbar and based their conclusion on only two spectra. Fourth, the authors observed hysteresis in the emission band upon release of pressure and suggested that a phase change may have occurred in the sample. Finally, Chen et al. used a constant excitation wavelength (488 nm) in their experiments. The large shift rate observed for $4f^55d$ emission in other systems suggests that a considerable shift in the absorption band used to excite the emission will occur between ambient pressure and 164 kbar. Consequently, it is conceivable that the absorption band can no longer be excited by 488 nm light at 164 kbar.

We are not aware of any published high pressure studies of the 5d → 4f luminescence of Ce^{3+}. Our group, however, has recently begun to undertake such studies. We are interested in the general problem of luminescence quenching of Ce^{3+} phosphors and its relationship to the energy of the 5d emitting state of Ce^{3+} relative to the conduction bandedge of the host lattice [214]. We are currently considering Ce^{3+} in Lu_2S_3 and $Y_3Al_5O_{12}$. Lu_2S_3 is representative of covalent host lattices. The energy of the emitting 5d state of Ce^{3+} in sulfides is determined primarily through the influence of the nephelauxetic effect on the 5d barycenter energy. $Y_3Al_5O_{12}$, in contrast, is representative of ionic host lattices and controls the energy of the emitting 5d state of Ce^{3+} through crystal field effects.

Initial results of a room temperature study of Ce^{3+}: Lu_2S_3 are shown in Fig. 10. The two emission features are due to transitions from the lowest energy $5d^1$ ex-

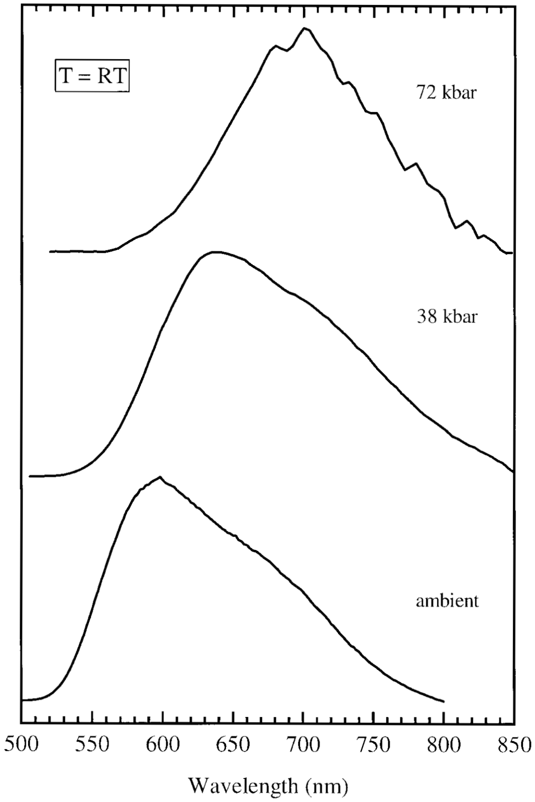

Fig. 10. Luminescence spectrum of Ce^{3+}: Lu_2S_3 as a function of pressure at room temperature. Excitation wavelength: 466 nm

cited state to the two crystal field components ($^2F_{5/2}$ and $^2F_{7/2}$) of the $4f^1$ ground state of Ce^{3+}. Shift rates of ~30 cm^{-1}/kbar were observed for the two components with pressure up to ~90 kbar. Above ~90 kbar, pronounced quenching of the Ce^{3+} emission was observed at room temperature. Future work will consider the origin of the emission quenching, its temperature dependence, and its relationship to the band structure of Lu_2S_3. We have also initiated a study of Ce^{3+}: $Y_3Al_5O_{12}$ and have observed much smaller red shifts (~10 cm^{-1}/kbar) for the two 5d → 4f luminescence components up to ~200 kbar with no quenching at room temperature.

3.2.4
Charge Transfer Emission in Transition Metal Complexes, Chains, and Layers

In addition to intracenter d → d emission, transition metal systems frequently exhibit charge transfer emission between metal centered and ligand centered orbitals. The molecular nature of isolated complexes leads to high compressibility and large pressure-induced changes in interatomic separations both within a complex and between complexes. Distances between chains and layers are also expected to be highly compressible in extended transition metal systems. As a result, large shifts in emission energy with pressure are expected for transition metal complexes, chains, and layers. In this section, we discuss representative studies of the effect of pressure on the energy of charge transfer emission bands. Since many of the basic ideas have been reported in the context of studies of a series of related systems, we organize this section accordingly.

3.2.4.1

Tetracyanoplatinate Chain Complexes – $Pt(CN)_4^{2-}$

The tetracyanoplatinates are well known columnar systems with interesting emission properties [215, 216]. The $Pt(CN)_4^{2-}$ unit is square planar (D_{4h} symmetry) and forms quasi one-dimensional chain-like structures in the solid state [217, 218]. The chains consist of stacked planar $Pt(CN)_4^{2-}$ units with short intrachain Pt-Pt bonds and long interchain Pt-Pt distances. Charge balancing mono-, di-, or trivalent cations and waters of hydration reside between chains. The interchain species control the intrachain Pt-Pt bond length and determine whether the Pt chain backbone is linear, zigzag, or helical [216, 218]. Neighboring $Pt(CN)_4^{2-}$ planar units within a chain are nearly parallel and oriented relative to each other with a torsion angle that varies with the cation. Torsion angles ranging from 0° (aligned) to 45° (staggered) have been reported. Depending on the cation, the molecular planes of the $Pt(CN)_4^{2-}$ units may also be tilted relative to the chain axis.

$Pt(CN)_4^{2-}$ chains exhibit intense, broad emission bands at ambient pressure. The emission has been attributed to a LUMO-HOMO charge transfer transition. The LUMO is comprised primarily of 6p (Pt) and π^* (CN) orbitals and the HOMO consists primarily of 5d (Pt) and 6s (Pt) orbitals. The intrachain Pt-Pt bond distances are sufficiently short to permit overlap of Pt orbitals. As a result, the LUMO orbitals combine to form a conduction band, the HOMO orbitals combine to form a valence band, and the emission can be viewed as an excitonic recombination. Distinct emission bands have been reported for delocalized (free) and localized (self-trapped) excitons [215, 216, 219]. The free exciton emission is polarized parallel to the $Pt(CN)_4^{2-}$ chains ($\vec{E} \| \vec{c}$) and the self-trapped exciton emission is polarized perpendicular to the chains ($\vec{E} \perp \vec{c}$). Ambient pressure emission studies have shown that the energy of emission decreases with decreasing intrachain Pt-Pt distance [215, 216, 220].

Yersin and colleagues have investigated the effect of pressure on the polarized emission properties of a number of $Pt(CN)_4^{2-}$ chain systems over the past several years [215, 216, 219–223]. The objective of their studies is to use pressure to examine the effect of intrachain Pt-Pt distance on the energy and intensity of exciton emission. In contrast to the effect of variations in the chemical identity of charge balancing cations, high pressure provides a method to continuously decrease the intrachain Pt-Pt distance.

Stock and Yersin [221] reported polarized emission spectra up to 23 kbar for single crystals of $Ba[Pt(CN)_4] \cdot 4H_2O$. At ambient pressure, the intrachain Pt-Pt separation is 3.32 Å and the peaks of the free exciton and self-trapped emission bands occur at ~21,000 cm^{-1} and ~19,500 cm^{-1}, respectively. Both emission bands showed large red shifts with pressure up to 6 kbar and above 12.7 kbar, but no shift between 6 kbar and 12.7 kbar. Stock and Yersin argued that a change in crystal structure occurred between 6 kbar and 12.7 kbar and proposed that pressure induced a decrease in the tilt angle of the molecular $Pt(CN)_4^{2-}$ planes with the chain axis. A change in tilt angle would not influence the intrachain Pt-Pt separation and would be consistent with the lack of shift. Stock and Yersin attributed the large red shifts to increased splittings of the valence (HOMO) and conduction (LUMO) bands with decreasing Pt-Pt separation at high pressure. Since the free exciton emission exhibited a larger red shift than the self-trapped emission (−280 cm^{-1}/kbar vs −195 cm^{-1}/kbar), the two emission peaks approached each other at high pressure. Extrapolation of the emission peak data indicates degeneracy of the two emission peaks at ~27.5 kbar.

Stock and Yersin also considered $Mg[Pt(CN)_4] \cdot 7H_2O$, a system with a much shorter Pt-Pt separation (3.15 Å) and much lower free exciton (~17,500 cm^{-1}) and self-trapped exciton (~16,800 cm^{-1}) emission energies at ambient pressure. Upon increasing pressure, the free exciton and self-trapped exciton emission bands shifted red at rates of −330 cm^{-1}/kbar and −260 cm^{-1}/kbar, respectively. No evidence of a structural phase change was observed. Using the ambient pressure bulk compressibility value reported by Hara et al. (0.0043 kbar^{-1}) [224], Stock and Yersin showed that the experimental pressure shifts could be expressed as linear functions of volume. A similar volume dependence has been reported at ambient pressure for systems with different cations [215, 216, 220, 222] and is consistent with an excitonic emission process [225]. As the two emission bands approached each other in energy at high pressure, the intensity of the self-trapped exciton band decreased. The intensity became essentially zero at the point of degeneracy (~14 kbar). In a follow-up paper, Rössler and Yersin [223] showed that the intensity decrease was due to a destabilization of the self-trapped exciton state relative to the free exciton state resulting from changes in exciton mass, deformation potential, and elastic constants at high pressure. Yersin et al. have also considered the effect of pressure on exciton emission in $Na_2[Pt(CN)_4] \cdot 3H_2O$ [222], $Ca[Pt(CN)_4] \cdot 5H_2O$ [222], $Y_2[Pt(CN)_4]_3 \cdot 21H_2O$ [226], $Eu_2[Pt(CN)_4]_3 \cdot 18H_2O$ [227, 228], $Tb_2[Pt(CN)_4]_3 \cdot 21H_2O$ [228], and $Sm_2[Pt(CN)_4]_3 \cdot 18H_2O$ [228].

3.2.4.2
Dicyanoaurate (I) Layers – $Au(CN)_2^-$

The dicyanoaurates are sheet-like compounds comprised of two-dimensional layers of linear $Au(CN)_2^-$ ions alternating with layers of charge balancing cations [229, 230]. The intralayer Au-Au distances are short (~3.1–3.7 Å) and vary with the charge balancing cation. For a given cation, one often observes two or more crystallographically distinct $Au(CN)_2^-$ ions and multiple Au-Au distances within a layer. The distance between $Au(CN)_2^-$ layers is large (~8 Å). $Au(CN)_2^-$ ions have LUMO states comprised of $6p(Au^+)$ and $\pi^*(CN^-)$ orbitals and HOMO states comprised of $5d_{z^2}(Au^+)$ and $6s(Au^+)$ orbitals [231–234]. In solution, the $Au(CN)_2^-$ ions are isolated and the HOMO-LUMO gap is ~40,000 cm^{-1}. In solids, orbital overlap between neighboring Au^+ ions occurs and bands form from the HOMO and LUMO orbitals. Splittings within the bands lead to a reduction in the bandgap and a red shift of the HOMO → LUMO absorption relative to the solution phase [232, 235]. The extent of orbital overlap depends on the intralayer Au^+-Au^+ separation and varies with the cations in the lattice.

At ambient pressure and room temperature, the dicyanoaurates exhibit broad emission bands in the UV-visible region of the spectrum. At low temperature, the emission bands possess shoulders and it has been proposed that each distinct emission band is due to a different Au^+ structural environment [230, 235]. Yersin and Riedl [219] have proposed that localized, spatially isolated $[Au(CN)_2]_n^{n-}$ clusters are present in the $Au(CN)_2^-$ layers. They argued that Au^+-Au^+ distances in the clusters would differ from the distances observed in the homogeneous, unclustered portions of the layer. As a result, multiple emission bands are expected. According to the model of Yersin and Riedl, emission bands from the clusters correspond to excited states that are delocalized over the region of the cluster and to self-trapped states of these clusters. These self-trapped excitons are similar to those that are observed in $[Pt(CN)_4]^{2-}$ chains.

Yersin and Riedl [219] also considered the effect of pressure on the room temperature emission properties of $K[Au(CN)_2]$, $Cs[Au(CN)_2]$, and $Cs_2Na[Au(CN)_2]_3$. Representative results are included in Fig. 11. The wide variation in emission energy at ambient pressure for the three compounds and the large pressure shifts indicate the strong sensitivity of the emission energy to the intralayer Au^+–Au^+ separation. The observed red shifts with pressure are $-120\ cm^{-1}$/kbar ($Cs_2Na[Au(CN)_2]_3$), $-150\ cm^{-1}$/kbar ($Cs[Au(CN)_2]$), and $-200\ cm^{-1}$/kbar ($K[Au(CN)_2]$). These large shifts reflect the compressible nature of the $Au(CN)_2^-$ layers and the high sensitivity of the HOMO and LUMO gap to changes in Au^+-Au^+ separation.

Strasser et al. [236] reported a similar red shift ($\sim -160\ cm^{-1}$/kbar) for $Tl[Au(CN)_2]$ up to 20 kbar. This system differs from those studied by Yersin and Riedl [219] because Tl^+ has 6p orbitals available that are capable of covalently interacting with the 5d orbitals of Au^+ [232, 237]. The similar pressure shifts reported for $Au(CN)_2^-$ emission in compounds with Tl^+, Cs^+, K^+, and Na^+ indicates that the effect of pressure is limited primarily to compression within the $Au(CN)_2^-$ layers and that interlayer compression effects are negligible up to 20 kbar.

3.2.4.3
Molecular Monomeric and Dimeric Complexes

Transition metal ions form monometallic and bimetallic complexes with a variety of organic ligands and frequently exhibit intense charge transfer emission. The emission properties are useful indicators of the extent of ligand-metal interactions in the complexes. High pressure studies provide an opportunity to systematically vary ligand-metal interactions and lead to a new understanding of the properties of metal complexes. The compressible nature of metal complexes lead to significant variations in structure and bonding with pressure.

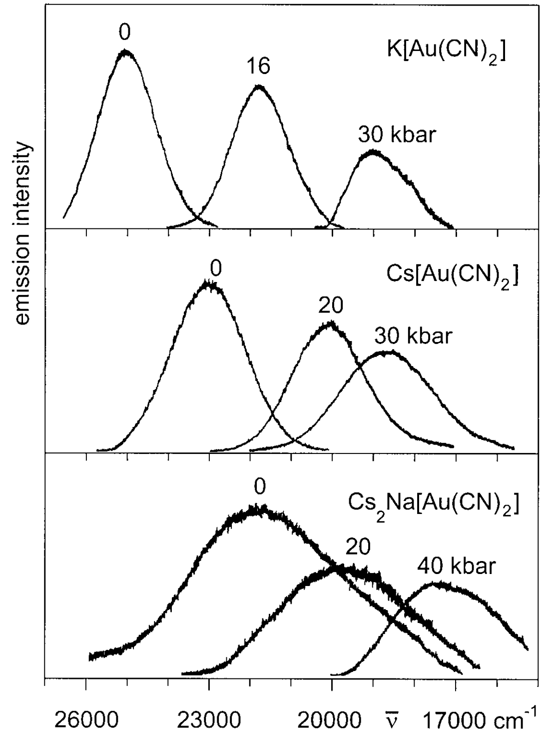

Fig. 11. Emission spectra of three $[Au(CN)_2^-]$ systems as a function of pressure at room temperature. Excitation wavelength: 325 nm

Yersin and Gallhuber [238] reported one of the first high pressure studies of charge transfer emission from a crystalline molecular organometallic complex. They reported the effect of pressure on the energy, linewidth, and intensity of charge transfer emission in $[Ru(bpy)_3](PF_6)_2$ (bpy = 2,2′-bipyridine). The emission occurs from π^* orbitals of bpy to 4d orbitals of Ru^{2+}. Yersin and Gallhuber observed a small red shift (~2–6 cm^{-1}/kbar), a decrease in linewidth and a decrease in emission intensity with pressure. The observed red shift was considerably smaller than that typically observed for intraligand $\pi \rightarrow \pi^*$ transitions (~20 cm^{-1}/kbar) and was attributed to enhanced 4d–π^* backbonding with pressure.

Lang et al. [239] considered the effect of pressure on the charge transfer emission of two Ru^{2+} complexes: $Ru(bpy)_3^{2+}$ and $Ru(bpy)_2(py)^+$ (py = pyridine). In both complexes, the charge transfer emission is due to a transition from π^* orbitals of bpy to 4d orbitals of Ru^{2+}. In contrast to Yersin and Gallhuber, Lang et al. reported emission red shifts of ~20 cm^{-1}/kbar for both complexes as crystalline solids. The emission intensity of $Ru(bpy)_3^{2+}$ decreased continuously with pressure while the emission intensity of $Ru(bpy)_2(py)^+$ increased up to ~20 kbar and then decreased with pressure. By dissolving the complexes in various solid state media and examining the effect of chemical environment on emission properties, Lang et al. were able to show that intermolecular interactions determined the luminescence efficiency of Ru(bpy)$_3^{2+}$ while intramolecular interactions were more important in Ru(bpy)$_2$(py)$^+$. Based on this finding, Lang et al. developed a structural model to explain the effect of pressure on emission intensity in Ru(bpy)$_2$(py)$^+$. According to the model, the increase in intensity observed at low pressure was proposed to be due to inhibition of the motion of the py ligand upon compression. At ~20 kbar, the inhibition was saturated and the ensuing intensity decrease was proposed to result from enhancement of non-radiative decay through the exponential energy gap law as the charge transfer emission shifted red. Similar arguments were used to explain the intensity decreases observed in Ru(bpy)$_3^{2+}$ and [LRe(CO)$_3$(phen)]$^+$ (L = 2,2′-phenanthroline) [240] with pressure.

Hiraga et al. [241] considered the effect of pressure on the fluorescence and phosphorescence transitions of dimeric $K_4[Pt_2(H_2P_2O_5)_4] \cdot 2H_2O$. At ambient pressure, the fluorescence transition peaks at 23,600 cm^{-1} and the phosphorescence transition peaks at 19,400 cm^{-1}. The two transitions exhibit red shifts of –17 cm^{-1}/kbar and –19 cm^{-1}/kbar, respectively, with pressure up to ~25 kbar. The shifts were attributed to a closure of the HOMO-LUMO gap of the complex with pressure due to a decreased intramolecular Pt-Pt distance. Above ~10 kbar, a new emission peak appeared as a low energy shoulder of the fluorescence transition. The new feature exhibited a large red shift (~–100 cm^{-1}/kbar) upon continued compression. Since the shift rate of the new feature is similar to that observed for excitonic transitions in extended linear and planar arrangements of metal complexes (see Sects. 3.2.4.1 and 3.2.4.2), Hiraga et al. proposed that the feature was excitonic in nature and resulted from a significant enhancement of interactions between neighboring dimeric complexes. According to their model, the intermolecular separation between complexes was reduced sufficiently to permit Pt-Pt interactions between complexes. As a result, a transition from the original dimeric molecular orbital structure to an extended band structure occurred and was accompanied by new excitonic emission.

3.3
Lifetimes of Excited Electronic States

In addition to altering the energies of electronic states, pressure also influences the lifetimes of excited states. Decay processes are affected when the coordination environment, energy level structure, or vibrational coupling of a luminescent center is altered by pressure. Changes in coordination symmetry can influence radiative decay rates by altering compliance with selection rules. Changes in energy level structure influence radiative decay rates by changing the activation barrier and Boltzmann population of thermally accessible competing emitting states. Changes in vibrational coupling influence radiative processes activated by vibronic intensity mechanisms.

Radiative decay rates are also affected when an emitting state is comprised of a quantum mechanical mixture of two or more pure electronic states that have different radiative decay rates and different shift behavior with pressure. Many emitting states, for example, consist of two or more electronic states coupled through spin-orbit or crystal field interactions. Since pressure typically alters the energy of each state contributing to a coupled excited state differently, the energy difference between the contributing states and therefore the strength of coupling will change with pressure. This effect alters radiative decay rates by changing the composition of the wavefunction of the emitting state and influencing the spin or orbital character of the resulting luminescence transition. This effect does not require the presence of a thermal Boltzmann population of the higher energy contributing electronic state(s).

Pressure influences non-radiative decay rates by altering activation barriers associated with thermally activated quenching processes. Pressure also influences vibrational energies and affects multiphonon non-radiative decay processes. This effect has not been studied in detail, but is generally viewed as negligible since the variation of phonon energies with pressure is not sufficiently large to have an important effect on multiphonon quenching.

In this section we review recent high pressure studies of luminescence lifetimes in transition metal and lanthanide systems. We focus on individual electronic transitions from isolated luminescent centers. Other phenomena, such as changes in energy transfer processes or electronic crossovers induced by pressure, can also influence emission lifetimes and will be discussed in later sections.

3.3.1
Transition Metal Systems

Relatively few studies of the effect of pressure on luminescence lifetimes have been reported. Most studies have considered the lifetime of the R-lines ($^2E \rightarrow {}^4A_2$) of ruby as a function of pressure with the objective of extending its utility as a pressure calibrant [111, 242–247]. Since concentration quenching occurs in ruby, the ambient and high pressure R-line lifetimes depend on the Cr^{3+} concentration. Dilute ruby ($< \sim 0.4$ wt% Cr^{3+} [248]) has a reported R-line lifetime of 3.0–3.1 ms at ambient conditions [243, 246–248]. Uroševic et al. [246] measured the effect of pressure on the R-line lifetime of ruby at room temperature and reported a linear dependence, $\tau\,(\mathrm{ms}) = 3.04 + 0.0312\,P\,(\mathrm{kbar})$, up to 118 kbar. Based on the large increase in lifetime with pressure, Uroševic et al. proposed that the ruby lifetime would be a more sensitive method than wavelength shift for calibrating pressure.

Uroševic et al. [246] also observed that the increase in ruby lifetime correlated with the increasing crystal field strength induced by pressure and noticed that a similar trend in Cr^{3+} R-line lifetime occurred at ambient pressure as the crystal field strength of the host lattice was increased. These observations prompted follow-up papers by Jovanic et al. [244, 245] that considered the theoretical dependence of the lifetime increase with pressure. Jovanic et al. incorporated predictions of the variation of the oscillator strength and lifetime of the ruby R-lines with pressure into the radial expansion model originally used by Ma et al. [147, 162, 163] to predict the variations of B, Dq, and electronic energies of ruby with pressure (see Sects. 3.2.1.1 and 3.2.1.2). They found excellent agreement with the experimental data of Uroševic et al. [246] up to 120 kbar as well as with the data of Eggert et al. [111] up to 1200 kbar.

Sato-Sorensen [242, 243] considered the effect of pressure on the lifetime of ruby with a high Cr^{3+} concentration (~1 wt%) and also observed a linear variation with pressure, τ (ms) = 2.6 + 0.022P (kbar), up to 427 kbar. The low ambient pressure lifetime was attributed to concentration quenching in the sample. Although not directly discussed by Sato-Sorensen, the smaller increase in lifetime with pressure relative to that reported by Uroševic et al. [246] is also presumably due to concentration quenching effects. A reduction of the Cr^{3+} interionic separation in concentrated ruby would increase the rate of energy transfer between Cr^{3+} ions and enhance concentration quenching.

Eggert et al. [111] have presented ruby lifetime results over the widest reported range of pressure, 0–1300 kbar. Their data indicate a linear increase of ~0.023 ms/kbar in room temperature lifetime up to ~700 kbar, followed by a leveling off at ~20 ms at higher pressure. The scatter in the lifetime data increases with increasing pressure and was attributed to local trigonal field distortions resulting from non-hydrostatic conditions. Eggert et al. also considered a perturbation model for describing the lifetime variation with pressure. Strictly speaking, the R-line transition of Cr^{3+} is both spin and parity forbidden. In the model of Eggert et al., the spin selection rule was relaxed through spin-orbit coupling between the ^2E and $^4T_2$ excited states and the parity selection rule was relaxed by the local trigonal distortion which acts to mix an unspecified, high lying odd parity state into the even parity $^4T_2$ state. Their resulting perturbation expression for the transition matrix element governing R-line emission is

$$\left\langle {}^2E|D|{}^4A_2\right\rangle = \left[\frac{\left\langle {}^2E|H_{so}|{}^4T_2\right\rangle}{\Delta E({}^4T_2 - {}^2E)}\right]\left[\frac{\left\langle {}^2E|V_{tr}|\gamma_-\right\rangle}{\Delta E(\gamma_- - {}^4T_2)}\right]\left\langle \gamma_-|D|{}^4A_2\right\rangle \tag{34}$$

where D is the electric dipole operator, H_{so} is the spin-orbit Hamiltonian, V_{tr} is the trigonal crystal field Hamiltonian, γ_- denotes the unspecified, high lying odd parity state, $\Delta E(^4T_2 - {}^2E)$ is the zero phonon energy difference between the $^4T_2$ and ^2E states, and $\Delta E(\gamma_- - {}^4T_2)$ is the zero phonon energy difference between the γ_- and $^4T_2$ states. Eggert et al. simplified the above expression by assuming that $\left\langle {}^2E|H_{so}|{}^4T_2\right\rangle$ and $\Delta E(\gamma_- - {}^4T_2)$ were both proportional to Dq and that $\left\langle \gamma_-|D|{}^4A_2\right\rangle$ is independent of pressure. With these assumptions, the predicted R-line lifetime of ruby becomes

$$\tau = A\,\frac{(\Delta E({}^4T_2 - {}^2E))^2}{\left\langle {}^4T|V_{tr}|\gamma_-\right\rangle^2} \tag{35}$$

where A is a constant. Eggert et al. argued that the value of $\left\langle {}^4T|V_{tr}|\gamma_-\right\rangle$ was proportional to their measured trigonal field splitting of the $^2T_1$ state as a function of pressure and obtained $\Delta E(^4T_2 - {}^2E)$ from their measured R-line shifts and a $^4T_2$ lineshape fitted from three point luminescence excitation spectra obtained as a function of pressure. The value of A was adjusted to match the measured ambient pressure lifetime and Eq. (35) was used to calculate the variation of the R-line lifetime with pressure. Eggert et al. obtained good agreement between their calculated and measured lifetimes. They also considered the effect of non-hydrostatic stresses on the trigonal field splitting and demonstrated the influence of these stresses on the measured lifetime. The work of Eggert et al.

clearly illustrates the necessity of understanding the stress conditions of a high pressure experiment when interpreting the results.

The lifetime variation of Cr^{3+} with pressure has also been considered in alexandrite ($BeAl_2O_4$) [114, 249] and several garnets [113, 139–141]. Jia et al. [114] observed a non-linear increase in the R-line lifetime of Cr^{3+} in the mirror sites of alexandrite from 0.5 ms (R_1, R_2) at ambient pressure to 3.5 ms (R_1) and 3.0 ms (R_2) at 68 kbar. They attributed the lifetime increase to a decreasing thermal population of the $^4T_2$ state resulting from an increase in the energy of the $^4T_2$ state with pressure. Jovanic [249] reported a similar increase in the R-line lifetime in alexandrite and interpreted the increase in the context of the radial expansion model described in their analysis of ruby [244, 245].

Our group has recently completed studies of the pressure dependence of the lifetime of the R-lines of Cr^{3+} in the garnets YAG ($Y_3Al_5O_{12}$), GGG ($Gd_3Ga_5O_{12}$), and GSGG ($Gd_3Sc_2Ga_3O_{12}$), and has considered the influence of the $^4T_2$ state on emission from the ^2E state in more detail [113, 140, 141, 250]. The three garnets are isostructural and differ in crystal field strength at ambient pressure.

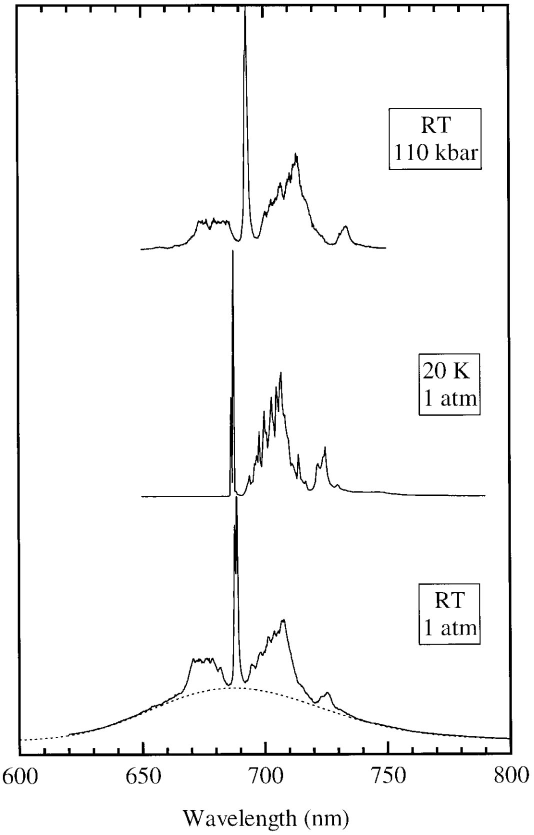

Fig. 12. Luminescence spectrum of Cr^{3+}:$Y_3Al_5O_{12}$ at selected temperatures and pressures. RT = Room Temperature. Excitation wavelength: 560 nm

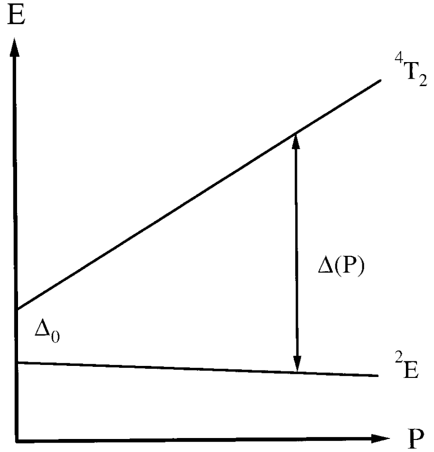

Fig. 13. Schematic illustration of the effect of pressure on the energy difference Δ between the $^4T_2$ and ^2E states of Cr^{3+}: $Y_3Al_5O_{12}$. Δ_0 ~ 800 cm^{-1} denotes the ambient pressure value and Δ(P) (cm^{-1}) ~ Δ_0 (cm^{-1}) + 9.8 (cm^{-1}/kbar)P represents the increase in Δ with pressure

Cr^{3+}: YAG has the highest crystal field strength and the highest energy difference between the $^4T_2$ and ^2E excited states. At ambient conditions, the $^4T_2$ state of Cr^{3+}: YAG is ~ 800 cm^{-1} higher in energy than the ^2E state and the luminescence spectrum (Fig. 12) consists of sharp, structured $^2E \rightarrow {}^4A_2$ emission superimposed on a broad, underlying spectrum (dotted curve) originating from the thermally populated $^4T_2$ state. The $^2E \rightarrow {}^4A_2$ emission consists of R_1 and R_2 zero phonon lines and accompanying Stokes and anti-Stokes vibrational sidebands. A decrease in temperature or an increase in pressure leads to the elimination of the underlying $^4T_2 \rightarrow {}^4A_2$ emission (Fig. 12). The intensity loss is a consequence of a depopulation of the $^4T_2$ state with decreasing temperature or increasing pressure. In the case of temperature, the effect is due to a simple Boltzmann depopulation upon cooling. An increase in pressure leads to an increase in the energy of the $^4T_2$ state relative to the ^2E state and to depopulation of the $^4T_2$ state by increasing the Boltzmann activation barrier $\Delta = E(^4T_2) - E(^2E)$ between the two states (Fig. 13).

Depopulation of the $^4T_2$ state leads to a significant increase in R-line lifetime with increasing pressure. At room temperature, the lifetime increases from 1.8 ms at ambient pressure to ~ 40 ms at 200 kbar (Fig. 14). Our initial attempt to model the lifetime variation with pressure was based on a pure electronic model in which vibrational states, vibronic coupling, and spin-orbit coupling effects were neglected. The pure electronic model is analogous to the approach used in deriving Tanabe-Sugano diagrams [134, 179, 251] and requires that we consider only the zero phonon ^2E and $^4T_2$ states when predicting the ^2E lifetime. The $^4T_2$ state is permitted to interact with the ^2E state only through thermal population effects. According to the model, the ^2E lifetime is given by [252]

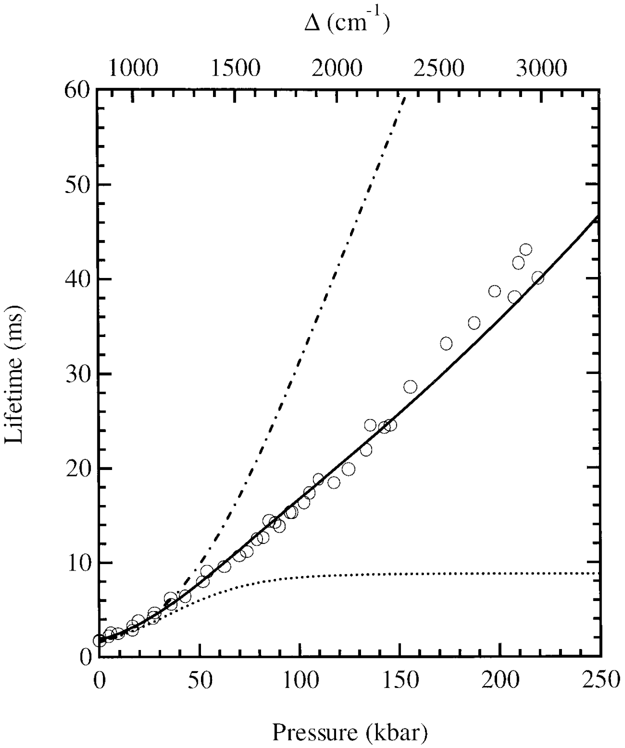

Fig. 14. Variation of the lifetime of the $^2E \rightarrow {}^4A_2$ transition of Cr^{3+}: $Y_3Al_5O_{12}$ with pressure at room temperature. Excitation wavelength: 580–600 nm. The *dotted curve* shows a prediction based on the pure electronic model (Eqs. 43 and 36) using $\Delta(P)$ (cm^{-1}) = 828 cm^{-1} + 9.8 (cm^{-1}/kbar) P, f_E = 114 s^{-1}, and f_T = 6135 s^{-1}. The *dot-dash curve* shows a prediction based on a simple spin-orbit coupling model that considers only the zero phonon ^2E and $^4T_2$ states. The model assumes $\Delta(P)$ (cm^{-1}) = 828 cm^{-1} + 9.8(cm^{-1}/kbar)P, f_E = 114 s^{-1}, f_T = 6135 s^{-1} and V_{SO} = 202 cm^{-1}. The *solid curve* is based on a single configuration coordinate model that includes spin-orbit coupling between vibrational states of the ^2E and $^4T_2$ states (Eq. 50). The prediction of this model is based on an optimization to the data. The optimization assumes the constant values S = 2.5, $\hbar\omega$ = 400 cm^{-1}, and V_{SO} = 202 cm^{-1}. Δ (cm^{-1}) = Δ_0 + 9.8 (cm^{-1}/kbar)P was also used. Δ_0 = 828 cm^{-1} and τ_T = 163 µs were obtained as best fit values to the lifetime data

$$\frac{1}{\tau} = \frac{f_E + f_T \dfrac{g_T}{g_E} \exp\left[-\dfrac{\Delta}{kT}\right]}{1 + \dfrac{g_T}{g_E} \exp\left[-\dfrac{\Delta}{kT}\right]} \tag{36}$$

where f_E and f_T are the total decay rates and $g_E = 4$ and $g_T = 12$ are the degeneracies of the ^2E and $^4T_2$ states, respectively. Since the $^4T_2 \rightarrow {}^4A_2$ transition is spin allowed and the $^2E \rightarrow {}^4A_2$ transition is spin forbidden, $f_T \gg f_E$.

In the pure electronic model, the energy difference Δ is the only pressure dependent term in Eq. (36). The ambient pressure value $\Delta(P = 0)$ is ~828 cm^{-1}. The variation in Δ with pressure can be determined by measuring the pressure shifts of the $^4T_2 \rightarrow {}^4A_2$ and $^2E \rightarrow {}^4A_2$ emission bands. The former shift rate can be determined by deconvoluting the emission spectrum as in Fig. 12 and monitoring the shift of the broad underlying band and the latter shift rate can be directly measured. We found shifts of 9 cm^{-1}/kbar and –0.8 cm^{-1}/kbar for the two transitions, respectively, and determined that Δ increases at a rate of 9.8 cm^{-1}/kbar (Fig. 13). Since emission from the $^4T_2$ state is suppressed at low temperature, the reciprocal of the limiting low temperature lifetime, 8.8 ms [253], provides an estimated value of $f_E = 114\ s^{-1}$ for Cr^{3+}: YAG. There is no way to stabilize emission from the $^4T_2$ state independent of emission from the ^2E state, so direct measurement of f_T in Cr^{3+}: YAG is not possible. If we treat f_T as an adjustable parameter and attempt to fit the room temperature lifetime data using Eq. (36), we found that we were unable to reproduce the data acceptably. The dotted curve in Fig. 14 shows a lifetime prediction using Eq. (36) and a representative $^4T_2 \rightarrow {}^4A_2$ emission lifetime of 163 μs ($f_T = 6135\ s^{-1}$) [139, 251]. We see from the prediction that consideration of the reduction of the thermal population of the $^4T_2$ state with pressure provides a reasonable fit to the lifetime data below ~60 kbar, but that the agreement becomes progressively worse at higher pressure. The pressure of ~60 kbar corresponds to the pressure above which we no longer observe $^4T_2 \rightarrow {}^4A_2$ emission intensity. We therefore see that the pure electronic model is unable to account for changes in lifetime that occur once the $^4T_2$ thermal population is essentially zero.

We continued by considering an improved electronic model [251, 252, 254] that includes spin-orbit coupling of the zero phonon ^2E and $^4T_2$ excited states. The presence of spin-orbit coupling provides a mechanism for incorporating spin-allowed character into the $^2E \rightarrow {}^4A_2$ transition and contributes to an increase in f_E. The extent of spin-orbit coupling depends on the spin-orbit coupling constant V_{so}:

$$V_{so} = \langle {}^4T_2 | H_{so} | {}^2E \rangle \tag{37}$$

and the energy difference Δ. The dependence of f_E on Δ can most simply be obtained from a perturbation theory model that considers spin-orbit coupling of only the zero phonon ^2E and $^4T_2$ states [251]. In such a model, the ^2E and $^4T_2$ states are mixed by the spin-orbit interactions according to the secular matrix

$$\begin{bmatrix} E(|{}^2E, 0\rangle) & V_{SO} \\ V_{SO} & E(|{}^4T_2, 0\rangle) \end{bmatrix} \tag{38}$$

where $|{}^2E, 0\rangle$ and $|{}^4T_2, 0\rangle$ designate the zero vibrational wavefunctions of the pure (unmixed) ^2E and $^4T_2$ states, respectively. The energies and wavefunctions resulting from the spin-orbit perturbation are

$$E_{1,2} = \frac{1}{2}\left[E(|{}^2E, 0\rangle) + E(|{}^4T_2, 0\rangle) \pm \sqrt{\Delta^2 + 4V_{SO}^2}\right] \tag{39}$$

and

$$\begin{aligned} \Psi_1 &= c\,|{}^2E, 0\rangle - d\,|{}^4T_2, 0\rangle \\ \Psi_1 &= c\,|{}^2E, 0\rangle + d\,|{}^4T_2, 0\rangle \end{aligned} \tag{40}$$

where the mixing coefficients c and d are given by

$$c=\sqrt{\frac{1}{2}}\left[1+\frac{\Delta}{\sqrt{\Delta^2+4V_{SO}^2}}\right]^{\frac{1}{2}}$$

$$d=\sqrt{\frac{1}{2}}\left[1-\frac{\Delta}{\sqrt{\Delta^2+4V_{SO}^2}}\right]^{\frac{1}{2}} \tag{41}$$

In the above equations, the subscripts "1" and "2" designate the mixed states that result from spin-orbit coupling of the pure ^2E and $^4T_2$ states.

The value of Δ controls which of the two states is lower in energy. In high field systems such as Cr^{3+}:YAG, Δ is positive and Ψ_1 corresponds to a lower energy mixed excited state that has predominantly ^2E character. In low field systems such as Cr^{3+}:$Lu_3La_2Ga_3O_{12}$, Δ is negative and Ψ_2 corresponds to a lower energy mixed excited state that has predominantly $^4T_2$ character. The transition from low field to high field behavior is illustrated in Fig. 15 which shows the variation of the squared mixing coefficients c^2 and d^2 (Eq. 41) as a function of Δ [250]. $\Delta = 0$ represents the case where the unmixed ^2E and $^4T_2$ states are degenerate and corresponds to maximum spin-orbit coupling (50% mixing). At large negative or large positive values of Δ, the ^2E and $^4T_2$ states are too far apart in energy to mix appreciably and we approach a pure electronic limit of unmixed states in

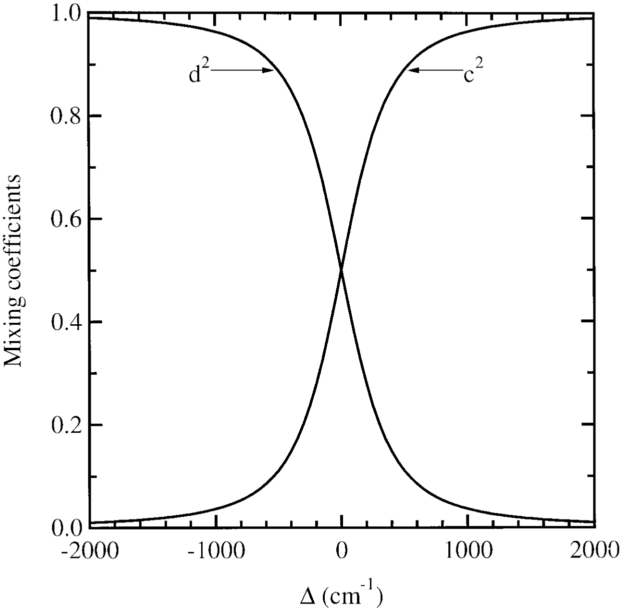

Fig. 15. Variation of the squared mixing coefficients c^2 and d^2 (Eq. 41) for the emitting state of Cr^{3+} with the energy difference Δ between the $^4T_2$ and ^2E states. The values $c^2 = 1$ and $d^2 = 1$ correspond to pure, unmixed ^2E and $^4T_2$ states, respectively. $\Delta < 0$ corresponds to low field behavior and $\Delta > 0$ corresponds to high field behavior

which the squared mixing coefficients tend toward 0 or 1. Δ values in the vicinity of zero correspond to appreciable spin-orbit coupling.

The increase in Δ with pressure leads to a decrease in the contribution of the $^4T_2$ state to the wavefunction of the ^2E emitting state in high field Cr^{3+} systems. As a result, the extent to which the emission is spin-allowed is reduced. This effect is independent of any thermal population effects and leads to a decrease in f_E with increasing pressure in high field Cr^{3+} systems. Thus both a reduction in the thermal population of the $^4T_2$ state and a reduction in $^4T_2-{}^2E$ spin-orbit mixing contribute to an increase in lifetime with pressure. The lifetime increase associated with spin-orbit coupling can be modeled by incorporating a pressure dependent contribution in f_E. f_E is proportional to the square of the transition matrix element associated with the luminescence transition. Using the spin-orbit mixed wavefunction Ψ_1 (Eq. 40) gives

$$\begin{aligned} f_E &\propto \langle {}^4A_2, 0|D|\Psi_1\rangle^2 = [c\langle {}^4A_2, 0|D|{}^2E, 0\rangle - d\langle {}^4A_2, 0|D|{}^4T_2, 0\rangle]^2 \\ &= d^2\langle {}^4A_2, 0|D|{}^2T_2, 0\rangle^2 \end{aligned} \tag{42}$$

where D is the electric dipole operator, the mixing coefficient d is given in Eq. (41), and the spin selection rule formally requires that the matrix element $\langle {}^4A_2|D|{}^2E\rangle$ be zero. Since the matrix element $\langle {}^4A_2|D|{}^4T_2\rangle$ is independent of the energy of the $^4T_2$ state, pressure influences the R-line lifetime through the mixing coefficient d (Eq. 41). The dependence can be most conveniently expressed by using Eq. (42) in the form

$$f_E(P) = f_E(P=0)\,\frac{(d(P))^2}{(d(0))^2} \tag{43}$$

Equation (43) can be substituted into Eq. (36) to give a prediction of the pressure dependence of the lifetime of Cr^{3+}:YAG based on a model that considers spin-orbit coupling of the zero phonon ^2E and $^4T_2$ states. Figure 14 includes a representative lifetime prediction based on this simple spin-orbit coupling model (dot-dash line). As in the pure electronic model, the prediction assumes that $f_E(P=0) = 114\ s^{-1}$ and $\Delta\ (cm^{-1}) = 828\ cm^{-1} + 9.8\,P$ (kbar). Since $f_T \gg f_E$, we further assume that pressure induced changes in spin-orbit coupling do not significantly affect f_T and use $f_T = 6135\ s^{-1}$. The final model parameter V_{SO} was set equal to a typical ambient pressure value, 202 cm^{-1} [254], and was assumed to be constant with pressure.

The prediction of the zero phonon spin-orbit coupling model clearly improves upon the prediction of the pure electronic model. Both models work well in the low pressure region (below ~60 kbar) where the thermal population of the $^4T_2$ state controls the lifetime. At higher pressure, the zero phonon spin-orbit coupling model qualitatively accounts for the continuing increase in lifetime and leads to the conclusion that the lifetime increase is due to a decreasing admixture of $^4T_2$ character in the emitting state. Quantitatively, however, the model overestimates the lifetime at high pressure. Refinements in the parameter values used in the model do not eliminate this deficiency.

Figure 14 also includes a more complete lifetime prediction (solid line) based on a single configurational coordinate model (Sect. 3.1) [113, 141]. The single configurational coordinate model is a generalization of the zero phonon spin-orbit coupling model (Eqs. 36 and 43) that incorporates the vibrational levels of the ^2E, $^4T_2$, and $^4A_2$ electronic states. The main elements of the model are depicted in Fig. 16 where α, β, and γ denote the vibrational quantum numbers of the ^2E, $^4T_2$, and $^4A_2$ states, respectively, and S is the Huang-Rhys factor of the $^4T_2$ state. The model assumes a single coupling phonon energy $\hbar\omega$ for all electronic states.

In the absence of spin-orbit coupling, the excited state energies and wavefunctions are given by

$$\begin{aligned} E_\alpha &= E_0 + \hbar\omega \\ T_\beta &= T_0 + \beta\hbar\omega = E_0 + \Delta + \beta\hbar\omega \end{aligned} \tag{44}$$

$$\begin{aligned} |^2E, \alpha\rangle &= |^2E\rangle\,|\alpha\rangle \\ |^2T_2, \beta\rangle &= |^2T_2\rangle\,|\beta\rangle \end{aligned} \tag{45}$$

where E_α and T_β refer to the energies of vibrational states α and β of the ^2E and $^4T_2$ electronic states, respectively; the wavefunctions are conventional Born-Op-

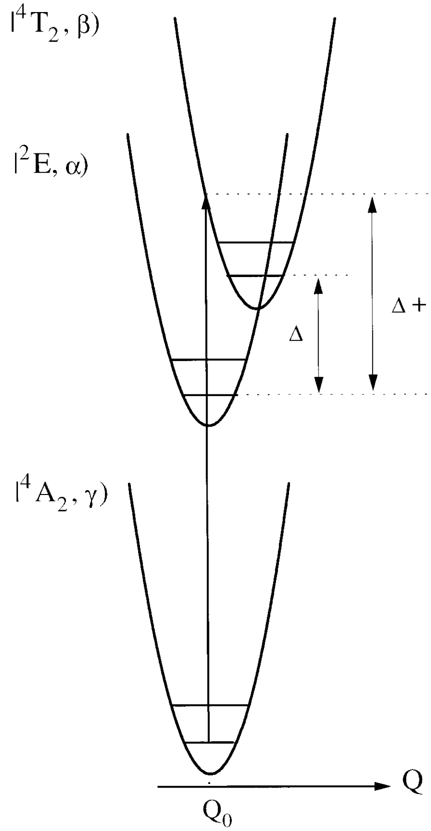

Fig. 16. Energy levels of Cr^{3+} in the context of the single configuration coordinate model. α, β, and γ label the vibrational levels of the ^2E, $^4T_2$, and $^4A_2$ states, respectively. Δ is the zero phonon energy difference between the $^4T_2$ and ^2E states and S is the Huang-Rhys factor

penheimer products of electronic and vibrational wavefunctions, and the vibrational wavefunctions correspond to harmonic oscillator wavefunctions.

In the presence of spin-orbit coupling, each vibrational state of the ^{2}E state can potentially mix with each vibrational state of the ^{4}T$_2$ state. The resulting energies and wavefunctions of the mixed states can be obtained by finding the eigenvalues and eigenvectors of a secular matrix with elements given by

$$\begin{aligned}
&\langle {}^2E, \alpha|H|{}^2E, \alpha'\rangle = (E_0 + \alpha\hbar\omega)\,\delta_{\alpha,\alpha'} \\
&\langle {}^4T_2, \beta|H|{}^4T_2, \beta'\rangle = (E_0 + \Delta + \beta\hbar\omega)\,\delta_{\beta,\beta'} \\
&\langle {}^2E, \alpha|H|{}^4T_2, \beta'\rangle = V_{\text{so}}\langle\alpha|\beta\rangle = V_{\alpha,\beta}
\end{aligned} \tag{46}$$

where $H = H_0 + H_{SO}$, H_0 represents the system in the absence of spin-orbit coupling, and the vibrational overlap factors $\langle\alpha|\beta\rangle$ can be computed from the Manneback recursion relations [135]. The effect of spin-orbit coupling is to modify the energies and wavefunctions given in Eqs. (44) and (45) by introducing non-zero off-diagonal elements into the secular matrix. The resulting wavefunctions Ψ are linear combinations of the wavefunctions given in Eq. (45) and are illustrated below for the zero phonon level of the mixed ^{2}E excited state:

$$\Psi({}^2E,0) = \sum_{\alpha} c^0_{E,\alpha}(\Delta)|{}^2E, \alpha\rangle + \sum_{\beta} c^0_{T,\beta}(\Delta)|{}^4T_2, \beta\rangle \tag{47}$$

The mixing coefficients depend on Δ and are obtained from the eigenvectors of the secular matrix. Similar equations can be written for all of the mixed vibrational states.

In the single configurational coordinate model, the individual ^{2}E vibrational states mix differently with each of the vibrational ^{4}T$_2$ states. As a result, the radiative decay rate $f_{E,\alpha}$ differs for each vibrational ^{2}E state. The radiative decay rate for a given vibrational ^{2}E state is the sum of transition rates to all vibrational states γ of the ^{4}A$_2$ ground state. For the transition $\Psi({}^2E,0) \rightarrow |{}^4A_{2,\gamma}\rangle$, for example, we have

$$\begin{aligned}
f_{E,0}(\Delta) &= k\sum_{\gamma}|\langle\Psi({}^2E,0)|D|{}^4A_2,\gamma\rangle|^2 \\
&= k\sum_{\beta}|(c^0_{T,\beta}(\Delta))^2\langle{}^4T_2|D|{}^4A_2\rangle^2 \\
&= \frac{1}{\tau_T}\sum_{\beta}(c^0_{T,\beta}(\Delta))^2
\end{aligned} \tag{48}$$

where τ_T is the lifetime of a pure (unmixed) ^{4}T$_2$ state. Similar expressions can be written for all vibrational states of the mixed ^{2}E and ^{4}T$_2$ and can be used to develop the following prediction for the ^{2}E lifetime of Cr^{3+}: YAG:

$$\frac{1}{\tau_{\text{tot}}} = \frac{\sum_{\alpha}\exp\left(-\frac{E_\alpha - E_0}{kT}\right)\cdot f_{E,\alpha} + 3\cdot\sum_{\beta}\exp\left(-\frac{T_\beta - E_0}{kT}\right)\cdot f_{T,\beta}}{\sum_{\alpha}\exp\left(-\frac{E_\alpha - E_0}{kT}\right) + 3\cdot\sum_{\beta}\exp\left(-\frac{T_\beta - E_0}{kT}\right)} \tag{49}$$

$$\frac{1}{\tau_{\mathrm{tot}}} = \frac{\frac{1}{\tau_{\mathrm{T}}}\sum_{\beta}|c_{\mathrm{T},\beta}(\Delta)|^2 + \frac{1}{\tau_{\mathrm{T}}}3\exp\left[-\frac{\Delta}{kT}\right]}{1+3\cdot\exp\left[-\frac{\Delta}{kT}\right]} \tag{50}$$

where $f_{E,\alpha}$ and $f_{T,\beta}$ refer to the decay rates from the α^{th} ^2E and β^{th} $^4T_2$ vibrational levels, respectively. If we assume that $f_{E,\alpha}$ and $f_{T,\beta}$ are independent of α and β, we can simplify Eq. (49) to obtain Eq. (50) where the mixing coefficients $c_{T,\beta}(\Delta)$ are the same as those given in Eq. (47) [141].

When Eq. 50 is fitted to the Cr^{3+}:$Y_3Al_5O_{12}$ lifetime data using 30 vibrational levels for each of the ^2E and $^4T_2$ states, we find excellent agreement with the data over a wide range of pressure (Fig. 14). In the fit, V_{SO}, S, and $\hbar\omega$ were set to reasonable ambient pressure values and held constant. $\Delta(P=0)$ and τ_T were treated as adjustable and the experimentally observed increase in Δ (9.8 cm^{-1}/kbar) was used. Equation 50 was also used to model the lifetime increases in the related Cr^{3+}:$Gd_3Sc_2Ga_3O_{12}$ (Fig. 17) and Cr^{3+}:$Gd_3Ga_5O_{12}$ (Fig. 18) systems [141].

The high pressure studies of the garnets demonstrate the important role of spin-orbit coupling in establishing the lifetime of Cr^{3+} and clearly illustrate that the $^4T_2$ state continues to exert a strong influence on the radiative decay rate of

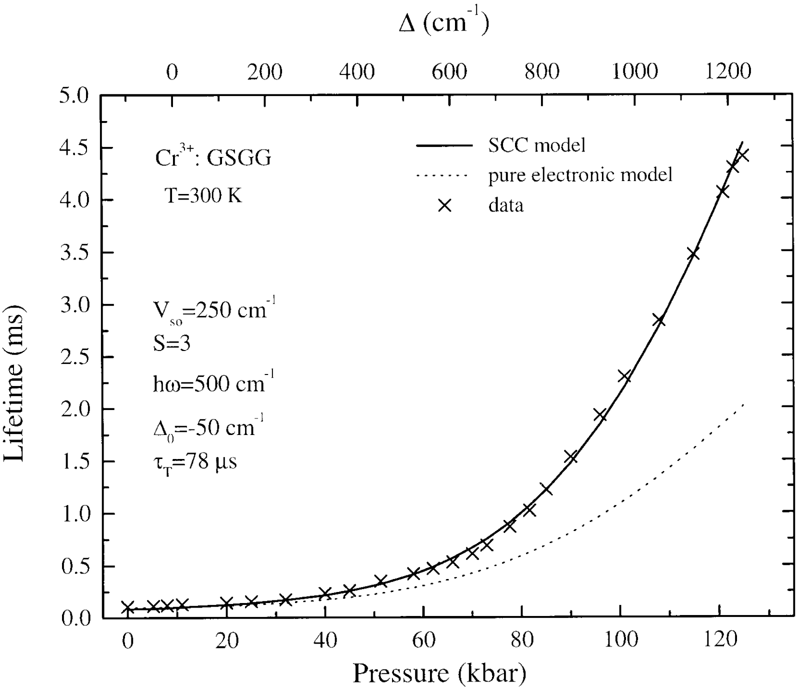

Fig. 17. Variation of the lifetime of the $^2E \rightarrow {}^4A_2$ transition of Cr^{3+}: $Gd_3Sc_2Ga_3O_{12}$ with pressure at room temperature. Two theoretical curves are shown. The parameter values correspond to those used in the single configuration coordinate (SCC) model. Excitation wavelength: 580 nm

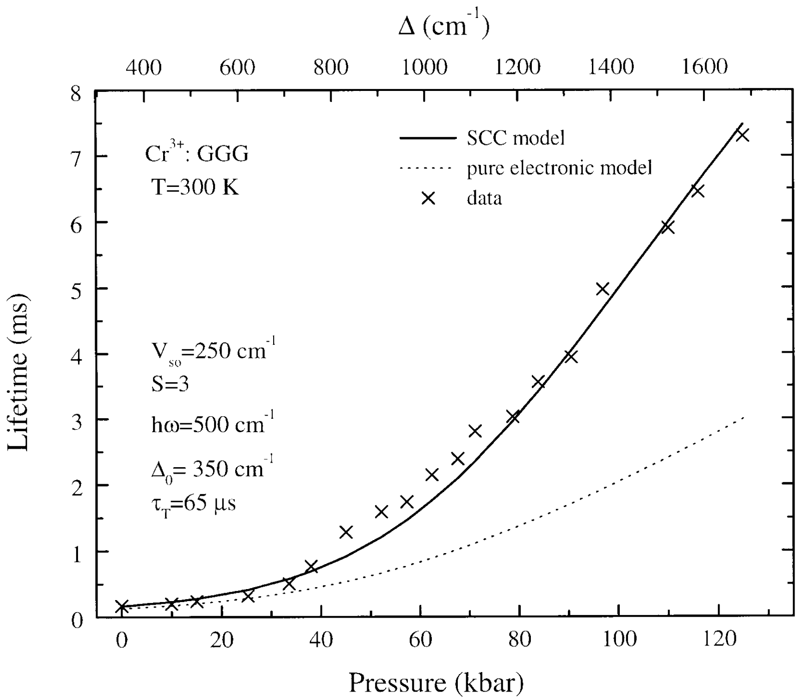

Fig. 18. Variation of the lifetime of the $^2E \rightarrow {}^4A_2$ transition of Cr^{3+}: $Gd_3Ga_5O_{12}$ with pressure at room temperature. Two theoretical curves are shown. The parameter values correspond to those used in the single configuration coordinate (SCC) model. Excitation wavelength: 580 nm

the ^2E state even when its thermal population is negligible and no spectral evidence of its participation in the luminescence is present. At 200 kbar in Cr^{3+}: YAG, for example, we estimate that the $^4T_2$ state is ~3000 cm^{-1} higher in energy than the ^2E state and yet the increase in ^2E continues unabated with no indication of leveling off. In follow-up work [113], we exploited the ability of pressure to eliminate the thermal $^4T_2$ contribution to the Cr^{3+}: YAG lifetime and systematically considered the effect of temperature on the radiative decay rate of the ^2E state. By considering temperature effects above 100 kbar, we were able to remove the overlapping thermal $^4T_2$ contribution and to isolate the thermally activated vibronic ^2E contribution to the radiative decay. This work illustrates the ability of pressure to resolve overlapping spectral processes and provides an example of how high pressure can be used to gain insight not attainable through variations of chemical composition at ambient pressure.

Galanciak et al. [139] also considered the effect of pressure on the lifetime of Cr^{3+} in a garnet system. They specifically examined Cr^{3+} in the garnet $Lu_3La_2Ga_3O_{12}$ and reported an increase in the lifetime of Cr^{3+} from 70 μs to 350 μs over a pressure range of 150 kbar. They successfully modeled the lifetime increase with an adiabatic electronic model. Their model is noteworthy because it is numerically more convenient than the configuration coordinate model used by us and therefore can be more readily extended to include multiple excited electronic states. As a result, Galanciak et al. were able to resolve specifically the ^2E and $^4T_2$ electronic states into their spin-orbit components when modeling the lifetime of Cr^{3+}. The adiabatic electronic model also offers promise for analyzing systems with symmetries lower than octahedral, a direction that we believe will be emphasized in future high pressure work because of the promise of using pressure to systematically influence low symmetry distortions and to extend our understanding of the relationship of local coordination to electronic structure [157, 158].

3.3.2
Lanthanide Systems

The available data on the variation of $4f \rightarrow 4f$ transition lifetimes with pressure are limited. The shielded nature of 4f states leads one to expect that pressure will have only a small effect on the lifetimes of 4f states. Unlike transition metal systems, the weak dependence of 4f energies on pressure suggests that variations in spin-orbit coupling of lanthanide states with pressure will be negligible. The one important difference between lanthanides and transition metals is that lanthanide ions typically emit from several excited states while transition metal ions normally emit only from the first excited state. As a result, it is more common to observe interactions between high energy emitting 4f states and charge transfer or interconfigurational states. The available pressure studies on lanthanide lifetimes have emphasized these interactions.

Webster and Drickamer [255] studied the $^5D_J \rightarrow {}^7F_J$ emission of Eu^{3+} ($4f^6$) doped at several concentrations in La_2O_2S as a function of pressure. The energy level diagram of Eu^{3+} is shown in Fig. 19. Emission spectra were measured upon excitation into the charge transfer state. At ambient pressure, emission occurs from the $^5D_{0,1,2}$ states to several of the ^7F_J states. Upon increasing pressure up to 110 kbar, the emission intensity from the $^5D_{0,1}$ states was observed to decrease steadily. On the contrary, emission intensity from the $^5D_2$ state increased between 0 kbar and 20 kbar, remained approximately constant between 20 kbar and 80 kbar, and decreased above 80 kbar. The decrease in $^5D_2$ intensity coincided with the onset of new emission from the $^5D_3$ state. In addition to intensities, Webster and Drickamer also measured the emission lifetimes from the $^5D_{1,2,3}$ states. The values of the lifetimes depended on the Eu^{3+} concentration, but the trends with pressure were uniform. The $^5D_1$ emission lifetime remained nearly constant with pressure while the $^5D_2$ emission lifetime increased between 0 kbar and 20 kbar and remained constant above 20 kbar. The $^5D_3$ lifetime could be measured above 70 kbar and was observed to increase up to 110 kbar.

The decreased $^5D_1$ emission intensity and constant $^5D_1$ lifetime with pressure indicate that pressure is influencing the population of the $^5D_1$ state rather than its non-radiative decay rate. Webster and Drickamer developed a ^5D_J excitation model based on feeding rates from the charge transfer state involved in the excitation process. According to the model [256, 257], the ^5D_J states are populated through transfer of excitation energy from the charge transfer state and depopulated by back transfer. Upon excitation, transfer occurs sequentially to the

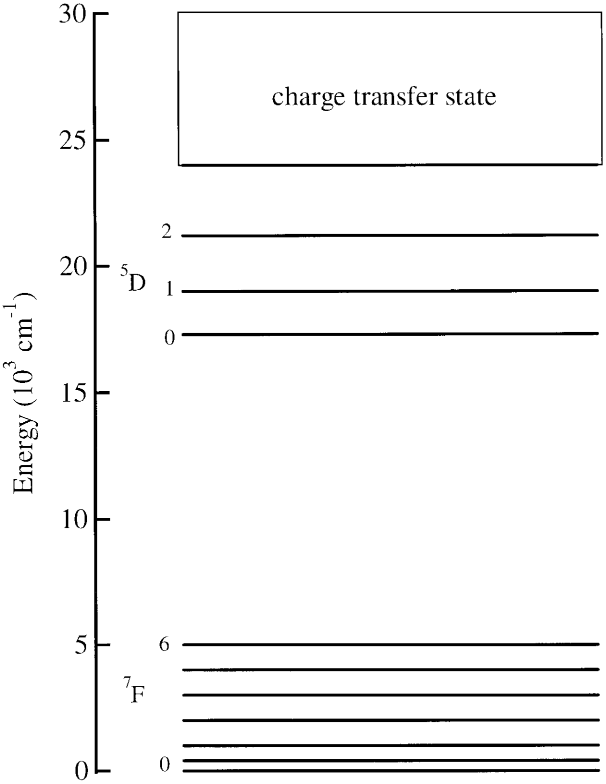

Fig. 19. Energy level structure of Eu^{3+} in La_2O_2S. The $^7F_{0-6}$ and $^5D_{0-2}$ states are derived from the ground $4f^6$ configuration of Eu^{3+}. The charge transfer state represents a metal-ligand charge transfer process

$^5D_{3,2,1,0}$ states. The rate of back transfer from a given ^5D_J state depends on the activation barrier separating the state and the charge transfer state. At ambient pressure, the activation energies from the $^5D_{0,1,2,3}$ states to the charge transfer state are 6300 cm^{-1}, 5100 cm^{-1}, 3000 cm^{-1}, and 1000 cm^{-1}, respectively. The low activation barrier associated with the $^5D_3$ state is responsible for its efficient depopulation and lack of emission intensity at room temperature.

Webster and Drickamer measured the variation of the energy of the charge transfer state with pressure and showed that it increased by ~ 2000 cm^{-1} between 0 kbar and 110 kbar. The increased charge transfer energy leads to increased activation barriers with the ^5D_J states. Since the activation barrier associated with the $^5D_3$ state is the smallest at ambient pressure, back transfer from the $^5D_3$ state will be most strongly inhibited with pressure. As a result, the population of the $^5D_3$ state progressively increases with pressure. Above ~ 70 kbar, the back transfer rate becomes sufficiently small that emission from the $^5D_3$ state is observed. The initial increase in the lifetime and intensity of the $^5D_2$ emission with pressure indicates that the $^5D_2$ state is also thermally depopulated at room temperature by back transfer to the charge transfer state at ambient pressure. Above ~20 kbar, the $^5D_2$ activation energy is high enough in energy to prevent significant back transfer. The activation energies of the $^5D_{0,1}$ states are sufficiently large at ambient pressure to prevent thermal depopulation. The observed emission intensity decreases with pressure for the $^5D_{0,1}$ states are a consequence of a reduction in population as the $^5D_{2,3}$ populations increase. Webster and Drickamer reported similar behavior for $Eu^{3+}:Y_2O_2S$.

Gleason et al. [258] also considered the effect of pressure on the lifetime of Eu^{3+} in La_2O_2S and agreed with the conclusions of Webster and Drickamer. Gleason et al. further investigated $Tb^{3+}(4f^8)$ emission in Gd_2O_2S and observed a quenching rather than an enhancement, of emission intensity from higher excited states of Tb^{3+}. The 4f energy level structure of Tb^{3+} is related to that of Eu^{3+} through the hole formalism and consists of a first excited $^5D_{4-0}$ manifold and a $^7F_{6-0}$ ground manifold. In both manifolds, energy increases with decreasing J. Unlike Eu^{3+}, Tb^{3+} does not have a charge transfer state in close proximity to the emitting ^5D_J states. Instead, Tb^{3+} has an interconfigurational $4f^75d$ state located ~2000 cm^{-1} above the $^5D_3$ state. At ambient pressure and room temperature, emission was observed from the $^5D_{3,4}$ states to several ^7F_J states. As the pressure was increased between 0 kbar and 15 kbar, a progressive quenching and elimination of emission intensity from the $^5D_3$ state was observed. The quenching was accompanied by a pronounced decrease in emission lifetime. The lifetime of the emission from the lower energy $^5D_4$ state, however, was unaffected by pressure. Gleason et al. attributed the behavior to a decrease in energy of the $4f^75d$ state relative to the ^5D_J states of the ground $4f^8$ configuration. They measured the shift in excitation of the $4f^75d$ state and observed a decrease in energy of ~2500 cm^{-1} between 0 kbar and 50 kbar. They argued that the decreased energy of the $4f^75d$ state reduced the activation barrier for thermal depopulation of the $^5D_3$ state. They also determined the $^5D_3$ lifetime variation with pressure using a model analogous to Eq. (36) and found good agreement with the experimental values.

Gleason et al. also commented on the opposite shift directions for the charge transfer state of Eu^{3+} and the interconfigurational state of Tb^{3+}. They argued that the energies of interconfigurational transitions are controlled by the nephelauxetic effect and decrease as a result of increased covalency at high pressure. Conversely, they argued that the energies of charge transfer states are influenced primarily by the electronegativity of the ligand anion. Since ligand electronegativity varies inversely with covalency in the nephelaxetic series, it is reasonable to expect opposite shift directions for charge transfer and interconfigurational states with pressure.

We recently completed a high pressure luminescence study of Sm^{2+} $(4f^6)$ in a series of MFCl ($M = Ba^{2+}, Sr^{2+}, Ca^{2+}$) hosts and considered the influence of the $4f^55d$ excited configuration on f → f emission properties [116]. Sm^{2+} is isoelectronic with Eu^{3+} and exhibits an emission spectrum dominated by the $^5D_J \rightarrow {}^7F_J$ transitions of the $4f^6$ ground configuration. The main difference between Sm^{2+} and Eu^{3+} is that the lower charge of Sm^{2+} makes it more covalent than Eu^{3+} and leads to a lower energy for the excited $4f^55d$ configuration. Our studies of Sm^{2+} have considered the depopulation of the ^5D_J states through thermal crossover to the $4f^55d$ configuration as well as electronic mixing of opposite parity 5d character into the ^5D_J emitting states. The former effect influences the non-radiative decay rate of Sm^{2+} while the latter effect influences the radiative decay rate. The objective of our study was to use pressure to influence the energy of the $4f^55d$ configuration relative to the ^5D_J states and to investigate systematically its effect on thermally activated crossover and 4f-5d electronic mixing processes.

A schematic energy level diagram of Sm^{2+}:SrFCl is shown in Fig. 20. At ambient pressure, emission is observed from the $^5D_{0,1,2}$ states of Sm^{2+} to several of the ^7F_J states (Fig. 21). Since the $4f^55d$ configuration is only slightly higher in energy than the ^5D_J states, the emission spectrum exhibits a strong temperature dependence. Figure 22 illustrates the effect of temperature at ambient pressure on the $^5D_{2,1,0} \rightarrow {}^7F_0$ transitions. At 12 K, emission occurs primarily from the $^5D_2$ state. Upon increasing temperature, thermal depopulation of the $^5D_2$ state to the $4f^55d$ configuration occurs followed by population of the $^5D_1$ state at interme-

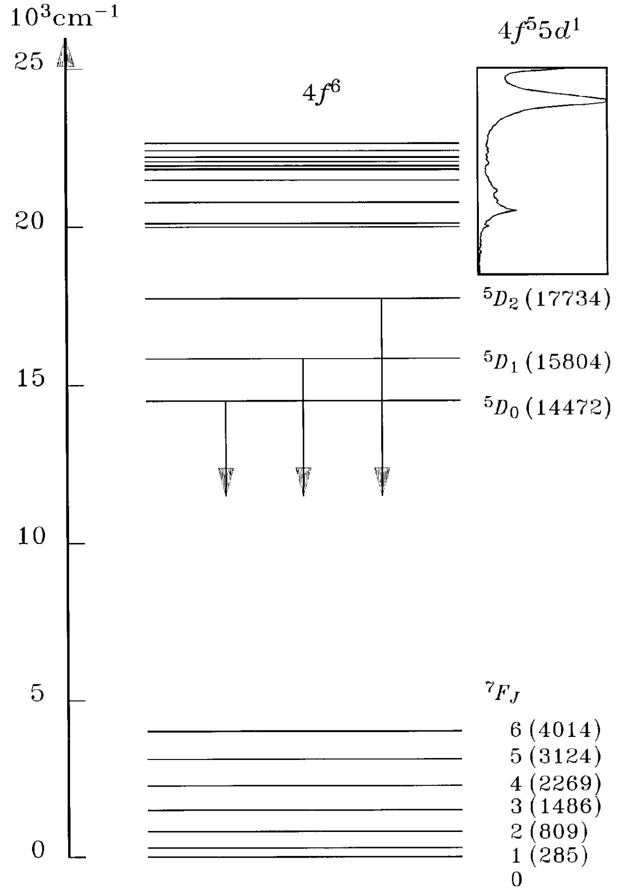

Fig. 20. Energy level structure of Sm^{2+} in SrFCl. States from the $4f^6$ and $4f^55d$ configurations overlap above ~19,000 cm^{-1}. The spectral inlay illustrates $4f^6 \rightarrow 4f^55d$ absorption at ambient pressure and room temperature

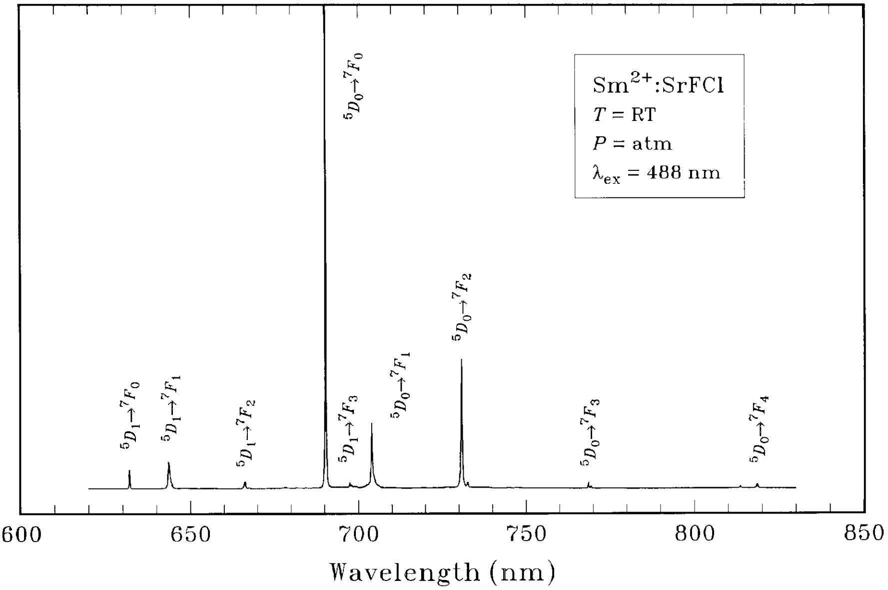

Fig. 21. Luminescence spectrum of Sm^{2+}: SrFCl at ambient pressure and temperature. Several transitions within the $4f^6$ ground configuration are labeled

diate temperatures and the $^5D_0$ state at high temperatures. The temperature dependent spectra reflect changes in the relative populations of the $^5D_{0,1,2}$ states. At room temperature, thermal depopulation of the $^5D_1$ state is efficient and the spectrum is dominated by emission from the $^5D_0$ state. We have presented a quantitative configuration coordinate model of the effect of temperature on the populations of the $^5D_{0,1,2}$ states [116]. The model includes radiative decay and non-radiative thermal crossover processes and adequately describes the effect of temperature on spectral intensities and lifetimes.

Population redistribution among the $^5D_{0,1,2}$ states was also observed upon increasing pressure at constant temperature and were attributed to decreasing thermal crossover activation barriers resulting from a red shift of the lowest energy $4f^55d$ state with pressure [116, 259]. The population redistribution effects observed with pressure were also reflected in lifetime measurements. Figure 23 shows the variation of the lifetimes of the $^5D_{1,0}$ states of Sm^{2+}: SrFCl with pressure. The $^5D_1$ lifetime was observed to decrease with pressure at room temperature and at 20 K. The shorter lifetime observed at room temperature is a consequence of thermal depopulation. At 20 K and low pressure we expect thermal depopulation of the $^5D_1$ state to be negligible and yet we still observed a decrease in lifetime with pressure. We also expect negligible thermal depopulation of the $^5D_0$ state at room temperature and 20 K and observed a decrease in the $^5D_0$ lifetime with pressure. The variation of $^5D_0$ lifetime with pressure at 20 K (not shown) is superimposable on the room temperature curve shown in Fig. 23.

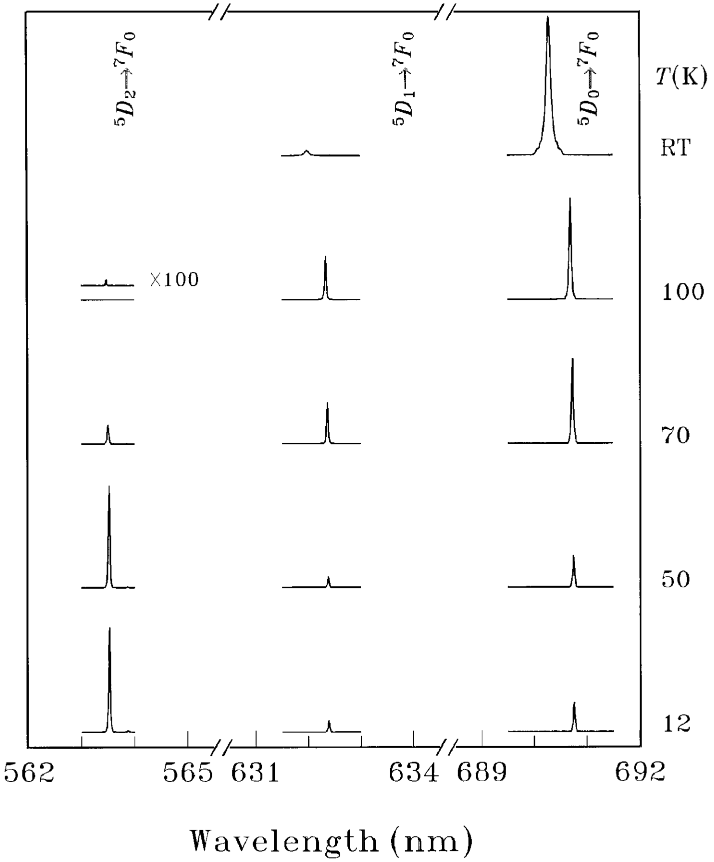

Fig. 22. Effect of temperature on the $^5D_{0-2} \rightarrow {}^7F_0$ emission of Sm^{2+}: SrFCl at ambient pressure. Excitation wavelength: 488 nm

The pressure dependent lifetime results indicate that as the energy of the $4f^55d$ configuration decreases with pressure, an effect in addition to thermal depopulation is contributing to the lifetime decreases of the $^5D_{0,1}$ states. Since the effect is important at low temperature, we have proposed and developed a model that considers the effect of pressure on the radiative decay rate of the $^5D_0$ state. The model considers both electric and magnetic dipolar contributions to the transition strength of the $^5D_0$ state and includes 4f-5d mixing though crystal field and spin-orbit interactions in second- [260] and third order [261]. The model shows that, as the $4f^55d$ configuration shifts red with pressure, the wavefunction of the $^5D_0$ state includes more opposite parity (5d) and heptet spin character. As a result, emission from the $^5D_0$ state to the ^7F_J levels becomes more allowed with increasing pressure and the radiative decay rate increases. Quantitative application of the model to the $^5D_0$ lifetime data of Sm^{2+}: SrFCl led to excellent agreement and a predicted red shift of ~23 cm^{-1}/kbar for the lowest

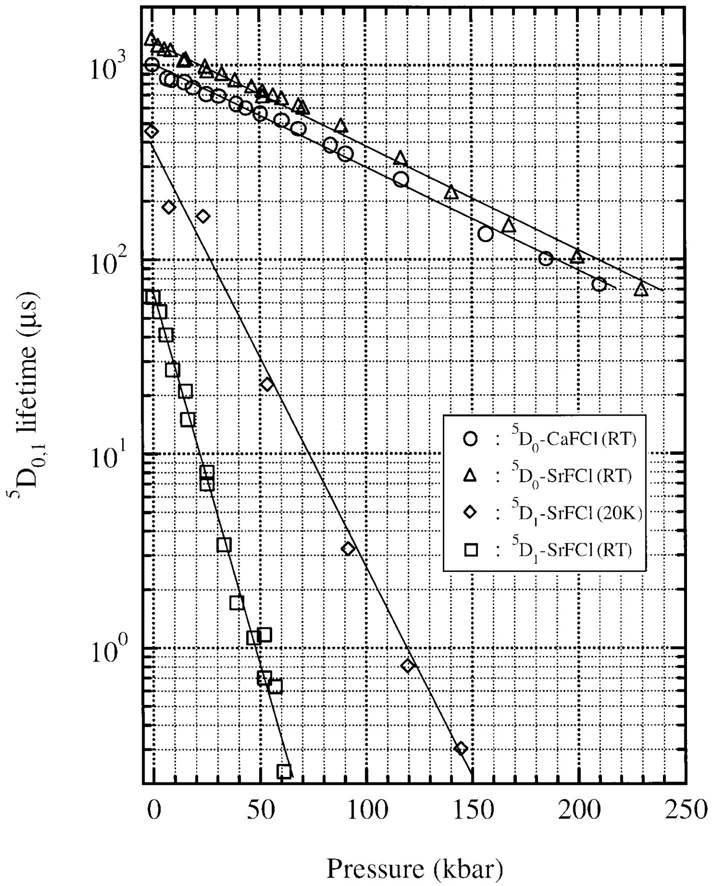

Fig. 23. Variation of the $^5D_0$ and $^5D_1$ lifetimes of Sm^{2+} in SrFCl and CaFCl with pressure. Excitation wavelength: 532 nm

energy state of the $4f^55d$ configuration. The model was also successful at predicting the pressure dependence of the lifetime of Sm^{2+}:CaFCl.

3.4
Excited State Electronic Crossovers

In the preceding sections, we have seen that the direction and magnitude of the variation of electronic energies with pressure depends on the nature of a given electronic state and its dependence on underlying crystal field and covalency effects. The differential response of electronic states to pressure provides an opportunity to use pressure to alter the ordering of electronic states and to stabilize new luminescence processes as a result. We refer to a re-ordering of electronic states as an electronic crossover and in this section we present examples of electronic crossovers from the recent luminescence literature of transition metal and lanthanide systems. Our focus will be on excited state electronic crossovers and their effect on luminescence properties.

3.4.1
Transition Metal Systems

In order to observe an electronic crossover of two excited states, a blue shift of the lower participating excited state normally must occur simultaneously with a red shift of the higher participating excited state. It is in principle possible to observe crossovers between states that shift in the same direction with appreciably different magnitudes, but no examples of this type have been reported. Electronic crossovers are likely in transition metal systems because of the wide variation in pressure shifts observed for electronic transitions in transition metal systems (see Sect. 3.2.1).

The first pressure-induced excited state electronic crossover in a luminescent transition metal system was reported by Dolan et al. [175] in a study of Cr^{3+}: K_2NaGaF_6. Cr^{3+} is an excellent candidate for observing an electronic crossover with pressure because, depending on its crystal field strength, it can exhibit either spin allowed $^4T_2 \rightarrow {}^4A_2$ emission (low field Cr^{3+}) or spin forbidden $^2E \rightarrow {}^4A_2$ emission (high field Cr^{3+}). The strong dependence of the energy of the $^4T_2$ state on crystal field strength leads to a strong increase in the energy of the $^4T_2 \rightarrow {}^4A_2$ transition with pressure (see Sect. 3.2.1.2) and the primary dependence of the ^2E energy on covalency effects leads to a weak decrease in the energy of the $^2E \rightarrow {}^4A_2$ transition with pressure (see Sect. 3.2.1.1). As a result, it becomes possible to induce a $^4T_2$-^2E electronic crossover in low field Cr^{3+} systems.

The Cr^{3+}: K_2NaGaF_6 system studied by Dolan et al. is a low field system and exhibits smooth broadband $^4T_2 \rightarrow {}^4A_2$ emission peaking at ~13,700 cm^{-1} at ambient pressure and room temperature. Upon increasing pressure, the emission exhibited a blue shift of ~18 cm^{-1}/kbar. Between ~25 kbar and ~61 kbar the broad emission band lost intensity and was replaced by a sharp, structured emission spectrum. Dolan et al. attributed the spectral transformation to a pressure induced ^2E-$^4T_2$ electronic crossover and assigned the structured emission spectrum to the zero phonon line and vibronic sidebands of the $^2E \rightarrow {}^4A_2$ transition. Later papers by the same group demonstrated analogous pressure induced ^2E-$^4T_2$ crossovers in isostructural Cr^{3+}: K_2NaScF_6 [176] and Cr^{3+}: Cs_2NaYCl_6 [142] beginning at ~50 kbar and ~80 kbar, respectively.

Similar crossovers have also been reported in Cr^{3+}:$KZnF_3$ [173], Cr^{3+}: $Na_3In_2Li_3F_{12}$ [174], Cr^{3+}:$La_3Lu_2Ga_3O_{12}$ [139], and $[Cr(urea)_6](ClO_4)_3$ [143]. The study of Cr^{3+}:$Na_3In_2Li_3F_{12}$ included a lifetime analysis and showed that a lifetime increase from ~310 μs to ~580 μs occurred during the crossover. The study of Cr^{3+}: $La_3Lu_2Ga_3O_{12}$ considered pressures extending ~50 kbar above the crossover and showed that the $^2E \rightarrow {}^4A_2$ transition shifted red at a rate of ~0.8 cm^{-1}/kbar. The lifetime increase and spectral shift at high pressure are consistent with the assignment of the emission to $^2E \rightarrow {}^4A_2$.

We have recently observed a similar $^2E-{}^4T_2$ electronic crossover in Cr^{3+}: $Gd_3Sc_2Ga_3O_{12}$ and have considered the interaction of the two states during the crossover in more detail [141]. Figure 24 shows the spectral transformation accompanying the electronic crossover. At ambient pressure, the ^2E and $^4T_2$ states of Cr^{3+}: $Gd_3Sc_2Ga_3O_{12}$ are nearly degenerate and the spectrum is dominated by the broad $^4T_2 \rightarrow {}^4A_2$ emission band because of the much faster radiative decay rate from the $^4T_2$ state. As the pressure was increased, the energy of the $^4T_2$ state increased relative to the ^2E state. As a result, the contribution of the $^4T_2$ state to the spectrum progressively decreased with increasing pressure and the spectrum transformed to the sharp, structured emission associated with the $^2E \rightarrow {}^4A_2$ transition. The lifetime increased from ~100 µs at ambient pressure to ~4.4 ms at 120 kbar (Fig. 17).

The stabilized $^2E \rightarrow {}^4A_2$ emission at high pressure consists of intense zero phonon lines and vibronic sidebands. A high resolution measurement of the zero phonon portion of the spectrum at 70 K is shown in Fig. 25. The zero phonon lines exhibited a blue shift at low pressure followed by a shift reversal at high pressure. The stabilization of sharp zero phonon lines between 5 kbar and 9 kbar

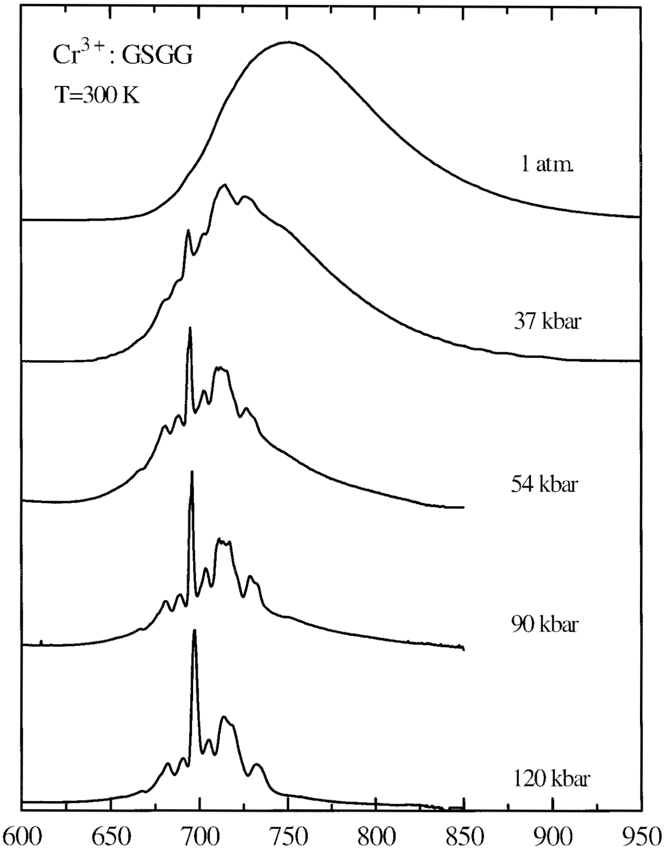

Fig. 24. Room temperature emission spectrum of Cr^{3+}: $Gd_3Sc_2Ga_3O_{12}$ at several pressures. Excitation wavelength: 514 nm

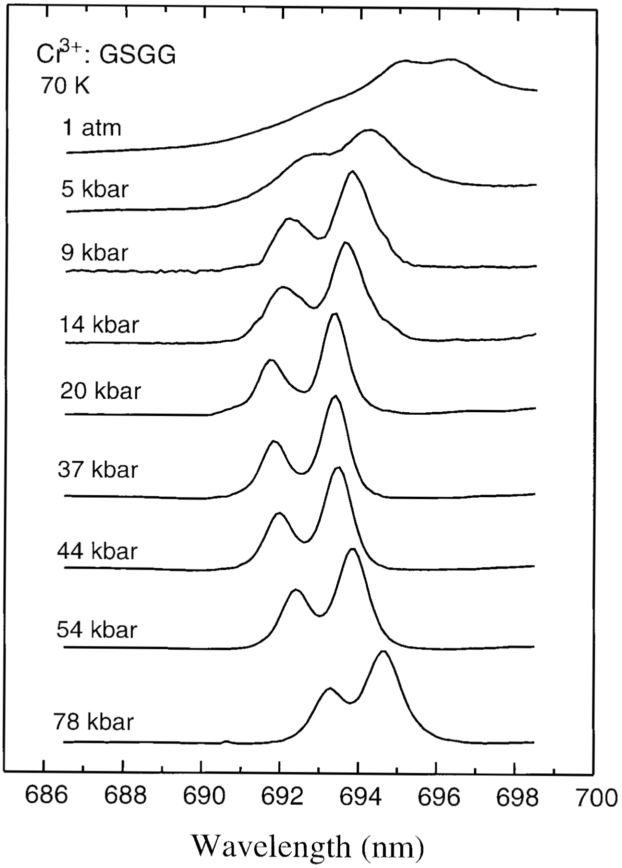

Fig. 25. High resolution R-line ($^2E \rightarrow {}^4A_2$) spectrum of Cr^{3+}:$Gd_3Sc_2Ga_3O_{12}$ at 70 K and several pressures. Excitation wavelength: 514 nm

indicates that the ^2E state is lower in energy than the $^4T_2$ state at 9 kbar and that the ensuing blue shift corresponds to ^2E emission. The pressure shift of the more intense, lower energy R_1 line is summarized in Fig. 26.

The initial blue shift of the R-lines cannot be explained on the basis of the discussion presented in Sect. 3.2.1.1 which argues that the ^2E state of Cr^{3+} should shift red with pressure due to enhanced covalency. The solid line shown in Fig. 26 represents a theoretical fit of the shift reversal using the single configuration coordinate model used previously to model the effect of pressure on spin-orbit coupling and luminescence lifetime of Cr^{3+} (Eqs. 46 and 47). The curve in Fig. 26 depicts the energy of the zero phonon ^2E state as a function of both pressure and $\Delta = E(^4T_2,0) - E(^2E,0)$. The zero phonon energy was obtained by diagonalizing the matrix defined by Eq. (46) and corresponds to the wavefunction given in Eq. (47). As in the lifetime prediction (Fig. 17), ambient pressure values of V_{SO}, S, and $\hbar\omega$ were used and held constant during the theoretical fit. Only the ambient pressure value of Δ was varied. Optimum agreement with the shift data

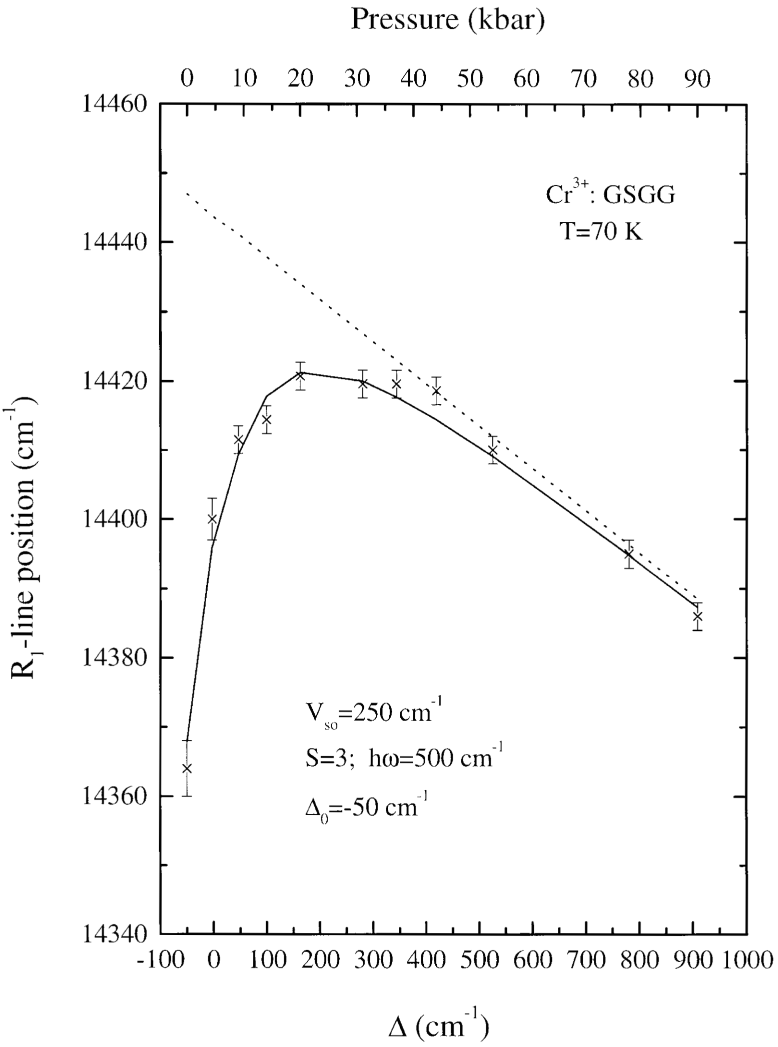

Fig. 26. The R_1-line energy Cr^{3+}: $Gd_3Sc_2Ga_3O_{12}$ at 70 K as a function of pressure and the ^2E-$^4T_2$ energy separation (Δ). The *solid line* shows the predicted energy from the single configuration coordinate model using the parameters listed in the figure. The *dashed line* shows the prediction of a pure electronic model that does not include spin-orbit coupling. The initial blue shift is due to the effects of spin-orbit coupling

was obtained when $\Delta_0 = -50$ cm^{-1}. The dashed line in Fig. 26 represents the predicted shift in the absence of spin-orbit coupling ($V_{SO} = 0$) and becomes increasingly valid when spin-orbit coupling effects become less important as the value of Δ increased at high pressure.

The single configuration coordinate model illustrates the important role played by the $^4T_2$ state in controlling the ^2E shift at low pressure. The initial blue shift of the ^2E state is a consequence of the spin-orbit mixing with the $^4T_2$ state. Although the $^4T_2$ state is higher in energy than the ^2E state at low pressure, it is sufficiently close in energy to contribute significantly to the ^2E wavefunction. Since a pure $^4T_2$ state exhibits a large blue shift with pressure while a pure ^2E state shows only a small red shift, it is easy to see how the $^4T_2$ state can control the shift behavior of the emitting state. As the pressure was increased and the $^4T_2$ state increased in energy, its contribution to the wavefunction of the emitting state decreased. As a result, the blue shift decreased and we ultimately observe the red shift customarily reported for the ^2E emission of Cr^{3+}.

3.4.2
Lanthanide Systems

The small pressure shifts of $f \rightarrow f$ transitions (see Sect. 3.2.2) imply only small changes in the relative energies of $4f^n$ states with pressure. As a result, electronic crossovers involving $4f^n$ states of lanthanides are uncommon and limited to closely spaced crystal field components within a given $^{2S+1}L_J$ term [193, 262]. Much larger shifts, however, are observed for the 5d states of lanthanides (Sect. 3.2.3) and it becomes possible to observe 5d-4f electronic crossovers in lanthanide systems.

The first report of a 5d-4f electronic crossover was by Yoo et al. in a study of Sm^{2+}:SrF_2 [212]. At ambient pressure, only $^5D_J \rightarrow {}^7F_J$ emission is observed in Sm^{2+}:SrF_2. At ~15 kbar, Yoo et al. noticed the onset of a broad emission band. Above ~15 kbar, the intensity of the broad emission band increased and the sharp $^5D_J \rightarrow {}^7F_J$ emission intensity decreased. Above ~40 kbar, only the broad emission was observed. Yoo et al. assigned the broad emission to a $4f^55d \rightarrow 4f^6$ transition and reported a red shift of 14.9 cm^{-1}/kbar for it up to 120 kbar.

We have recently extended the pressure range of our study of Sm^{2+}:SrFCl (see Sect. 3.3.2) in an attempt to induce an excited state $4f^55d-4f^6$ electronic crossover. We attributed the pressure-induced decrease in the ^5D_J lifetimes of Sm^{2+}:SrFCl to enhanced 4f–5d crystal field and spin-orbit mixing resulting from a red shift of the $4f^55d$ state. In Fig. 27 we show luminescence spectra at selected pressures. At low pressure we observed sharp line spectra from the ^5D_J states. Beginning at ~150 kbar, we began to observe a broad emission band superimposed on the ^5D_J emission. As the pressure was increased to ~300 kbar, the broad emission band continued to gain intensity and ultimately dominated the spectrum. Although we have not fully analyzed the data, we believe that the broad spectral band corresponds to emission from the $4f^55d$ state and that an excited state $4f^55d-4f^6$ electronic crossover has occurred. An interesting aspect of the data is the strong red shift (~ –5 cm^{-1}/kbar) observed for the $^5D_0$ state. This shift is much larger than the shift normally reported for $4f \rightarrow 4f$ transitions and is probably related to strong mixing of the $^5D_0$ and $4f^55d$ states. Future work will consider this effect in more detail.

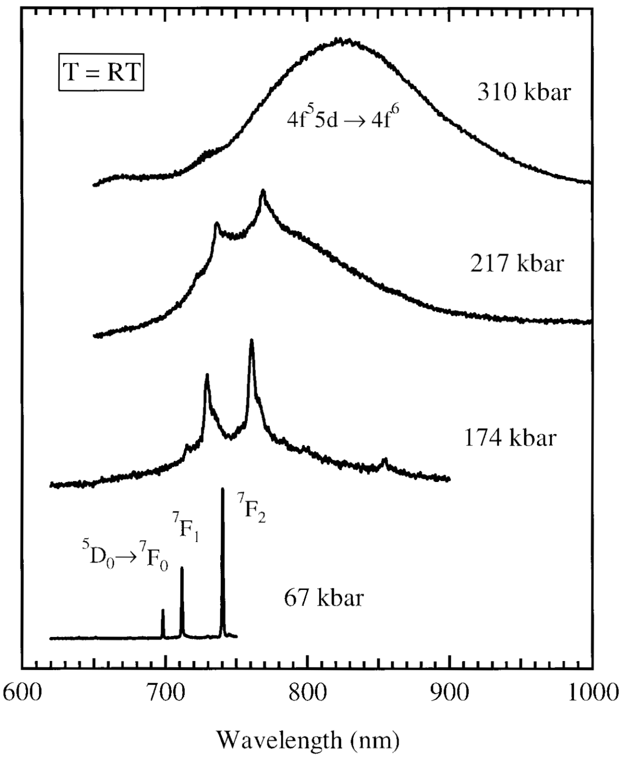

Fig. 27. Luminescence spectrum of Sm^{2+}: SrFCl at room temperature and several pressures. At low pressure, intraconfigurational $^5D_0 \rightarrow {}^7F_J$ emission was observed. At high pressure, a transformation to a broadband spectrum was observed. The broadband spectrum has been tentatively assigned to an interconfigurational $4f^5 5d \rightarrow 4f^6$ transition

3.5
Energy Transfer Phenomena

Energy transfer among or between transition metal and lanthanide ions is a common phenomenon and one that can be used to gain fundamental insight into molecular processes. Energy transfer also provides flexibility in the design of optical materials and represents a method for improving the efficiency of many luminescent systems. In the conventional Förster-Dexter theory [263, 264], the rate of energy transfer depends on the spectral overlap of donor emission and acceptor absorption and on the interatomic distance between the donor and acceptor ions. The distance dependence varies as R^{-n} where R is the donor-acceptor separation and $n = 6, 8, 10$, respectively, for the dipole-dipole, dipole-quadrupole, and quadrupole-quadrupole mechanisms of energy transfer. Pressure can influence energy transfer by altering the donor-acceptor separation or the donor-acceptor spectral overlap. The decrease in donor-acceptor separation expected upon compression will contribute to an enhancement of energy transfer rate. The magnitude of the decrease in donor-acceptor separation will depend on the compressibility of the host lattice and can generally be expected to be small in oxide lattices, intermediate in halide and sulfide lattices, and large in organic lattices or metal complexes. The effect of pressure on spectral overlap depends on the nature of the electronic states involved in energy transfer and their shift behavior with pressure. In principle, pressure can be used to create or destroy the donor emission-acceptor absorption resonance condition required for energy transfer and can therefore enhance or diminish spectral overlap. In this section, we discuss recent results that illustrate the potential of high pressure to provide new insight into energy transfer processes.

3.5.1

Lanthanide and Transition Metal Doped Inorganic Lattices

One of the early studies of the effect of pressure on energy transfer was presented by Merkle et al. [265] in a study of the stoichiometric laser material NdP_5O_{14}. The material is an interesting one because it is one of a small number of known materials with a high lanthanide concentration that exhibits minimal concentration quenching of emission. Merkle et al. considered the lifetime and emission properties of Nd^{3+} in NdP_5O_{14} and $Nd_{0.1}Y_{0.9}P_5O_{14}$. Their lifetime studies showed a decrease by a factor of close to 2 in the lifetime of the $^4F_{3/2}$ state of Nd^{3+} with pressure up to 70 kbar in NdP_5O_{14} and essentially no lifetime change in the lightly doped $Nd_{0.1}Y_{0.9}P_5O_{14}$ system. Merkle et al. considered several possible origins for the lifetime decrease in the stoichiometric system and concluded that it was due to changes in interionic Nd^{3+}–Nd^{3+} interactions rather than to changes in the radiative or non-radiative decay rates of individual Nd^{3+} ions. They considered concentration quenching due to enhanced cross-relaxation and enhanced energy migration to traps and showed that the latter was consistent with the high pressure lifetime results. The study by Merkle et al. demonstrated the ability of pressure to increase the diffusion coefficient for energy migration by decreasing interionic separations.

Blanzat et al. [266] also used high pressure to investigate the weak concentration quenching effects observed in the stoichiometric systems $La_{1-x}Tb_xP_5O_{14}$, $La_{1-x}Eu_xP_5O_{14}$, and $Eu_{1-x}Tb_xP_5O_{14}$. They considered the lifetimes of the $^5D_4$ level of Tb^{3+} and the $^5D_2$ level of Eu^{3+}. In $La_{1-x}Tb_xP_5O_{14}$ and $La_{1-x}Eu_xP_5O_{14}$, they observed lifetimes that were independent of composition and that decreased with increasing pressure. They argued in agreement with Merkle et al. [265], that pressure enhanced the rate of energy migration to quenching traps. In the mixed system $Eu_{1-x}Tb_xP_5O_{14}$, Blanzat et al. observed decreases in both the Eu^{3+} and Tb^{3+} lifetimes with increasing pressure over a wide range of compositions. They attributed the lifetime decreases to enhanced, reversible energy transfer between the $^5D_4$ state of Tb^{3+} and the $^5D_2$ state of Eu^{3+} due to improved spectral overlap resulting from the pressure-induced shifts in the electronic states.

We have recently considered energy transfer in the Cr^{3+}:Tm^{3+}:YAG system [267, 268]. At ambient pressure, energy transfer occurs from the thermally and spin-orbit coupled ^2E and $^4T_2$ states of Cr^{3+} to the overlapping $^3F_2$, $^3F_3$ states of Tm^{3+} (Figs. 28 and 29). Once excited, Tm^{3+} decays non-radiatively and subse-

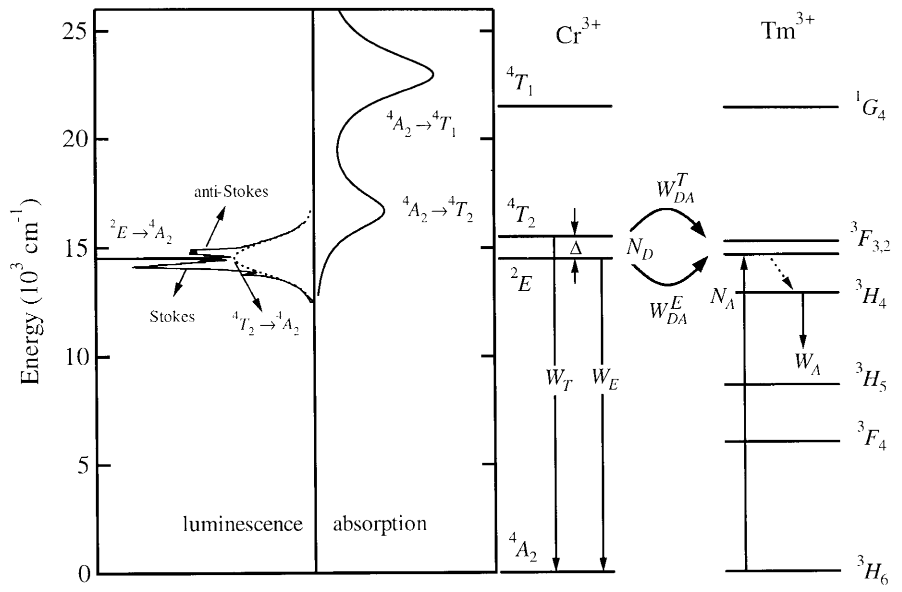

Fig. 28. Energy levels of Cr^{3+} and Tm^{3+} in $Y_3Al_5O_{12}$. Energy transfer occurs from the ^2E and $^4T_2$ levels of the donor, Cr^{3+}, to the $^3F_2$ and $^3F_3$ levels of the acceptor, Tm^{3+}. W_{DA}^E and W_{DA}^T represent the rates of energy transfer from the $^4T_2$ and ^2E states of Cr^{3+}, respectively. W_T and W_E are the decay rates (radiative+non-radiative) of the $^4T_2$ and ^2E states of Cr^{3+}, respectively. W_A is the decay rate (radiative+non-radiative) of the $^3H_4$ state of Tm^{3+}. The *left side* of the figure shows the $^4T_2$, $^2E \rightarrow {}^4A_2$ emission and $^4A_2 \rightarrow {}^4T_2$, $^4T_1$ absorption bands of Cr^{3+}

quently emits from the $^3H_4$ and $^3F_4$ states to the $^3H_6$ ground state. At ambient pressure and room temperature, $\Delta = E(^4T_2) - E(^2E) = \sim 800$ cm^{-1} and energy transfer occurs from both the ^2E and thermally populated $^4T_2$ states. Upon increasing pressure at room temperature, Δ increased and the thermal population of the $^4T_2$ state decreased (see Sect. 3.3.1). As a result, with pressure we progressively eliminated the contribution of the $^4T_2$ state to the energy transfer process and continually approached a state in which energy transfer occurred from a pure ^2E state. By characterizing the energy transfer process at high pressure and back extrapolating, we have an opportunity to resolve the competing energy transfer processes from the ^2E and $^4T_2$ states at ambient pressure.

Our experiments consisted of measuring the decay curves of Cr^{3+} in 0.2% Cr^{3+}:0.7%Tm^{3+}:YAG as a function of temperature and pressure. Representative pressure dependent decay curves at room temperature are shown in Fig. 30. The decay curves indicate a decrease in the decay rate of Cr^{3+} with increasing pressure. The rate of decrease, however, differs from that observed for Cr^{3+} in Cr^{3+}:YAG (Fig. 14) where no energy transfer occurs. In order to separate the contributions of intracenter (^2E, $^4T_2$ radiative and non-radiative decay to the $^4A_2$ ground state) and intercenter (^2E, $^4T_2$ energy transfer to Tm^{3+}) processes to the decay, we analyzed the decay curves using a rate equation model. According to the model, the time dependence of the excited state population of Cr^{3+} is

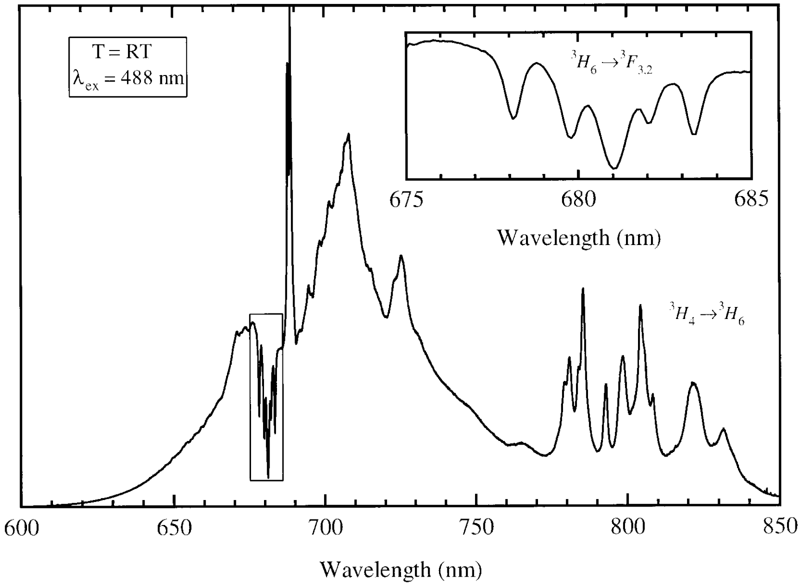

Fig. 29. Emission spectrum of Cr^{3+}:Tm^{3+}:$Y_3Al_5O_{12}$ at ambient pressure and room temperature upon excitation of Cr^{3+} at 488 nm. The spectrum consists of $^4T_2, {}^2E \rightarrow {}^4A_2$ emission from Cr^{3+} between ~620 nm and ~775 nm and $^3H_4 \rightarrow {}^3H_6$ emission of Tm^{3+} between ~775 nm and ~850 nm. The Tm^{3+} emission is a consequence of $Cr^{3+} \rightarrow Tm^{3+}$ energy transfer. The depression in the Cr^{3+} emission spectrum represents wavelengths over which Cr^{3+} emission overlaps Tm^{3+} absorption (*inset*)

given by

$$N_D(t) = N_D(0) \exp(-W_D t) \exp[-P_{DA}(t)] \tag{51}$$

where D and A denote the donor (Cr^{3+}) and acceptor (Tm^{3+}) species, respectively, W_D is the intracenter decay rate of Cr^{3+}, and $P_{DA}(t)$ is an energy transfer rate function. In the absence of migration among Cr^{3+} centers, $P_{DA}(t)$ can be written as a sum of transfer rates from Cr^{3+} to Tm^{3+} ions in successive coordination shells s in the YAG lattice. If we let N_s denote the number of Tm^{3+} ions in coordination shell s and R_s denote the distance from Cr^{3+} to a Tm^{3+} ion in coordination shell s, we can write

$$P_{DA}(t) = \sum_s N_s \ln\{1 - C_A + C_A \exp[-W_{DA}(R_s)t]\} \tag{52}$$

where C_A is the Tm^{3+} concentration (number density) and $W_{DA}(R_s)$ is the rate of energy transfer from Cr^{3+} to a single Tm^{3+} acceptor located at a distance R_s. In the Förster-Dexter model, $W_{DA}(R_s) = \frac{\alpha_{DA}^m}{R_s^m}$ where m = 6, 8, or 10 and α_{DA}^m is proportional to the donor emission-acceptor absorption overlap integral.

Equations (51) and (52) were used to fit the pressure dependent decay curves at room temperature. In the fits we considered the first eight acceptor coordination shells, assumed a dipole-dipole energy transfer mechanism (m = 6) and al-

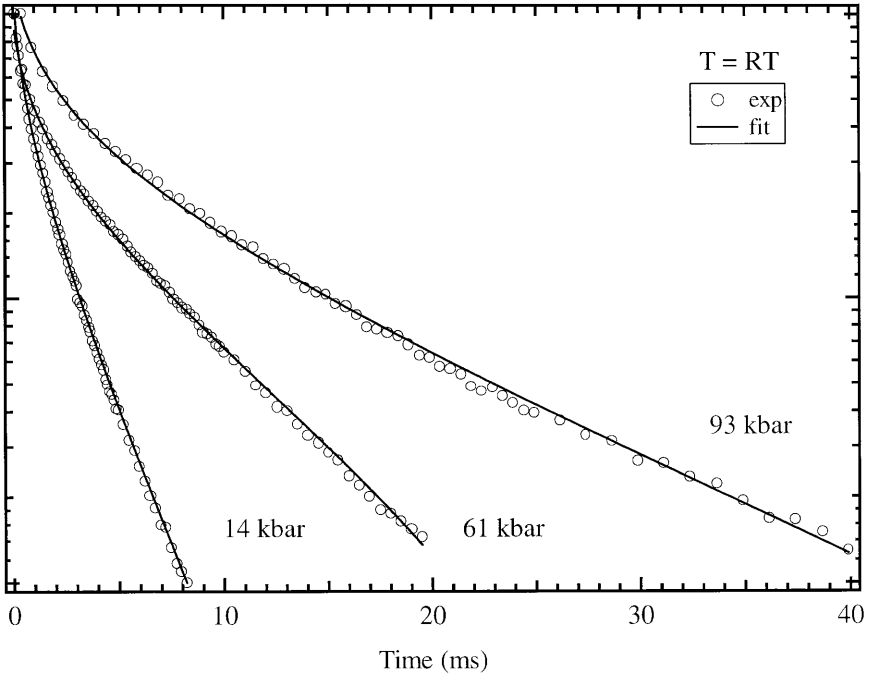

Fig. 30. Experimental decay curves of Cr^{3+} emission in Cr^{3+}:Tm^{3+}:$Y_3Al_5O_{12}$ at room temperature at three pressures. Excitation wavelength: 580 nm

lowed W_D and $W_{DA} = \sum_s W_{DA}(R_s)$ to vary. The solid curves in Fig. 30 depict representative fits. The values of W_D obtained agreed well with the pressure dependent lifetime data of Cr^{3+}: YAG (Fig. 14). The resulting values of W_{DA} are shown in Fig. 31. The results indicate a factor of ~4 decrease in the rate of energy transfer as the thermal population of the $^4T_2$ state is eliminated with increasing pressure. The limiting high pressure transfer rate of ~100 ms^{-1} corresponds to the room temperature transfer rate from a pure ^2E state. The constancy of the ^2E transfer rate at high pressure indicates that little change in ^2E-$^3F_2$,$^3F_3$ spectral overlap occurs with pressure and that the observed decrease in transfer rate is due only to the decrease in $^4T_2$ thermal population. Back extrapolation of the ^2E energy transfer rate to ambient pressure indicates that the room temperature transfer rate from the $^4T_2$ state is ~300 ms^{-1} and that the $^4T_2$ state accounts for ~75% of the energy transfer events at ambient conditions even though it is ~800 cm^{-1} higher in energy than the ^2E state. The leveling of the ^2E transfer rate also shows that the ^2E energy transfer rate is independent of the extent of ^2E-$^4T_2$ spin-orbit coupling. This result is in contrast to the ^2E lifetime of Cr^{3+}: YAG which continued to increase significantly with pressure even after the $^4T_2$ thermal population had been eliminated (see Sect. 3.3.1). The solid curve shown in Fig. 31 represents a theoretical fit of the transfer rate based on a model that includes a temperature dependent $^4T_2$ contribution, a temperature dependent

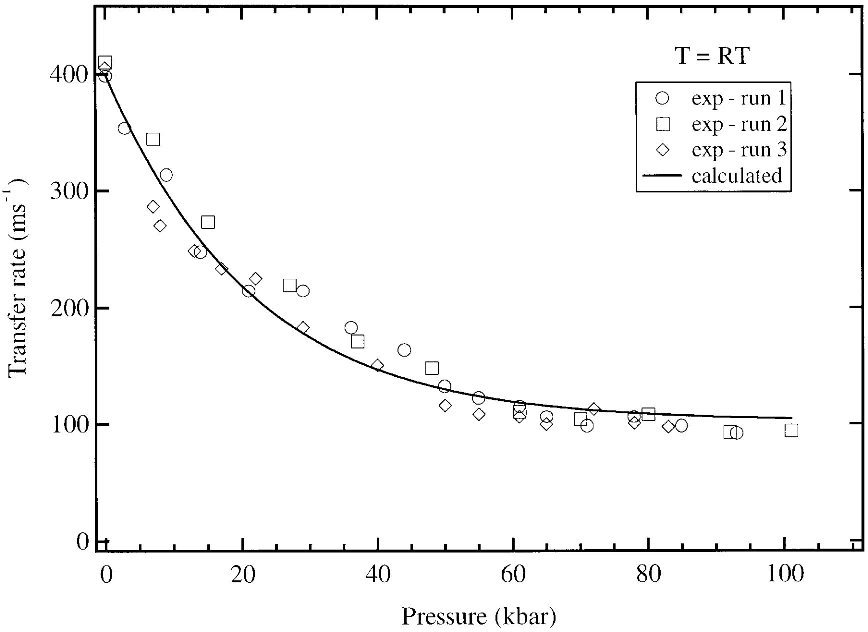

Fig. 31. Variation of the $Cr^{3+} \rightarrow Tm^{3+}$ energy transfer rate in $Cr^{3+}:Tm^{3+}:Y_3Al_5O_{12}$ with pressure

anti-Stokes ^2E contribution, and a temperature independent zero phonon ^2E contribution [268]. Through simultaneous variations of temperature and pressure, we were able to resolve completely and quantify the three separate effects that contribute to $Cr^{3+} \rightarrow Tm^{3+}$ energy transfer in YAG.

3.5.2
Lanthanide Containing Complexes

Yersin et al. [227, 228, 269–271] have considered the effect of pressure on energy transfer from charge transfer states of $Au(CN)_2^-$ layers and $Pt(CN)_4^{2-}$ chains to excited $4f^n$ states of lanthanide cations. In their initial studies of pressure effects in $Au(CN)_2^-$ and $Pt(CN)_4^{2-}$ complexes, Yersin et al. [219–222, 227, 228, 236] considered systems containing charge balancing alkali or alkaline earth cations and focused on properties of the charge transfer transitions (Sect. 3.2.4). In the presence of charge balancing lanthanide cations, energy transfer from the charge transfer states of $Au(CN)_2^-$ and $Pt(CN)_4^{2-}$ becomes possible [272, 273]. The energy transfer studies of Yersin et al. [227, 269, 270] were motivated by the large pressure shifts observed for the charge transfer transitions of $Au(CN)_2^-$ and $Pt(CN)_4^{2-}$ and the small pressure shifts associated with $f \rightarrow f$ transitions (see Sect. 3.2.2). The large difference in shift rates indicates that pressure will have a significant influence on energy transfer processes from $Au(CN)_2^-$ layers and $Pt(CN)_4^{2-}$ chains to lanthanide cations through variations in spectral overlap.

Yersin et al. [269] recently reported on energy transfer in $Eu[Au(CN)_2]_3 \cdot 3H_2O$. At ambient pressure, excitation into the charge transfer absorption band leads to emission only from the $^5D_0$ and $^5D_1$ states of Eu^{3+}. The absence of charge transfer emission has been attributed to efficient transfer of the excitation energy from the donor $Au(CN)_2^-$ ions to the acceptor Eu^{3+} ions. Upon application of pressure, charge transfer emission gradually appeared and ultimately dominated the spectrum (Fig. 32). Weak charge transfer emission was first observed at 13 kbar and exhibited a red shift of 130 cm^{-1}/kbar. Yersin et al. [269] attributed the appearance of the charge transfer emission to a progressive reduction of the donor-acceptor spectral overlap with pressure due to the large shift of the charge transfer emission band of the donor. Back extrapolation of the peak donor emission energy leads to a predicted energy of 23,600 cm^{-1} at ambient pressure and suggests that energy transfer occurs through the $^5L_6$ and/or $^5D_3$ states of Eu^{3+} at ambient pressure.

The ~60 kbar pressure range covered by Yersin et al. [269] was large enough to systematically shift the charge transfer emission into and out of resonance with the $^5D_{3,2,1}$ excited states of Eu^{3+}. Even though the charge transfer state was in direct resonance with the $^5D_2$ state at ~16 kbar, charge transfer emission was observed. This result indicates that energy transfer occurs more efficiently at ambient pressure than ~16 kbar and suggests in particular that energy transfer to the $^5L_6$ state is efficient because of the high oscillator strength of the $^7F_0 \rightarrow {}^5L_6$ transition. At ~16 kbar, resonance with the $^5L_6$ state no longer exists and charge transfer emission competes more favorably with energy transfer to the ^5D_J states. Between 30 kbar and 60 kbar, the charge transfer emission shifts into and then out of resonance with the $^5D_1$ state of Eu^{3+}. Over this pressure range, Yersin et al. showed, in accordance with Förster-Dexter theory, that the intensity of $^5D_0$ emission intensity varied linearly with the spectral overlap of the charge transfer emission and $^7F_0 \rightarrow {}^5D_1$ absorption bands. They also showed that increased overlap with the $^7F_0 \rightarrow {}^5D_0$ absorption band did not improve energy transfer efficiency.

Yersin et al. also examined energy transfer to lanthanide ions in $Pt(CN)_4^{2-}$ chains [227, 228, 271]. In $Eu_2[Pt(CN)_4]_3 \cdot 18H_2O$, they found efficient energy transfer from the self trapped exciton to the $^5D_1$ state of Eu^{3+} at ambient pressure. An increase in pressure led to a red shift of the self trapped exciton emission and an elimination of spectral overlap between the self trapped exciton emission and the $^5D_1$ state. As a result, $^5D_1$ emission was no longer observable upon excitation of the self trapped exciton state. Since the shift of the self trapped exciton emission with pressure led to spectral overlap with the $^5D_0$ state, energy transfer and emission from the $^5D_0$ state were observed after energy transfer to the $^5D_1$ state was no longer possible. In contrast to $Eu[Au(CN)_2]_3 \cdot 3H_2O$, efficient energy transfer to the $^5D_0$ state was observed in $Eu_2[Pt(CN)_4]_3 \cdot 18H_2O$. Above ~20 kbar, the self trapped exciton emission band had shifted to below the energy of the $^5D_0$ state and energy transfer was no longer observed. Similar energy transfer effects were observed in $Sm_2[Pt(CN)_4]_3 \cdot 18H_2O$ with increasing pressure [271].

One unexpected finding in the energy transfer study of $Eu_2[Pt(CN)_4]_3 \cdot 18H_2O$ was the inability of the free exciton emission band to produce energy

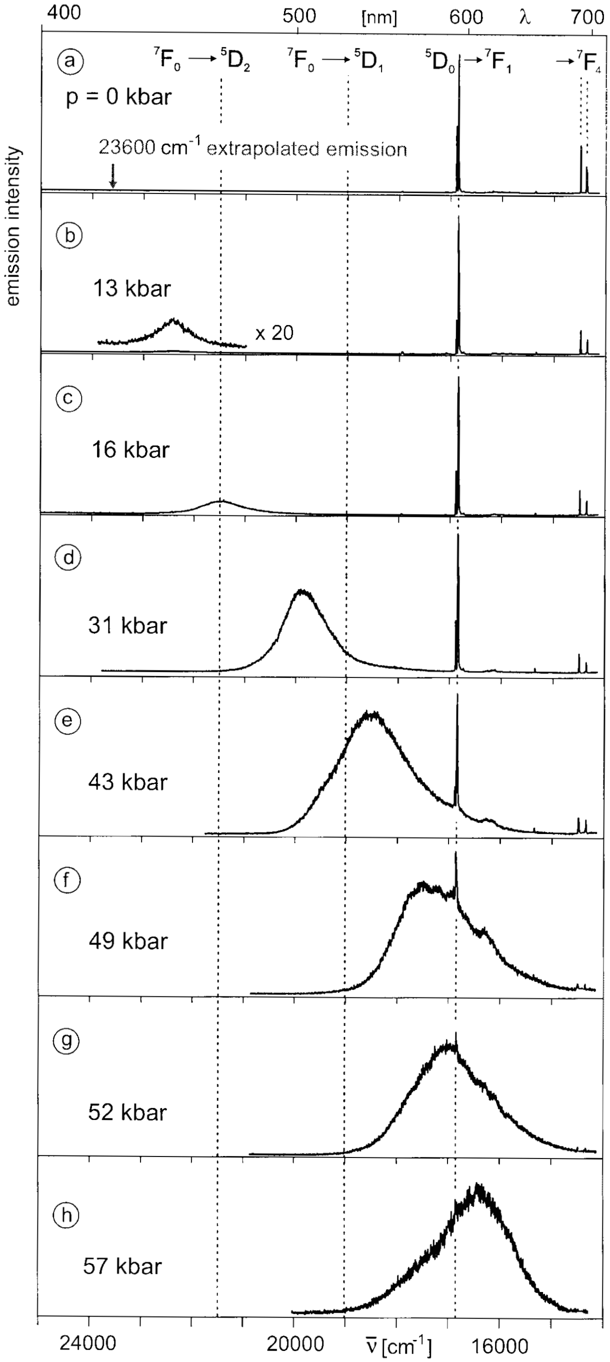

Fig. 32a–h. Emission spectrum at 20 K of single crystal $Eu[Au(CN)_2]_3 \cdot 3H_2O$ at selected pressures. Excitation wavelength: 363.8 nm

transfer to the ^5D_J states of Eu^{3+}. At ambient pressure, the free exciton emission band is observed and overlaps the $^5D_2$ state of Eu^{3+}. The absence of $^5D_2$ emission at ambient pressure indicates that energy transfer from the free exciton emission state is inefficient. With increasing pressure, the free exciton emission shifted red and was brought successively into resonance with the $^5D_1$ and $^5D_0$ states. No evidence for energy transfer from the free exciton state to either state was observed. Once the self trapped exciton emission had shifted below the $^5D_0$ state, energy transfer was no longer observed even though strong overlap of the free exciton emission band with the $^5D_0$ state was present.

The energy transfer studies of Yersin et al. provide excellent examples of how pressure can be used to tune and de-tune the energy resonance condition required for energy transfer. For a given degree of spectral overlap, their results also indicate that donors can preferentially transfer energy to certain excited states of acceptors and that some donor emission transitions are more effective at energy transfer than others. Based on their findings, it appears that "selection rules" for energy transfer may exist.

3.6
Site Selective Spectroscopy

A common complicating effect in the interpretation of the emission spectra of transition metals and lanthanides in solids is the presence of multiple bonding environments. Dopants are often incorporated into more than one crystallographic site in host lattices and exhibit emission spectra characteristic of several bonding sites. Emission spectra of dopants in a given crystallographic site can also differ due to local distortions, strain effects, defects or statistical differences in the chemical identity of one or more nearest or more distant neighbors. These effects lead to inhomogeneous broadening of spectral lines. Amorphous phases represent extreme examples of inhomogeneous broadening. Transition metal and lanthanide doped glasses exhibit broad emission spectra that consist of a superposition of contributions from dopant ions in bonding sites that vary with respect to local coordination geometry and coordination number. Dopant-dopant interactions also influence emission spectra in crystalline or amorphous hosts and in metal complexes.

A current challenge in the area of luminescent materials is achieving an understanding of the range of bonding sites occupied by dopants and the resolving the contribution of individual bonding sites to the observed emission properties. At ambient pressure, site selective spectroscopic information is typically obtained through high resolution, wavelength selective excitation studies (fluorescence line narrowing) or time resolved methods [274–276]. In wavelength selective excitation studies, the objective is to use a narrow line laser to excite selectively dopants in different bonding sites. In the absence of energy transfer, only the selectively excited dopants emit and we ideally obtain a spectrum that is characteristic of one bonding site. By tuning the excitation laser, it is possible to sample all dopant sites in a system and to resolve the contribution of distinct sites to the inhomogeneous emission properties. Wavelength selective excitation methods are effective when the absorption transitions of different sites are well resolved in wavelength. In practice, wavelength selective methods have proven most useful for lanthanide dopants because of the sharp nature of f → f transitions. The sharp $^4A_2 \rightarrow {}^2E$ transition of Cr^{3+} has also been used to distinguish multiple Cr^{3+} bonding sites in high field crystals and glasses [277]. Time resolved methods seek to distinguish multiple sites on the basis of site-to-site differences in emission decay time and are effective when emission lifetime varies appreciably with coordination environment.

The ability of pressure to alter the energy of electronic states provides an additional degree of freedom for distinguishing and resolving multiple dopant bonding environments in solids. Differences in local structure and bonding are expected to lead to different pressure shifts for electronic transitions of dopants in different sites. The application of pressure therefore provides an opportunity for resolving multiple bonding sites on the basis of energy and can potentially be used when dopant emission bands are broad or strongly overlapping. The ability of pressure to alter luminescence lifetimes provides a similar opportunity in time resolved studies.

The few high pressure site selective studies that have appeared illustrate the potential that pressure offers for gaining new insight into systems with multiple dopant bonding environments. We have recently completed a study of the low field system Cr^{3+}:$LiTaO_3$ [278]. The system is currently of interest because of its promising ferroelectric, photorefractive, and non-linear optical properties. Because of charge mismatch, the nature of incorporation of Cr^{3+} into the $LiTaO_3$ lattice remains an open question. Cr^{3+} could potentially occupy Li^+ or Ta^{5+} sites with charge compensation occurring through vacancies or interstitials. At ambient pressure, Cr^{3+}:$LiTaO_3$ exhibits broad $^4T_2 \rightarrow {}^4A_2$ emission. The broad appearance of the spectrum precludes the identification of different Cr^{3+} sites. The objective of our study was to use pressure to induce a low field to high field transition in Cr^{3+}: $LiTaO_3$. The spectral narrowing associated with the transition (see Sect. 3.4) should permit resolution of individual Cr^{3+} sites.

Figure 33 shows the effect of pressure on the luminescence spectrum of Cr^{3+}:$LiTaO_3$ at 20 K. Between 16 kbar and 25 kbar, we observed a low field to high field transition and stabilization of sharp $^2E \rightarrow {}^4A_2$ emission (see Sect. 3.4.1). An enlargement of the $^2E \rightarrow {}^4A_2$ emission at 20 K is shown in Fig. 34. Our temperature dependent studies at high pressure have indicated that the three features shown in Fig. 34 correspond to R_1 lines of three distinct Cr^{3+} sites. The feature labeled "A" corresponds to a low concentration high field site initially present at ambient pressure (see inset of Fig. 33). Features "B" and "C" correspond to distinct sites with low crystal field strength at ambient pressure. Our results therefore indicate that the broad emission band observed at ambient pressure consists of overlapping $^4T_2 \rightarrow {}^4A_2$ emission from two different Cr^{3+} sites.

Olsen et al. [279] completed a site selective spectroscopic study of Eu^{3+}: CaF_2 as a function of temperature and pressure. Eu^{3+} substitutes for Ca^{2+} in the CaF_2 system without altering the overall cubic symmetry of the lattice. The excess charge of Eu^{3+} is compensated by interstitial fluorides which can be located either adjacent to or distant to Eu^{3+}. As a result, several Eu^{3+} bonding sites are found in CaF_2 with Eu^{3+} ions occurring as either isolated or clustered species. The principle isolated Eu^{3+} sites include the A site (tetragonal Eu^{3+} with a fluoride in the nearest

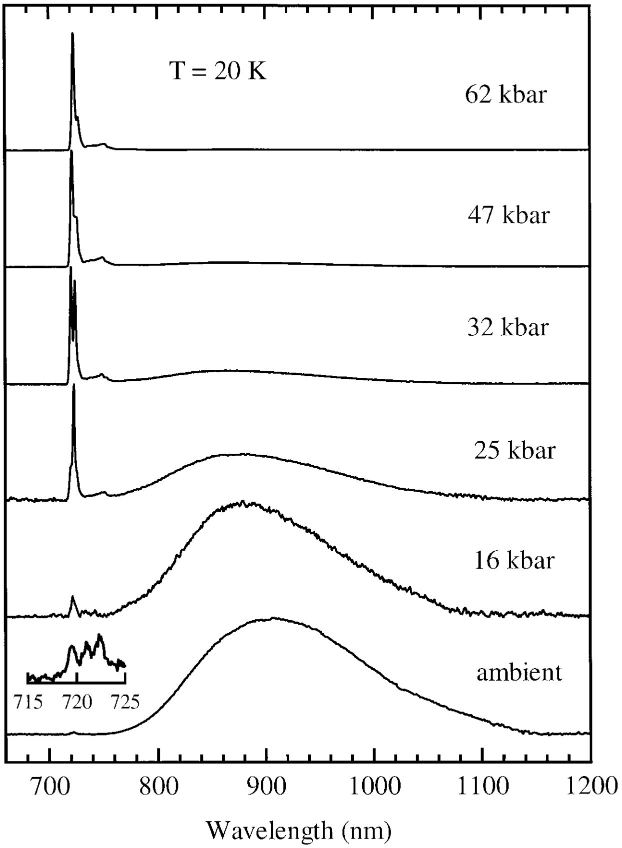

Fig. 33. Luminescence spectrum of Cr^{3+}:$LiTaO_3$ as a function of pressure at 20 K. The *inset* shows an enlargement of weak $^2E \rightarrow {}^4A_2$ emission near 720 nm resulting from a low concentration of high field Cr^{3+} sites at ambient pressure. The spectral transformation from low field to high field behavior with increasing pressure is evident. Excitation wavelength: 620 nm

neighbor interstitial position) and the O site (cubic Eu^{3+} with distant fluoride charge compensation). Clustered sites include dimers (2Eu · 3F complex) and trimers (3Eu · 4F complex). High resolution site selective spectroscopic methods can be used to distinguish and quantify the different Eu^{3+} defect complexes.

Olsen et al. [279] considered the effect of pressure on the relative concentrations of different Eu^{3+} sites in CaF_2. Their strategy was to use pressure as a thermodynamic variable to alter the equilibrium between the different Eu^{3+} defect complexes. In their experiments, they first fixed the pressure on Eu^{3+}:CaF_2 to a value between 0 kbar and 20 kbar and then varied temperature (up to 420 °C) in order to dissociate existing defect complexes, induce fluoride mobility, and form a new, pressure dependent equilibrium distribution of defects. In samples treated at 420 °C and 11 kbar, they observed an increase in A site concentration, a comparable decrease in O site concentration, and decreases in concentration of

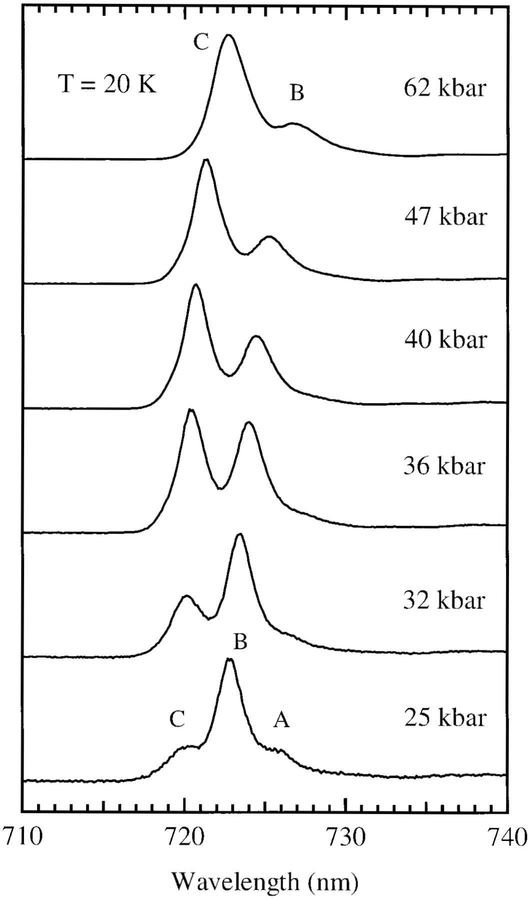

Fig. 34. High resolution scans of the $^2E \rightarrow {}^4A_2$ emission observed in Cr^{3+}:$LiTaO_3$ above ~20 kbar. The features labeled A, B, and C correspond to R_1 lines of Cr^{3+} ions in three distinct structural bonding environments. Excitation wavelength: 620 nm

several low concentration, unidentified minority sites. The intensity changes were reversible upon release of pressure and annealing at high temperature. Above 20 kbar, no changes in the relative spectral intensities of the different Eu^{3+} sites were observed upon heating to 400 °C. Olsen et al. argued that fluoride interstitials were immobile above 20 kbar due to a pressure-induced increase in association energy of each defect complex initially present at room temperature. Olsen et al. [279] developed a defect equilibrium model to describe the effect of pressure on fluoride diffusion and the relative concentrations of A and O sites. The ability of pressure to alter defect equilibria in Eu^{3+}:CaF_2 permitted Olsen et al. to demonstrate the importance of strained lattice regions in determining the state of aggregation of Eu^{3+} ions, the influence of competing processes between Eu^{3+} sites on defect distribution, and the inadequacy of simple mass action consideration in establishing the defect chemistry.

In addition to distinguishing bonding sites, site selective emission studies can be used to probe the effect of pressure on local coordination environment in systems with multiple dopant bonding environments. Site selective optical methods are commonly used as structural probes in amorphous phase systems because of the limited local structural information available from X-ray measurements. We recently completed a high pressure fluorescence line narrowing study of Eu^{3+}-doped Na_2O-$2SiO_2$ glass [280]. Amorphous silicates are important constituents of the Earth's interior and occur naturally at high pressure conditions. The objective of our study was to develop an optical method for examining the effect of pressure on coordination environment in an amorphous system at high pressure. We used Eu^{3+} as an optical probe because its $^7F_0 \rightarrow {}^5D_0$ absorption transition involves two non-degenerate states and cannot be split by a crystal field. As a result, the linewidth of the $^5D_0 \rightarrow {}^7F_0$ emission is a reflection of the number of distinct Eu^{3+} bonding environments in a glass.

Our experiments consisted of using a narrow line tunable dye laser to selectively excite the $^7F_0 \rightarrow {}^5D_0$ transition of Eu^{3+}. In principle, each distinct Eu^{3+} bonding environment possesses a unique $^7F_0 \rightarrow {}^5D_0$ absorption energy. By systematically tuning the excitation laser through the inhomogeneously broadened $^7F_0 \rightarrow {}^5D_0$ absorption band, we can obtain a series of emission spectra corresponding to the range of Eu^{3+} bonding environments present in a glass.

Our study included fluorescence line narrowing measurements of Eu^{3+}: Na_2O-$2SiO_2$ glass as a function of pressure up to 210 kbar [280]. A representative series of selectively excited emission spectra is depicted in Fig. 35 which shows results for four different excitation wavelengths at 66 kbar. The variation of the $^5D_0 \rightarrow {}^7F_{1,2}$ spectral features with excitation wavelength indicates that different Eu^{3+} bonding sites are excited. The $^5D_0 \rightarrow {}^7F_0$ emission was not measured directly in order to prevent saturation of the detector, but was instead measured in excitation by measuring the $^5D_0 \rightarrow {}^7F_2$ emission intensity while scanning the excitation wavelength. The results are summarized in Fig. 36. Each filled square represents the peak energy of $^5D_0 \rightarrow {}^7F_0$ emission and the ends of each length bar represent the wavelengths corresponding to half of the peak intensity. The $^5D_0 \rightarrow {}^7F_0$ transition exhibited a red shift up to ~ 40 kbar with no significant change in linewidth. Between ~ 40 kbar and ~150 kbar the peak energy changed only slightly, but a significant increase in linewidth was observed. Above ~ 150 kbar the linewidth increase ceased and a red shift was observed.

An increased splitting of the three $^5D_0 \rightarrow {}^7F_1$ features with decreasing excitation wavelength was observed at all pressures (Fig. 35). The increased splitting indicates that the crystal field strength of the Eu^{3+} bonding sites increased with decreasing excitation wavelength. By resolving the spectra into components and analyzing in the context of crystal field theory [281, 282], we obtained the pressure dependence of the B_{kq} crystal field parameters and determined the variation in average crystal field strength as a function of pressure. We found that the average crystal field strength decreased between 0 kbar and 40 kbar and increased above 40 kbar. Lifetime measurements of the $^5D_0$ state upon excitation at the peak of the $^7F_0 \rightarrow {}^5D_0$ excitation band indicated a lifetime increase between 0 kbar and 40 kbar and a decrease above 40 kbar.

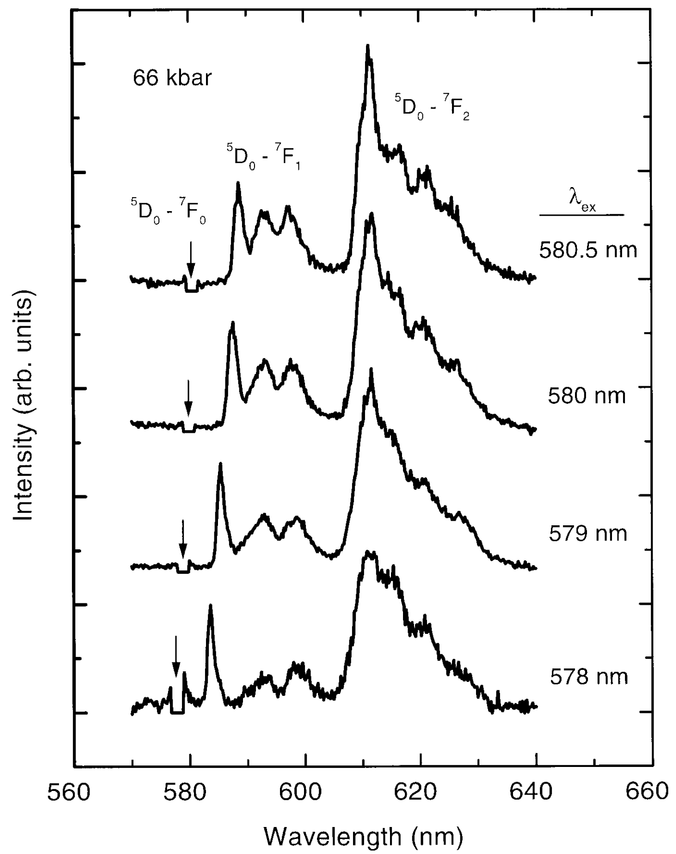

Fig. 35. High pressure fluorescence line narrowing spectra of Eu^{3+} in Na_2O-$2SiO_2$ glass at 77 K and 66 kbar. The excitation wavelength of each spectrum is indicated by the downward arrow and is listed to the right of each spectrum. Spectra are normalized to the $^5D_0 \rightarrow {}^7F_1$ peak intensity

The spectral, crystal field strength and lifetime data indicate that different processes occur below and above 40 kbar. Below 40 kbar, the data indicate minor structural perturbation of the set of Eu^{3+} sites present at ambient pressure. The decrease in crystal field strength below 40 kbar suggests that direct Eu-O bond compression is not important at low pressure and that pressure primarily influences the angular positions of the nearest neighbor ligands. The increased linewidth observed above ~40 kbar indicates that new Eu^{3+} bonding sites are created at high pressure. The crystal field strength data indicate that the new sites are high crystal field sites. We have proposed a model of the behavior observed above ~40 kbar that attributes the formation of new high field Eu^{3+} sites to a pressure-induced decrease in non-bridging oxygen concentration in the glass. We believe that the decrease in non-bridging oxygen concentration is due to an increase in the oxygen coordination number of Si from 4 to 5 and eventually 6 with pressure. As the Si atoms of the glass matrix compete more effectively

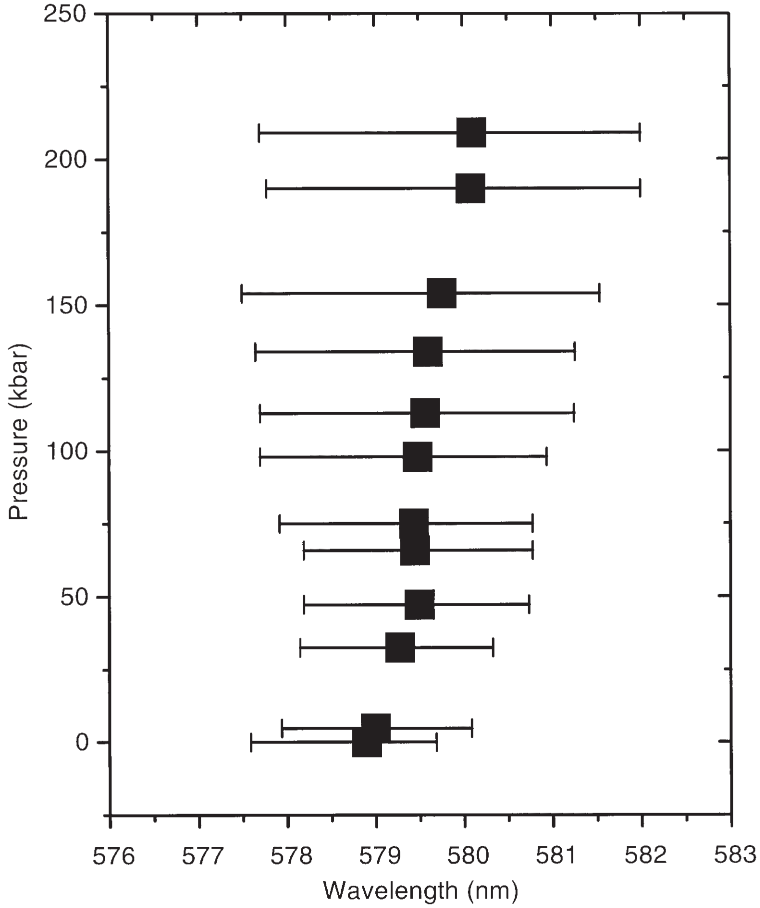

Fig. 36. Peak maximum (■) and full width at half maximum (*length bar*) of the $^7F_0 \rightarrow {}^5D_0$ excitation spectrum of Eu^{3+} in Na_2O-$2SiO_2$ glass as a function of pressure at 77 K. The ends of the length bar denote the wavelengths corresponding to half of the peak intensity on the low and high energy sides of the excitation band. The excitation spectra were measured by scanning a dye laser across the $^7F_0 \rightarrow {}^5D_0$ absorption band while monitoring the $^5D_0 \rightarrow {}^7F_2$ emission at 612 nm

for oxygen coordination, fewer oxygens are available for coordination to Eu^{3+}. As a result, the average coordination number of Eu^{3+} decreases and the oxygens that remain coordinated to Eu^{3+} bond more strongly. The strong bonding is consistent with the observed increase in crystal field strength above ~40 kbar and implies a stronger vibrational coupling of Eu^{3+} to the glass matrix. Increased vibrational coupling is consistent with the line broadening and lifetime decrease observed above ~40 kbar.

Our study represents the first example of high pressure fluorescence line narrowing spectroscopy and demonstrates the ability of site selective spectroscopy to gain new insight into the effect of pressure on local structure in amorphous phases. The study suggests that high field Eu^{3+} sites in silicate glasses consist of Eu^{3+} ions bonded to a small number of oxygens with short bond lengths and high bond strengths rather than to Eu^{3+} ions weakly bonded to a large number of distant oxygens. The study also showed that high field Eu^{3+} sites are characterized by high energy $^7F_0 \rightarrow {}^5D_0$ absorption, large site specific homogeneous linewidths, and short $^5D_0$ fluorescence lifetimes.

4
Summary

In this review, we have summarized recent accomplishment in the area of high pressure luminescence spectroscopy. We have attempted to demonstrate the unique understanding and insight possible from high pressure studies of luminescent materials. Our focus has been on the luminescence properties of transition metal and lanthanide ions in solids and complexes. We have considered the effects of pressure on the basic properties of d → d, f → f, d → f, and charge transfer transition and have presented several recent examples from the literature that illustrate the ability of pressure to influence the energy, lifetime, intensity, and lineshape of luminescence transitions. We have also shown that pressure is a useful method for resolving overlapping spectra and competing energy transfer processes. Finally, we discussed the use of luminescence spectroscopy as a probe of high pressure structural phenomena in amorphous phases and in crystals with multiple transition metal bonding sites.

A central theme of the review has been the demonstration of the ability of pressure to systematically influence the static and dynamic luminescence properties of excited electronic states through continuous decreases in bond lengths and interatomic distances. This continuous tuning capability complements the discrete tuning capability traditionally obtained through chemical means and leads to new opportunities for developing structure-bonding-property correlations. High pressure also permits us to increase our understanding of luminescence phenomena by stabilizing structures, phases, and electronic states that are not attainable through chemical modifications and by resolving competing excited state processes.

Acknowledgements. The author most gratefully acknowledges Y.R. Shen, P.R. Wamsley, U. Hömmerich, M.J. Lochhead, and A. Riedener for their contributions to the work reported from his group in the article. Y.R. Shen is also gratefully acknowledged for his assistance in the preparation of the article. Special thanks go to M. Grinberg for enlightening discussions, to W.M. Yen for his encouragement, and to W. Holzapfel for providing a rewarding sabbatical experience. Extra special thanks go to H.G. Drickamer for his guidance and support during the formative stages of the author's career.

5
References

1. Kikas J, Laisaar A, Suisalu A, Kuznetsov A, Ellervee A (1998) Phys Rev B 57:14
2. Ellervee A, Kikas J, Laisaar A, Suisalu A (1993) J Lumin 56:151
3. Brillante A, Della Valle, Ulrich C, Syassen K (1997) J Chem Phys 107:4628

4. Hara K, Bulgarevich DS, Kahimoto O (1996) J Chem Phys 104:9431
5. Yang G, Li Y, White JO, Drickamer HG (1999) J Phys Chem B 103:7853
6. Yang G, Li Y, White JO, Drickamer HG (1999) J Phys Chem B 103:5181
7. Dreger ZA, Drickamer HG (1997) J Phys Chem A 101:1422
8. Drickamer HG (1990) Ann Rev Mat Sci 20:1
9. Lang JM, Drickamer HG (1993) J Phys Chem 97:5058
10. Drickamer HG (1989) Physica A 156:179
11. Berg O, Chronister EL (1997) J Chem Phys 106:4401
12. Baer BJ, Chronister EL (1994) J Chem Phys 100:23
13. Brillante A, Della Valle RG, Strössner K, Syassen K (1988) J Lumin 40/41:278
14. Chan IY, Chung WM (1988) Chem Phys Lett 150:437
15. Sesselmann T, Richter W, Haarer D (1987) J Lumin 36:263
16. Sesselmann T, Richter W, Haarer D, Morawitz H (1987) Phys Rev B 36:7601
17. Gafert J, Friedrich J, Parak F, Fidy J (1993) J Lumin 56:157
18. Gradl G, Zollfrank J, Breinl W, Friedrich J (1991) J Chem Phys 94:7619
19. Asami K, Naka T, Ishiguro M (1986) Phys Rev B 34:5658
20. Tshuimoto T, Nishimura H, Nakayama M (1997) J Lumin 72/74:895
21. Tsujimoto T, Nishimura H, Nakayama M (1996) Phys Rev B 54:16,579
22. Beerwerth F, Fröhlich D (1988) Phys Rev B 38:4250
23. Lipp MJ, Daniels WB (1991) Phys Rev Lett 67:2810
24. Lipp MJ, Yoo CH, Daniels WB (1994) Phys Rev B 50:6564
25. Zhang H, Daniels WB, Cohen RE (1994) Phys Rev B 50:70
26. Lang JM, Dreger ZA, Drickamer HG (1992) J Appl Phys 71:1914
27. Lang JM, Dreger ZA, Drickamer HG (1992) J Phys Chem 96:85
28. Riemann K (1996) High P Res 15:73
29. Mang A, Reimann K, Rübenacke S, Steube M (1996) Phys Rev B 53:16,283
30. Reimann K, Steube M, Brandt O, Yang H, Ploog KH (1998) J Appl Phys 84:2971
31. Prins AD, Sly JL, Dunstan DJ (1996) Phys Status Solidi B 198:57
32. Liu X, Samuelson L, Piston ME, Gerling M, Nilsson S (1990) Phys Rev B 42:11791
33. Samuelson L, Nilsson S (1988) J Lumin 40/41:127
34. Venkateswaren U, Chandrasekhar M, Chandrasekhar HR, Wolfram T, Fischer R, Masselink WT, Morkoc H (1985) Phys Rev B 31:4106
35. Wolford DJ, Kuech TF, Steiner TW, Bradley JA, Gell MA, Ninno D, Jaros M (1988) Superlatt & Microstr 4:525
36. Suski T, Perlin P, Teisseyre H, Leszczynski M, Grzegory I, Jun J, Bockowski M, Porowski S, Moustakas TD (1995) Appl Phys Lett 67:2188
37. Liu ZX, Pau S, Syassen K, Kuhl J, Kim W, Morkoc H, Khan MA, Sun CJ (1998) Phys Rev B 58:6696
38. Shan W, Ager JU, Walukiewicz W, Haller EE, McCluskey MD, Johnson NM, Bour DP (1998) Phys Rev B 58:R10,191
39. Worl LA, Meyer TJ (1988) Chem Phys Lett 143:541
40. Hammack WS, Drickamer HG, Lowery MD, Hendrickson D (1986) Chem Phys Lett 132:231
41. Politis TG, Drickamer HG (1981) J Chem Phys 75:3203
42. Lee SH, Waltz WL, Demmer DR, Walters RT (1985) Inorg Chem 24:1531
43. Huppert DH, Jayaraman A, Maines RG, Steyert DW, Rentzepis PM (1984) J Chem Phys 81:5596
44. Schellenberg P, Friedrich J (1993) J Lumin 56:143
45. Salman OA, Drickamer HG (1982) J Chem Phys 77:3337
46. Tran D, Bourassa JL, Ford PC (1997) Inorg Chem 36:439
47. Beswick CL, Shalders RD, Swaddle TW (1996) Inorg Chem 35:991
48. Van Eldik R (1986) Angew Chem Intl Ed Engl 25:673
49. Kotowski M, Van Eldik R (1989) Coord Chem Rev 93:19
50. Hiraga T, Kitamura N, Kim HB, Tazuke S, Mori N (1989) J Phys Chem 93:2940
51. Fröhlich D, Niewsand W, Pohl UW, Wrzesinski J (1995) Phys Rev B 52:14,652

52. Ge W, Schmidt WS, Sturge MD, Pfeiffer LN, West KW (1994) J Lumin 59:163
53. Jia W, Liu H, Wang Y, Hömmerich U, Eilers H, Hoffman K, Yen WM (1994) J Lumin 59:279
54. Chai M, Brown JM (1996) Geophys Res Lett 23:3539
55. Shen XA, Gupta YM (1993) Phys Rev B 48:2929
56. Horn PD, Gupta YM (1989) Phys Rev B 39:973
57. Mao HK, Hemley RJ (1998) In: Hemley RJ (ed) Ultrahigh pressure mineralogy (Rev mineral, vol 37). Mineralogical Society of America, Washington D. C.
58. Hemley RJ, Ashcroft NW (1998) Physics Today 51:26
59. Holzapfel WB, Isaacs NS (ed) (1997) High pressure techniques in chemistry and physics. Oxford University Press, Oxford
60. Eremets MI (1996) High pressure experimental methods. Oxford University Press, New York
61. Eliezer S, Ricci RA (ed) (1996) High pressure equations of state: theory and applications. North Holland, New York
62. Holzapfel WB (1996) Rep Prog Phys 59:29
63. Holzafpel WB (1991) Europhys Lett 16:67
64. Bassett WA, Shen AH, Bucknum M, Chou IM (1993) Rev Sci Instrum 64:2340
65. Manghnani MH, Yagi T (ed) (1998) Properties of Earth and planetary materials at high pressure and temperature. American Geophysical Union, Washington D. C.
66. Stebbins JF, Dingwell DB, McMillan P (ed) (1995) Structure and dynamics of silicate melts (Rev mineral, vol 32)
67. Callen HB (1985) Thermodynamics and an introduction to thermostatistics, 2nd edn. Wiley, New York
68. Jayaraman A (1984) Sci Amer 250:54
69. Trautman R, Griffin BJ, Scharf D (1998) Sci Amer 279:82
70. Jayaraman A (1986) Rev Sci Instrum 57:1013
71. Hemley RJ, Mao HK, Goncharov AF, Hanfland M, Struzhkin V (1996) Phys Rev Lett 76:1667
72. Ruoff AL, Li T (1995) Ann Rev Mat Sci 25:249
73. Evans WJ, Silvera IF (1998) Phys Rev B 57:14,105
74. Duffy TS, Wang Y (1998) In: Hemley RJ (ed) Ultrahigh pressure mineralogy (Rev mineral, vol 37). Mineralogical Society of America, Washington D. C.
75. Weir CE, Lippincott ER, Van Valkenburg A, Bunting EN (1959) J Res Nat Bur Stand A 63:55
76. Jayaraman A (1986) Rev Mod Phys 55:65
77. Dunstan DJ, Spain IL (1989) J Phys E 22:913, 923
78. The gasket is typically stainless steel. Be is sometimes used in X-ray scattering experiments because of its low atomic number. Re and Mo gaskets are frequently used at pressures above 1 mbar because of their high strength
79. Merrill L, Bassett WA (1974) Rev Sci Instrum 45:290
80. Bruno MS, Dunn KJ (1984) Rev Sci Instrum 55:940
81. Moss WC, Goettel KA (1987) Appl Phys Lett 50:25
82. Mao HK, Bell PM, Dunn KJ, Chrenko RM, DeVries RC (1979) Rev Sci Instrum 50:1002
83. Chervin JC, Syfosse G, Besson JM (1994) Rev Sci Instrum 65:2719
84. Takano KJ, Wakatsuki M (1991) Rev Sci Instrum 62:1576
85. Patterson DE, Margrave JL (1990) J Phys Chem 94:1094
86. Forman RA, Piermarini GJ, Barnett JD, Block S (1972) Rev Sci Instrum 176:284
87. Piermarini GJ, Block S, Barnett JD, Forman RA (1975) J Appl Phys 46:2774
88. Piermarini GJ, Block S (1975) Rev Sci Instrum 46:973
89. Decker DL (1971) J Appl Phys 42:3239
90. Eggert JH, Goettel KA, Silvera IF (1989) Phys Rev B 40:5724
91. Mao HK, Xu J, Bell PM (1986) J Geophys Res 91:4673
92. Mao HK, Bell PM, Shaner JW, Steinberg DJ (1978) J Appl Phys 49:3276
93. Zhao MG (1998) J Chem Phys 109:8003
94. Ragan DD, Gustavsen R, Schiferl D (1992) J Appl Phys 72:5539
95. Yen J, Nicol M (1992) J Appl Phys 72:5535

96. Munro RG, Piermarini GJ, Block S, Holzapfel WB (1985) J Appl Phys 57:165
97. Jahren AH, Kruger MB, Jeanloz R (1992) J Appl Phys 71:1579
98. Kottke T, Williams F (1983) Phys Rev B 28:1923
99. Hess NJ, Schiferl D (1990) J Appl Phys 68:1953
100. Yusa H, Yagi T, Arashi H (1994) J Appl Phys 75:1463
101. Liu J, Vohra YK (1994) Appl Phys Lett 64:3386
102. Lorenz B, Shen YR, Holzapfel WB (1994) High P Res 12:91
103. Shen YR, Holzapfel WB (1995) Phys Rev B 51 : 15,752
104. Datchi F, LeToullec R, Loubeyre P (1997) J Appl Phys 81 : 3333
105. Leger JM, Chateau C, Lacam A (1990) J Appl Phys 68 : 2351
106. Arashi H, Ishigame M (1982) Jap J Appl Phys 21:1647
107. Wamsley PR, Bray KL (1994) J Lumin 60/61:188
108. Hua H, Vohra YK (1997) Appl Phys Lett 71:2602
109. Chopelas A, Boehler R (1984) Mat Res Soc Symp Proc 22:275
110. Sato-Sorensen Y (1986) J Appl Phys 60:2985
111. Eggert JH, Goettel K, Silvera IF (1989) Phys Rev B 40:5733
112. Jovanic BR (1992) Chem Phys Lett 190:440
113. Shen YR, Bray KL (1997) Phys Rev B 56:10,882
114. Jia W, Shang YS, Tang RM, Yao ZY (1984) J Lumin 31/32:272
115. Jovanic BR (1996) J Lumin 68:43
116. Shen YR, Bray KL (1998) Phys Rev B 58:11,944
117. Anderson OL, Isaak DG, Yamamoto S (1989) J Appl Phys 65:1534
118. Jamieson JC, Fritz JN, Manghnani MH (1992) In: Akimoto S, Manghnani MH (eds) High pressure research in geophysics. Center for Acad Publ, Tokyo
119. Schiferl D, Fritz JN, Katz AI, Schaefer M, Skelton EF, Qadri SB, Ming LC, Manghnani MH (1987) In: Manghnani MH, Syono Y (ed) High pressure research in mineral physics. Terra Scientifc, Tokyo
120. Gu G, Vohra YK (1993) Phys Rev B 47:11,559
121. Schmidt SC, Schiferl D, Zinn AS, Ragan DD, Moore DS (1991) J Appl Phys 69:2793
122. Schiferl D, Nicol M, Zaug JM, Sharma SK, Cooney TF, Wang SY, Anthony TR, Fleischer JF (1997) J Appl Phys 82:3256
123. Otto JW, Vassiliou JK, Frommeyer G (1998) Phys Rev B 57:3253
124. Burnett JH, Cheong HM, Paul W (1990) Rev Sci Instrum 61:3904
125. Piermarini GJ, Block S, Barnett JD (1973) J Appl Phys 44:5377
126. Fujishiro I, Piermarini GJ, Block S, Munro RG (1981) Proc 8th Intl AIRAPT Conference, Uppsala, Sweden
127. Tkachev SN, Bass JD (1996) J Chem Phys 104:10,059
128. Smith G, Langer K (1982) In: Schreyer W (ed) High pressure researches in geoscience. E Schweizerbartische Verlagsbuchhandlung, Stuttgart
129. Ragan DD, Clarke DR, Schiferl D (1996) Rev Sci Instrum 67:494
130. Walker J (1979) Rep Prog Phys 42:108
131. Pankove JI, Qiu CH (1994) In: Spear KE, Dismukes JP (ed) Synthetic diamond: emerging CVD science and technology. Wiley, New York
132. Desgreniers S, Vohra YK, Ruoff AL (1989) Sol St Comm 70:705
133. Otto JW, Vassiliou JK, Frommeyer G (1997) J Synchrotron Rad 4:155
134. Henderson B, Imbusch F (1989) Optical spectroscopy of inorganic solids. Oxford Science Publications, Oxford
135. Struck CW, Fonger WH (1991) Understanding luminescence spectra and efficiency using W_p and related functions. Springer, Berlin Heidelberg New York
136. Funamori N, Funamori M, Jeanloz R, Hamaya N (1997) J Appl Phys 82:142
137. Jia W, Shang YS, Tang RM, Yao ZY (1984) J Lumin 31/32:272
138. Liu J, Tang R, Wang Y, Jia W, Shang Y, He S (1988) J Lumin 40/41:419
139. Galanciak D, Perlin P, Grinberg M, Suchocki A (1994) J Lumin 60/61:223
140. Wamsley PR, Bray KL (1994) J Lumin 59:11
141. Hömmerich U, Bray KL (1995) Phys Rev B 51:12,133

142. Rinzler AG, Dolan JF, Kappers LA, Hamilton DS, Bartram RH (1993) J Phys Chem Sol 54:89
143. Yersin H, Huber P, Gietl G, Trümbach D (1992) Chem Phys Lett 199:1
144. Zhao MG, Xu JA, Bai GR, Xie HS (1983) Phys Rev B 27:1516
145. Duclos SJ, Vohra YK, Ruoff AL (1990) Phys Rev B 41:5372
146. Munro RG (1977) J Chem Phys 67:3146
147. Ma D, Wang Z, Chen J, Zhang Z (1988) J Phys C 21:3585
148. Abu-Eid RM (1976) In: Strens RGJ (ed.) Physics and chemistry of minerals and rocks. Wiley, New York
149. Richet P, Xu J, Mao HK (1988) Phys Chem Min 16:207
150. Jephcoat AP, Hemley RJ, Mao HK (1988) Physica B 150:115
151. Smith G, Langer K (1983) Neues Jahrb Mineral Monatsh 12:541
152. Mayrhofer K, Hochberger K, Gebhardt W (1988) J Phys C 21:4393
153. House GL, Drickamer HG (1977) J Chem Phys 67:3230
154. Lang JM, Dreger ZA, Drickamer HG (1992) J Appl Phys 71:1914
155. Lee BH (1970) J Appl Phys 41:2988
156. Strössner K, Ves S, Hönle W, Gebhardt W, Cardona M (1986) In: Engström O (ed) Proc 18th Intl Conf Phys Semicond. Singapore, World Press
157. Shen YR, Bray KL (1997) Phys Rev B 56:R473
158. Shen YR, Riedener A, Bray KL (2000) Phys Rev B 61:9277
159. Deka C, Bass M, Chai BHT, Shimony Y (1993) J Opt Soc Am B 10:1499
160. Goldschmidt ZB (1978) In: Gschneidner KA, Eyring L (ed) Handbook on the physics and chemistry of rare earths. North Holland, New York
161. Cohen RE (1987) Geophys Res Lett 14:37
162. Ma D, Zheng X, Xu Y, Zhang Z (1986) Phys Lett A 115:245
163. Ma D, Chen J, Wang Z, Zhang Z (1988) Phys Lett A 126:377
164. Anderson OL (1966) J Phys Chem Solids 27:547
165. Ma D, Zheng X, Zhang Z, Xu Y (1987) Phys Lett A 121:97
166. Zhao MG (1998) J Chem Phys 109:8003
167. Newman DJ, Ng B, Poon YM (1984) J Phys C 17:5577
168. Moreno M, Barriuso MT, Aramburu JA (1994) Int J Quant Chem 52:829
169. Zheng W (1996) Phys Status Solidi B 196:297
170. Zheng W (1995) J Phys Condens Mater 7:8351
171. Zheng W, Li W, Wu SY (1999) Phys Status Solidi A 173:437
172. Burns RG (1993) Mineralogical applications of crystal field theory, 2nd edn. Cambridge University Press, Cambridge New York Melbourne
173. Freire PTC, Pilla O, Lemos V (1994) Phys Rev B 49:9232
174. de Viry D, Denis JP, Tercier N, Blanzat B (1987) Sol St Commun 63:1183
175. Dolan JF, Kappers LA, Bartram RH (1986) Phys Rev B 33:7339
176. Dolan JF, Rinzler AG, Kappers LA, Bartram RH (1992) J Phys Chem Solids 53:905
177. Kenney JW, Clymire JW, Agnew SF (1995) J Am Chem Soc 117:1645
178. Riesen H, Güdel Hul (1987) J Chem Phys 87:3166
179. Sugano S, Tanabe Y, Kamimura H (1970) Multiplets of transition metal ions in crystals. Academic Press, New York
180. Ves S, Strössner K, Gebhardt W, Cardona M (1986) Phys Rev B 33:4077
181. Burns RG (1987) In: Manghnani MH, Syono Y (eds) High pressure research in mineral physics. American Geophysical Union, Washington D.C., p 361
182. Marco de Lucas MC, Rodriquez F, Moreno M (1994) Phys Rev B 50:2760
183. Rodriquez F, Moreno M (1986) J Chem Phys 84:692
184. Moreno M, Barriuso MT, Aramburu JA (1992) J Phys Condens Matter 4:9481
185. Morrison CA, Leavitt RP (1982) In: Gschneidner KA, Eyring L (ed) Handbook on the physics and chemistry of rare earths. North-Holland, Amsterdam
186. Gruber JB, Hills ME, Allik TH, Jayasankar CK, Quagliano JR, Richardson FS (1990) Phys Rev B 41:7999
187. Gregorian T, d'Amour-Sturm H, Holzapfel WB (1989) Phys Rev B 39:12,497

188. Tröster T, Gregorian T, Holzapfel WB (1993) Phys Rev B 48:2960
189. Bungenstock C, Tröster T, Holzapfel WB, Bini R, Ulivi L, Cavalieri S (1998) J Phys Condens Matter 10:9329
190. Shen YR, Holzapfel WB (1995) Phys Rev B 52:12,618
191. Wang Q, Bulou A (1995) Sol St Comm 94:309
192. Wang Q, Bulou A (1993) J Phys Condens Matter 5:7657
193. Liu S, Chi Y, Zhao X, Wang L, Zou G (1998) Rev High Pressure Sci Technol 7:712
194. Wang Q, Lun L, Zhang D, Chi Y, Wang L (1992) J Phys Condens Matter 4:6491
195. Chi Y, Liu S, Wang L, Zou G, Wang Q (1998) Rev High Pressure Sci Technol 7:754
196. Liu S, Chi Y, Gao C, Wang L, Zou G (1998) Rev High Pressure Sci Technol 7:757
197. Shen YR, Englisch U, Chudinovskikh, Porsch F, Haberkorn R, Beck HP, Holzapfel WB (1994) J Phys Condens Matter 6:3197
198. Chang NC, Gruber JB, Leavitt RP, Morrison CA (1982) J Chem Phys 76:3877
199. Chi Y, Liu S, Shen W, Wang L, Zou G (1986) Physica 139/140B:555
200. Chi Y, Liu S, Li H, Zhao X, Wang L (1997) J Alloys & Cmpds 256:1
201. Nishimura G, Tanaka M, Kurita A, Kushida T (1991) J Lumin 48/49:473
202. Changxin G, Bilin L, Yuefen H, Hongbin C (1991) J Lumin 48/49:489
203. Liu S, Chi Y, Ma L, Wang L, Zou G (1986) Physica 139/140B:559
204. Shen YR, Holzapfel WB (1995) J Phys Condens Matter 7:6241
205. Shen YR, Holzapfel WB (1995) Phys Rev B 51:6127
206. Jayasankar CK, Reid MF, Tröster T, Holzapfel WB (1993) Phys Rev B 48:5919
207. Newman DJ (1971) Adv Phys 20:197
208. Newman DJ, Ng B (1989) Rep Prog Phys 52:699
209. Shannon RD (1976) Acta Cryst A 32:751
210. Shen YR, Bray KL (1998) Phys Rev B 58:5305
211. Tyner CE, Drickamer HG (1977) J Chem Phys 67:4116
212. Yoo CS, Radousky, HB, Holmes, NC, Edelstein NM (1991) Phys Rev B 44:830
213. Chen G, Shihua W, Haire RG, Peterson JR (1994) Appl Spect 48:1026
214. Yen WM (1999) J Lumin 83/84:399
215. Yersin H, Gliemann G (1978) Ann NY Acad Sci 313:539
216. Gliemann G, Yersin H (1985) Structure and Bonding 62:89
217. Krogmann K, Stephan D (1968) Z Anorg Chem Allg Chem 362:290
218. Holzapfel W, Yersin H, Gliemann G (1981) Z Kristallog 157:47
219. Yersin H, Riedl U (1995) Inorg Chem 34:1642
220. Stock M, Yersin H (1978) Sol St Comm 27:1305
221. Stock M, Yersin H (1976) Chem Phys Lett 40:423
222. Yersin H, Hidvegi I, Gliemann G, Stock M (1979) Phys Rev B 19:177
223. Rössler U, Yersin H (1982) Phys Rev B 26:3187
224. Hara Y, Shirotani I, Ohashi Y, Asaumi K, Minomura S (1975) Bull Chem Soc Jpn 48:403
225. Day P (1980) J Mol Struct 59:109
226. Daniels W, Yersin H, Stock M, Gliemann G (1981) Sol St Comm 40:937
227. Yersin H, Von Ammon W, Stock M, Gliemann G (1979) 18/19:774
228. Yersin Y (1978) J Chem Phys 68:4707
229. Blom N, Ludi A, Bürgi H-B, Ticky K (1984) Acta Cryst C40:1767
230. Markert JT, Blom N, Roper G, Perregaux AD, Nagasundaram N, Corson MR, Lude A, Nagle JK, Patterson HH (1985) Chem Phys Lett 118:258
231. LaCasce JH, Turner WA, Corson MR, Dolan PJ, Nagle JK (1987) Chem Phys 118:289
232. Assefa Z, Destefano F, Garepapaghi MA, LaCasce JH, Oulette S, Corson MR, Nagle JK, Patterson HH (1991) Inorg Chem 30:2868
233. Mason WR (1973) J Am Chem Soc 95:3573
234. Sano M, Adachi H, Yamatera H (1982) Bull Chem Soc Jpn 55:1022
235. Nagasundaram N, Roper G, Biscoe J, Chai JW, Patterson HH, Blom N, Ludi A (1986) Inorg Chem 25:2947
236. Strasser J, Yersin H, Patterson HH (1998) Chem Phys Lett 295:95
237. Ziegler T, Nagle JK, Snijders JG, Baerends EJ (1989) J Am Chem Soc 111:5631

238. Yersin H, Gallhuber E (1984) Inorg Chem 23:3745
239. Lang JM, Dreger ZA, Drickamer HG (1993) Inorg Chem 97:2289
240. Lang JM, Dreger ZA, Drickamer HG (1992) Chem Phys Lett 192:299
241. Hiraga T, Uchida T, Kitamura N, Kim HB, Tazuke S, Yagi T (1989) J Am Chem Soc 111:7466
242. Sato-Sorensen Y (1986) J Appl Phys 60:2985
243. Sato-Sorensen Y (1987) In: Manghnani MH, Syono Y (ed) High pressure research in mineral physics. American Geophysical Union, Washington D.C.
244. Jovanic B, Zekovic Lj, Radenkovic B (1991) Phys Scripta 43:446
245. Jovanic BR (1992) Chem Phys Lett 190:440
246. Uroöevic V, Panic B, Jovanic B, Zekovic Lj, Savic P (1989) Chem Phys Lett 155:325
247. Merkle LD, Spain I, Powell RC (1981) J Phys C 14:2027
248. Brown GC (1964) J Appl Phys 35:3062
249. Jovanic BR (1996) J Lumin 68:43
250. Hömmerich U, Bray KL (1995) Phys Rev B 51:8595
251. Struve B, Huber G (1985) Appl Phys B 36:195
252. Healy SM, Donnelly CJ, Glynn TJ, Imbusch GF, Morgan GP (1990) J Lumin 46:1
253. Hehir JP, Henry MO, Larkin JP, Imbusch GF (1974) J Phys C 7:2241
254. Donnelly CJ, Healy SM, Glynn TJ, Imbusch GF, Morgan GP (1988) J Lumin 42:119
255. Webster G, Drickamer HG (1980) J Chem Phys 72:3740
256. Struck CW, Fonger WH (1970) J Lumin 2:456
257. Struck CW, Fonger WH (1970) J Chem Phys 52:6364
258. Gleason JK, Offen HW, Turley WD (1993) Inorg Chem 32:639
259. Shen Y, Bray KL (1999) Mat Sci Forum 315/317:243
260. Wybourne BG (1968) J Chem Phys 48:2596
261. Burdick GW, Downer MC (1993) In: Kitai AH (ed) Solid state luminescence. Chapman and Hall, London
262. Urland W, Hochheimer HD, Kourouklis GA, Kremer R (1986) Physica 139/140B:553
263. Förster T (1949) Z Naturf A 4:321
264. Dexter DL (1953) J Chem Phys 21:836
265. Merkle LD, Spain IL, Powell RC (1981) J Phys C 14:2027
266. Blanzat B, Tercier N, Denis JP, Barthou C (1984) J Phys (Paris) C8:71
267. Wamsley PR, Bray KL (1995) J Lumin 63:31
268. Shen YR, Riedener A, Bray KL (2000) Phys Rev B 61:11,460
269. Yersin H, Trümbach D, Strasser J, Patterson HH, Assefa Z (1998) Inorg Chem 37:3209
270. Yersin H (1978) J Chem Phys 68:4707
271. Yersin H, Stock M (1982) J Chem Phys 76:2136
272. Assefa Z, Shankle G, Patterson HH, Reynolds R (1994) Inorg Chem 33:2187
273. Assefa Z, Patterson HH (1994) Inorg Chem 33:6194
274. Yen WM (1986) In: Zschokke I (ed.) Optical spectroscopy of glasses. D Reidel, New York
275. Weber MJ (1986) In: Yen WM, Selzer PM (eds) Laser spectroscopy of solids, 2nd edn. Springer, Berlin Heidelberg New York
276. Yen WM (1979) J Lumin 18/19:639
277. Bergin FJ, Donegan JF, Glynn TJ, Imbusch GF (1986) J Lumin 34:307
278. Shen YR, Bray KL, Grinberg M, Barzowska J, Soklska I (2000) Phys Rev B 61:14263
279. Olsen LR, Wright AO, Wright JC (1996) Phys Rev B 53:14,135
280. Lochhead MJ, Bray KL (1995) Phys Rev B 52:15,763
281. Brecher C, Riseberg LA (1976) Phys Rev B 13:81
282. Belliveau TF, Simkin DJ (1989) J Non-Cryst Sol 110:127

Excited State Spectroscopy and Excited State Dynamics of Rh(III) and Pd(II) Chelates as Studied by Optically Detected Magnetic Resonance Techniques

Max Glasbeek

Laboratory for Physical Chemistry, University of Amsterdam, Nieuwe Achtergracht 129,
1018 WS Amsterdam, The Netherlands
E-mail: glasbeek@fys.chem.uva.nl

In this paper we review optically detected magnetic resonance (ODMR) investigations of a series of Rh^{3+} ($4d^6$) and Pd^{2+} ($4d^8$) complexes in the lowest excited electron spin triplet state. Starting with a brief survey of the technique of optical detection of magnetic resonance, zero-field and low-magnetic field ODMR results are reviewed for the tris-diimine chelates $[Rh(phen)_n(bpy)_{3-n}]^{3+}$, where phen = 1,10-phenanthroline, bpy = 2,2′-bipyridine, and n = 0, 2, or 3, and for the mixed cyclometalated chelates $[Rh(thpy)_x(phpy)_{2-x}(bpy)]^+$, with thpy = 2,2′-thienylpyridinate, $phpy^-$ = 2-phenylpyridinate, and x = 1, or 2. The ODMR data reveal fine structure splittings in the phosphorescent excited state of the complexes comparable in magnitude to those known for the nonchelated ligand molecules in the excited triplet state. Anisotropy studies of the ODMR spectra for the single crystals in low magnetic fields show that the lowest electronic excitation in the complexes is a triplet state indeed and that this state is localized on a single ligand molecule per metal ion site. From microwave recovery experiments, performed under conditions that the spin-lattice relaxation can be neglected ($T \leq 2$ K), detailed information concerning the triplet sublevel lifetimes is obtained. The lifetimes are on the millisecond timescale, i. e., three orders of magnitude shorter than for the nonchelated ligand molecules. The lifetime shortening as well as the observed spin-selective radiative decay of the triplet sublevels of the ligand molecule are discussed in detail on the basis of enhanced spin-orbit couplings caused by the central (heavy) metal ion. Optically detected spin coherence experiments (transient nutation and spin echo decay) are also discussed. The results show that the homogeneous line broadening of the ODMR transitions of the metal complexes in the emissive triplet state is approximately 100 kHz. The homogeneous broadening is attributed to the effects of flip-flop motions of ligand proton spins that randomly modulate the triplet electron spin levels on account of dipolar electron spin – nuclear spin couplings. Finally, recent ODMR and PMDR (phosphorescence microwave double resonance) experiments performed for the Pd^{2+}-chelates, $Pd(thpy)_2$ and $Pd(qol)_2$ (with qol^- = 8-hydroxyquinolinate) in Shpol'skii matrices are discussed. The lowest excited electronic state in these molecules is also emissive and ODMR spectra at zero- and low magnetic fields have been observed. For $Pd(thpy)_2$ only one zero-field ODMR transition could be measured, but it is argued that this transition originates in an excited triplet state. The results of the microwave recovery experiments could be related to time-resolved emission experiments in high magnetic fields. Spin selectivity in the vibronic line emission is demonstrated by means of PMDR.

Keywords. Rh(III)- and Pd(II) trischelates, Cyclometalated complexes, Excited triplet state, Optically detected magnetic resonance, Triplet spin dynamics, Triplet spin coherence, Spin-selective decay, (De)localization of electronic excitation

Topics in Current Chemistry, Vol. 213

1
Introduction

The photophysics and photochemistry of luminescent transition metal ions coordinated by organic ligands have received widespread interest for many years [1]. In part, the interest stems from the applicability of metal complexes as photocatalysts [2–4], as photosensitizer material in solar energy conversion [5, 6], in molecular diodes [7, 8], chemical sensors [9, 10] or biosensors [11–13], and in supramolecular clusters that mimic biological light harvesting systems [14, 15]. Numerous optical spectroscopic studies have contributed in obtaining the information necessary for a better understanding of the structure and chemical bonding of the transition metal compounds. The results of such studies are well documented and several reviews have appeared in recent years [1]. Of special interest are the properties of the lowest excited states because these states most critically determine the emissive, charge transfer, and charge redistribution processes. The optical excitation of the transition metal complex is usually classified as metal-localized (e.g., dd*-type), ligand-localized (e.g., $\pi\pi^*$-type), or as metal-to-ligand charge transfer (MLCT, $d\pi^*$-type) [16]. A variety of spectroscopic techniques including high-resolution absorption, emission, line-narrowing, time-resolved, and coherent Raman techniques have been conducted to elucidate the spectral and dynamical properties of the lowest excited states of transition metal complexes [1c, d, 17]. Typically, using narrow band lasers, the optimized spectral resolution is of the order of 1 cm^{-1}.

In recent years, it has been shown for some luminescent d^6-metal ion chelates that the excited-state properties are amenable to investigation by means of excited-state magnetic resonance techniques [18–23]. Typically, in these complexes with aromatic ligands the lowest excited state is a ligand-localized $^3\pi\pi^*$ state. For (uncoordinated) aromatic molecules it is well known that the photoexcited $^3\pi\pi^*$ state can be studied by means of magnetic resonance [24]. In this paper a review is given of analogous magnetic resonance studies of the excited state of d^6- and d^8-metal chelates.

Compared to the high-resolution optical experiments, the spectral resolution attained in magnetic resonance is better by at least three orders of magnitude. Generally, the three triplet-state sublevels are split in zero magnetic field and thus give rise to a sublevel fine structure [25–27]. A major purpose of triplet-state magnetic resonance spectroscopy is to determine the magnitude of the fine structure splittings because such (zero-field) splittings fully characterize the electronic spin density distribution of the metal-chelate excited triplet state. It has long been known that triplet-state fine structure can be probed by means of electron spin resonance (ESR) [28, 29]. For phosphorescent states, on the other hand, the extremely useful method of optical detection of magnetic resonance (ODMR) is often applicable [30]. ODMR offers a number of advantages when compared with ESR. First, whereas in ESR excited-state studies may become difficult because, due to the limited lifetime of the paramagnetic system, the signal-to-noise ratio may have decreased drastically, ODMR is well-suited for emissive states with lifetimes as short as a few microseconds. Second, ODMR studies of the excited triplet state are possible without the application of a magnetic field. In ESR, the spectra for the triplet state are usually highly anisotropic, thus often necessitating the use of single crystals. Anisotropy effects do not occur in zero-field spectroscopy and very often information concerning electronic structure, magnetic, radiative, and non-radiative decay of the excited state can be obtained with unprecedented detail (see below). Third, in the ODMR experiment the sensitivity of optical detection is retained, i.e., the detection enhancement factor with respect to ESR detection roughly equals the ratio of the frequencies of the optical photon and the microwave quantum. Fourth, ODMR pulse techniques, not available in conventional ESR spectrometers, allow for a detailed study of the triplet state sublevel dynamics. Thus valuable information about triplet substate symmetries and intrinsic triplet spin relaxation processes can be obtained.

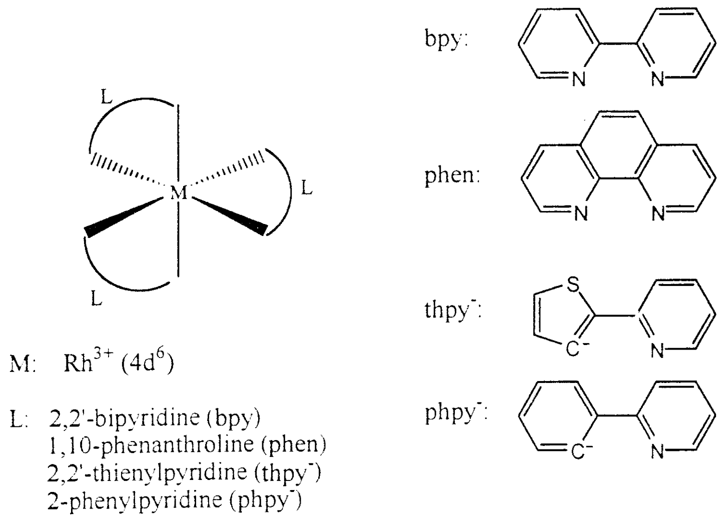

Fig. 1. Schematic structures of the Rh^{3+} chelates treated in this paper and the abbreviations of the ligand molecules

In this paper we review ODMR investigations of a number of Rh^{3+} (4d^6) and Pd^{2+} (4d^8) cyclometalated complexes with ligand-localized excited triplet states. The schematic structures of the treated d^6-metal chelates are shown in Fig. 1. Since in the complexes of interest here the triplet state is aromatic ligand-localized, the triplet-state fine structure splittings are predominantly determined by the dipolar interactions among the two unpaired electron spins [31]. Triplet states arising from metal-centered dd* excitations, by contrast, are characterized by fine structure splittings dominated by spin-orbit couplings of the central metal ion [26, 31]. ODMR of such metal-centered excited states will not be discussed here (for a review see [31]).

We begin with a brief survey of the fine structure characteristics of a ligand-centered phosphorescent triplet state. This is followed by some considerations concerning the ODMR experiment and finally we review results of recent ODMR investigations with focus on the information regarding structure and dynamics complementary to optical work.

2
Triplet State Fine Structure

For the organometal chelates considered here, photoexcitation produces a phosphorescent ligand-localized $^3\pi\pi^*$ excited state. A schematic picture showing the relevant photophysical processes is given in Fig. 2. Usually the lowest triplet state is formed by intersystem crossing (ISC) from the initially excited singlet state. Fine structure splittings within the triplet state arise from electron spin dipole-dipole interactions (in first order perturbation theory [25, 27–29]) and spin-orbit couplings (in second order). In zero magnetic field, the threefold

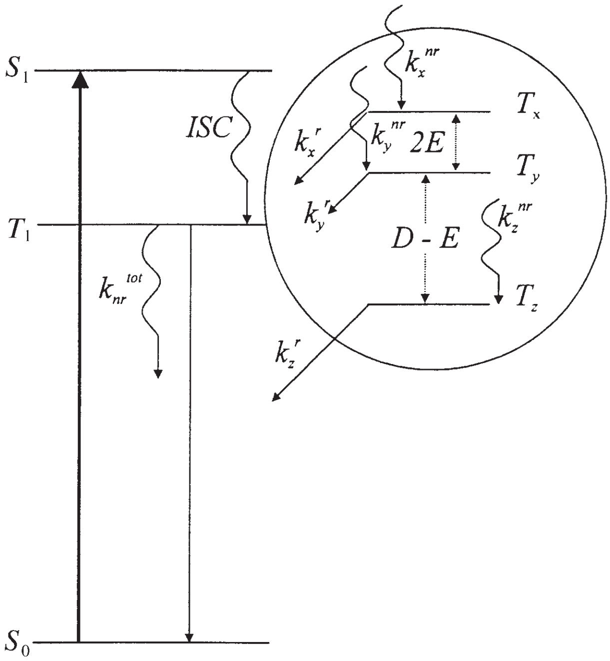

Fig. 2. Level scheme and photocycle at photoexcitation. Triplet state fine structure is given on enlarged scale. The various rate constants of photophysical processes are also indicated. k_i^{nr} is the non-radiative feeding rate and k_i^r is the radiative decay rate of sublevel *i*. k_{tot}^{nr} is the total nonradiative decay rate constant for the triplet state

spin degeneracy of the triplet state is lifted by introducing a spin Hamiltonian of the form

$$H_S = \vec{S}\,\vec{\vec{D}}\vec{S} \tag{1}$$

where *S* is the total triplet spin operator and *D* is the second-order quadrupole tensor with components representative of spatial integrals (see below). By definition, in the main axes frame of the spin system, the spin Hamiltonian reduces to

$$H_S = -XS_x^2 - YS_y^2 - ZS_z^2 \tag{2}$$

where *X*, *Y*, and *Z* are the principal values of the *D*-tensor that determine the splittings of the three triplet spin sublevels in zero magnetic field. Since the *D*-tensor is traceless ($X + Y + Z = 0$), the spin Hamiltonian may be rewritten as

$$H_S = D\left(S_z^2 - \frac{1}{3}S^2\right) + E(S_x^2 - S_y^2) \tag{3}$$

in which

$$D = -\frac{3}{2}Z \tag{4}$$

and

$$E = -\frac{1}{2}(X - Y) \tag{5}$$

Spin-orbit coupling (SOC) shifts the triplet spin level energies in second order by

$$\Delta E_i = \sum_j \frac{\langle T_i | H_{SOC} | \phi_j >< \phi_j | H_{SOC} | T_i \rangle}{E_{T_i} - E_{\phi_j}} \tag{6}$$

where T_i is representative of a triplet spin sublevel, $\mathbf{H}_{SOC}$ is representative of the spin-orbit coupling, and E_{T_i} and E_{ϕ_j} are the energies of levels T_i and ϕ_j respectively [32]. The first order contributions of the dipolar spin-spin interactions to the zero-field splitting parameters D and E are determined by [25–27]

$$D = \frac{3}{4}(g\mu_B)^2 \left\langle \Psi \middle| \frac{\mathbf{r}^2 - 3z^2}{\mathbf{r}^5} \middle| \Psi \right\rangle \tag{7}$$

and

$$E = \frac{3}{4}(g\mu_B)^2 \left\langle \Psi \middle| \frac{y^2 - x^2}{\mathbf{r}^5} \middle| \Psi \right\rangle \tag{8}$$

In Eqs. (7) and (8), $\mathbf{r}$ is the vector linking the two spins, g is the Landé factor, and μ_B is the Bohr magneton. It follows that D is representative of the degree of delocalization of the electronic distribution, whereas E expresses its deviation from axial symmetry. The spin eigenfunctions of Eq. (2) may be given as linear combinations of the three eigenfunctions of the S_z spin operator, $T_{\pm 1}$ or T_0:

$$\begin{aligned} |T_x\rangle &= \frac{1}{\sqrt{2}} |T_{-1} - T_{+1}\rangle \\ |T_y\rangle &= \frac{i}{\sqrt{2}} |T_{-1} + T_{+1}\rangle \\ |T_z\rangle &= |T_0\rangle \end{aligned} \tag{9}$$

Note that

$$\begin{aligned} &S_u T_u = 0 \quad \text{for } u = x, y, z \\ &S_x T_y = -S_y T_x = iT_z \end{aligned} \tag{10}$$

etc., by cyclic permutation. From Eq. (10) it follows that the triplet spin angular momentum in each of the three zero-field triplet sublevel eigenstates is quenched (i.e., $\langle S_u \rangle = 0$), or equivalently, the vector representing the spin lies in the plane perpendicular to the molecular u axis.

3
Triplet Spin Resonance and ODMR

For the metal-ion chelates of interest here, the triplet state excitation is mainly localized on aromatic ligand molecules. For aromatic molecules in the triplet state, fine structure splittings are typically in the range 0.1–10 GHz, i.e., the magnetic transitions of the triplet state are in the microwave regime. The $T_u \rightarrow T_v$ spin transition is induced when a resonant microwave field linearly polarized perpendicular to the *uv*-plane is applied.

At first sight, since for an electronic dipole transition the electron spin angular momentum is conserved, radiative decay of the excited triplet state to the singlet ground state is not expected to occur. However, due to the (small) effects of spin-orbit coupling, triplet and singlet configurations become contaminated and the triplet-to-singlet dipole transition becomes partially allowed. The perturbed triplet state sublevels may be written as

$$^3\Psi_\mathrm{i} = {}^3\Psi_\mathrm{i}^0 + \sum_k \frac{\langle {}^1\Psi_\mathrm{k}^0 | H_\mathrm{SOC} | {}^3\Psi_\mathrm{i}^0 \rangle}{\Delta E_\mathrm{ki}} \, {}^1\Psi_\mathrm{k}^0 \tag{11}$$

where $^3\Psi_\mathrm{i}^0$ denotes the unperturbed triplet substate, $^1\Psi_\mathrm{k}^0$ is the admixed singlet state, and ΔE_ki is the energy difference between the triplet and singlet states. For organic molecules, the phosphorescence rate constants are usually less than 100 s^{-1}. The phosphorescence rates for metal complexes, on the other hand, are $10^4 - 10^6\ \mathrm{s}^{-1}$ or higher. The difference is mainly caused by the stronger spin-orbit coupling induced by the heavy atoms. The effect is reminiscent of the heavy atom effect in halonaphthalenes [33–35] and is discussed further in Sects. 6.2 and 7.3.

The spin-orbit coupling operator, H_SOC, transforms according to the totally symmetric representation of the point group symmetry of the molecule and mixes states of the same total symmetry only. The triplet-state spin functions transform as the *u* components of an axial vector. For nonaxially symmetric molecules this implies that the spin sublevels have different symmetry and hence also different total (orbital $\otimes$ spin) symmetry. Thus, SOC may cause a spin-selective mixing of the triplet substates with singlet states of different symmetry. This results generally in very different radiative and nonradiative decay rates for the three spin components of the triplet state. Also, the intersystem crossing rate is determined by SOC. Hence, the populating rates of the triplet spin states may also differ greatly. In all, SOC is pertinent to spin selectivity in the populating and depopulating kinetics of the triplet sublevels.

One can take advantage of the distinct rate constants for populating and depopulating of the spin levels (cf. scheme of Fig. 2) in an ODMR experiment. Generally, following optical excitation, the populations of the triplet state sublevels differ appreciably. On the one hand this is so because of the aforementioned spin selectivity in the optical pumping and decay cycle and on the other hand because the experiment is performed under ‘low-temperature conditions’, i.e., spin-lattice relaxation is slow enough so that thermal equilibrium among the triplet sublevels is not established. When a microwave field is applied, a triplet spin transition is induced if the microwave frequency is on-resonance with the energy difference of a pair of triplet sublevels. Microwave resonance effects a change of the spin sublevel populations. This population change gives rise to a change in the total phosphorescence intensity due to the differences in the radiative character of the triplet substates. Conversely, one can distinctively measure the emission spectrum belonging to the triplet state responsible for the

ODMR signal. Here we refer to the Phosphorescence Microwave Double Resonance (PMDR) spectrum that is obtained by an optical scan through the emission spectrum while maintaining the microwave frequency on-resonance. By applying amplitude modulation of the microwaves and phase-sensitive optical detection, one selects out the optical emission spectrum characteristic of the species with the triplet-state spin resonance. The PMDR technique is particularly useful when the emission consists of overlapping spectra due to different molecular species. When the emission is from excited triplet states with different zero-field splittings one can easily separate the PMDR spectra from the different species. Also, the PMDR technique is helpful for assigning the origin of vibronic bands in high-resolution emission spectra [36]. The same idea applies for the optical absorption spectrum or fluorescence spectrum, thus giving the techniques of Absorption Microwave Double Resonance (ADMR) [37] and Fluorescence Microwave Double Resonance (FMDR) [38].

4
Optically Detected Spin Dynamics

4.1
Introduction

Studies of dynamical processes in photoexcited transition metal complexes are important for a better understanding of processes like intramolecular population relaxation, interligand excitation transfer, charge transfer, localized and delocalized energy migration, etc. Since dynamical interactions give rise to spectral broadening, it may seem at first sight that line shape studies might be helpful in obtaining experimental information. In practice, however, spectral broadening due to the aforementioned dynamic processes is overruled by the effects of inhomogeneous broadening (IB). IB arises from static interactions like strain, lattice imperfections, density fluctuations, chemical impurities, etc. Thus, homogeneous broadening (HB), arising from the dynamical interactions in the system, cannot be directly determined from the spectra. Several powerful techniques have been developed to overcome the problems posed by IB. We mention fluorescence line narrowing [39], hole burning [40], coherent transients [41, 42], and single molecule spectroscopy [43]. In this review we include ultra-high resolution optical-microwave pulse experiments [44], as applied to transition metal complexes. As in advanced magnetic resonance pulse methods [45], in these experiments information about the dynamics is obtained directly in the time domain rather than the frequency domain. The spectral resolution achieved by means of the double resonance pulse techniques is better than 100 kHz.

It is experimentally possible to distinguish between ‘population relaxation’ and ‘pure dephasing’ dynamics. In the population relaxation experiment, a saturating resonant microwave pulse causes an abrupt change of the populations of the triplet-state sublevels. Population relaxation ensues due to radiative and non-radiative decay out of the triplet state sublevels and due to spin-lattice relaxation. Experimentally, the temporal behavior of this population relaxation is probed. Further details are given in Sect. 4.2.

In the 'pure dephasing' measurement, a very short and intense microwave pulse (with a duration of a few tens of nanoseconds), resonant with one of the triplet spin transitions, prepares the system in a 'coherent superposition state'. The state is said to be coherent because two conditions are met. First, the microwave pulse is short and intense enough to prepare the molecule in a superposition of the zero-field spin eigenstates of Eq. (9). This superposition state is typified in that the molecule now has an oscillatory magnetic moment, at the resonance frequency, instead of a quenched magnetic moment (as followed in Sect. 2 from Eq. 10). Second, the magnetic moments of all molecules oscillate *in*-phase. Consequently, the phase coherence is manifested as a macroscopic oscillating magnetic moment. This moment has a limited lifetime, however. Due to randomly fluctuating perturbations the oscillation frequency of the magnetic moment of each molecule in the superposition state becomes randomly modulated. As a result, these dynamic (secular) interactions give rise to 'irreversible' destruction of the phase coherence in the ensemble of molecules. Such dynamic interactions are responsible for the homogeneous line broadening or (pure) irreversible spin dephasing. From the monitoring of the 'pure dephasing', information concerning the intrinsic molecular dynamics is obtained. A variety of experimental methods have been developed for the measurement of the pure dephasing dynamics. One of these is the 'spin echo' experiment [44, 45]; further discussion is given in Sect. 4.3.

Quite often, spin dephasing times are orders of magnitude shorter than the decay times measured in the (incoherent) population relaxation experiments. For a few transition metal chelates in the excited triplet state we will argue later that the homogeneous spin dephasing is determined by hyperfine interactions of the triplet electron spin with randomly flipping ligand nuclear spins.

4.2
Optically Detected Population Decay

Usually, for triplet states with zero-field splitting parameters of the order of 0.1 cm^{-1}, the sublevel decay rates are measured at low temperatures ($T \leq 2$ K). Under these conditions there is almost no spin-lattice relaxation (SLR), i.e., its rate is negligible compared to the (de)populating rate constants. One has then that steady-state pumping of sublevel T_u leads to

$$n_\mathrm{u} = \frac{K_\mathrm{u}}{k_\mathrm{u}} \qquad (12)$$

where n_u is the steady state population of T_u, and K_u and k_u are the feeding and depletion rate constant, respectively. Since the three sublevels, in general, have different populating and depopulating rates, appreciable spin alignment (i.e., population differences between the triplet sublevels) in the excited triplet state results. A large spin alignment is favorable for measuring ODMR.

Spin selectivity in the sublevel decay is of course manifested in the sublevel lifetime, k_u^{-1}. Lifetimes of the individual triplet sublevels are measured by means of optically detected microwave recovery [46] or adiabatic rapid passage experiments [47]. In the microwave recovery experiment, a microwave pulse at resonance with one of the spin transitions changes the population of level, *i*, from its steady-state value n_i^0 to n_i. In the limit of negligible SLR, the level population recovers according to

$$n_i(t) = [n_i(0) - n_i^0]\exp(-k_i t) + n_i^0 \tag{13}$$

where $n_i(0)$ is the population of level T_i at the moment the microwave power is switched off ($t = 0$). Since the total phosphorescence intensity is given as

$$I(t) = c\, n_u(t)\, k_u^r + c\, n_v(t)\, k_v^r \tag{14}$$

with *c* being a proportionality factor, the time dependence of the microwave recovery signal is given as

$$I(t) - I^0 = c\,[n_u(0) - n_u^0]\, k_u^r \exp(-k_u t) + c\,[n_v(0) - n_v^0]\, k_v^r \exp(-k_v t) \tag{15}$$

where

$$I^0 = c\, n_u^0 k_u^r + c n_v^0 k_v^r \tag{16}$$

The microwave-induced population transfer is from level T_u to level T_v (or vice versa), hence $n_u(0) - n_u^0$ and $n_v(0) - n_v^0$ are equal but of opposite sign. By fitting the phosphorescence transient following the microwave pulse to Eq. (15), the decay rates of levels T_u and T_v are determined. Alternatively, in the adiabatic rapid passage experiment, the microwave frequency is swept rapidly through resonance. Assuming that during the sweep population relaxation can be ignored, the result of the rapid sweep is population inversion between the resonantly coupled levels. Thus in Eq. (15) one has that $n_u(0) = n_v^0$ and $n_v(0) = n_u^0$. The subsequent temporal evolution of the phosphorescence is still given by Eq. (15). It follows that, at temperatures low enough so that SLR is frozen out, the microwave recovery and the adiabatic passage experiments both yield the lifetimes of the resonantly coupled spin levels.

Complementary to the method of microwave-recovery, the method of microwave-induced delayed phosphorescence (MIDP) is sometimes used for studying population kinetics. MIDP is particularly suited for two-level systems in which only one of the levels is radiative, whereas the other, dark level, is long-living. The microwave recovery is mostly applied when both levels are radiative. In the MIDP experiment the exciting light is chopped (or pulsed). In the dark time, after optical excitation, a resonant microwave pulse is applied at the delay time t_d. At t_d, the population still present in the non-radiative level is in part transferred to the radiative level. Thus a phosphorescence intensity change is induced, the amplitude of which is proportional to the population present in the non-radiative level, at time t_d. Measurement of the amplitude decay with t_d gives the decay transient for the non-radiative level. The (fast) decay of the delayed phosphorescence transient at times $t > t_d$ is typical of the decay of the radiative level.

4.3
Optically Detected Spin Coherence

As mentioned in Sect. 4.1, spin *coherence* is generated by an intense microwave pulse resonant with one of the spin transitions within the excited triplet state.

For a short and intense enough microwave pulse resonant, for example, with the $T_x \leftrightarrow T_z$ transition, a superposition state of the form

$$\Psi(t) = a_x(t)\,|T_x\rangle + a_z(t)\,|T_z\rangle \tag{17}$$

is produced [44]. The ratio a_x/a_z is determined not only by the microwave power but also by the pulse duration. It is anticipated therefore that by variation of the microwave pulse duration one can change the composition of the superposition state Ψ, say from pure T_x to a mixture of T_x and T_z, pure T_z, and so on. Assuming that the radiative properties of T_x and T_z are quite different, the radiative character of the state Ψ will change as the ratio a_x/a_z is varied. Experimentally one can verify this by monitoring the change of the phosphorescence intensity as a function of the pulse duration. Figure 3a illustrates such a 'transient nutation' as probed for $[Rh(bpy)_3](ClO_4)_3$ in the phosphorescent triplet state [19,48]. The fi-

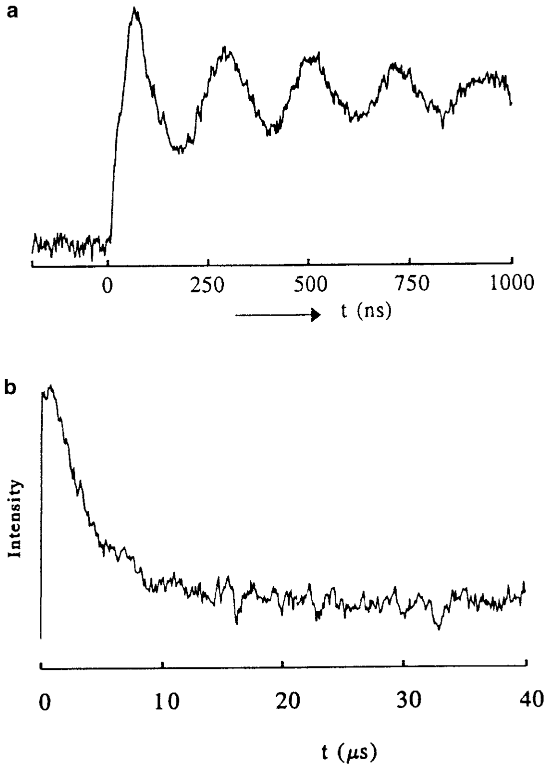

Fig. 3a,b. **a** 'Transient nutation' signal as probed for the $T_x \leftrightarrow T_z$ zero-field transition at 2320 MHz of $[Rh(bpy)_3](ClO_4)_3$, in the phosphorescent triplet state, upon switching on the microwave power. The oscillations occur as the microwave pulse duration is increased. Photoexcitation is near 320 nm, detection is at 456 nm; temperature is 1.4 K. **b** Optically detected echo amplitude decay for the 2320 MHz zero-field transition of $[Rh(bpy)_3](ClO_4)_3$ as obtained by applying a $\pi/2$–τ–π–τ–$\pi/2$ pulse sequence when increasing 2τ

gure illustrates that the superposition state and thus its radiative character can be controlled by variation of the microwave pulse duration. The modulation pattern in Fig. 3a is direct evidence of induced *coherence* in the triplet spin system, i.e., not only the individual molecules are in a superposition state characterized by $a_x a_z \neq 0$, but one also has that the *ensemble average* of $a_x a_z$ (i.e., the off-diagonal density matrix element $\rho_{xz} = \overline{a_x a_z}$) is non-zero. The damping of the so-called Rabi oscillations in Fig. 3a shows that the phase coherence has a limited lifetime. It is important to note, however, that in this case the damping time is not characteristic of the pure dephasing dynamics. As noted in Sect. 4.1, IB is very prominent and in fact it is the inhomogeneous spread of the spin resonance frequencies that causes the transient nutation signal to die out rapidly.

From magnetic resonance spectroscopy [49] it is well-known that IB effects are adequately circumvented by the tricks of a spin echo experiment. For instance, in a two-pulse echo experiment, IB effects are averaged out and one probes spin dephasing determined by time-dependent fluctuations characteristic of HB only (and not IB). More specifically, a $\pi/2$–τ–π microwave pulse sequence is applied, where the first $\pi/2$ pulse creates a coherent superposition state for which $a_x / a_z = 1$ and the π pulse, applied at time τ after the first pulse, generates a spin coherence (the echo) at time 2τ after the initial pulse. The echo amplitude is traced with τ. The echo amplitude decay time is characteristic of the pure dephasing dynamics. For phosphorescent triplet states it is possible to make the echo optically detectable by means of a final $\pi/2$ "probe" pulse applied at time τ' after the second pulse [44]. In Fig. 3b, the optically detected echo amplitude decay for the $T_x \leftrightarrow T_z$ zero-field transition at 2320 MHz of $[Rh(bpy)_3](ClO_4)_3$ in the triplet state, as obtained by applying a $\pi/2$–τ–π–τ–$\pi/2$ pulse sequence when increasing 2τ, is shown [48]. The echo amplitude decay time, typical of the pure dephasing dynamics, in this particular experiment is found to be 3.1 ± 0.6 μs [48].

An advantage of the probe-pulse method is the fact that the excitation and detection are completely decoupled. Therefore, there is no instrumental dead-time. Furthermore, sensitive optical detection is used and in a few favorable cases the spin coherence of only $\sim 10^4$ excited molecules could still be detected.

5
Experimental

A block diagram of the ODMR set-up used by us [50] is given in Fig. 4. The sample is mounted inside a slow-wave helix immersed in a liquid helium bath. Optical excitation is by means of continuous wave or pulsed laser beams; in some cases a conventional high-pressure mercury or xenon lamp is used. The excitation beam is directed through the quartz windows of the helium cryostat perpendicular to the detection pathway. Microwaves generated in a sweep oscillator are coupled by coaxial lines to a semi-rigid cable in the cryostat. A helix is attached to the end of the semi-rigid cable. The microwaves transmitted by the helix are almost linearly polarized along the helix axis. Microwave amplification is achieved by means of traveling-wave-tube (TWT) amplifiers up to 20 W. Maximum power input is obtained by matching the coupling to the helix by means of

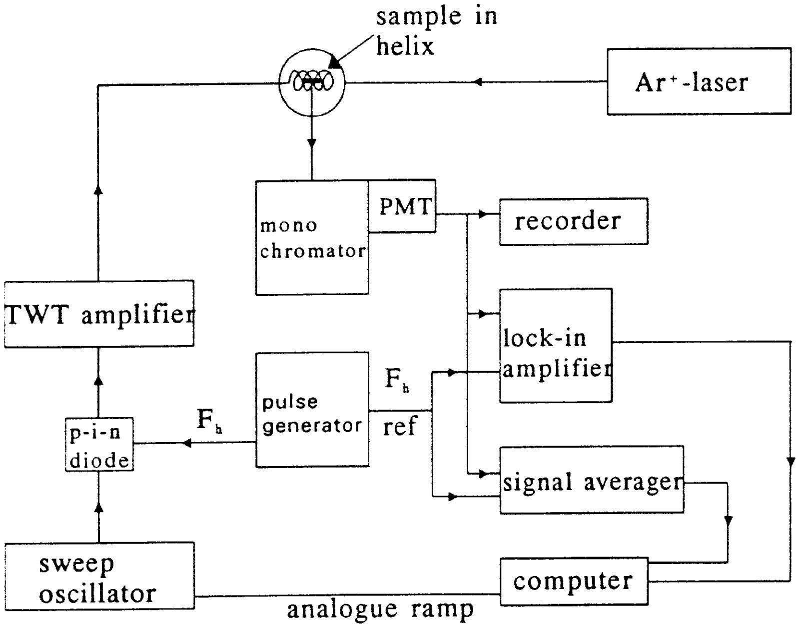

Fig. 4. Scheme of ODMR set-up

an EH-tuner inserted on top of the semi-rigid cable. The frequency range covered by our zero-field ODMR spectrometer is from 0.1 GHz up to 12 GHz.

A programmable pulse generator produces the pulse sequences that drive the *p-i-n* diode switches in the microwave circuit. To resolve the microwave-induced changes in the phosphorescence intensity from the steady-state emission (usually a few percent or less) phase sensitive detection of the photomultiplier output at the microwave sequence repetition frequency (F_h is typically 150–350 Hz) is applied using a lock-in amplifier.

6
Rh^{3+}-Trisdiimine Chelates

6.1
ODMR

It has long been recognized that the emissive state of Rh(III)-(aza)-aromatic compounds is primarily of ligand-localized $^3\pi\pi^*$ nature [51–54]. This assignment for the Rh^{3+} ($4d^6$) chelate emission is mainly based on the resemblance of the emission spectra of the free and coordinated ligand molecules. Komada et al. [18] were the first to demonstrate the feasibility of optically detected magnetic resonance for the luminescent state of Rh(III) complexes. The experiments revealed that the fine structure splittings of the complexes in the triplet state are of the order of those for the free ligand molecules in the excited triplet state. We have performed similar zero-field and low-field ODMR studies for compounds of the form $[Rh(phen)_n(bpy)_{3-n}](ClO_4)_3$, where n = 0, 2, or 3, and phen = 1, 10-phenanthroline, bpy = 2, 2′-bipyridine [19, 48, 55, 56]. Moreover, for single crystals the anisotropy of the ODMR spectra could be studied in the presence of small magnetic fields. The results of these experiments unambiguously prove the triplet spin nature of the emissive state. Figure 5 shows the low-temperature emission spectra for these compounds. Compared with the free ligand emission, the 0–0 emission is red shifted by about 1300 cm^{-1} [55]. The zero-field ODMR spectra measured for the $[Rh(phen)_n(bpy)_{3-n}](ClO_4)_3$ compounds [50] are shown in Fig. 6. Here again the line widths (~100 MHz) are broader compared with the widths of the ODMR signals of the pure ligand molecules (10 MHz). Table 1 lists the zero-field ODMR frequencies for the chelates and the free ligand molecules. The resonance frequencies characteristic of the zero-field ODMR

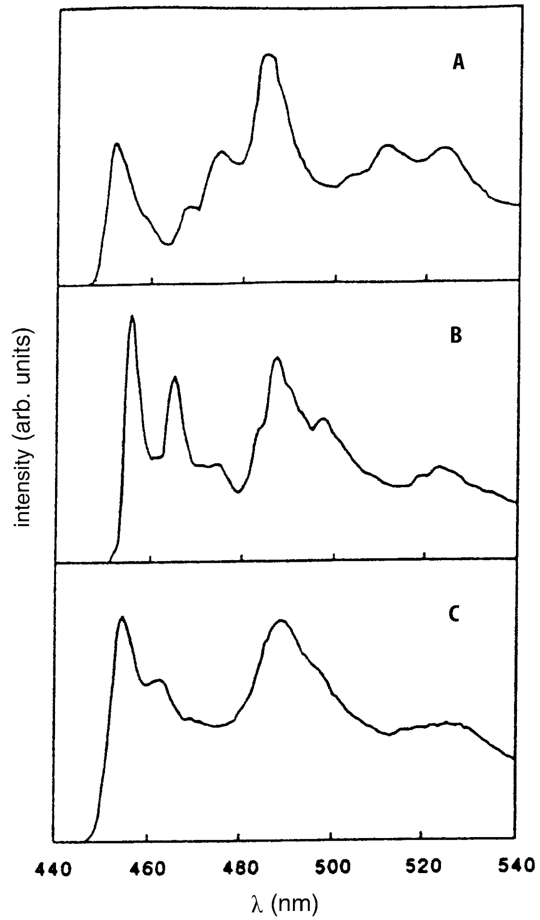

Fig. 5A–C. Phosphorescence spectra of single crystals of: A $[Rh(bpy)_3](ClO_4)_3$; **B** $[Rh(phen)_3](ClO_4)_3$; C a powder sample of $[Rh(phen)_2(bpy)](ClO_4)_3$. Photoexcitation at 320 nm; T = 1.4 K

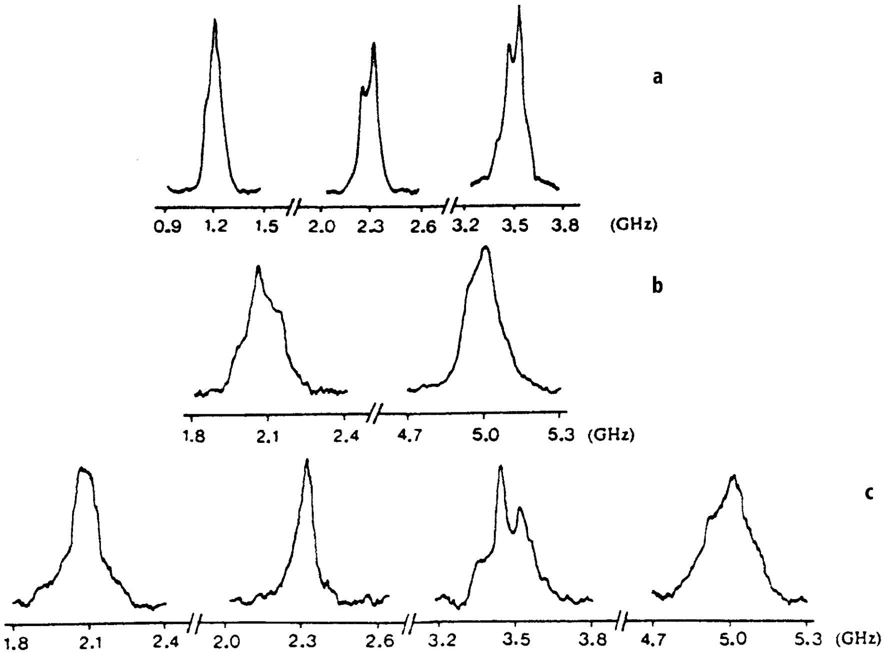

Fig. 6a–c. Zero-field ODMR spectra as observed for single crystals of: **a** $[Rh(bpy)_3](ClO_4)_3$; **b** $[Rh(phen)_3](ClO_4)_3$; **c** a powder sample of $[Rh(phen)_2(bpy)](ClO_4)_3$. Photoexcitation at 320 nm; T = 1.4 K. The apparent structures in the microwave resonances are due to a variation of the microwave power with the microwave frequency

Table 1. ODMR frequencies (GHz) as determined for $[Rh(phen)_n(bpy)_{3-n}](ClO_4)_3$ for n = 0, 2, and 3 and the free ligand molecules phen and bpy at 1.4 K. For n = 2 the ODMR frequencies in the left column are for the excitation localized at bpy and those in the right column are for the excitation localized at the phen ligand. Asterisk indicates that the transition has not been observed. The data for bpy and phen were taken from [18]

$[Rh(phen)_n(bpy)_{3-n}](ClO_4)_3$						
Transition	bpy	n = 0	n = 2		n = 3	phen
2|E|	0.76	1.18	*	2.05	2.08	1.66
|D|−|E|	2.99	2.32	2.28	*	*	2.91
|D|+|E|	3.75	3.49	3.44	5.03	5.00	4.57

transitions of the complexes show a striking resemblance with those of the corresponding pure ligands, thus providing further support that the luminescence is from an excited $^3\pi\pi^*$ state. The mixed complex (n = 2) shows a rather different behavior. For this compound an emission from both ligands had been reported [57]. The emission shows that both ligands, bpy and phen, can serve as traps for the optical excitation. In zero-field ODMR, as many as four transitions are observed that coincide with the ODMR frequencies of the pure $Rh(bpy)_3^{3+}$ and

$Rh(phen)_3^{3+}$ compounds (cf. Table 1). This is indicative that the excitation in the mixed ligand compound is ligand localized, be it bpy or phen. This is further supported by means of PMDR measurements. For instance, Fig. 7 shows the PMDR spectra obtained for the 5.0 GHz transition of $[Rh(phen)_3](ClO_4)_3$ and $[Rh(phen)_2(bpy)](ClO_4)_3$, respectively.

From the similarity of the PMDR spectra in Fig. 7 it follows that both compounds have similar emissive states. Since both compounds have the phen ligand in common, microwave excitation localized within this ligand is involved in the ODMR transition at 5.0 GHz. Similarly, when the PMDR experiment was repeated for the 2.3 GHz ODMR transition of $[Rh(phen)_2(bpy)](ClO_4)_3$, the PMDR result is the same as for $Rh(bpy)_3^{3+}$. Thus from PMDR measurements it is established that in the mixed compound both ligands may serve as the trap for the triplet state excitation. Depending on the details of the environment of the excited complex in the solid either the phen or the bpy ligand excitation may be lowest in energy. Thus for the mixed complexes the emission of both ligands is due to the inhomogeneity in the surroundings. That the excitation is also ligand localized in the pure $Rh(bpy)_3^{3+}$ and $Rh(phen)_3^{3+}$ cations is not obvious a priori, although the comparable results for the fine structure splittings of the free ligand molecules and for the mixed compound already suggest that this should be so. Localization of the triplet excitation is expected to be reflected in the orientation of the fine structure main axes in the molecule. For instance, if tri-

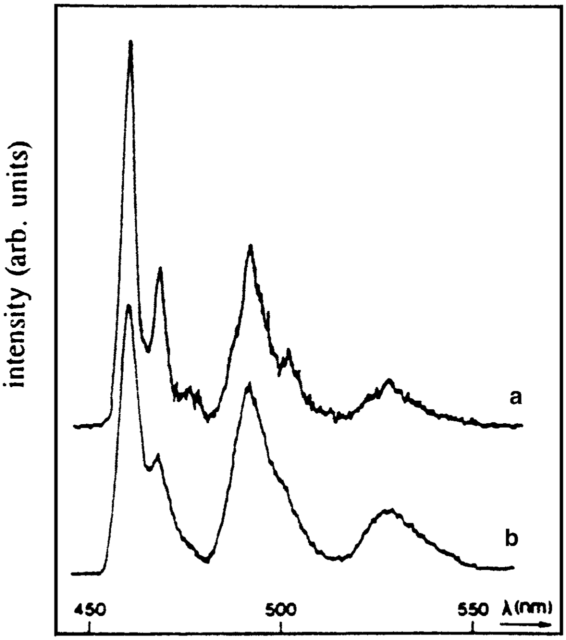

Fig. 7. Phosphorescence microwave double resonance (PMDR) spectrum as observed for the 5.0 GHz transition in the excited triplet state of (a) $[Rh(phen)_3](ClO_4)_3$ and (b) $[Rh(phen)_2(bpy)](ClO_4)_3$. Photoexcitation at 320 nm; T = 1.4 K

gonal symmetry is preserved for $Rh(bpy)_3^{3+}$ in the crystal, the $^3\pi\pi^*$ excitation would be delocalized and its spin distribution would exhibit axial symmetry, i.e., the zero-field splitting parameter E would be zero (cf. Eq. 8). This is certainly not the case for the $Rh(bpy)_3^{3+}$ and $Rh(phen)_3^{3+}$ cations since from the ODMR data for both species we know that $E \neq 0$. From ODMR anisotropy measurements in the presence of a magnetic field, the orientation of the magnetic main axes in the molecule could be determined [55]. In these experiments relatively small magnetic fields were used (near 500 G) because at higher magnetic field strengths, due to the strong mixing of the triplet spin functions, the sublevels have similar radiative properties and ODMR is no longer observable. Under the influence of a magnetic field, shifts and splittings of the ODMR lines are induced. The details of the angular dependences of the ODMR transitions upon rotation of the crystal in the magnetic field are given elsewhere [55]. The results for the $[Rh(bpy)_3](ClO_4)_3$ single crystal are consistent with the presence of six magnetically distinguishable sites in the unit cell (the $[Rh(bpy)_3](ClO_4)_3$ crystal has R3c space group symmetry [58]). From the simulations of the ODMR anisotropy patterns for the six inequivalent triplet sites, the orientation of the corresponding fine structure main axes in the unit cell could be determined. It appeared that these main axes coincide with those of six bpy ligand molecules for which the position in the unit cell could be specified. If we allow for the possibility that the $^3\pi\pi^*$could also be on the other ligand molecules in the unit cell (in all there are 12 more ligand sites), the ODMR spectrum would consist of many more ODMR lines than actually observed. Summing up the conclusions from the low-field ODMR measurements, we have (i) the Zeeman splittings and the anisotropy of the ODMR transitions provide unambiguous evidence that the emissive state of $[Rh(bpy)_3](ClO_4)_3$ is a triplet state, and (ii) for each $Rh(bpy)_3^{3+}$ cation in the unit cell, the triplet state excitation is localized on one specific bpy ligand only. Apparently, due to the influence of the crystalline environment, the equivalence between the three ligand molecules that exists in an isolated cation is lifted. Conclusions from high-resolution optical experiments by Humbs and Yersin support this view [59].

6.2
Triplet Sublevel Kinetics

The lifetimes of the sublevels of the excited triplet state of the Rh-trisdiimine complexes have been determined using the microwave recovery and adiabatic rapid passage techniques mentioned in Sect. 4.2. At (pumped) liquid helium temperatures it turned out that the triplet state sublevels have distinct lifetimes. As an example, we show in Fig. 8 the optically detected adiabatic transient signal as monitored for the zero-field $|D|-|E|$ resonance, at 2320 MHz, of the photoexcited $[Rh(bpy)_3](ClO_4)_3$ single crystal, at 1.4 K. The microwave frequency scan was at a rate of 2×10^6 Hz/s. Similar transients were obtained by rapid scans through the zero-field microwave transitions for the other compounds of the $[Rh(phen)_n(bpy)_{3-n}](ClO_4)_3$ series. The transients fitted a biexponential function of the form

$$f(t) = A \exp(-k_a t) - B \exp(-k_b t) \tag{18}$$

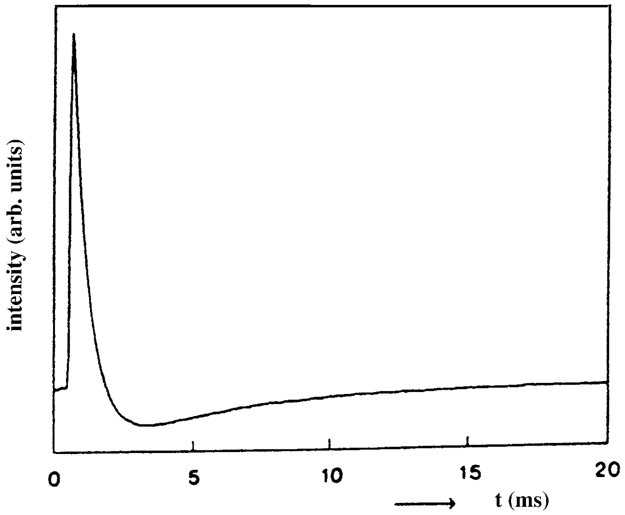

Fig. 8. Adiabatic rapid passage signal observed by monitoring the phosphorescence intensity at 456 nm of [Rh(bpy)$_3$](ClO$_4$)$_3$ after a rapid microwave sweep through the zero-field $|D|-|E|$ resonance, at 1.4 K

From the best fits, the kinetic rate constants, k_a and k_b, and the ratio of the radiative rate constants, A/B, of the resonantly coupled spin levels could be obtained. The lifetimes of the triplet sublevels in the various chelates [56] are collected in Table 2. Evidently, the sublevel lifetimes are on the millisecond time scale, and about three orders of magnitude shorter than the phosphorescence lifetimes of the free ligand molecules (bpy: $\tau_p = 0.8$ s; phen: $\tau_p = 1.4$ s [60, 61]). For [Rh(bpy)$_3$](ClO$_4$)$_3$ the radiative rate constants are in the ratio $T_x : T_y : T_z = 10:1:2$, showing that the T_x sublevel is the most active in the radiative as well as nonradiative processes [62]. The shortening of the triplet state sublevel lifetimes for the Rh(III)-chelates as compared to the triplet sublevel lifetimes of the free ligand molecules is reminiscent of the heavy atom effect as, for example, observed for halonaphthalenes [33–35]. In the latter, the mixing of $^1\pi\pi^*$ states with $^1n\pi^*$ and $^1\sigma\pi^*$ excitations is enhanced by SOC within the heavy atom. In

Table 2. Lifetimes (ms) of the triplet sublevels of [Rh(phen)$_n$(bpy)$_{3-n}$](ClO$_4$)$_3$ for n = 0, 2, and 3, at 1.4 K. For n = 2 the data in the left column are for the excitation at the bpy ligand, the data in the right column refer to the phen ligand molecule

[Rh(phen)$_n$(bpy)$_{3-n}$](ClO$_4$)$_3$

Sublevel	n = 0	n = 2		n = 3
T_y	6.7	5.0	11.5	9.2
T_z	4.5	4.4	3.0	2.2
T_x	0.6	0.5	3.5	3.4

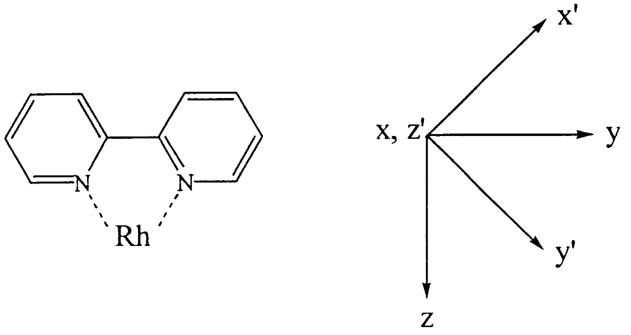

Fig. 9. Orientation of the molecular axes x, y, z of a Rh(bpy) fragment (C_{2v} symmetry). The primed axes x', y', z' correspond to the main axes system of the $Rh(bpy)_3^{3+}$ chelate

Rh(III)-chelates, however, the radiative decay of the $^3\pi\pi^*$ is enhanced by SOC-induced mixing with $^1d\pi^*$ and/or $^1dd^*$ excitations. This is nicely illustrated in the case of $[Rh(bpy)_3](ClO_4)_3$. As followed from the ODMR results, the excitation is localized on one of the bpy ligand molecules, so we consider an excitation of the Rh(bpy) fragment as in Fig. 9. Referring to the axis frame given in Fig. 9, the most active radiative level is the out-of-plane component T_x (T_x: T_y: T_z= 10:1:2, see above). Normally, for aza-aromatic molecules, the out-of-plane component carries very little radiative character [25], so here the opposite is the case. To understand this we consider the optical transition moment

$$M_{S_\phi \leftarrow T_1^\tau} = \sum_j \frac{\langle S_0 | \mu | S_j \rangle \langle S_j | H_{SOC} | T_1^\tau \rangle}{E_{T_1} - E_{S_j}} \tag{19}$$

where S_j and T_1 refer to the molecular singlet and the lowest excited triplet state, respectively, E_j refers to the energy of state $|j\rangle$ and H_{SOC} and μ denote the SOC Hamiltonian and electric dipole operator, respectively. We adopt the usual one-center approximation, i.e.,

$$H_{SOC} = \sum_i \xi_M(\mathbf{r}_i)\, \mathbf{l}_{M,i}\, \mathbf{s}_i \tag{20}$$

The lowest $^3\pi\pi^*$ excitation in bpy is $^3B_2\,(\pi_{a2}, \pi_{b1}{}^*)$ [18]. Table 3 lists the Rh^{3+} d-orbitals given the bpy axis system of Fig. 9 and their representations in O_h symmetry. Out of the set of t_{2g} orbitals only the d_{yx} and the d_{zx} orbitals have the proper symmetry to form π-type molecular orbitals with the π-orbitals of the bpy fragment. In particular, the d_{yx} orbital combines with a π-orbital of a_2 sym-

Table 3. Symmetries of Rh^{3+} d-orbitals in the bpy x, y, z reference frame (C_{2v}) expressed in the basis set d-orbitals in the x', y', z'-frame (Fig. 9)

$d_{y^2-z^2}$	$(d_{x'y'})$	: $a_1(C_{2v})$	$t_{2g}(O_h)$
d_{yx}	$(d_{z'x'} + d_{z'y'})$	: $a_2(C_{2v})$	$t_{2g}(O_h)$
d_{zx}	$(d_{z'x'} - d_{z'y'})$	: $b_1(C_{2v})$	$t_{2g}(O_h)$
d_{x^2}	$(d_{z'^2})$	: $a_1(C_{2v})$	$e_g(O_h)$
d_{zy}	$(d_{x'^2-y'^2})$	: $b_2(C_{2v})$	$e_g(O_h)$

metry and, similarly, d_{zx} forms a molecular orbital with a π-orbital of b_1 symmetry. The $^3B_2$ state thus becomes of the form $c_1\ ^3(\pi_{a2},\pi_{b1}{}^*) + c_2\ ^3(d_{yx},\pi_{b1}{}^*) + c_3\ ^3(\pi_{a2}, d_{zx})$. The d_{y2-z2} orbital, on the other hand, may participate in σ-type bonding. As remarked before, SOC mixes the triplet configuration with singlet configurations of the same total symmetry (orbital $\otimes$ spin). SOC-induced mixing of the $^3(\pi_{a2},\pi_{b1}{}^*)$ configuration with $^1\pi\pi^*$ configurations is relatively weak because only three-center integrals can contribute in this case and these are very small [25, 31]. SOC is strongest for electrons near the Rh^{3+}-ion; hence the major contribution to the matrix element $\langle H_{SOC}\rangle$ in Eq. (20) is expected to involve $^1d\pi^*$-configurations. In C_{2v} symmetry, which is the symmetry of the bpy ligand, the T_x, T_y, and T_z spin sublevels belong to the B_2, B_1, and A_2 representations, and thus the total symmetries for the spin-orbital functions of the $^3B_2$ state are A_1, A_2, and B_1, respectively. One has then that $^3(T_x,d_{yx},\pi_{b1}{}^*)$ mixes with $^1(d_{zx},\pi_{b1}{}^*)$, and also that $^3(T_y, d_{yx},\pi_{b1}{}^*)$ mixes with $^1(d_{zy},\pi_{b1}{}^*)$, and finally, $^3(T_z, d_{yx},\pi_{b1}{}^*)$ mixes with $^1(d_{y2-z2},\pi_{b1}{}^*)$. However, since the T_y sublevel is of A_2 total symmetry, and the transition dipole moment for this symmetry is forbidden in C_{2v}, there is no emission from the T_y sublevel. Moreover, the mixing of the T_z level is expected to be small because it involves mixing with an energetically high-lying $^1(\sigma + \delta d_{y2-z2},\pi_{b1}{}^*)$ excitation. The result is that in this scheme the radiation is dominantly due to the T_x-level, whereas the T_z-level is weakly radiative. This is precisely what has been found experimentally [48, 56]. The triplet state lifetimes for $[Rh(phen)_3](ClO_4)_3$ and $[Rh(phen)_2(bpy)](ClO_4)_3$ can be discussed in a similar way. Here too enhanced decay as compared with the lifetimes of the lowest triplet state of free *o*-phenanthroline is due to SOC-effects of the central Rh^{3+}-ion which causes enhanced mixing triplet and singlet configurations [31, 48, 56]. More generally we conclude that, due to the bonding of the ligand molecules with the central metal ion, SOC near the central metal ion is transferred to the π-electron system of the organic chelate system, thus resulting in an enhanced mixing between the singlet and triplet configurations.

6.3
Triplet Sublevel Coherence

As shown in Fig. 3 a, spin coherence is manifested in the optically detected transient nutation signal for $[Rh(bpy)_3](ClO_4)_3$ in the phosphorescent triplet state. In this experiment, one observes that the phosphorescence intensity becomes modulated as the pulse length of microwave pulses, resonant with the $|D|-|E|$ transition, is gradually increased. The modulation is evidence that the microwave excitation induces a spin coherence in the ensemble of molecules in the photoexcited triplet state [44]. Moreover, from the transient nutation experiment one obtains the information about the duration of the pulses needed in a spin echo experiment. In the case of the example, the $\pi/2$ pulse is 100 ns and the π pulse has a length of 200 ns. Similarly, transient nutation signals for the other zero-field spin resonances could be obtained. The optically detected spin echo decay as measured for the $|D|-|E|$ zero-field transition for $[Rh(bpy)_3](ClO_4)_3$ at 1.2 K is shown in Fig. 3b. The signal fits a monoexponential decay function with a characteristic phase memory time of $T_M = 3.1 \pm 0.2$ µs. Table 4 summarizes the

Table 4. Phase memory time T_M (μs) and homogeneous line width Γ_h in brackets (kHz) as determined for the zero-field ODMR transitions of $[Rh(thpy)_2(bpy)]^+$, $[Rh(thpy)(phpy)(bpy)]^+$, $[Rh(phpy)(thpy)(bpy)]^+$, $Rh(bpy)_3^{3+}$, and $Rh(phen)_3^{3+}$. Asterisk means spin echo was not detected

Transition	$Rh(TTB)^+$	$Rh(TPB)^+$	$Rh(PTB)^+$	$[Rh(bpy)_3](ClO_4)_3$	$[Rh(phen)_3](ClO_4)_3$
$2\|E\|$	3.42 (93)	*	*	3.0 ± 0.3 (106)	3.2 ± 0.6 (99)
$\|D\|-\|E\|$	3.14 (101)	4.32 (74)	1.70 (187)	3.1 ± 0.2 (102)	*
$\|D\|-\|E\|$	*	*	*	3.3 ± 0.3 (96)	*

results for the zero-field transitions of $[Rh(bpy)_3](ClO_4)_3$ and $[Rh(phen)_3](ClO_4)_3$. In the case of $[Rh(phen)_3](ClO_4)_3$ only for the $2\,|E|$ transition could the echo be detected, the S/N ratio for the other transitions being too low to allow reliable values for T_M. The results for the dephasing times imply that typically the homogeneous line widths of the zero-field spin transitions are of the order of 100 kHz. On the other hand, in the normal zero-field ODMR spectrum line widths of 100 MHz or more are found. Obviously, inhomogeneous broadening of the ODMR transitions of the d^6-metal ion chelates exceeds homogeneous broadening by at least three orders of magnitude. Note also that the sublevel lifetimes are of the millisecond time scale; this is three orders of magnitude longer than the dephasing times. The homogeneous line widths of the zero-field spin transitions therefore are not due to population relaxation processes of the triplet state, but are the result rather of pure dephasing process(es). The value of 3.1 μs for the spin dephasing times for $[Rh(bpy)_3](ClO_4)_3$ and $[Rh(phen)_3](ClO_4)_3$ in the photoexcited triplet state is well within the usual range of 1–10 μs for spin transitions of aromatic and azo-aromatic systems like naphthalene and quinoline [63]. In these systems dephasing is usually due to dynamic dipolar interactions between flipping proton spins of the aromatic molecule and the triplet spin system. It is also very likely that for the Rh^{3+}-trisdiimine molecules, in the triplet state, dipolar couplings between the fluctuating proton spins of the ligand fragments and the triplet spin contribute to the electron spin dephasing. This is supported by the experimental result that the dephasing times for the Rh^{3+}-trisdiimine complexes show no temperature dependence (at least up to 4.2 K) as expected for pure spin-spin interactions. The similar dephasing times for the d^6-metal ion complexes and the free ligand molecules is another illustration that the triplet state excitation in the complex is localized on a ligand molecule with a spin distribution very similar to that for the free ligand molecule.

7
Rh^{3+}-Mixed Cyclometalated Chelates

7.1
Introduction

In addition to the Rh^{3+}-trisdiimine chelates, Rh^{3+}-chelates with the general formula $[Rh(thpy)_x(phpy)_{2-x}(bpy)]^+$, with $thpy^-$ = 2,2′-thienylpyridinate, $phpy^-$ =

2-phenylpyridinate, bpy = 2,2′-bipyridine, and x = 1,2 have been investigated by means of optically detected magnetic resonance spectroscopy [64–67]. The optical properties of the $Rh^{3+}(4d^6)$- and $Ir^{3+}(5d^6)$-mixed chelates of the form, $[M(thpy)_x(phpy)_{2-x}(bpy)]^+$, have been reviewed recently [68, 69]. The luminescence observed for the Ir^{3+} $(5d^6)$ complexes has been assigned as due to a ^{3}MLCT transition [69]. The Rh^{3+} complexes, on the other hand, show exclusively ^{3}LC luminescence [70, 71]. In fact, for the complexes containing the $thpy^-$ as cyclometalating ligand the excitation is trapped at this ligand. In case this ligand is absent, the excitation is preferentially centered at the phpy ligand and not the bpy ligand. The $^3\pi\pi^*$ excitation of the $phpy^-$ ligand lies about 3000 cm^{-1} above that for the $thpy^-$ ligand, but about 1000 cm^{-1} below that for bpy [68]. In analogy to the Rh^{3+} tris-diimine complexes, one might consider the possibility that the ligand-centered emission for the $[Rh(thpy)_x(phpy)_{2-x}(bpy)]^+$ (x = 1, 2) complexes originates in an excited triplet state. Of course, if feasible, the ODMR technique would be the best way to verify directly the triplet state nature of the excited state. Indeed, for the above-mentioned complexes substitutionally doped in a single crystal of $[Rh(phpy)_2(bpy)]PF_6$, ODMR spectra could be measured at liquid helium temperatures.

7.2
ODMR of Mixed Rh^{3+} Cyclometalated Chelates

7.2.1
$[Rh(thpy)_2(bpy)]^+$

There is only one way for the $[Rh(thpy)_2(bpy)]^+$ cation to fit into the crystal lattice, with the two $thpy^-$ ligands replacing the host $phpy^-$ ligands. In the $[Rh(thpy)(phpy)(bpy)]^+$ cation, both cyclometalating ligands, $thpy^-$ and $phpy^-$, can occupy either of the two available non-bpy sites per molecule, giving rise to two inequivalent complex conformations in the crystal lattice. We adopt the notation $Rh(TPB)^+$ and $Rh(PTB)^+$ for the two different conformations; $[Rh(thpy)_2(bpy)]^+$ will be referred to as $Rh(TTB)^+$. Figure 10 a shows the high-energy part of the emission spectrum, at 1.4 K, for $Rh(TTB)^+$ doped in the $[Rh(PPB)]PF_6$ single crystal [64]. The electronic origin is at 520.7 nm (19,204 cm^{-1}). As discussed elsewhere [54], the vibrational structure is characteristic of an emissive $\pi\pi^*$ state localized on a $thpy^-$ ligand. Furthermore, it was determined that, at 4.2 K, the emitting level lifetime is 204 μs [72]. This long lifetime is indicative of a spin-forbidden optical transition. ODMR experiments, performed in zero magnetic field, resulted in three resonance signals (cf. Fig. 11). The frequencies of the resonances were found to be 1730 MHz, 2580 MHz, and 4310 MHz. The line widths of the ODMR transitions vary from 13 MHz to 45 MHz. For the pure (i.e., undoped) $[Rh(thpy)_2(bpy)]PF_6$ single crystal, two ODMR transitions, at 1720 MHz and 2640 MHz, respectively, were observed [64]. The line widths of these signals have values between 100 MHz and 200 MHz. The PMDR spectra taken for the three zero-field transitions are shown in Fig. 10b–d. These spectra have the characteristics of the normal emission spectrum and thus confirm that the ODMR transitions belong to the emissive

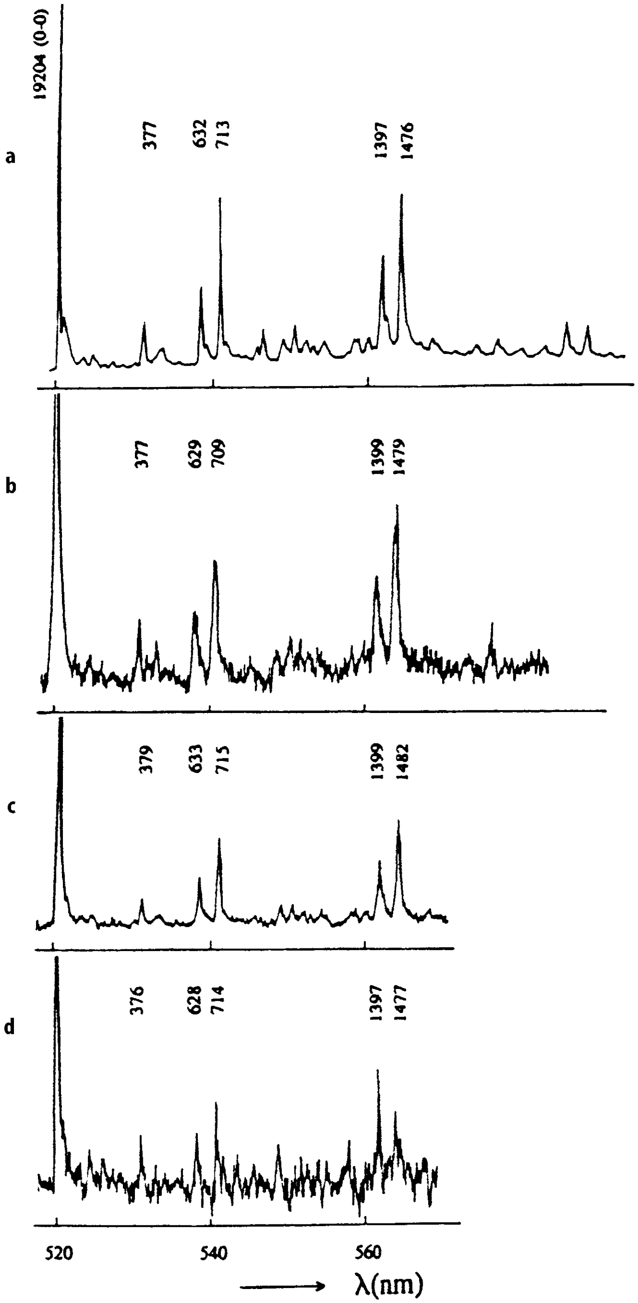

Fig. 10 a–d. **a** High-energy part of the emission spectrum of 1% doped $[Rh(thpy)_2(bpy)]^+$ in $[Rh(phpy)_2(bpy)]PF_6$, at 1.4 K. Excitation is at 488 nm. **b** PMDR spectrum for the $2|E|$ transition at 1730 MHz. **c** PMDR spectrum of the $|D|-|E|$ transition at 2580 MHz. **d** PMDR spectrum of the $|D|+|E|$ transition at 4310 MHz. Frequencies of vibrational satellites are as indicated

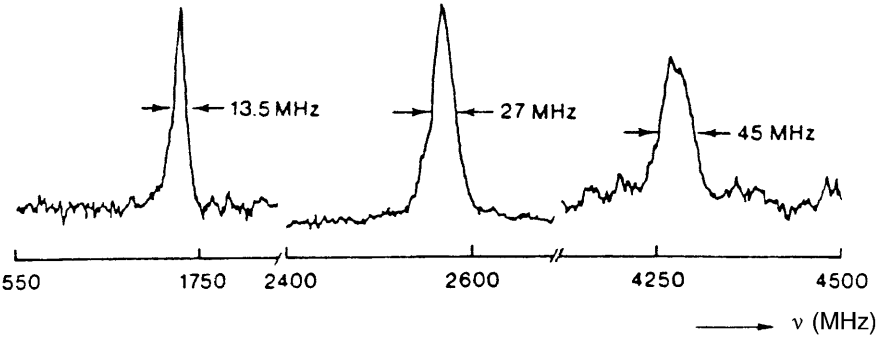

Fig. 11. Zero-field ODMR transitions of 1% doped $[Rh(thpy)_2(bpy)]^+$ in $[Rh(phpy)_2(bpy)]PF_6$ at 1.4 K. Excitation is at 488 nm, detection is at 0–0 transition at 19,204 cm

state of $Rh(TTB)^+$. In a magnetic field, the ODMR transitions show Zeeman shifts and splittings, as well as anisotropic behavior [64]. Detailed analysis of the ODMR spectra in magnetic fields up to about 1200 G appeared possible [64, 73]. It could be shown that the emissive state, for which the fine structure is measured in ODMR, is indeed an electron spin triplet state. Furthermore, from the angular dependence of the ODMR spectra in a magnetic field, it was established that out of the two $thpy^-$ ligand molecules per Rh^{3+}-complex the triplet state is localized on one ligand molecule only. By comparing the orientation of the magnetic main axes of the triplet state to the crystallographic positions of the two $thpy^-$ ligand molecules per Rh^{3+}-complex it was determined which of the two ligand molecules actually trapped the optical excitation and therefore has the lower excitation energy. From the analysis of the anisotropy of the ODMR spectra in the magnetic field it was concluded that there are four magnetically inequivalent positions for the ligand molecule, in the crystal unit cell, at which the excitation can be localized [64] (cf. Fig. 12). The orientation of the principal axes (x, y, z) of the fine structure tensor is as given in Fig. 13.

Note that the direction of the z axis is now perpendicular to the molecular plane, in agreement with the notion that the symmetry of the thpy fragment is C_s. It should be added, however, that fits of similar good quality for the angular dependencies of the ODMR lines in a magnetic field was obtained choosing the direction of the principal axes as the x', y', z' axis frame in Fig. 13. Previously, from optical experiments [72], the orientation of the transition moment of the lowest-energy excitation was found to lie approximately parallel to the x' axis shown in Fig. 13. Anyhow, the ODMR results clearly show that the fine structure z axis is perpendicular to the molecular $thpy^-$ plane and that the x and y axes are not lifted out of the $thpy^-$ plane.

The experimentally determined values for the zero-field splitting parameters, $|D| = 3445$ MHz and $|E| = 865$ MHz, are typical for the $thpy^-$ ligand localized triplet state. Note that these values differ appreciably from those found above for the bpy ligand. Thus the values of the fine structure parameters also reflect that the triplet state is localized on the $thpy^-$ ligand and not on the bpy ligand. Assuming that dipolar spin-spin interactions predominantly contribute to the

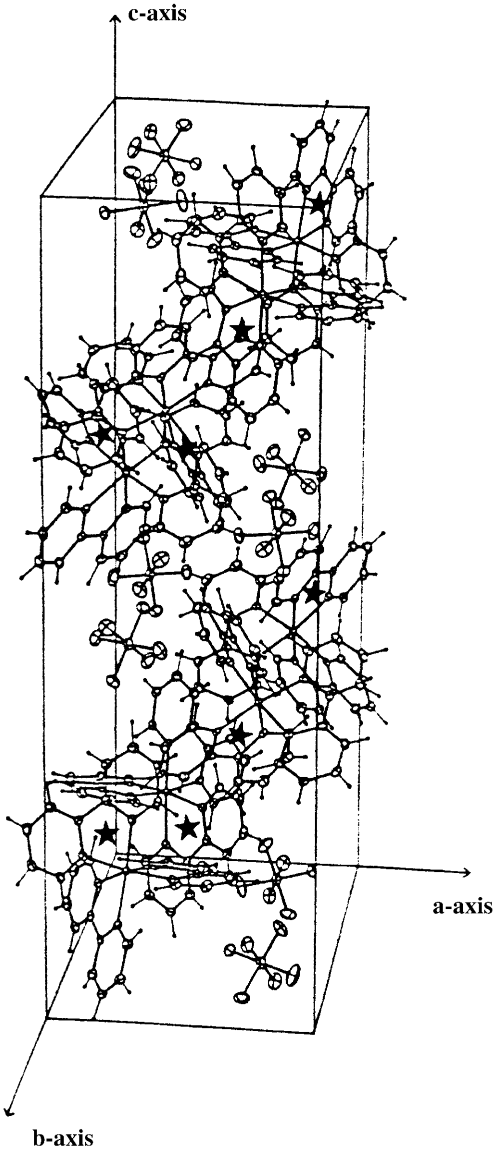

Fig. 12. Schematic of the unit cell of a single crystal of $[Rh(phpy)_2(bpy)]PF_6$ (orthorhombic symmetry) with eight complex cations. The positions of the $thpy^-$ ligands that trap the photoexcitation in $[Rh(thpy)_2(bpy)]^+$ are marked with an *asterisk*

zero-field splitting parameters, and applying the classical expression for dipolar couplings, we roughly estimate the average distance between the unpaired electron spins to be 2.5 Å. Note that this estimated value is another indication that the triplet state excitation is localized on just one of the two $thpy^-$ ligand fragments per cation complex site only.

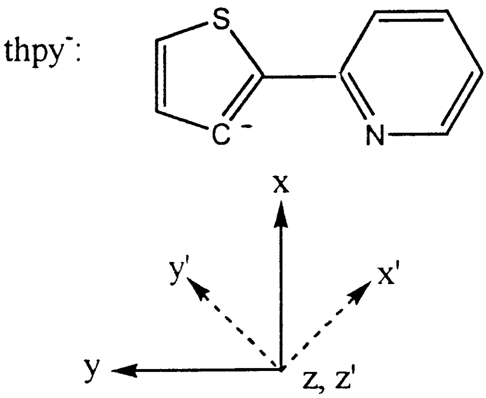

Fig. 13. Orientation of the *x*, *y*, *z* and *x'*, *y'*, *z'* molecular main axes for the thienylpyridine ligand as defined in the text

7.2.2

[Rh(thpy)(phpy)(bpy)]$^+$

The [Rh(thpy)(phpy)(bpy)]$^+$ complex cations can substitute the cations of the [Rh(phpy)$_2$(bpy)]PF$_6$ host crystal in two different ways since the two phpy$^-$ ligand molecular sites per Rh^{3+} cation occupy crystallographically different positions. Thus two complex conformations in the crystal exist, which we denote as Rh(TPB)$^+$ and Rh(PTB)$^+$. Previously, two zero-phonon line transitions in the emission spectrum for the [Rh(thpy)(phpy)(bpy)]$^+$ complex have been reported [74]. These lines, at 517.9 nm and 519.9 nm, were attributed to the emissions of the Rh(PTB)$^+$ and Rh(TPB)$^+$ species, respectively. Upon photoexcitation at 488 nm an ODMR spectrum characteristic of the emissive states of [Rh(thpy)(phpy)(bpy)]$^+$ in the host crystal could be measured [65]. In fact, the two conformations, Rh(TPB)$^+$ and Rh(PTB)$^+$, could also be distinguished in ODMR by selective detection at the respective zero-phonon transitions. The two ODMR spectra, obtained for Rh(TPB)$^+$ and Rh(PTB)$^+$, respectively, are given in Fig. 14. The resonance frequencies of the observed zero-field ODMR transitions are given in Table 5. PMDR spectra for all resonance frequencies were characteristic of the emission of the thienylpyridine ligand, as in Rh(TTB)$^+$. It follows that the excited state, for which the ODMR transitions are observed, is localized at the thienylpyridine ligand in the Rh(TPB)$^+$ and Rh(PTB)$^+$ complexes. As before, the triplet state nature of the ligand-localized excitations in Rh(TPB)$^+$ and Rh(PTB)$^+$ is evidenced from the ODMR results in the presence of an externally applied magnetic field [65]. Distinct anisotropies were measured for all ODMR transitions belonging to either the Rh(TPB)$^+$ or the Rh(PTB)$^+$ species [65]. The triplet state character of the emissive state is confirmed from the analysis of the results in the magnetic field (analysis is not given here). Computer simulation of the experimentally observed anisotropy confirms that the emissive state is localized at the thpy$^-$ ligand in the Rh(TPB)$^+$ and Rh(PTB)$^+$ complexes [65]. It was

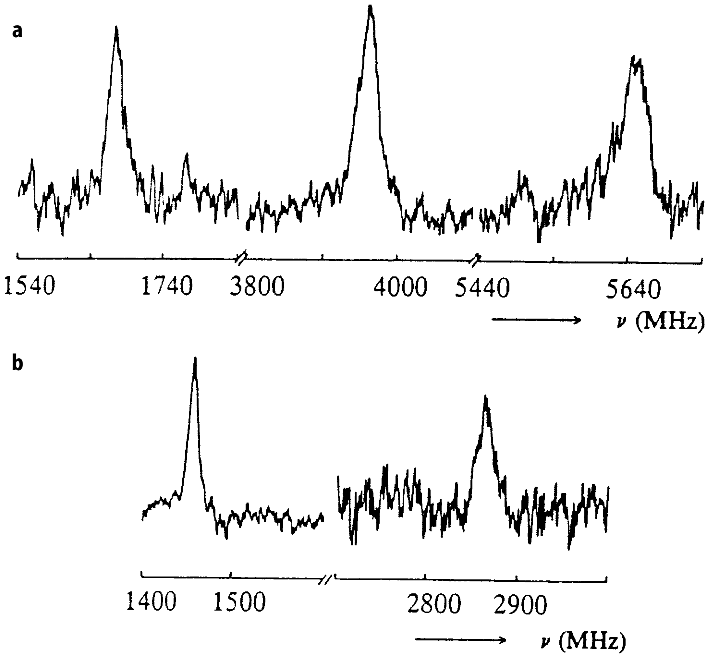

Fig. 14a,b. Zero-field ODMR spectrum for: **a** [Rh(thpy)(phpy)(bpy)]$^+$; **b** [Rh(phpy)(thpy)(bpy)]$^+$, detected at 519.9 nm and 517.9 nm, respectively. T = 1.4 K

Table 5. Zero-field ODMR frequencies (MHz) for [Rh(thpy)$_2$(bpy)]$^+$, [Rh(thpy)(phpy)(bpy)]$^+$, [Rh(phpy)(thpy)(bpy)]$^+$, doped in single crystal of [Rh(phpy)$_2$(bpy)]PF$_6$, in the excited triplet state

	Rh(TTB)$^+$	Rh(TPB)$^+$	Rh(PTB)$^+$	Rh(bpy)$_3^{3+}$	
2|E|	$T_z \leftrightarrow T_y$	1730	1670		1180
|D|−|E|	$T_z \leftrightarrow T_x$	2570	3970	1480	2320
|D|−|E|	$T_y \leftrightarrow T_x$	4310	5640	2870	3490

shown in Sect. 7.2.1 that in Rh(TTB)$^+$, in the same host crystal, the triplet state excitation is trapped at one of the two thpy$^-$ ligands per complex. It turns out that the localization of the excitation in Rh(TPB)$^+$ involves (crystallographically speaking) the same thpy$^-$ site, i.e., the orientation of the fine structure main axes for the two species is alike. In Rh(PTB)$^+$, on the other hand, the other thpy$^-$ ligand site traps the triplet state excitation and for the latter appreciably different zero-field splitting parameters are found (cf. Table 5). Thus the different crystal field environment for the thpy$^-$ excitation is not only reflected in the slightly different positions for their zero-phonon emissions (519.9 nm and 517.9 nm), but also in the different spin distributions in the triplet state as manifested by the disparity of the zero-field splitting parameters.

7.3
Triplet Sublevel Kinetics

The lifetimes of the triplet-state sublevels of the mixed tris-cyclometalated Rh^{3+}-complexes, $Rh(TTB)^+$, $Rh(TPB)^+$, and $Rh(PTB)^+$, were determined from optically detected microwave recovery and adiabatic rapid passage experiments performed at 1.4 K [66, 75]. Typically, transients as displayed in Fig. 15 were obtained. The transients could be fitted in all cases to a bi-exponential of the form of Eq. (18). The ratio A/B equals the ratio of the radiative rate constants of the resonant sublevels. In Table 6 the resultant rate constants for the dopants $Rh(TTB)^+$, $Rh(TPB)^+$ and $Rh(PTB)^+$ are collected. It is now obvious why for $Rh(PTB)^+$ the 2 $|E|$ zero-field ODMR transition could not be observed: the T_z and T_y sublevels have almost equal radiative probabilities. It is noted that the bi-

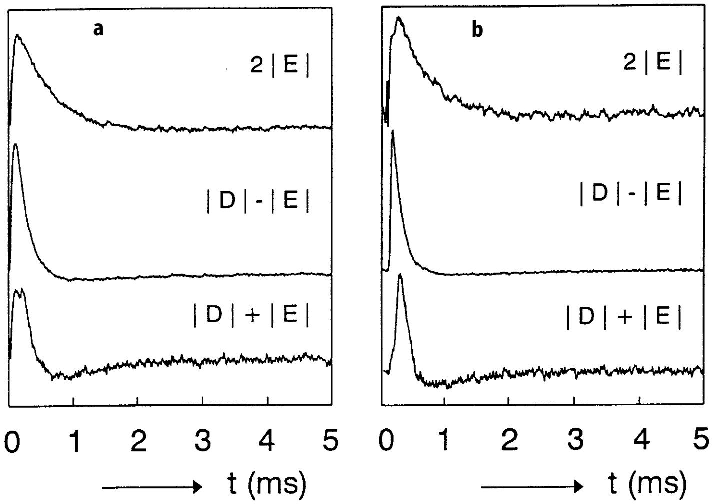

Fig. 15a,b. **a** Optically detected microwave recovery transients for the three zero-field ODMR transitions of $[Rh(thpy)_2(bpy)]^+$ in the excited triplet state. Detection is at 520.7 nm. **b** Optically detected adiabatic rapid passage transients for the three zero-field ODMR transitions of $[Rh(thpy)(phpy)(bpy)]^+$ in the excited triplet state. Detection is at 519.9 nm, T = 1.4 K

Table 6. Total decay rate constant $k_I^{tot}(10^3\,s^{-1})$ and relative radiative decay rate k_I^r for $[Rh(thpy)_2(bpy)]^+$, $[Rh(thpy)(phpy)(bpy)]^+$, $[Rh(phpy)(thpy)(bpy)]^+$, $Rh(bpy)_3^{3+}$, in the excited triplet state

	$Rh(TTB)^+$		$Rh(TPB)^+$		$Rh(PTB)^+$		$Rh(bpy)_3^{3+}$	
	k_i^{tot}	k_i^r	k_i^{tot}	k_i^r	k_i^{tot}	k_i^r	k_i^{tot}	k_i^r
T_y	1.33	0.22	1.69	0.3	0.83	0.11	0.15	0.1
T_z	0.83	0.07	0.67	0.06	1.45	0.14	1.67	1
T_x	5.26	1	5.62	1	6.06	1	0.22	0.2

exponential nature of the transients shows that the spin levels, at 1.4 K, are thermally isolated, or equivalently, spin-lattice relaxation is negligible.

Radiative decay rates were calculated from the oscillator strengths that were obtained from the absorption spectrum in which the triplet state was directly excited [68]. It was concluded that the radiative decay of the $^3\pi\pi^*$ state, localized on the thienylpyridine ligand, is about two orders of magnitude faster for the chelate as compared to that for the free ligand (35 ms for the free ligand as compared to 0.5 ms for the chelated ligand [76, 77]). The enhancement of the radiative decay rate constant for the phosphorescence of the metal chelate is, as discussed in Sect. 6.2, reminiscent of the heavy-atom effect in halogenated aromatic molecules [33–35]. We will now discuss in further detail the mechanism for radiative decay out of the lowest triplet state for the three complexes, Rh(TTB)$^+$, Rh(TPB)$^+$, and Rh(PTB)$^+$.

7.3.1
Rh(TTB)$^+$

With reference to the molecular axis frame of Fig. 16, it is recalled from the ODMR results that the ligand-localized triplet state excitation in Rh(TTB)$^+$ is on the fragment (of C_s symmetry) marked with the single asterisk. We consider now, as in Sect. 6.2, that the transition moment for radiative decay of the triplet state is determined by $\langle H_{SOC}\rangle$ of Eq. (19), with a major contribution from the SOC

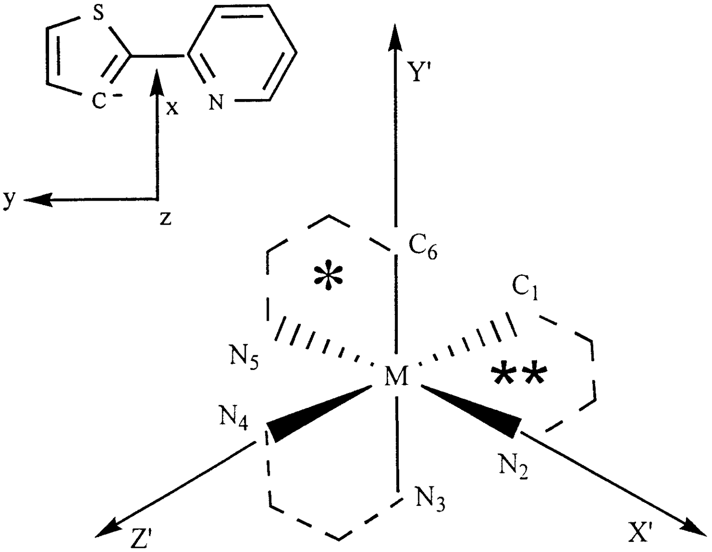

Fig. 16. Orientation of the fine structure tensor main axes for a thienyl ligand anion (C_s symmetry). In the x', y', z' axis system of the metal complex cation, a single asterisk refers to the thpy$^-$ ligand at which the triplet state is localized in [Rh(thpy)$_2$(bpy)]$^+$ and [Rh(thpy)(phpy)(bpy)]$^+$, whereas the double asterisk labels the thpy$^-$ ligand at which the triplet state is localized in [Rh(phpy)(thpy)(bpy)]$^+$

of the Rh^{3+} electrons. Thus singlet excitations mixed into the triplet states by H_{SOC} are of the form $^{1}(\pi + \delta d_{\pi})\pi^*$ or $^{1}(\sigma + \delta d_{\pi})\pi^*$. Let us first consider the radiative character of a triplet state mixed with singlet configuration of the type $^{1}(\pi + \delta d_{\pi})\pi^*$, i.e., the admixed configuration achieves its metal d-character in a molecular orbital involving π-bonding between the metal and the ligand that traps the excitation. The relevant π-bonding metal orbitals are formed by the set of t_{2g} d-orbitals, as in the case of $Rh(bpy)_3^{3+}$ (cf. Sect. 6.2) [48].

Note that the ligand (marked by the single asterisk in Fig. 16) has its main z axis parallel to the z' axis of the octahedral complex reference frame, whereas its main x and y axes are rotated about the z axis by 45° with respect to the main axes x' and y' of the complex. Out of the set t_{2g} orbitals (in O_h symmetry) only the metal $d_{x'z'}$ and $d_{y'z'}$ orbitals are suited for π-bonding with the ligand molecular π-orbitals (see also Table 7). Taking into account the symmetry of the Rh^{3+} d-orbitals (see Table 7), the $^{1}\pi\pi^*$ configuration is mixed with $^{1}d\pi^*$ configurations of the type, $^{1}A'(d_{y'z'} \pm d_{x'z'})\pi_{a''}^*$. H_{SOC} being totally symmetric, the triplet configuration $^{3}(\pi + \delta d_{\pi})\pi^*$ must be of A′ total symmetry. The orbital part $(\pi + \delta d_{\pi})\pi^*$ is of $a'' \otimes a'' = a'$ symmetry in C_s. Then only the $^{3}A'T_z$ triplet sublevel, which is the only one of the three triplet-state sublevels with a' symmetry, is expected to be mixed by H_{SOC} with $^{1}A'(d_{y'z'} \pm d_{x'z'})\pi_{a''}^*$. Consequently, when in the SOC scheme one exclusively considers metal-ligand π-bonding, only the T_z triplet sublevel will be emissive. As is seen from Table 6, a quite different result is obtained experimentally. Instead of the T_z level, the T_x level is the most radiative sublevel, the T_z level being even almost non-emissive. Furthermore, the T_y sublevel is also emissive in contrast with the π-bonding model. We conclude that the enhanced singlet-triplet mixing does not involve molecular orbitals that originate from π-bonding between the metal d-orbitals and the ligand π-orbitals.

As a next possibility we now consider SOC-induced mixing of the configuration of the lowest triplet with configurations of the type $^{1}(\sigma + \delta d_{\sigma})\pi^*$. In particular, d_{σ} is $d_{x'^2-y'^2}$ and/or $d_{z'^2}$, derived from e_g in O_h symmetry. The symmetry of the admixed $^{1}d_{\sigma}\pi^*$ singlet configuration is then obtained as $a' \otimes a'' = a''$. Within the one-center approximation for H_{SOC}, the singlet configuration mixes with configurations of the type $^{3}(d_{y'z'} \pm d_{x'z'})\pi^*$. Since the orbital part transforms as a', it follows that the triplet spin function is required to transform as a'' symmetry. Thus, when the triplet sublevels mix with singlet configurations involving σ-type molecular orbitals, the T_x and T_y substates become radiative. See also Table 8a.

Table 7. d-Orbital representations in O_h and C_s point groups

d-Orbitals	O_h	C_s ($[Rh(thpy)_2(bpy)]^+$-fragment)	C_s ($[Rh(phpy)(thpy)(bpy)]^+$-fragment)
$d_{x'y'}$	t_{2g}	a'	a''
$d_{x'z'}$	t_{2g}	a''	a'
$d_{y'z'}$	t_{2g}	a''	a''
$d_{x'^2-y'^2}$	e_g	a'	a'
$d_{z'^2}$	e_g	a'	a'

Table 8. SOC schemes for (a) $[Rh(thpy)_2(bpy)]^+$ (for $[Rh(thpy)(phpy)(bpy)]^+$ the scheme is similar), and (b) $[Rh(phpy)(thpy)(bpy)]^+$, substitutionally doped into the $[Rh(phpy)_2(bpy)]PF_6$ host crystal. Columns 4 and 5 show the d-orbitals generated upon operation of H_{SOC} on the orbitals given in the top row

a)

C_S	k_i^r	O_h	$H_{SOC}\vert{}^3(d_{y'z'} + d_{x'z'})\ \pi^*\rangle$	$H_{SOC}\vert{}^3(d_{y'z'} - d_{x'z'})\ \pi^*\rangle$
T_x	1	$\frac{1}{\sqrt{2}}(T_{y'} + T_{x'})$	$d_{x'^2-y'^2}$ (σ)	$d_{x'y'}/d_{y'^2}$ (non-bonding/σ)
T_y	0.22	$\frac{1}{\sqrt{2}}(T_{y'} - T_{x'})$	$d_{x'y'}/d_{z'^2}$ (non-bonding/σ)	$d_{x'^2-y'^2}$ (σ)
T_z	0.07	$T_{z'}$	$d_{y'z'} - d_{x'z'}$ (π)	$d_{y'z'} + d_{x'z'}$ (π)

b)

C_S	k_i^r	O_h	$H_{SOC}\vert{}^3(d_{y'z'} + d_{x'z'})\ \pi^*\rangle$	$H_{SOC}\vert{}^3(d_{y'z'} - d_{x'z'})\ \pi^*\rangle$
T_x	1	$\frac{1}{\sqrt{2}}(T_{z'} + T_{x'})$	$d_{x'^2-y'^2}, d_{z'^2}$ (σ)	$d_{x'y'}/d_{z'^2}$ (non-bonding/σ)
T_y	0.11	$\frac{1}{\sqrt{2}}(T_{z'} - T_{x'})$	$d_{x'z'}/d_{x'^2-y'^2}, d_{z'^2}$ (non-bonding/σ)	$d_{x'^2-y'^2}, d_{z'^2}$ (σ)
T_z	0.14	$T_{y'}$	$d_{y'z'} - d_{x'y'}$ (π)	$d_{y'z'} + d_{x'y'}$ (π)

Experimentally, the T_x indeed has the highest radiative character and also the T_y substate is radiative, although less by a factor of five. It is concluded that the enhanced radiative decay for the excited triplet state of $Rh(TTB)^+$ is due to mixing of the triplet state with a singlet configuration of the type ${}^1\sigma'\pi^*$, where $\sigma' = \sigma + \delta d_\sigma$. For completeness we note that so far triplet-singlet mixing of $\pi'\pi^*$ configurations was considered. Similar arguments hold of course when decay out of a ${}^3\pi\pi'^*$ configuration is considered. In this case, mixing with ${}^1\pi\sigma'^*$ configurations is relevant for the radiative decay process, where now σ' is an antibonding molecular orbital built from d_σ^* and ligand σ orbitals. However, the energy difference between the metal and ligand orbitals is expected to be larger, due to the large ligand field splitting of the cyclometalating $thpy^-$ ligand, shifting the d_σ^* orbitals to higher energy. The result is reduced mixing of the d_σ^* and ligand σ orbitals.

7.3.2
Rh(TPB)⁺

For this complex cation the zero-phonon emission is peaked at 519.9 nm. The ODMR data showed that the emission is due to an excited triplet state localized on the $thpy^-$ anion [65]. This anion is positioned at the same crystallographic site as the energy trapping site of $Rh(TTB)^+$ [64, 65]. The lifetimes and emissive properties of the triplet sublevels of the $Rh(TPB)^+$ species are very similar to that of $\mathrm{Rh(TTB)^+}$ (see Table 6). It is inferred that the mechanisms for the radiative decay of $\mathrm{Rh(TPB)^+}$ and $\mathrm{Rh(TTB)^+}$ are very much alike. Again SOC mixes triplet and singlet configurations in which metal character is obtained through σ-bonding of the metal d-orbitals and ligand anion orbitals [66].

7.3.3
Rh(PTB)$^+$

Using the molecular axis frame of Fig. 16, the position of the $\mathrm{thpy^-}$ ligand, at which the photoexcitation becomes trapped in the $\mathrm{Rh(PTB)^+}$ complex ion, is marked by the double asterisk. The z axis of this ligand coincides with the y' axis of the complex cation, whereas the x, y axes are rotated by 45° with respect to the complex x', z' axes. As a result, in this cation π'-type molecular orbitals are constructed from metal $\mathrm{d}_{x'y'}$ and $\mathrm{d}_{y'z'}$ orbitals and ligand π orbitals. The SOC mechanism then predicts for $\mathrm{Rh(PTB)^+}$ that singlet configurations of the form $^1(\pi + \delta \mathrm{d}_{\pi})\pi^*$ become mixed only with the T_z triplet state sublevel (see Table 8b, last row). In contrast with $\mathrm{Rh(TTB)^+}$ and $\mathrm{Rh(TPB)^+}$, the experimental result for this sublevel in $\mathrm{Rh(PTB)^+}$ is that its radiative character is no longer negligible and in fact appears to be very similar to that of the T_y level. Thus the difference of the inequivalent $\mathrm{thpy^-}$ sites within the $\mathrm{Rh(TPB)^+}$ cations is not only manifested by a difference in the zero-phonon positions in the respective emission spectra and the values of the zero-field splitting parameters of the triplet states of the two species, but also in the details of the radiative properties of the triplet-state sublevels.

Considerations of spin-orbit induced mixing of $^1(\sigma + \delta \mathrm{d}_{\sigma})\pi^*$ configurations with the excited triplet state configuration yield the prediction that the triplet state T_y level (in the case of a $^3(\mathrm{d}_{y'z'} - \mathrm{d}_{x'y'})\pi^*$ excited configuration) or the T_x level (in the case of a $^3(\mathrm{d}_{y'z'} + \mathrm{d}_{x'y'})\pi^*$ excited configuration) of the $\mathrm{thpy^-}$ ligand should attain emissive character (see also Table 8b). Experimentally, the in-plane T_x level is the strongest radiative level in $\mathrm{Rh(PTB)^+}$, analogous to $\mathrm{Rh(TTB)^+}$ and $\mathrm{Rh(TPB)^+}$. From this we infer that (i) as for $\mathrm{Rh(TTB)^+}$ and $\mathrm{Rh\,(TPB)^+}$, σ-overlap between the central metal d orbitals and the orbitals of the $\mathrm{thpy^-}$ anion, at which the excitation is localized, is of great relevance in determining the SOC-induced radiative properties of the $\mathrm{thpy^-}$ emission of $\mathrm{Rh\,(PTB)^+}$, and (ii) the excited configuration responsible for the $\mathrm{thpy^-}$ localized emission of $\mathrm{Rh(PTB)^+}$ is most likely of the form $^3(\pi + \delta(\mathrm{d}_{y'z'} + \mathrm{d}_{x'y'}))\pi^*$. As noted before, for $\mathrm{Rh(PTB)^+}$ the emissive decay from the T_z sublevel cannot be ignored. This probably shows that for this complex SOC with $^1(\pi + \delta \mathrm{d}_{\pi})\pi^*$ is more important than in the case of $\mathrm{Rh(TTB)^+}$ and $\mathrm{Rh(TPB)^+}$.

7.3.4
Discussion

To account for the radiative properties of the triplet state sublevels of the $\mathrm{Rh(TTB)^+}$, $\mathrm{Rh(TPB)^+}$, and $\mathrm{Rh(PTB)^+}$ complexes we have discussed above that SOC-induced mixing with $^1\sigma'\pi^*$-type configurations plays an important role, whereas for the $\mathrm{Rh^{3+}}$ tris-diimine triplet states mixing with $^1(\pi_\mathrm{L} + \delta \mathrm{d}_{\pi})\pi^*$ configurations is prevalent. The kinetic data of Table 6 illustrate the sensitivity of emissive kinetics to the replacement of one or more of the chelating ligands. The influence of ligand substitution in metal complexes has been discussed to some extent in the literature [31, 68, 78, 79]. The results of the ODMR experiments give complementary information in the following way. First, we consider the characteristics of the molecular orbital scheme of Fig. 17a, applicable in the case of pseudo-octahedral complexes like $\mathrm{Rh(bpy)_3^{3+}}$ and $\mathrm{Rh(phen)_3{}^{3+}}$. Levels 1 and 1′ represent the σ-bonding and anti-bonding molecular orbitals derived from the metal ion e_g-type d orbitals and ligand σ-type orbitals, 2 and 2′ denote the levels resulting from the π-type overlap between the t_{2g}-type d-orbitals and the π-orbitals of the ligand molecules, and finally 3 and 4 contain the blocks of ligand π- and π^*-orbitals that are non-bonding. In this scheme, $\sigma\pi^*$-type and $\pi\pi^*$-type excitations are energetically quite different and thus SOC-induced mixing of $^1\sigma\pi^*$-type configurations with $^3\pi\pi^*$-type configurations will be negligible on account of the large denominator in Eq. (11). On the other hand, mixing of $^3\pi\pi^*$-type configurations with close-lying excitations of the type $^1(\pi + \delta \mathrm{d}_\pi)\pi^*$, where the $(\pi + \delta \mathrm{d}_\pi)$ orbital belongs to block 2, are quite significant. This will result in a radiative out-of-plane T_z triplet sublevel, as is confirmed by the ODMR measurements.

It is noted that the proposed SOC effects discussed here are different from the mixing scheme discussed by Komada et al. [18]. The latter authors consider mixing between $^3\pi\pi^*$ and $^1\mathrm{d}\pi^*$ involving two-center integrals on Rh. As indicated by Azumi and Miki [31], the magnitude of this mixing is smaller than the mixing with ligand localized $^1\sigma\pi^*$ or $^1\mathrm{n}\pi^*$ excitations that give rise to the long lifetime of the triplet state in the free ligand. Furthermore, the mechanism proposed by Komada et al. [18] requires two center integrals for the optical transition moment and these are expected to be much smaller than the ligand localized one center integrals.

In $\mathrm{Rh(TTB)^+}$, $\mathrm{Rh(TPB)^+}$, and $\mathrm{Rh(PTB)^+}$, where, compared to the aforementioned tris-diimine complexes, two diimine ligand molecules have been replaced by cyclometalating ligands, the substitutional ligands have a stronger covalency of the metal-carbon σ-bond than the metal-nitrogen σ-bond. For the ordering of the levels in the scheme of Fig. 17 this implies that effectively the energies of the metal d-orbitals and the ligand σ-orbitals are much closer to each other than in the case of the tri-diimine complexes. This is reflected in Fig. 17b. Excitations like $^1(\pi + \delta \mathrm{d}_\pi)\pi^*$ (derived from a 2 → 4 excitation) or $^1(\sigma + \delta \mathrm{d}_\sigma)\pi^*$ (derived from 1 → 4 excitation) are SOC-mixed with the $^3\pi\pi^*$ excitation representative of the lowest triplet state. It is quite possible that the excitation energy for the $^1(\sigma + \delta \mathrm{d}_\sigma)\pi^*$ configuration is well below that for the $^1(\pi + \delta \mathrm{d}_\pi)\pi^*$ excitation and this offers the explanation for the radiative properties of the mixed cyclometalated Rh-complexes.

In conclusion, the emissive properties of the lowest excited triplet state of the $\mathrm{Rh^{3+}}$ complexes are mainly determined by the heavy atom effect. The SOC mechanism mixes $^1(\pi + \delta \mathrm{d}_\pi)\pi^*$ (in the case of $\mathrm{Rh(bpy)_3^{3+}}$ and $\mathrm{Rh(phen)_3{}^{3+}}$) and $^1(\sigma + \delta \mathrm{d}_\sigma)\pi^*$ (in the case of $\mathrm{Rh(TTB)^+}$, $\mathrm{Rh(TPB)^+}$, and $\mathrm{Rh(PTB)^+}$) configurations. Of course, the admixed d-orbital character implies charge transfer (CT) character of the ligand-localized $^3\pi\pi^*$ excited state. Assuming comparable

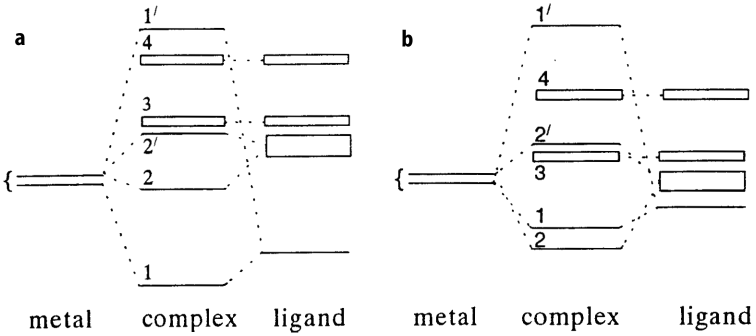

Fig. 17a, b. **a** General picture for orbital ordering in trisdiimine complexes (with each ligand coordinated to central metal ion by a pair of N atoms. **b** Level scheme for cyclometalated complexes (with coordination of metal ion to one C atom and one N atom per ligand)

denominators in Eq. (11), when comparing the cyclometalating complexes and the trisdiimine complexes, a stronger d_σ–σ overlap (in the cyclometalating complexes) than d_π–π overlap (in the trisdiimine complexes) thus leads to stronger CT character in the excited triplet state of the cyclometalating complexes.

7.4
Optically Detected Spin Coherence

Optically detected spin echo decay measurements have been performed for the $|D|-|E|$ transitions in the lowest triplet state of $Rh(TTB)^+$, $Rh(TPB)^+$, and $Rh(PTB)^+$ as well as the $2|E|$ transition of $Rh(TTB)^+$ [67]. The transients obtained at 1.4 K are shown in Fig. 18. The measured transients are monoexponentially decaying with characteristic decay times representative of the phase memory time, T_M. The experimental results for T_M, together with the corresponding homogeneous line width of the zero-field ODMR transition, $\Gamma_h = (\pi T_M)^{-1}$, are given in Table 4. For comparison, the dephasing times for $Rh(bpy)_3^{3+}$ and $Rh(phen)_3^{3+}$ have been included. Compared to the inhomogeneous line widths of 15–45 MHz of the zero-field ODMR transitions, the homogeneous line widths (~100 kHz) are about two orders of magnitude less. The spin dephasing times, on the other hand, are orders of magnitude shorter than the lifetimes of the triplet sublevels, so homogeneous line broadening is due to pure dephasing processes (see Sect. 4.1). Most likely, for the metal complexes this dephasing has its origin in hyperfine couplings of the electron triplet spin moment to proton spins in the ligand molecule. Random flipping of nuclear spins near the electron spin will cause changes in the local field felt by the latter, thus resulting in a variation of its precessional frequency and a loss of phase coherence in the ensemble. This mechanism is supported by the behavior of the spin echo decay in a small magnetic field. Fields up to about 20 G could be applied; at higher field strengths the S/N for the echo signal became too small for reliable results. In a magnetic field, the spin dephasing is faster, i.e., homogeneous broadening is increased. Typically, the dephasing times decreased from about 3.2 μs at zero magnetic field to

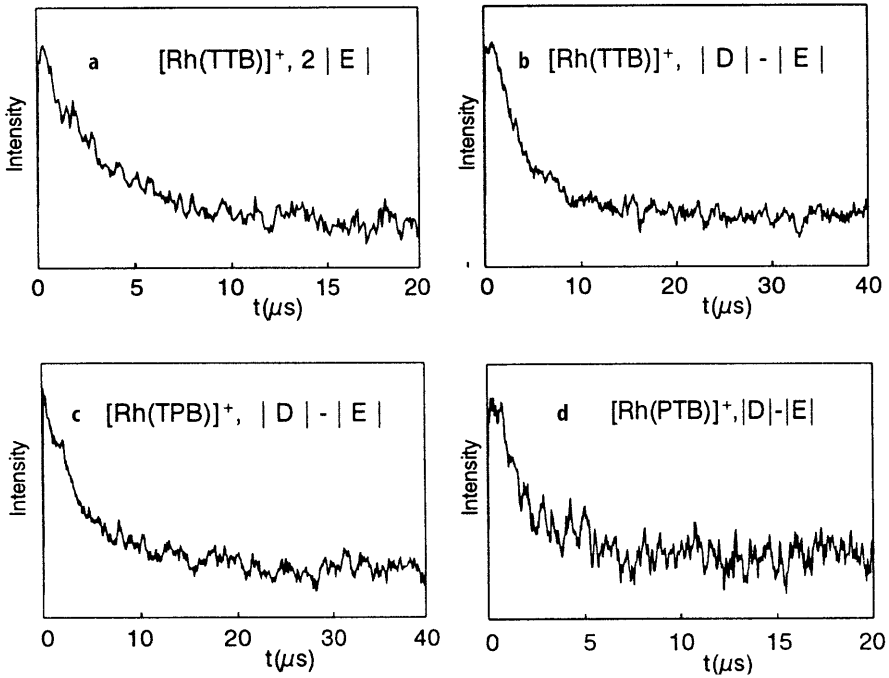

Fig. 18a–d. Optically detected spin echo decay curves in zero magnetic field for: **a** the 2 $|E|$ transition at 1725 MHz of [Rh(thpy)$_2$(bpy)]$^+$; **b** the $|D|-|E|$ transition at 2580 MHz of [Rh(thpy)$_2$(bpy)]$^+$; **c** the $|D|-|E|$ transition at 3970 MHz of [Rh(thpy)(phpy)(bpy)]$^+$; **d** the $|D|-|E|$ transition at 1485 MHz of [Rh(phpy)(thpy)(bpy)]

about 1.0 μs in a field of 20 G. The enhanced dephasing rate in a magnetic field is typical of the proposed dephasing mechanism. Note that in zero magnetic field the magnetic moment of the triplet spin is quenched ($\langle S_i \rangle = 0, i = x, y,$ or z). It follows that hyperfine interactions, $\vec{S}\vec{I}$, are quenched in first order as well and can be effective only in second order. When a magnetic field is applied, however, the triplet spin quenching is partially lifted and hyperfine interactions with flipping nuclear spins now also contribute in first order to the dephasing process. No anisotropy for the dephasing dynamics was measured in a magnetic field. Probably isotropic hyperfine interactions are dominant for the dephasing interactions. Isotropic hyperfine interactions arise from σ-type molecular orbital character mixed into the π-orbitals forming the $^3\pi\pi^*$ configuration [27]. As discussed before, in the case of Rh(TTB)$^+$, Rh(TPB)$^+$, and Rh(PTB)$^+$, $^1(\sigma + \delta d_\sigma)\pi^*$ configurations are mixed into the $^3\pi\pi^*$ state, thus increasing the magnitude of the isotropic hyperfine interactions. In the case of Rh(bpy)$_3^{3+}$ and Rh(phen)$_3^{3+}$, the $^3\pi\pi^*$ state is primarily mixed with $^1(\pi + \delta d_\pi)\pi^*$-type configurations. We expect therefore much smaller isotropic interactions in the lowest triplet state of the latter two compounds and this may be the reason why for Rh(bpy)$_3^{3+}$ and Rh(phen)$_3^{3+}$ in the lowest triplet state the enhancement of the spin echo decay rate in a magnetic field remained unobserved.

8
Pd^{2+}-Chelates

8.1
Introduction

In addition to the ODMR investigations of $Rh^{3+}(4d^6)$-chelates, recently similar studies have been performed for the $Pd^{2+}(4d^8)$-complexes, $Pd(thpy)_2$ and $Pd(qol)_2$ (with $qol^- = $ 8-hydroxyquinolinate) [80, 81]. Optical investigations of $Pd(thpy)_2$ (with $(thpy)^-$: 2,2′-thienylpyridinate, see Fig. 1) doped into an *n*-octane Shpol'skii matrix revealed highly resolved emission spectra and showed that the phosphorescent triplet state decays with three lifetime components of $\tau_I = 1200$ µs, $\tau_{II} = 235$ µs, and $\tau_{III} = 130$ µs characteristic of the triplet state sublevels [82–84]. The emission data of $Pd(qol)_2$ in an *n*-octane Shpol'skii matrix have been reported recently [81, 85]. Two distinct emissive sites in the matrix were found, with electronic origins at 16,090 cm^{-1} (77%) and 16,167 cm^{-1} (23%), respectively. From the Zeeman splittings of the optical line transitions in magnetic fields up to 12 T, the emission for the two sites was assigned as $T_1 \rightarrow S_0$.

8.2
ODMR of $Pd(thpy)_2$

Although the fine structure splitting, being characteristic of the triplet state of $Pd(thpy)_2$, remained unresolved in the high-resolution emission spectrum, an upper limit of about 1 cm^{-1} could be given. Furthermore, time-resolved phosphorescence spectra displayed different time dependences for the vibrational satellites in the high-resolution emission spectra [83]. This result shows a disparity in the emissive properties of the triplet state sublevels. It was suggested that optical detection of magnetic resonance in the excited triplet state of the $Pd(thpy)_2$ complex might be successful. Indeed, the triplet spin nature of the emissive excited state could be confirmed by means of zero-magnetic field ODMR, optically detected EPR (electron paramagnetic resonance) in the presence of small magnetic fields, and pulsed microwave recovery experiments [80].

Figure 19 shows the zero-field ODMR spectrum for $Pd(thpy)_2$ detected at the electronic origin of the emission spectrum at 18,418 cm^{-1} (542.95 nm). The microwave frequency corresponding to the peak of the signal is found at 2886 MHz; the signal line width is 20 MHz (FWHM). In the frequency range from 300 MHz up to 8000 MHz no other zero-field ODMR signal could be observed. The ODMR transition of Fig. 19a is likely to be characteristic of one of the three possible microwave transitions of the excited triplet state. Assuming two zero-field splitting parameters, *D* and *E*, several possibilities may be considered to account for the absence of the other transitions between the three sublevels in the zero-field ODMR spectrum [86]: (i) the resonance frequencies of the other transitions are outside the microwave range that was experimentally accessible to us (up to 8000 MHz), (ii) the disparity in the radiative decay rates of the resonantly coupled spin states is too small to make ODMR observable, and

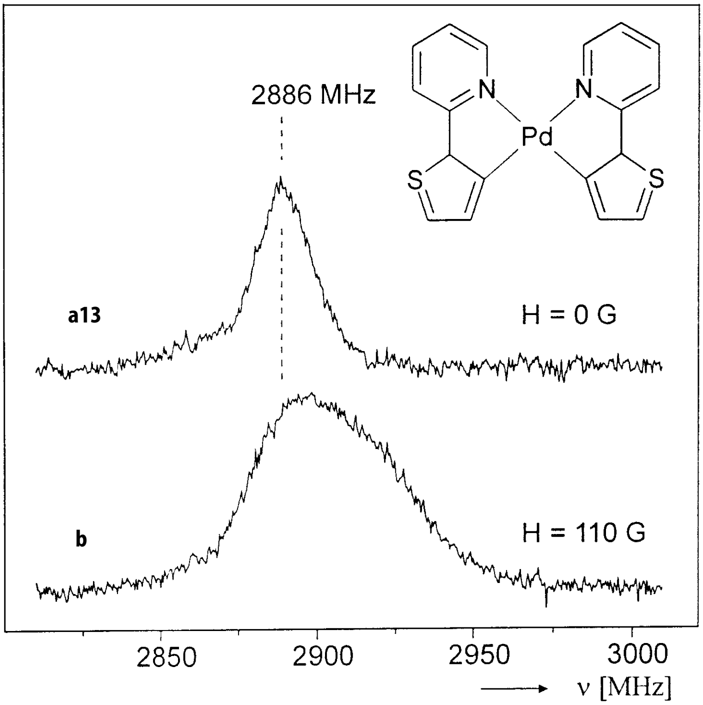

Fig. 19 a, b. **a** Zero-field ODMR spectrum of Pd(thpy)$_2$ in an *n*-octane Shpol'skii matrix. Excitation at 330 nm, detection at 542.9 nm, T = 1.4 K. **b** ODMR spectrum of the same system in a magnetic field with $H = 110$ G

(iii) the population differences among the triplet state sublevels are too small to allow for ODMR detection. In addition to the normal zero-field ODMR experiment, an optically detected EEDOR (electron-electron double resonance [86]) was also attempted. In this experiment, a second microwave source connected to a second helix was used. The frequency of this second microwave source was swept over the range from 300 MHz up to 8000 MHz, while the frequency of the first microwave source was kept constant at the resonance frequency of 2886 MHz. In zero-field, no additional lines could be observed in the EEDOR experiment for photo-excited Pd(thpy)$_2$. It is concluded that the other zero-field ODMR transitions are well outside the microwave frequency range applied.

In the presence of small magnetic fields (< 400 G) in the normal ODMR experiment, the ODMR signal showed a Zeeman shift as illustrated in Fig. 19b. In addition to the slight shift of the maximum of the ODMR signal by approximately 10 MHz, the ODMR transition is broadened and asymmetrically shaped. When the magnetic field is higher than about 400 G, the ODMR signal becomes too broad (FWHM > 600 MHz) and the signal intensity too weak to allow for ODMR studies at these higher field strengths.

As discussed by McCauley et al. [87, 88] for a triplet state with $D \geq 3E > 0$ in the low-field limit, the ODMR transition in the triplet state measured for a sample of randomly oriented molecules would show a positive frequency shift (with respect to the zero-field case) for the $2E$ and $D+E$ transitions and a negative shift for the D–E transition. Moreover, the $2E$ transition is expected to have its steepest rise on the low-frequency side and a larger broadening on the high-frequency wing which leads to an asymmetric transition. The experimental result of Fig. 19b is thus suggestive of a $2E$ transition and a D being larger than $3E$. Numerical analysis of the Zeeman shifts [80] showed that best fits to the experimental data were obtained for the spin Hamiltonian parameter values: $|D| \geq 6600$ MHz and $|E| = 1443$ MHz, and $g \approx 2$. These values for the fine structure parameters are significantly larger than the values of $D = 3440$ MHz and $E = 865$ MHz given before for $[Rh(thpy)_2(bpy)]^+$ and $D = 4805$ MHz and $E = 835$ MHz for $[Rh(thpy)(phpy)(bpy)]^+$, respectively (Table 5). In the case of the mixed-chelate Rh(III) complexes, it was discussed in Sect. 7.2 that the triplet state is mainly of $^3\pi\pi^*$ character with the triplet state excitation localized on one of the $(thpy)^-$ ligands. However, in contrast to the results obtained for the mixed-chelate rhodium (III) complexes, for the $Pd(thpy)_2$ compound little further experimental detail can be given as regards the orientation of its magnetic main axes because for this compound no single crystal experiments could be performed and consequently every information of the orientation of the magnetic axes in the molecule is lost. The larger fine structure parameter values reported here for the excited triplet state of $Pd(thpy)_2$ as compared to those for the Rh(III)-chelates must be attributed to the influence of the transition metal ion. In particular, in the case of the Pd(II)-complex, spin-orbit interactions are more important in determining the magnitude of the fine structure splittings than in the case of the Rh(III)-complex. A similar conclusion has also been drawn from a comparison of highly resolved emission and excitation spectra of $[Rh(bpy)_3]^{3+}$ and $Pd(thpy)_2$. The importance of metal d-orbital character, which carries spin-orbit coupling, is more expressed in $Pd(thpy)_2$ (compare [82–84, 89, 90]). Equivalent conclusions have also been drawn by Chen et al. [91] who studied the phosphorescent state of palladium phthalocyanines (PdPcs) in Shpol'skii matrices. The zero-field splitting for the PdPc molecules in the triplet state (which could not be resolved in the optical experiments) was estimated to be as large as $D \approx 2$ cm^{-1} (60 GHz) and $E \approx 0$.

Applying a microwave pulse resonant with the zero-field transition at 2886 MHz while continuous wave optical excitation of the $Pd(thpy)_2$ complex yielded the microwave recovery signal shown in Fig. 20. The transient fits a bi-exponential function; see Eq. (18), with $\tau_a\ (=1/k_a) = 134 \pm 6$ µs, $\tau_b\ (=1/k_b) = 1200 \pm 50$ µs, $A = 0.05$, and $B = -0.02$. These values are in excellent agreement with the previously reported lifetimes determined in the high-resolution optical experiments [83]. The third lifetime-component of 235 µs found in the latter experiments is thus not displayed in the microwave recovery signal. This tells us that the 2886 MHz microwave is resonant with the triplet sublevels $|I\rangle$ (long living state) and $|III\rangle$ (short living state) of the nomenclature of [83], while sublevel $|II\rangle$ is not involved in the microwave resonance experiment.

Interestingly, the time-resolved and highly resolved emission spectra [83] show that, in particular, these triplet sublevels exhibit very different emission spectra with respect to their vibrational satellite structures. The long living state

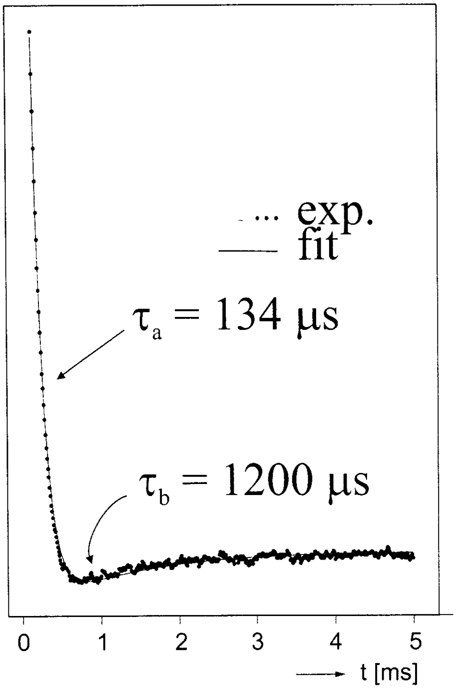

Fig. 20. Optically detected microwave recovery of Pd(thpy)$_2$ in an *n*-octane Shpol'skii matrix at the zero field transition frequency 2886 MHz. Best fit is to $f(t) = A \exp(-t/\tau_a) + B \exp(-t/\tau_b)$, $A = 0.05$, $B = -0.02$, $\tau_a = 134$ μs, $\tau_b = 1200$ μs

$|\mathrm{I}\rangle$ is mainly vibronically (Herzberg-Teller, HT) deactivated, while the emission from state $|\mathrm{III}\rangle$ is dominated by vibrational satellites due to Franck-Condon (FC) activities, whereby both types of vibrational modes exhibit different frequencies. This behavior makes it attractive to measure a phosphorescence microwave double resonance (PMDR) spectrum. In this case the intensity change of the emission induced by the microwave resonance at 2886 MHz, involving the two triplet spin levels $|\mathrm{I}\rangle$ and $|\mathrm{III}\rangle$, is measured. The PMDR spectrum reveals interesting intensity changes (Fig. 21). By means of signal averaging detection it could be determined that, for example, the negative sign of the 229, 261, 528, and 710 cm^{-1} vibrational satellites in the PMDR spectrum corresponds to an emission intensity decrease upon inducing the microwave transition, while the positive signs at the electronic origin and the 211, 376, 447, 650, and 716 cm^{-1} satellites are connected to intensity increases. Previous time-resolved optical measurements of the emission spectrum of Pd(thpy)$_2$ have shown that, for example, the 528 cm^{-1} satellite (which results from HT-activity) originates *only* from the longest living triplet spin sublevel state $|\mathrm{I}\rangle$ with the lifetime of 1200 μs) [83]. From the observation of this microwave-induced intensity decrease of the 528 cm^{-1} satellite in the emission spectrum it follows therefore that, under continuous wave optical excitation, the steady-state population of the triplet sub-

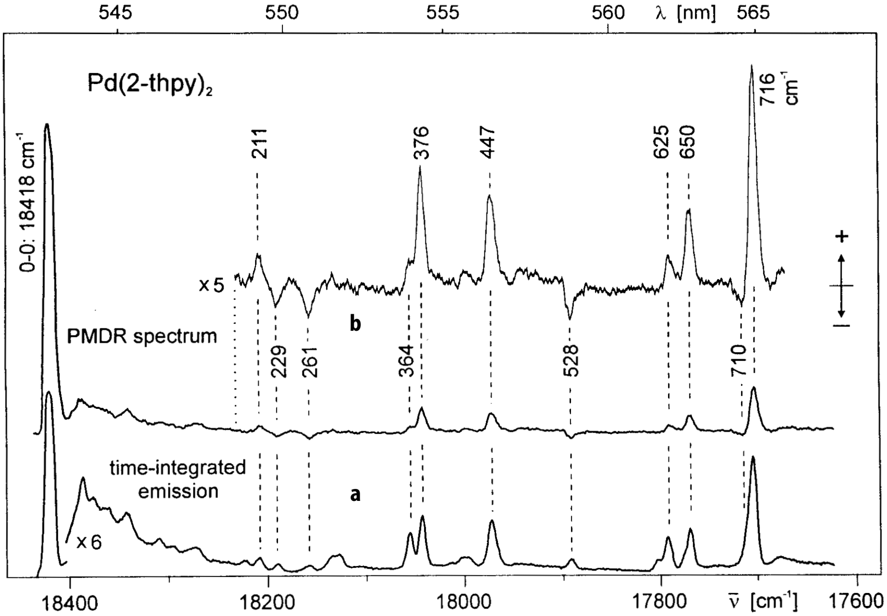

Fig. 21a,b. **a** Time-integrated emission spectrum of Pd(thpy)$_2$ in an *n*-octane Shpol'skii matrix at 1.4 K. **b** PMDR spectrum for zero-field ODMR transition at 2886 MHz. (+) is microwave-induced intensity increase of the emission from the short-lived triplet sublevel III, (−) is microwave-induced intensity decrease of the emission from the long-lived sublevel I

state with the lifetime of 1200 µs is larger than for the substate with a lifetime of 134 µs. Since the population of the level $|III\rangle$ with a lifetime of 134 µs is enhanced in the microwave recovery experiment, we conclude that the modes at 376, 447, 650, and 716 cm^{-1} are more strongly coupled to the triplet sublevel $|III\rangle$.

8.3
ODMR of Pd(qol)$_2$

Pd(qol)$_2$ is another Pd^{2+}(4d^8)-complex in a Shpol'skii matrix for which the lowest excited triplet state could be studied by ODMR [81]. Figure 22 shows the zero-field ODMR spectra as detected at the two electronic origins for the two sites of Pd(qol)$_2$ in the *n*-octane matrix.

For each of the two sites, labeled "1" and "2" respectively, two zero-field ODMR transitions could be observed. The resonance frequencies for these transitions are given in Table 9. Conversely, the emission spectrum belonging to each of the ODMR transitions was also measured in a phosphorescence microwave double resonance (PMDR) experiment. The PMDR spectra obtained for the two resonances at 2356 MHz and 2329 MHz, as well as the normal emission spectrum, are presented in Fig. 23. As illustrated in the figure, in PMDR one can separate the emission spectra for sites 1 and 2 in the matrix. Table 9 summarizes the main optical, ODMR, and PMDR results.

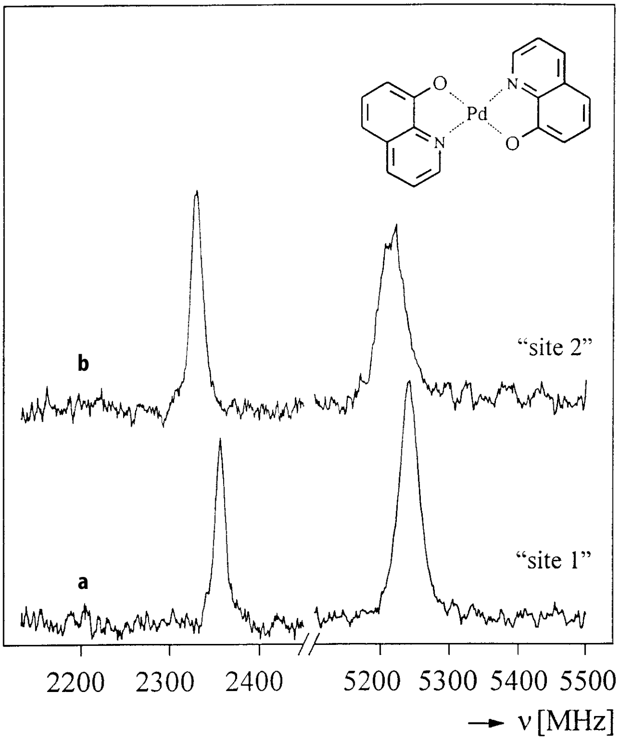

Fig. 22a,b. Zero-field ODMR spectrum of Pd(qol)$_2$, in an *n*-octane Shpol'skii matrix, in the excited triplet state. Excitation at 457 nm, T = 1.4 K, for: **a** site "1", detection wavelength 621.5 nm (16090 cm^{-1}); **b** site "2", detection wavelength 618.7 nm (16167 cm^{-1})

Table 9. Emission, ODMR line positions and triplet state sublevel lifetimes of Pd(qol)$_2$ in Shpol'skii matrix at 1.4 K. Ratio of zero-phonon line intensities for sites "1" and "2" is given in brackets

	Zero-phonon emission (cm^{-1})	2 *E* (MHz) ($\varepsilon_{III}-\varepsilon_I$)	*D*-*E* (MHz) ($\varepsilon_I-\varepsilon_{II}$)	Lifetimes triplet substates (ms)		
				I	II	III
Site "1"	16090 (77%)	2356	5240	90	0.180	0.080
Site "2"	16167 (23%)	2329	5220	80	0.180	0.100

We note that the transition frequencies of 2356 MHz and 2329 MHz of the zero-field signals for Pd(qol)$_2$ are comparable in magnitude to the 2886 MHz transition in Pd(thpy)$_2$. This suggests therefore that the observed two transitions at the lower microwave frequencies correspond to the 2*E* transition of sites "1" and "2" of Pd(qol)$_2$, respectively. This is further substantiated by the behavior of these transitions in small magnetic fields (< 400 G). As the magnetic field strength is increased, the ODMR signals are shifted, broadened, and rapidly

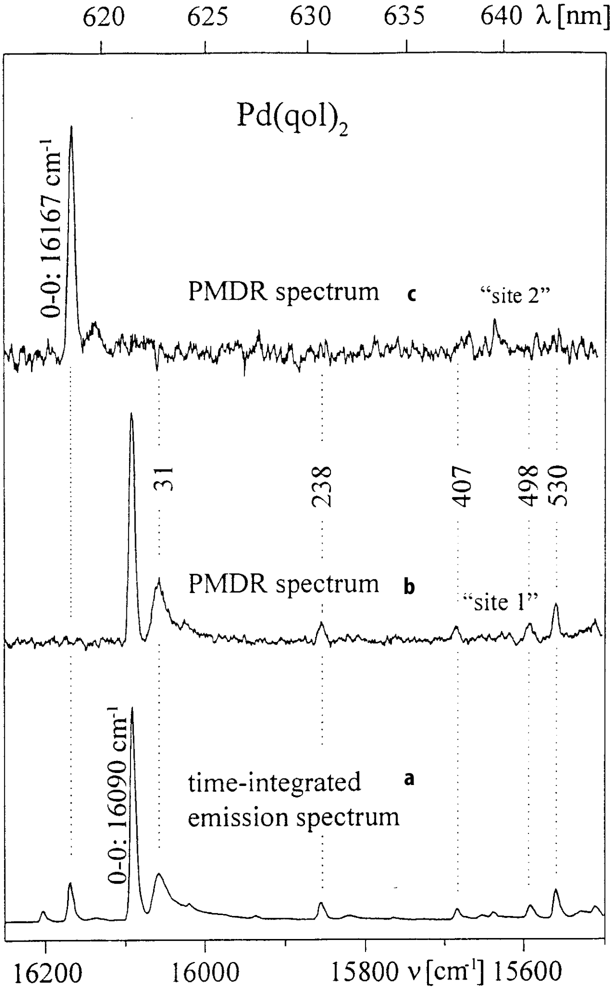

Fig. 23a, b. **a** Time-integrated emission spectrum of Pd(qol)$_2$ in *n*-octane at $T = 1.4$ K. Excitation is at 457 nm. **b** PMDR spectrum for zero-field microwave transition at 2356 MHz of site "1". **c** PMDR spectrum for zero-field microwave transition at 2329 MHz of site "2"

decreased in intensity. At fields higher than about 400 G, the signals became too weak to be observed. In Fig. 24a we show typical ODMR data for the low- and high-frequency ODMR transitions of site "1" for a few magnetic field strengths. The results in a magnetic field are compatible with the limiting case that $D \geq 3E > 0$. We thus assign the zero-field ODMR transitions at 2356 MHz and 5240 MHz to the $2E$ and $D-E$ triplet spin transitions, respectively. We conclude for site "1" that $D = 6418$ MHz and $E = 1178$ MHz. Since the ODMR spectra were obtained for an ensemble of randomly oriented molecules in the triplet state, further specification of the orientation of the magnetic axes within the Pd(qol)$_2$ molecule cannot be given.

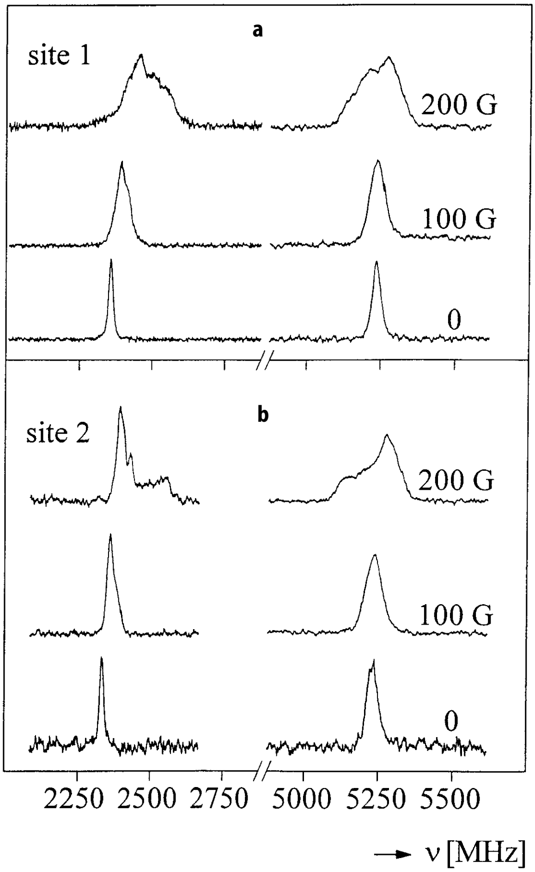

Fig. 24a,b. ODMR spectra of Pd(qol)$_2$ under the influence of small applied magnetic fields. Field strengths are as indicated; **a** spectrum of site "1"; **b** spectrum of site "2"

The ODMR results obtained for site "2" are similar. As illustrated in Fig. 24b, the low-frequency transition at 2329 MHz is shifted to higher frequencies as the magnetic field strength is increased. Furthermore, the resonance has its steepest rise on the low-frequency side and a larger broadening at the high-frequency side as expected for the magnetic field effect on a $2E$ transition [87, 88]. In a magnetic field, the maximum of the high-frequency zero-field signal for site "2" at 5220 MHz shows a positive shift, whereas the broadening is at the low-frequency wing in accordance with the behavior expected for the $D-E$ transition in the low-field limit in case $D \geq 3E > 0$. We conclude for site "2" that $D = 6385$ MHz and $E = 1165$ MHz.

For both sites, "1" and "2", one expects that the $D+E$ transition is at a frequency near 7570 MHz. Experimentally, however, no ODMR signal near that frequency could be measured. Alternatively, it was attempted to measure the $D+E$ transition in an optically detected EEDOR experiment; still no additional signal was observed.

The zero-field splitting parameters for the phosphorescent triplet state of site "1" of $Pd(qol)_2$ are comparable to those for $Pd(thpy)_2$; the latter has $D \geq 6600$ MHz and $E = 1443$ MHz [80]. On the other hand, compared to the Rh^{3+}-chelates, with zero-field splittings of $D \cong 3000-4000$ MHz and $E \cong 800-900$ MHz, the zero-field splitting parameter values for the Pd-complexes are significantly higher. Recently, the emissive state of $Pd(qol)_2$ has been discussed to be of intraligand charge transfer character [92]. Although the dominant part of the HOMO and LUMO orbitals in $Pd(qol)_2$ is of π-type, a fractional part of this orbital may be of central atom *d*-orbital character. Because of second order SOC, this will be of influence on the magnitude of the zero-field splittings in the excited triplet state. Spin-orbit coupling is stronger for Pd than for Rh, hence the Pd-complexes will show larger zero-field splittings.

The lifetimes of the sublevels of $Pd(qol)_2$ in the emissive triplet state were determined by means of microwave recovery experiments. At 1.4 K, the triplet state sublevels are thermally isolated from each other, and the individual lifetimes of the microwave-pumped spin levels are reflected in the biexponential kinetics of the recovery signal [81]. Figure 25 shows a typical transient, probed for the $D-E$ transitions for site "1". Labeling the triplet substates as $|I\rangle$, $|II\rangle$, and $|III\rangle$, such that $\varepsilon_{III} > \varepsilon_I > \varepsilon_{II} > 0$ (i.e., $2E = \varepsilon_{III} - \varepsilon_I$, $D-E = \varepsilon_I - e_{II}$), the sublevel lifetimes as determined for site "1" from the fits are $\tau_I = 90$ ms, $\tau_{II} = 180$ µs, and $\varepsilon_{III} = 80$ µs. These results are in very good agreement with the triplet sublevel lifetimes as determined from phosphorescence decay measurements [85]. Likewise, for site

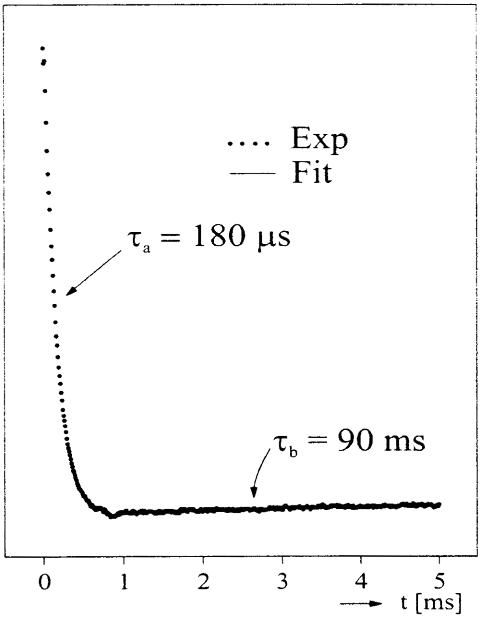

Fig. 25. Zero-field microwave recovery signal for the $|D|-|E|$ transition at 5240 MHz for $Pd(qol)_2$ in a Shpol'skii matrix at 1.4 K. The drawn curve is a fit to $f(t) = A\ \exp(-t/\tau_A) + B\ \exp(-t/\tau_B)$, $A = 6.3$, $B = -0.2$, $\tau_A = 180$ µs, $\tau_B = 90$ ms

"2", $\tau_{\mathrm{I}}=80$ ms, $\tau_{\mathrm{II}}=180$ µs, and $\tau_{\mathrm{III}}=100$ µs, has been obtained. Recall that the $D+E$ zero-field ODMR transition remained unobserved. Thus from the time-resolved experiments it follows that this transition is between the triplet state sublevels with the shortest lifetimes. In this respect the situation is similar to $\mathrm{Pd(thpy)_2}$ in the phosphorescent triplet state. For $\mathrm{Pd(thpy)_2}$ the resonance between the sublevels with lifetimes of 134 µs and 235 µs remained unobserved in zero-field ODMR [80]. Most likely, the two sublevels with the shortest lifetimes show little population difference and therefore this will largely affect the detectability of the ODMR transition between them.

9
Concluding Remarks

We have discussed that optical magnetic double resonance methods are very powerful in unraveling the details of the energetic splittings, the kinetics, and the radiative properties of the spin sublevels of the lowest excited triplet state in a series of $\mathrm{Rh^{3+}}$ and $\mathrm{Pd^{2+}}$ chelates. The zero- and low-magnetic field ODMR results show that for the $\mathrm{Rh^{3+}}$ and $\mathrm{Pd^{2+}}$ complex molecules, doped in a single crystal or Shpol'skii matrix, the excited triplet state excitation is localized at a single ligand site only, even in the cases of $\mathrm{Rh(phen)^{3+}}$ and $\mathrm{Rh(bpy)^{3+}}$. For the latter complexes the excitation localization is due to the influence of the crystal environment. The problem of localization or delocalization of the excited state excitation in metal complexes has been extensively discussed in the literature [17a, 89, 93, 94]. The ligand-localized excitations reported here are typical of metal complexes with relatively small spin-orbit coupling effects.

Time-resolved ODMR experiments yield the information about the radiative character of the triplet state sublevels. Whereas for the discussed $\mathrm{Rh^{3+}}$ and $\mathrm{Pd^{2+}}$ complexes there is little influence of the metal ions on the magnitude of the fine structure splittings in the triplet states (the fine structure splittings in the complexes and the free ligand molecules are found to be comparable), there is a significant influence of the metal ions on the lifetimes of the triplet spin sublevels: in the complexes these are three orders of magnitude shorter than for the free ligand molecules. The influence of spin-orbit couplings from the metal ion in the complexes on the radiative properties of the triplet state sublevels has been considered in some detail. In a molecular-orbital approach for the $\mathrm{Rh^{3+}}$-trisdiimine complexes it appears that π-bonding between the metal d-orbitals and ligand π-orbitals is important in explaining the radiative properties, whereas for the cyclometalated $\mathrm{Rh^{3+}}$-complexes σ-bonding between the metal d-orbitals and ligand orbitals is important for understanding the radiative decay process. This is a consequence of the stronger bonding in the cyclometalated complexes as compared to the trisdiimine chelates. Another conclusion from the effect of the mixing of the metal ion d-orbitals and the ligand π- or σ-orbitals is that these effects are a manifestation of MLCT and apparently only the radiative properties of the $\mathrm{Rh^{3+}}$-complexes reflect MLCT effects. Optically detected spin coherence measurements for a few $\mathrm{Rh^{3+}}$ complexes have also been reviewed. These experiments allow the determination of the homogeneous line widths and spin dephasing kinetics of the spin transitions in the excited triplet state in zero field. It is found that the time scale of the spin dephasing dynamics in the metal chelates and cyclometalating complexes is very similar to that for the free ligand molecules in the phosphorescent triplet state. It is inferred that the homogeneous line width of the spin transitions in the metal complexes is determined by hyperfine interactions of the electron triplet spin with the fluctuating proton spins in the ligand molecule at which the electronic excitation is localized.

For the Pd^{2+}-chelates larger fine structure splittings were observed than for the Rh^{3+} complexes, due to the stronger spin-orbit couplings. The feasibility of measuring ODMR spectra for the Pd^{2+} complexes is found to be limited by the frequency span possible with the ODMR spectrometer. Optical hole-burning and line-narrowing techniques may sometimes be applied to resolve the zero-field splittings in the excited state as was shown for Ir^{3+} complexes [95] and Pt^{2+} complexes [96]. PMDR of the $Pd(thpy)_2$ in the excited triplet state reveals a spin selectivity in the vibrational satellite lines of the emission spectrum. Thus the PMDR method provides distinct information as concerns the vibronic deactivation of the excited triplet state sublevels.

Acknowledgements. I gratefully acknowledge the collaboration with all co-workers quoted in this review. I am especially indebted to Drs Jaco Westra, Claudia Giesbergen, and Werner Humbs, and for technical assistance to Rolf Sitters. The investigations were supported in part by the Council for Chemical Sciences of the Netherlands Organization for Scientific Research (CW-NWO).

10
References

1. For reviews, see: (a) Maestri M, Balzani V, Deuschel-Cornioly C, von Zelewsky A (1992) Adv Photochem 17:1; (b) Kalyanasundaram K (1992) Photochemistry of polypyridine and porphyrin complexes. Academic Press, London; (c) Yersin H (ed) (1994) Electronic and vibronic spectra of transition metal complexes. Top Curr Chem 171, Springer, Berlin Heidelberg New York, vol I; (d) Yersin H (ed) (1997) Electronic and vibronic spectra of transition metal complexes. Top Curr Chem 191, Springer, Berlin Heidelberg New York, vol II; (e) Roundhill DM (1994) Photochemistry and photophysics of metal complexes. Plenum, New York
2. Yin XL, Moss JR (1999) Coord Chem Rev 181:27
3. Tazuke S, Kitamura N, Kim HB (1989) In: Norris JR, Meisel D (eds) Photochemical energy conversion. Elsevier, New York, p 96
4. Nickel U, Chen YH, Schneider S, Silva MI, Burrows HD, Formosinho SJ (1994) J Phys Chem 98:2883
5. O'Regan B, Grätzel M (1991) Nature 353:737
6. Kalyanasundaram K, Grätzel M (1998) Coord Chem Rev 177:347
7. Marfurt J, Zhao W, Walder L (1994) J Chem Soc Chem Commun:p 51b
8. Aoki A, Abe Y, Miyashita T (1999) Langmuir 15:1463
9. Draxler S, Lippitsch ME, Klimant I, Kraus H, Wolfbeis OS (1995) J Phys Chem 99:3162
10. Kneas KA, Xu WY, Demas JN, DeGraff BA (1997) Appl Spectrosc 51:1346
11. Holmlin RE, Yao JA, Barton JK (1999) Inorg Chem 38:174
12. Holmlin RE, Barton JK (1995) Inorg Chem 34:7
13. Vicendo P, Mouysset S, Paillous N (1997) Photochem Photobiol 65:647
14. Lehn JM (1995) Supramolecular chemistry. Verlag Chemie, Weinheim
15. Balzani V, Campagna S, Denti G, Juris A, Serroni S, Venturi M (1998) Account Chem Res 31:26

16. Crosby GA (1983) J Chem Educ 60:791
17. (a) Yersin H, Humbs W, Strasser J (1997) Top Curr Chem 191:153; (b) Riesen H, Krausz ER (1993) Comments Inorg Chem 14:323; (c) Orman LK, Chang YJ, Yabe T, Xu X, Yu SC, Hopkins JB (1989) J Chem Phys 90:1469; (d) Schoonover JR, Strouse GF (1998) Chem Rev 98:1335; (e) Myers AB (1997) J Raman Spectrosc 28:389; (f) Rector KD, Fayer MD (1998) Int Rev Phys Chem 17:261; (g) Lees AJ (1998) Coord Chem Rev 177:3; (h) Bloembergen N (1999) Rev Mod Phys 71:S283; (i) Lian TQ, Bromberg SE, Asplund MC, Yang H, Harris CB (1996) J Phys Chem 100:11,994
18. Komada Y, Yamauchi S, Hirota N (1986) J Phys Chem 90:6425
19. van Oort E, Sitters R, Scheijde JH, Glasbeek M (1987) J Chem Phys 87:2394
20. Kamyshny AL, Suisalu AP, Aslanov LA (1992) Coord Chem Rev 117:1
21. Miki H, Azumi T (1994) J Phys Chem 98:6059
22. Miki H, Kimachi S, Satomi R, Azumi T, Onishi M (1994) Chem Phys Lett 218:563
23. Kimachi S, Satomi R, Miki H, Azumi T, Onishi M (1997) J Phys Chem A 101:345
24. El-Sayed MA (1975) Annu Rev Phys Chem 26:235
25. McGlynn SP, Azumi T, Kinoshita M (1969) Molecular spectroscopy of the triplet state. Prentice-Hall, Englewood Cliffs New York
26. Abragam A, Bleaney B (1970) Electron paramagnetic resonance of transition ions. Clarendon, Oxford
27. Carrington A, McLachlan AD (1967) Introduction to magnetic resonance. Harper, New York
28. van der Waals JH, de Groot MS (1967) In: Zahlan AB The triplet state. Cambridge, New York, p 101
29. El-Sayed MA (1974) In: Lim EC (ed) Excited states. Academic Press, New York, vol 1, p 35
30. Clarke RH (ed) (1982) Triplet state ODMR spectroscopy. Wiley, New York
31. Azumi T, Miki H (1997) In: Yersin H (ed) Electronic and vibronic spectra of transition metal complexes, vol II. Top Curr Chem 191, Springer, Berlin Heidelberg New York, p 1
32. Jones CR, Maki AH, Kearns DR (1973) J Chem Phys 59:873
33. Friedrich J, Metz F, Dörr F (1975) Mol Phys 30:289
34. Saigusa H, Azumi T (1979) J Chem Phys 71:1408
35. Latas KJ, Nishimura AM (1978) J Phys Chem 82:491
36. Tinti DS, El-Sayed MA, Maki AH, Harris CB (1969) Chem Phys Lett 3:343
37. Hoff AJ (1993) Meth Enzymology 227:290
38. van Dorp WG, Schaafsma TJ, Soma M, van der Waals JH (1973) Chem Phys Lett 21:221
39. Personov RI (1983) In: Agranovich VM, Hochstrasser RM (eds) Spectroscopy and excitation dynamics of condensed molecular systems. North-Holland, Amsterdam, p 555
40. Völker S (1989) Ann Rev Phys Chem 40:499
41. Burns MJ, Liu WK, Zewail AH (1983) In: Agranovich VM, Hochstrasser RM (eds) Spectroscopy and excitation dynamics of condensed molecular systems. North-Holland, Amsterdam, p 301
42. Mukamel S (1995) Principles of nonlinear optical spectroscopy. Oxford, New York
43. Plakhotnik T, Donley EA, Wild UP (1997) Annu Rev Phys Chem 48:181
44. Brenner HC (1982) In: Clarke RH (ed) Triplet state ODMR spectroscopy. Wiley, New York, p 185
45. Ernst RR, Bodenhausen G, Wokaun A (1987) Principles of nuclear magnetic resonance in one and two dimensions. Clarendon, Oxford
46. Chan IY (1982) In: Clarke RH (ed) Triplet state ODMR spectroscopy. Wiley, New York, p 1
47. Winscom CJ, Maki AH (1971) Chem Phys Lett 12:264
48. Westra J, Glasbeek M (1991) Chem Phys Lett 180:41
49. Slichter CP (1996) Principles of magnetic resonance. Springer, Berlin Heidelberg New York
50. Westra J (1993) PhD thesis, University of Amsterdam
51. DeArmond MK, Carlin CM (1981) Coord Chem Rev 36:325
52. Carstens DWH, Crosby GA (1970) J Mol Spectry 34:113
53. Zilian A, Maeder U, von Zelewsky A, Güdel HU (1989) J Am Chem Soc 111:3855
54. Maestri M, Sandrini D, Balzani V, Maeder U, von Zelewsky A (1987) Inorg Chem 26:1323

55. Westra J, Glasbeek M (1990) Chem Phys Lett 166:535
56. Westra J, Glasbeek M (1992) J Lumin 53:92
57. Halper W, DeArmond MK (1972) J Lumin 5:225
58. Kiriakidis CE, Westra J, Glasbeek M, Stam CH (unpublished)
59. Humbs W, Yersin H (1996) Inorg Chem 35:2220
60. Yagi M, Schlyer D, Maki AH (1991) Chem Phys 157:209
61. Ikeda S, Yamamoto S, Azumi T, Crosby GA (1992) J Phys Chem 96:6593
62. Oort E van, Glasbeek M (1989) In: Keijzers CP, Reijerse EJ, Schmidt J (eds) Pulsed EPR: a new field of applications. North Holland, Amsterdam p 227
63. Schmidt J, van der Waals JH (1979) In: Kevan L, Schwartz RN (eds) Time domain electron spin resonance. Wiley, New York, p 343
64. Giesbergen CPM, Sitters R, Frei G, Zilian A, Güdel HU, Glasbeek M (1992) Chem Phys Lett 197:451
65. Giesbergen CPM, Terletski C, Frei G, Güdel HU, Glasbeek M (1993) Chem Phys Lett 213:597
66. Giesbergen CPM, Glasbeek M (1993) J Phys Chem 97:9942
67. Giesbergen CPM, Glasbeek M (1994) J Lumin 60/61:853
68. Colombo MG, Hauser A, Güdel HU (1994) In: Yersin H (ed) Electronic and vibronic spectra of transition metal complexes, vol I. Top Curr Chem 171, Springer, Berlin Heidelberg New York, p 143
69. Colombo MG, Brunold TC, Riedener T, Güdel HU, Fortsch M, Bürgi HB (1994) Inorg Chem 33:545
70. Zilian A, Frei G, Güdel HU (1993) Chem Phys 173:513
71. Sandrini D, Maestri M, Balzani V, Maeder U, von Zelewsky A (1988) Inorg Chem 27:2640
72. Frei G, Zilian A, Raselli A, Güdel HU, Bürgi HB (1992) Inorg Chem 31:4766
73. Giesbergen CPM (1995) PhD thesis, University of Amsterdam
74. Zilian A, Güdel HU (1992) Inorg Chem 31:830
75. Glasbeek M, Giesbergen CPM (1996) J Lumin 66/67:236
76. Maestri M, Sandrini D, Balzani V, Maeder U, von Zelewsky A (1987) Inorg Chem 26:1323
77. Barigelletti F, Sandrini D, Maestri M, Balzani V, von Zelewsky A, Chassot L, Jolliet P, Maeder U (1988) Inorg Chem 27:3644
78. Didier P, Ortmans I, Kirsch-De Mesmaeker A, Watts RJ (1993) Inorg Chem 32:5239
79. Brozik JA, Crosby GA (1998) J Phys Chem A 102:45
80. Glasbeek M, Sitters R, van Veldhoven E, von Zelewsky A, Humbs W, Yersin H (1998) Inorg Chem 37:5158
81. Yersin H, Donges D, Nagle JK, Sitters R, Glasbeek M (2000) Inorg Chem 39:770
82. Yersin H, Schützenmeier S, Wiedenhofer H, von Zelewsky A (1993) J Phys Chem 97:13,496
83. Schmidt J, Wiedenhofer H, von Zelewsky A, Yersin H (1995) J Phys Chem 99:226
84. Becker D, Yersin H, von Zelewsky A (1995) Chem Phys Lett 235:490
85. Donges D, Nagle JK, Yersin H (1997) J Lumin 72:658
86. Kuan TS, Tinti DS, El-Sayed MA (1970) Chem Phys Lett 4:507
87. McCauley EM, Lasko CL, Tinti DS (1991) Chem Phys Lett 178:109
88. McCauley EM, Lasko CL, Tinti DS (1992) J Phys Chem 96:1146
89. Yersin H, Humbs W, Strasser J (1997) Coord Chem Rev 159:325
90. Wiedenhofer H, Schützenmeier S, von Zelewsky A, Yersin H (1995) J Phys Chem 99:13,385
91. Chen WH, Riekhoff KE, Voigt EM (1985) Chem Phys 95:123
92. Donges D, Nagle JK, Yersin H (1997) Inorg Chem 36:3040
93. Riesen H, Wallace L, Krausz E (1997) Int Rev Phys Chem 16:291
94. Yersin H, Humbs W (1999) Inorg Chem 38:5820
95. Riesen H, Krausz E (1992) J Luminesc 53:263
96. Yersin H, Trümbach D, Wiedenhofer H (1999) Inorg Chem 38:1411

Luminescent Metal Complexes: Diversity of Excited States

Arnd Vogler, Horst Kunkely

Institut für Anorganische Chemie, Universität Regensburg, 93040 Regensburg, Germany
E-mail: Arnd.Vogler@chemie.uni-regensburg.de

The photoluminescence of metal complexes has attracted much recent interest since it can be utilized for a variety of applications such as optical sensors and LEDs. Moreover, the emission behavior provides a probe for the investigation of photoreactions including artificial photosynthesis. In this review, emitting compounds are classified according to the nature of their excited states: metal-centered, ligand-to-metal charge transfer, metal-to-ligand charge transfer, ligand-to-ligand charge transfer, metal-to-metal charge transfer, ligand-centered (or intraligand), and intraligand charge transfer excited states. Complexes of transition metals (d^n with $n = 0 - 10$), main group metals (s^2), lanthanides and actinides (f^n) are included in our discussion. However, this review does not cover the photoluminescence of metal complexes comprehensively, but illustrates this subject by selected examples. The viewpoint is that of a coordination chemist and not of a spectroscopist. Accordingly, molecular complexes which emit under ambient conditions are preferably chosen.

Keywords. Metal complexes, Luminescence, Excited states

Topics in Current Chemistry, Vol. 213

1
Introduction

The luminescence of metal complexes is a rapidly expanding research field. In 1970 Fleischauer and Fleischauer published the first review on this subject [1]. In the meantime the number of publications has increased considerably. While prior to 1970 isolated observations had been reported, systematic studies have now led to a fairly good understanding of the luminescence properties of metal complexes. The interest in this area is based on various circumstances. Luminescence spectroscopy is an important tool in photochemistry since it provides a deeper insight in excited state processes in general. Of course, the emission behavior of metal complexes is also rather interesting in its own right. In particular, potential applications have attracted much attention. Luminescence spectroscopy is a sensitive analytical method. Emissive metal complexes are now important optical sensors [2–4]. Other uses, e.g., in LED [5] or laser technology have been developed or may be anticipated.

While spectroscopists have uncovered many details of the emissive complexes by using sophisticated techniques and theories, coordination chemists are now utilizing luminescence spectroscopy increasingly in order to characterize their compounds. In this context it seems timely to point out some important features of this subject as viewed by the inorganic chemist. For this purpose qualitative descriptions and simplified models are quite useful to facilitate the comprehension of this matter by the non-spectroscopist.

Emissive metal complexes may be classified by various criteria such as the position of the metal in the periodic table or the valence electron configuration at the metal. While such criteria are quite useful other categories are even more appealing. In the following presentation, metal complexes are arranged according to the type of excited state. This seems to be a suitable unifying concept because irrespective of other properties of complexes excited states of the same nature have much in common.

In a metal complex the metal-ligand bonds are generally polar. The molecular orbitals are then not equally delocalized between metals and ligands but predominantly located at the metal or the ligands. The electronic transitions and excited states are classified according to this localization [6–8]:

- Metal-centered, MC
- Ligand-to-Metal Charge Transfer, LMCT
- Metal-to-Ligand Charge Transfer, MLCT
- Ligand-to-Ligand Charge Transfer, LLCT
- Metal-to-Metal Charge Transfer, MMCT
- Ligand-Centered, LC (or Intraligand, IL)
- Intraligand Charge Transfer, ILCT

The following discussion does not cover the luminescence of metal complexes comprehensively. The different types of excited states are illustrated by selected examples. This choice was guided by the authors' interests. Frequently, our own observations are included to provide competent comments. Since our viewpoint is that of a coordination chemist and not of a spectroscopist, we preferably selected molecular complexes which emit in fluid solution at room temperature. However, when these conditions are not met the emission of solid materials or emission at low temperatures are included, too. The metal complexes are characterized by the following data:

- Compound
- Type of emission (fluorescence, fl and phosphorescence, ph)
- Emission maximum, $\lambda_{\max}$
- Solvent
- Temperature
- Emission quantum yield, ϕ
- Emission lifetime, τ

2
Metal-Centered Excited States

2.1
Mononuclear Complexes

2.1.1
dd States

Typical transition metal complexes with a partially filled d-shell at the metal are characterized by low-energy dd (or ligand field, LF) states [8]. Frequently, these dd states are not luminescent but reactive [9–13]. Ligands are then substituted because LF states are often antibonding with respect to metal-ligand interactions. Nevertheless, a considerable number of transition metal compounds with emissive LF excited states are known. However, in many cases this luminescence appears only at low temperatures. Moreover, spin selection rules are not strictly obeyed, in particular by metals of the second and third transition series. Intersystem crossing is then facilitated and the rate of spin-forbidden emission (phosphorescence) is increased. As a consequence a phosphorescence may also be observed at room temperature.

2.1.1.1
d^1 Metals

Despite the simplicity of the d^1 configuration there is only very little known on the LF luminescence of d^1 complexes. Since the ground state as well as the LF states are spin doublets the emission is a spin-allowed process. Well known is the fluorescence of Ti(III) in sapphire [14] which is used as a near IR laser source [15–18]. A few d^1 complexes have been shown to be fluorescent as molecular systems (Fig. 1) [19, 20]:

$[Mo^VOCl_4(CH_3CN)]^-$ fl. $\lambda_{max} = 950$ nm, CH_3CN, r.t. $\phi = 4.4 \times 10^{-4}$, $\tau = 110$ ns (1)

$Cp_2Nb^{IV}Cl_2$ fl. $\lambda_{max} = 620$ nm, C_2H_5OH, 77 K $\phi \sim 10^{-3}$ (2)

where Cp = Cyclopentadienyl

2.1.1.2
d^2 Metals

The d^2 ions Cr^{4+}, Mn^{5+}, and Fe^{6+} in tetrahedral $[MO_4]^{n-}$ complexes emit from LF states when they are doped into suitable host lattices [21], e.g.,

K_2CrO_4:Fe^{6+} ph. $\lambda_{max} = 1600$ nm, solid, 15 K (3)

The phosphorescence appears as a sharp-line spectrum. Octahedral complexes which contain a d^2 metal of the second and third transition row and two strong

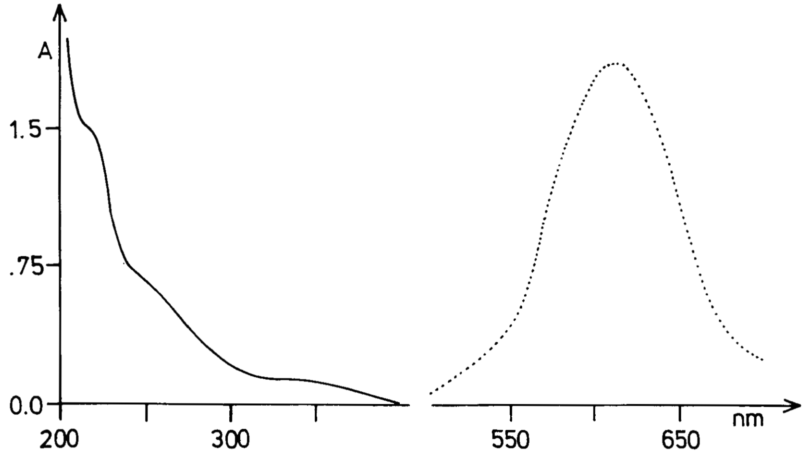

Fig. 1. Electronic absorption (*continuous line*) and emission (*dotted line*) spectrum of Cp_2NbCl_2. Absorption: in CH_3CN, 1.29×10^{-4} mol l^{-1}, at room temperature, 1-cm cell. Emission: in EtOH, at 77 K, $\lambda_{exc} = 350$ nm; intensity in arbitrary units

π-donor ligands, in particular oxide, in a *trans* position are also luminescent [22, 23], e.g.,

$[Re^{V}Cl(N)(dmpe)_2]^+$ ph. $\lambda_{max} = 507$ nm, CH_3CN, r.t. (4)
dmpe = $Me_2P\text{-}CH_2\text{-}CH_2PMe_2$ $\phi = 10^{-3}$, $\tau = 0.36$ µs

$[Os^{VI}O_2(14TMC)]^{2+}$ ph. $\lambda_{max} = 620$ nm, CH_3CN, r.t
$\tau = 1$ µs (5)
14TMC = 1,4,8,11-tetramethyl-1,4,8,11-tetraazacyclotetradecane

2.1.1.3
d^3 Metals

Octahedral chromium(III) complexes are classical examples of emitting d^3 metals [24]. While the ground states are quartets the lowest-energy LF states are either also quartets (with low-field ligands) or doublets (with strong-field ligands). Accordingly, the emission is a fluorescence (e.g., $[CrF_6]^{3-}$, $\lambda_{max} = 779$ nm) [24] or a phosphorescence (e.g., $[Cr(CN)_6]^{3-}$, $\lambda_{max} = 810$ nm) [24, 25]. In some cases both emission types are present simultaneously [24, 26, 27], e.g.,

$[Cr(urea)_6]^{3+}$ fl. $\lambda_{max} = 797$ nm and ph. $\lambda_{max} \sim 703$ nm (6)
glycerin/H_2O, 77 K, $\tau = 68$ µs

Some Cr(III) complexes display an LF emission in fluid solution [24, 28], e.g.,

$[Cr(bipy)_3]^{3+}$ ph. $\lambda_{max} = 727$ nm, H_2O, r.t.
$\phi = 9 \times 10^{-4}$, $\tau = 48$ µs (7)

2.1.1.4
d^4 Metals

The d^4 electron configuration is frequently stabilized by a metal-metal interaction in polynuclear complexes. The luminescence of such clusters will be discussed below. However, d^4 ions in solid matrices are known to emit. For example, octahedral $[\mathrm{Os^{IV}Cl_6}]^{2-}$ in various host lattices shows an LF emission. A NIR → VIS upconversion was achieved with $\mathrm{Os^{4+}}$ in $\mathrm{Cs_2ZrCl_6}$ [29].

2.1.1.5
d^5 Metals

Complexes of d^5 metals of the first transition row generally exist in a high spin configuration with sextet ground states. All LF transitions are then spin-forbidden. Accordingly, only a phosphorescence is possible. Indeed, a variety of compounds with $\mathrm{Mn^{2+}}$ in tetrahedral or octahedral environments are known to phosphoresce from their lowest-energy LF quartet states. However, this emission was observed only in the solid state [30], e.g.,

$$\mathrm{(NEt_4)_2[MnCl_4]} \qquad \text{ph. } \begin{array}{l} \lambda_{\max} = 524\text{ nm, solid, r.t.} \\ \phi = 0.32,\ \tau = 9 \times 10^{-3}\text{ s} \end{array} \tag{8}$$

It is not clear why this luminescence does not appear in solution. Complexes of d^5 metals of the second and third transition row do not seem to show an LF emission. Such metal ions exist only in low-spin configurations. In octahedral complexes they then possess an electron hole in their $d\pi$ subshell. It follows that such compounds are often characterized by low-energy LMCT transitions [8]. Accordingly, LF emissions are not likely to occur.

2.1.1.6
d^6 Metals

Generally, d^6 metals of the first transition row form octahedral complexes with singlet (low-spin) or quintet (high-spin) ground states. The majority of these complexes is not emissive. In the case of low-spin complexes, the lowest-energy LF excited states are singlets, triplets, and quintets. The absence of luminescence may be related to the presence of such quintets [31]. If they are populated in the deactivation cascade they are not expected to be emissive since their radiative lifetime would be exceedingly long owing to the very low probability of a quintet to singlet ground state transition. These quintets should then be easily intercepted by competing deactivations. Complexes with strong-field ligands may have triplets as lowest-energy LF excited states. Accordingly, an LF emission may be seen [32–34], e.g.,

$$\mathrm{K_3[Co(CN)_6]} \qquad \text{ph. } \begin{array}{l} \lambda_{\max} = 694\text{ nm, solid, 77 K} \\ \tau = 0.65\text{ ms} \end{array} \tag{9}$$

Owing to their large ligand-field splittings, octahedral complexes of d^6 metals of the second and third transition row occur only in singlet ground states. Their lowest-energy LF excited states are triplets. A variety of such complexes shows an LF phosphorescence. The radiative lifetimes are shortened due to large spin-orbit couplings [35–39]:

$Ru(C_5H_5)_2$ ph. $\lambda_{max} = 588$ nm, solid, 60 K
$\phi = 0.004$, $\tau = 20$ μs (10)

$[Rh^{III}(NH_3)_6]^{3+}$ ph. $\lambda_{max} = 612$ nm, alcohol/water, 77 K
$\tau = 19$ μs (11)

$K_2[Pt^{IV}Cl_6]$ ph. $\lambda_{max} = 690$ nm, solid, 77 K
$\tau \sim 0.5$ ms (12)

2.1.1.7
*d*⁷ Metals

With the exception of Co^{2+}, mononuclear complexes of d^7 metals are rather rare. Moreover, molecular Co(II) compounds do not seem to be luminescent. Observations on the emission of Co(II) are essentially restricted to solid state systems. The tetrahedral $[CoO_4]^{6-}$ moiety incorporated in various host lattices is well known to show an LF emission [40], e.g.,

$ZnSiO_4{:}Co^{2+}$ ph. $\lambda_{max} = 652$ nm, solid, 15 K (13)

The emission from an LF doublet to the quartet ground state appears as a sharp line spectrum.

2.1.1.8
*d*⁸ Metals

Various mononuclear square-planar Pd(II) and Pt(II) complexes with singlet ground states are known to emit from their lowest-energy LF triplets [41]. However, this emission generally appears only at low temperatures and is frequently observed for solid compounds [42, 43], e.g.,

$K_2[PtCl_4]$ ph. $\lambda_{max} = 778$ nm, solid, 5 K (14)

At room temperature in solution Pt(II) complexes apparently do not show LF emissions.

2.1.1.9
*d*⁹ Metals

The d^9 electron configuration is represented by numerous Cu(II) complexes which are often blue owing to the presence of LF absorptions in the red region [8]. Ground and LF excited states are spin doublets. Accordingly, LF emissions are spin-allowed. Emissive molecular Cu(II) complexes seem to be unknown, but Cu^{2+} in solid matrices has been shown to show an LF luminescence [44, 45], e.g.,

$CdS{:}Cu^{2+}$ fl. $\lambda_{max} = 1604$ nm, solid, 4 K
$\tau = 500$ ns (15)

2.1.2
ds States

MC transitions from nd to (n+1) s orbitals are not easily identified. Such absorptions occur at relatively high energies where they may be obscured by bands of different origin. Fortunately, in d^{10} complexes LF transitions do not exist and the identification of the ds transitions is facilitated. Some linear Au(I) complexes indeed show ds absorptions as their longest-wavelength bands [46, 47]. At low temperatures in glassy solutions or in the solid state even at room temperature a few Au(I) complexes have been shown to emit from these ds excited states (Fig. 2) [48], e.g.,

$[Au^ICl_2]^-$ ph. $\lambda_{max} = 687$ nm, ethanol, 77 K $\phi = 0.1$ (16)

$NBu_4[Au^ICl_2]$ ph. $\lambda_{max} = 642$ nm, solid, r.t. (17)

$[Au^IBr_2]^-$ ph. $\lambda_{max} = 660$ nm, ethanol, 77 K (18)

$NBu_4[Au^IBr_2]$ ph. $\lambda_{max} = 592$ nm, solid, r.t. (19)

A phosphine [49] as well as a carbonyl [50] complex of Au (I) have also been suggested to emit from a ds triplet state [50], e.g.,

$Au^I(CO)Cl$ ph. $\lambda_{max} = 663$ nm, solid, r.t. (20)

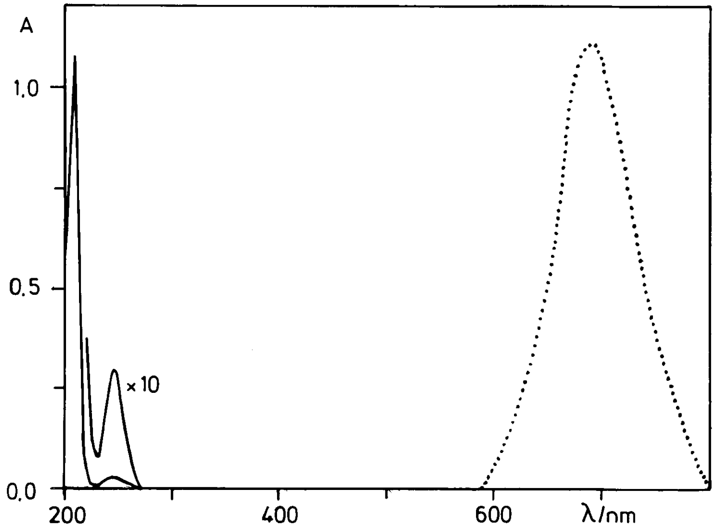

Fig. 2. Electronic absorption (*continuous line*) and emission (*dotted line*) spectra of $NBu_4[AuCl_2]$. Absorption: in CH_3CN, 1.64×10^{-4} mol l^{-1}, at room temperature, 1-cm cell. Emission: in EtOH, at 77 K, $\lambda_{exc} = 250$ nm; intensity in arbitrary units

2.1.3
dp States

Generally, nd → (n + 1)p MC transitions occur at higher energies than nd → (n + 1) s transitions. However, p-orbitals may be pushed below s orbitals by overlap with π^* orbitals of suitable ligands. Since the corresponding MOs are considerably mixed, the d → p transitions contain large MLCT contributions. It is then not clear if an MC assignment is justified. Nevertheless, dp excited states of this type have been identified in a few trigonal-planar d^{10} complexes. The emission of these compounds apparently originates from dp triplets [51], e.g.,

$$Pd(PPh_3)_3 \qquad \text{ph. } \lambda_{max} = 635\text{ nm, 2-MeTHF}, \quad \tau = 6.6\ \mu s \tag{21}$$

$$Pt(PPh_3)_3 \qquad \text{ph. } \lambda_{max} = 705\text{ nm, 2-MeTHF}, \quad \tau = 0.6\ \mu s \tag{22}$$

Similar emissions were observed for the tetrahedral complexes [52]:

$$Pd(PPh_3)_4 \qquad \text{ph. } \lambda_{max} = 660\text{ nm, THF, r.t.}, \quad \phi = 0.02, \tau = 3.6\ \mu s \tag{23}$$

$$Pt(PPh_3)_4 \qquad \text{ph. } \lambda_{max} = 740\text{ nm, THF, r.t.}, \quad \phi = 4 \times 10^{-4}, \tau = 0.7\ \mu s \tag{24}$$

Phosphine complexes of Rh(I) and Ir(I) are also emissive [53–55]. The luminescence may originate from dp excited states. However, since these dp states are heavily mixed with MLCT states a simple dp assignment is certainly not appropriate [55].

2.1.4
sp States

Halide complexes of main-group metal ions with an s^2 electron configuration are frequently luminescent under ambient conditions [56, 57]. The absorption and emission spectra (Table 1) [57] can be explained on the basis of a simple energy level diagram of a free s^2 ion (Scheme 1). The emission comes from the

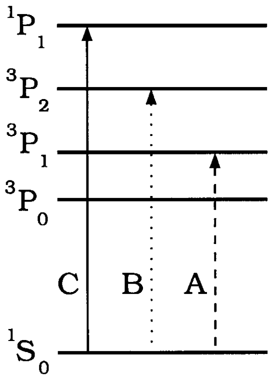

Scheme 1. Energy level scheme of a free s^2 ion

Table 1. Absorption- and emission data for several s^2 complexes in solution at room temperature

Group number (Periodic table)		**13**	**14**				**15**				**16**
Element		Tl(I)	Ge(II)	Sn(II)	Pb(II)		Sb(III)		Bi(III)		Te(IV)
Complex		Tl^+_{aq}	$GeCl_3^-$	$SnCl_3^-$	$PbCl_3^-$	$PbCl_4^{2-}$	$SbCl_4^-$	$SbCl_6^{3-}$	$BiCl_4^-$	$BiCl_6^{3-}$	$TeCl_6^{2-}$
Absorption	A-Band [nm]	213	280	292,272	273	294	283	306	319	333	410,385
	(ε; l mol^{-1}cm^{-1})	(4575)	(30)	(300, 700)	(8100)	(8200)	(1600)	(1600)	(5100)	(10,300)	(700, 1900)
	B-Band [nm]	–	–	–	–	–	225	267	–	–	323
	(ε)						(3500)	(5000)			(3000)
	C-Band [nm]	–	218,225	216, 226, 236	205	–	235	242	227	231	304, 287, 277
	($\varepsilon \times 10^{-3}$)		(4.9, 4.8)	(12.9, 17.3, 14.0)	(22.8)		(5.0)	(13.3)	(12.3)	(36.0)	(8.0, 9.0, 8.6)
Emission	λ_{max} [nm]	370	535	510	538	518	740	520	720	475	[a]
	ϕ (argon-sat.)	0.52	0.081	0.068	0.159	0.144	0.0061	0.0013	0.01	0.004	
	Lifetime [µs]	0.36 ± 08	[b]	[b]	17 ± 1	68 ± 2	1.2	4.7	< 0.2	1.8	
Stokes Shift [cm^{-1}]			17,000	15,900	18,000	14,700	21,800	13,500	17,500	9000	

[a] Only an emission at 77 K was observed.

[b] Owing to photochemical instability, reliable lifetimes could no be determined.

$^3P_1$ sp excited state. The huge Stokes shifts are related to considerable structural changes which take place in the sp excited states. Many of these complexes have a less symmetrical structure in the ground state owing to a second order Jahn-Teller effect but lose this distortion in the sp state. While these emissions have been systematically studied only recently, the luminescence of s^2 ions in the solid state has been known for many years [58–61].

2.1.5
ff States

Lanthanide compounds play an important role in the field of luminescence spectroscopy. The excited state properties of lanthanide ions Ln^{3+} have been extensively discussed in many reviews [62–66]. Here, only a few general aspects are mentioned.

The electronic spectra of Ln^{3+} with f^n electron configurations are determined by electronic transitions between f orbitals. Since the f electrons are largely shielded from the environment they behave as inner and not valence electrons. Accordingly, the absorption and emission spectra consist of very narrow bands.

Transitions between f orbitals of Ln^{3+} are strictly parity-forbidden. Moreover, many ff transitions are also spin-forbidden although spin-orbit coupling attenuates the forbiddeness. Nevertheless, both restrictions have important consequences. The bands have very low absorption coefficients and the radiative lifetimes of ff states are rather large ($\sim 10^{-3}$ s). Owing to the small absorption coefficients of Ln^{3+} the excitation can be facilitated by suitable ligands which absorb the light and subsequently transfer the excitation energy to the emissive Ln^{3+} ion. In addition, appropriate ligands may prevent radiationless deactivations. This behavior is illustrated by various Eu^{3+} and Tb^{3+} complexes which emit an intense red and green luminescence, respectively [67, 68], e.g.,

$Eu^{III}(TTA)_3$ ph. $\lambda_{max} = 612$ nm, acetone, r.t.
TTA = thenoyl-trifluoro-acetonate $\phi = 0.56$, $\tau = 565$ µs (25)

$Tb^{III}(acac)_3$ ph. $\lambda_{max} = 543$ nm, ethanol, r.t.
acac = acetylacetonate $\phi = 0.19$, $\tau = 820$ µs (26)

2.1.6
fd States

Some lanthanide ions such as Ce^{3+}, Sm^{2+}, Eu^{2+}, and Yb^{2+} are characterized by low-energy transitions which involve the promotion of a 4f electron to a 5d orbital [61, 69]. Such fd states may be luminescent [70, 71], e.g.,

$[Eu^{II}(C2.2.1)]^{2+}$ $\lambda_{max} = 450$ nm, CH_3OH/H_2O, r.t.
$\phi = 10^{-3}$, $\tau = 1.5$ ns (27)

$[Ce^{III}(C2.2.1)]^{3+}$ fl. $\lambda_{max} = 360$ nm and 340 nm, H_2O, r.t.
$\phi = 1$, $\tau = 50$ ns (28)

C 2.2.1

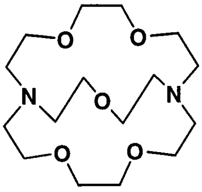

Structure 1

The electronic transition between the $4f^1$ ground state and $5d^1$ excited state of Ce^{3+} is completely allowed as electric dipole transition. Accordingly, the emission lifetimes are rather short and the fluorescence quantum yield may even reach unity.

2.2
Cluster Complexes

2.2.1
Binuclear Complexes

Binuclear complexes with direct metal-metal interaction can be classified according to the bond order (BO) in the ground state from zero to four.

2.2.1.1
Bond Order = 0

Binuclear d^8 complexes which contain two square planar components may be arranged in a face-to-face fashion. Since a metal-metal bond is not present, both mononuclear moieties are kept together by bridging ligands or solid state effects. Nevertheless, a metal-metal interaction occurs by the overlap of the d_z^2 and p_z orbitals at both metals. This generates four σ MOs which are occupied by four electrons: $(\sigma_z^{b2})^2$, $(\sigma_z^{*2})^2$, $(\sigma_z^{b})^0$, $(\sigma_z^{*})^0$. The M-M bond order is then zero. However, the lowest-energy transition from σ_z^{*2} to σ_z^{b} leads to an MC excited state which is characterized by a metal-metal bond (BO=1). Several binuclear d^8 complexes have been shown to emit from such $\sigma_z^{*2}\ \sigma_z^{b}$ MC states [13, 72], e.g.,

$[Pt^{II}_2(\mu\text{-}P_2O_5H_2)_4]^{4-}$ fl. $\lambda_{max} = 407$ nm, H_2O, r.t., $\tau = 8-40$ ps
$[P_2O_5H_2]^{2-} =$ ph. $\lambda_{max} = 514$ nm, H_2O, r.t., $\tau = 9$ µs (29)
pyrophosphite

The appearance of a fluorescence in addition to the phosphorescence is quite surprising since platinum should facilitate intersystem crossing.

Various dimeric Au^I complexes are also emissive [13, 73]. In these d^{10} complexes the lowest-energy transition involves the promotion of an electron from an MO which is antibonding with respect to dd overlap to a σ_p^b orbital. Again, the Au-Au bond order is zero in the ground state and 1 in the MC excited state. A variety of such binuclear Au^I complexes shows a phosphorescence, frequently in solution at room temperature [74], e.g.,

$[\mathrm{Au^{I}(dppm)}]_2^{2+}$ ph. $\lambda_{max} = 593$ nm, CH_3CN, r.t.
dppm = bis(diphenylphosphino)methane $\phi = 0.31$, $\tau = 21$ μs (30)

A similar situation exists for dimeric complexes of main group metals with an s^2 electron configuration. The metal-metal interaction of s and p orbitals creates the following MOs: σ_s^b, σ_s^*, σ_p^b, and σ_p^*. In the ground state only the σ_s orbitals are occupied and an M-M bond is not present while in the lowest MC sp excited state with orbital occupation $(\sigma_s^b)^2$ $(\sigma_s^*)^1$ $(\sigma_p^b)^1$ a metal-metal bond is formed [75]. Such MC states may be emissive [75], e.g.,

$[\mathrm{Tl^{I}(S_2CNEt_2)}]_2$ ph. $\lambda_{max} = 608$ nm, CH_3CN, r.t. (31)

2.2.1.2
Bond Order = 1

Many transition metals with a d^7 electron configuration form dimeric complexes with an M-M single bond in the ground state. The bonding MO σ_z^{b2} is occupied by two electrons. The complexes $[(CO)_5M^0\text{-}M^0(CO)_5]$ with M=Mn or Re are typical representatives. Unfortunately, their σ_z^{b2} σ_z^{*2} MC excited states are not emissive but reactive owing to the absence of an M-M bond in the excited state [13, 76]. However, a photochemical homolysis of the M-M bond can be prevented by bridging ligands. Accordingly, such complexes can show an emission from a $\sigma\sigma^*$ state [77], e.g.,

$Re_2(CO)_6(\mu\text{-dmpm})_2$ ph. $\lambda_{max} = 690$ nm, 2-methylpentane, 77 K
dmpm = bis(dimethyl phosphino)methane $\tau = 31$ μs (32)

Various binuclear Pt(III) complexes with Pt-Pt single bonds are also luminescent [13, 72].

2.2.1.3
Bond Order = 4

Binuclear complexes with M-M quadruple bonds are formed by metal ions with a d^4 electron configuration. Metal-metal interaction leads to a σ, two π, and a δ bond. The lowest-energy transition $\delta^b\delta^*$ state reduces the bond order from 4 to 3 but does not induce an M-M bond cleavage. On the contrary, the $\delta\delta^*$ state is emissive [13]. For example, $Mo^{II}X_4(PMe_3)_4$ complexes with X=Cl, Br, and I show such an MC fluorescence [78], e.g.,

$Mo^{II}Cl_4(PMe_3)_4$ fl. $\lambda_{max} = 673$ nm, 2-methylpentane, 300 K
$\phi = 0.23$, $\tau = 140$ ns (33)

2.2.2
Trinuclear Complexes

Trinuclear complexes may consist of a linear or triangular arrangement of three metal atoms or ions. Such linear Au_3^I compounds have been shown to be luminescent and the emitting state is again derived from an MC dp triplet in analogy to various binuclear Au(I) complexes [73, 79], e. g.,

$[Au_3(dmmp)_2]^{3+}$ ph. $\lambda_{max} = 580$ nm, CH_3CN, r. t., $\tau = 7$ µs
dmmp = bis(dimethyl- (34)
phosphinomethyl)
methylphosphine

The dmmp ligand bridges all three Au^+ ions. Heterotrinuclear complexes are also known to display phosphorescence which may be attributed to MC excited states [80].

The emission of trinuclear complexes is not restricted to linear M_3 structures. Triangular M_3 compounds have also been observed to emit from MC excited states. An example is $Pd^{II}(acetate)_2$ which exists as trimer in the solid state as well as in solution (Fig. 3) [81]:

$Pd^{II}_3(acetate)_6$ fl. $\lambda_{max} = 475$ nm and ph. $\lambda_{max} = 595$ nm
benzene, r. t. (35)

It is suggested that the metal d and p orbitals of the Pd^{II}_3 moiety interact in a similar fashion as in binuclear face-to-face complexes of Pd(II) and Pt(II) (see above). The luminescence is assumed to originate from a $\sigma^*_d\ \sigma^b_p$ excited state.

Some mercury cluster compounds have been found to be luminescent [82]. For bonding interactions in these clusters it is sufficient to consider only the Hg 6s orbitals in a first approximation. Three mercury atoms may be combined to linear or trigonal structures. The stability of both arrangements depends on the number of valence electrons. In the case of Hg_3^{2+} four electrons are available which stabilize a linear structure while for Hg_3^{4+} two electrons favor a trigonal geometry. Both clusters are kept together by one bond [82]. While Hg_3^{2+} exist as

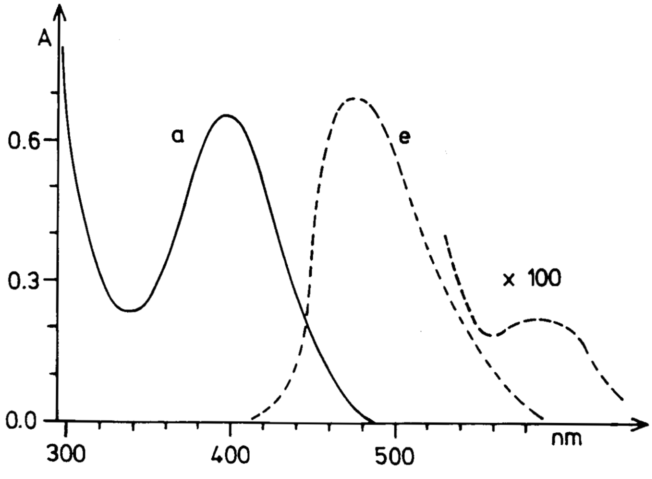

Fig. 3. Electronic absorption (*continuous line*) and emission (*dotted line*) spectrum of 1.22×10^{-3} mol l^{-1} $Pd_3(acetate)_6$ in benzene at r.t. Emission: $\lambda_{exc} = 420$ nm; intensity in arbitrary units

an isolated cluster ion, Hg_3^{4+} is stabilized by bridging phosphines. Both cluster ions are luminescent(Fig. 4) [83, 84]:

Hg_3^{2+} ph. λ_{max} = 645 nm, CF_3SO_3H, r.t. (36)

$[Hg_3(dppm)_3]^{4+}$ dppm = diphenylphosphinomethane ph. λ_{max} = 658 nm, ethanol, 77 K (37)

The emissions come from MC states which are derived from Hg 5s orbitals.

2.2.3
Tetranuclear Complexes

Tetranuclear clusters frequently contain a tetrahedral or square-planar M_4 moiety. Generally, the metal atoms or ions are bridged by ligands. Nevertheless, a direct metal-metal interaction seems to be present, but sometimes rather weak.

Tetrahedral M_4 clusters are often bridged by halide ions. The resulting M_4X_4 fragments form a cubane structure. Additional ligands may be coordinated terminally. Transition metal as well as main-group metal clusters of this type have been observed to emit [85], e.g.,

$[Me_3Pt^{IV}I]_4$ ph. λ_{max} = 735 nm, toluene, 77 K (38)

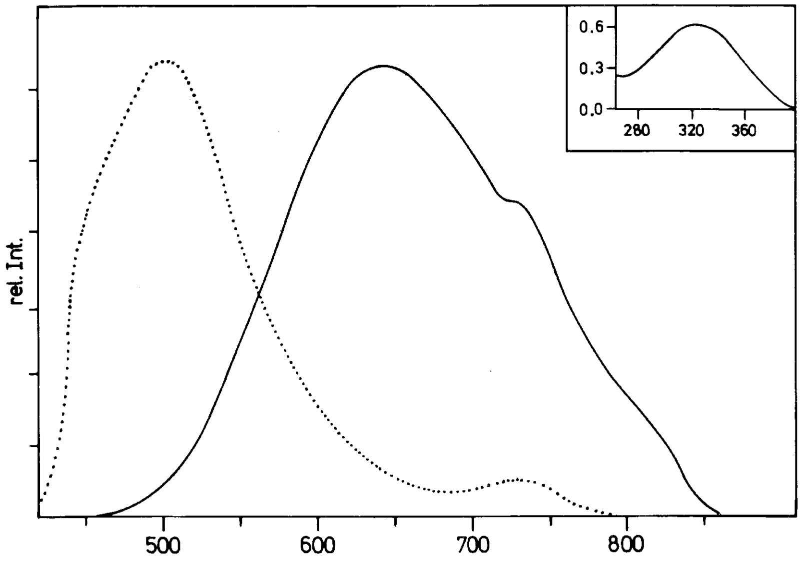

Fig. 4. Electronic emission and absorption (*inset*) spectra of Hg_3^{2+} in CF_3SO_3H. Emission at 77 K (*dotted line*) and r.t. (*continuous line*), λ_{exc} = 320 nm; intensity in arbitrary units. Absorption: 5.9×10^{-4} mol l^{-1}, 1-cm cell

The mononuclear components of this cluster can be viewed as pseudooctahedral $Pt^{IV}Me_3I_3$ complexes. The lowest-energy excited state of these fragments are LF states. The emission of $[Me_3Pt^{IV}I]_4$ is suggested to originate from LF triplets at the d^6 Pt^{IV} metal ions, but is modified by metal-metal interactions.

Numerous complexes of the general composition $[LCu^{I}X]_4$ with bridging X (halide) and terminal L (e.g., amines, pyridine, phosphines) ligands are luminescent under ambient conditions [86, 87]. The identification of the emissive excited states is complicated by the presence of different electronic transitions such as MC ds, MLCT, and LMCT at comparable energies. Accordingly, simple assignments are not appropriate.

Various tetranuclear Ag(I) and Au(I) complexes are also luminescent [86]. In some cases the M_4 moiety exists in a planar arrangement. Again, the emissive excited states may be of mixed origin. However, the luminescence of some tetranuclear Au^{I} clusters was assigned to a MC ds excited state [88], e.g.,

$$[Au^{I}(\text{piperidine})Cl]_4 \qquad \text{ph. } \lambda_{max} = 700 \text{ nm, ethanol, 77 K} \tag{39}$$

Main-group metal ions with an s^2 electron configuration are not only emissive in mononuclear complexes. Cluster compounds including tetrahedral M_4 structures may be luminescent too [89], e.g.,

$$[Tl^{I}OCH_3]_4 \qquad \text{ph. } \lambda_{max} = 640 \text{ nm, methanol, r.t.} \tag{40}$$

The emissive excited state is derived from an MC sp state, but shifted to lower energies by metal-metal interaction.

2.2.4
Hexanuclear Complexes

The cation $[M_6^{II}X_8]^{4+}$ with M = Mo, W, and X = halogen represent an important family of cluster compounds which consist of an M_6 octahedron and face-bridging halide ligands. Six additional terminal ligands including halides may be attached to the metal ions. The M_6 cluster is characterized by strong metal-metal interactions. The frontier orbitals are composed by metal d-orbitals. Accordingly, the lowest-energy transitions occur between delocalized MOs of d-parentage. The clusters are luminescent and the emission originates from such MC excited states [13, 90], e.g.,

$$[Mo_6^{II}Cl_{14}]^{2-} \qquad \begin{array}{l}\text{ph. } \lambda_{max} = 805 \text{ nm, } CH_3CN\text{, r.t.}\\ \phi = 0.19,\ \tau = 180\ \mu s\end{array} \tag{41}$$

Cluster complexes of the composition $M_6^{I}(mtc)_6$ with M = Cu and Ag and mtc^- = di-*n*-propylmonothiocarbamate are also luminescent. The emission is certainly related to that of the tetranuclear Cu(I) complexes [86, 87] (see above). The lowest-energy transitions of these d^{10} clusters may be MC ds transitions with LMCT contributions. Accordingly, the emissive states should be of MC/LMCT character, but modified by metal-metal interaction [91], e.g.,

$$Ag_6(mtc)_6 \qquad \begin{array}{l}\text{ph. } \lambda_{max} = 607 \text{ nm, toluene, 77 K,}\\ \tau = 131\ \mu s\end{array} \tag{42}$$

Essentially the same picture should apply to $[Cu^I(PPh_3)H]_6$ which contains a Cu^I_6 octahedron, bridging hydride and terminal phosphine ligands [92]:

$$[Cu^I(PPh_3)H]_6 \qquad \text{ph. } \lambda_{max} = 730 \text{ nm, toluene, 77 K} \qquad (43)$$

Hexanuclear main-group metal clusters which are composed of s^2 metal ions can be luminescent, too (Fig. 5) [93], e.g.,

$$Sn^{II}_6O_4(OCH_3)_4 \qquad \text{ph. } \lambda_{max} = 564 \text{ nm, solid, 77 K} \qquad (44)$$

This complex contains bridging oxide and methoxide ligands. It was suggested that the emissive state is derived from an MC sp transition. The large Stokes shift ($\Delta\bar{\nu} \sim 13{,}000 \text{ cm}^{-1}$) was attributed to metal-metal interaction. In a later study it has been concluded that this Stokes shift is caused by a Jahn-Teller distortion [94].

2.2.5
Polymeric Complexes

The luminescence of metal complexes can also be based on metal-metal interaction in polymeric complexes. While $[Pt^{II}(CN)_4]^{2-}$ is not luminescent as isolated complex, solid salts frequently show an intense emission even at r.t. [95], e.g.,

$$Ba[Pt^{II}(CN)_4] \times 4H_2O \qquad \lambda_{max} = 513 \text{ nm, solid, r.t.} \qquad (45)$$

Such solids consist of columnar structures which are composed of square planar $[Pt(CN)_4]^{2-}$ complexes. Perpendicular to these planes (z-axis) a metal-metal in-

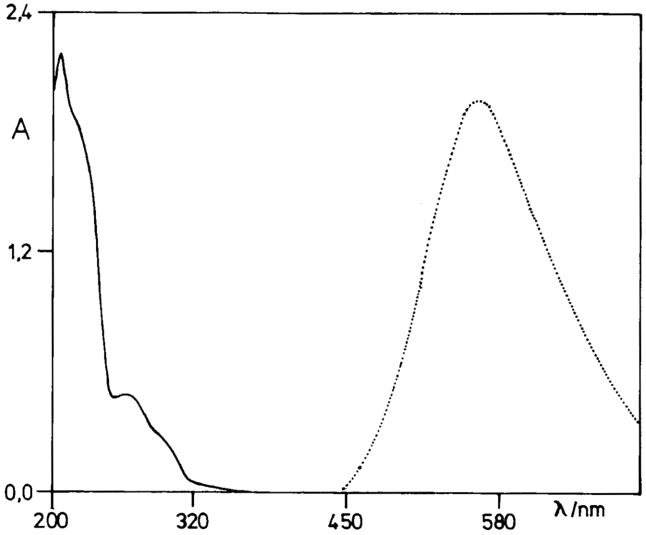

Fig. 5. Electronic absorption (*continuous line*) and emission (*dotted line*) spectra of $[Sn_6O_4(OCH_3)_4]$. Absorption: in *n*-hexane, $\sim 1 \times 10^{-4}$ mol l^{-1} at r.t., 1-cm cell. Emission: in the solid state at 77 K; λ_{exc} = 300 nm; intensity in arbitrary units

teraction takes place. The lowest-energy transition involves delocalized states which are derived from the d_z^2 and p_z orbitals of the d^8 metal ions. The emission originates from these MC excited states. Oligomeric $[Pt(CN)_4]^{2-}$ complexes which exist in concentrated aqueous solution are also emissive from such MC dp excited states [96].

3
Ligand-to-Metal Charge Transfer Excited States

3.1
d^0 Metals

The most promising candidates which might show a luminescence from LMCT states are complexes with transition metals in high oxidation states and a d^0 electron configuration. LMCT transitions occur then at relatively low energies and any interference by LF transitions is avoided. Indeed, such emissive LMCT states have been known for many years. However, these observations were restricted to solid state systems [61] while the luminescence from LMCT states of molecular complexes has been detected only recently. Many of these compounds are organometallics with cyclopentadienyl (Cp) or simple σ-bonding carbanions as ligands. In the first report on this subject the emission of permethylscandocene chloride was described [97]:

$$(C_5Me_5)_2Sc^{III}Cl \qquad \text{ph.} \ \lambda_{max} = 520 \text{ nm, isooctane/methylcyclohexane, r.t.} \quad \tau = 2\ \mu s \tag{46}$$

It was suggested that the luminescence originates from an excited state with a large $Cl^- \rightarrow Sc^{III}$ LMCT contribution, but a $Cp^- \rightarrow Sc^{III}$ LMCT state is certainly a reasonable alternative.

A variety of other cyclopentadienyl complexes are also characterized by luminescent LMCT states [98], e.g.,

$$(C_5Me_5)\,Ta^{V}Cl_4 \qquad \text{ph.} \ \lambda_{max} = 578 \text{ nm, } CH_2Cl_2\text{, r.t.} \quad \phi = 0.002,\ \tau = 0.9\ \mu s \tag{47}$$

The emissive state is apparently a $(C_5Me_5)^- \rightarrow Ta^V$ LMCT state. This assignment also applies to complexes of the general composition $(C_5R_5)_2Ti^{IV}X_2$ and $(C_5R_5)\,Ti^{IV}X_3$ with R = H, CH_3, and X = F, Cl, Br [99], e.g.,

$$Cp_2TiCl_2 \qquad \text{ph.} \ \lambda_{max} = 672 \text{ nm, solid, 77 K,} \quad \tau = 730\ \mu s \tag{48}$$

With X = I or CH_3 the compounds are not luminescent. The emission of $(C_5R_5)_2Zr^{IV}Cl_2$ with R = H (λ_{max} = 452 nm) and R = Me (λ_{max} = 494 nm) certainly also originates from $(C_5R_5)^- \rightarrow Zr^{IV}$ LMCT states [100]. Finally, several zirconium(IV) thiolate complexes $(C_5H_5)_2Zr^{IV}(SC_6H_4R)_2$ have been observed to emit (λ_{max} = 520–620 nm) [100]. The luminescence was assigned to a thiolate → Zr^{IV} LMCT state.

Complexes of the type $RRe^{VII}O_3$ with R = carbanion are catalytically active organometallics. At r.t. in solution they are light-sensitive [101, 102], but one of these compounds has been observed to emit at low temperatures [102]:

$MeRe^{VII}O_3$ ph. $\lambda_{max} = 640$ nm, ethanol/water, 77 K (49)

The lowest-energy transition of $MeRe^{VII}O_3$ is of the LMCT type and involves the promotion of an electron from the Me-Re σ-bond to an acceptor orbital of d-parentage which is strongly Re-O π-antibonding. It is this LMCT state which is emissive.

The polymers $[M^{VI}N(OR)_3]_n$ with M = Mo and W display a low-temperature emission [103], e.g.,

$[W^{VI}N(OCMe_3)_3]_n$ ph. $\lambda_{max} = 513$ nm, solid, 77 K, $\tau = 60$ μs (50)

It has been suggested that the lowest-energy transition involves the tungsten–nitride moiety. Accordingly, the emissive state should be an $N^{3-} \rightarrow W^{VI}$ LMCT state. There is spectroscopic evidence that the lowest energy LMCT transition terminates at an MO which is strongly W-N antibonding. However, the donor orbital could also be derived from the rather reducing alcoholate ligands.

A variety of imido complexes of d^0 metals (Ti^{IV}, Nb^V, Ta^V) also luminesce from LMCT states [104–107], e.g.,

$Ta^V(NPh)Cl_3$ ph. $\lambda_{max} = 629$ nm, $C_2H_4Cl_2$, r.t.
(dimethoxyethane) $\phi = 0.008$, $\tau = 0.2$ μs (51)

The imido ligand seems to be the donor site of the lowest-energy LMCT transition.

3.2
d^5 Metals

Luminescent LMCT states of complexes with a partially filled d-shell at the metal have rarely been observed. The reason for this is not quite clear. However, it seems likely that most complexes which have low-energy LMCT states also have LF states in the same energy region. This interference may prevent the observation of emissive LMCT states. Moreover, LMCT states are frequently quite reactive.

A complex with a lowest-energy LMCT state should be composed of a strongly oxidizing metal with a large LF splitting and strongly reducing ligands with a high LF strength [108]. Suitable examples are octahedral d^5 complexes of second and third row transition metals. The electron hole in the t_{2g} d-subshell facilitates the occurrence of low-energy LMCT transitions. Indeed, several such complexes with emissive LMCT states are known (Fig. 6) [108–110], e.g.,

$[Ru^{III}(CN)_6]^{3-}$ fl. $\lambda_{max} = 525$ nm, ethanol, 77 K (52)

$Re^{II}(C_5Me_5)_2$ fl. $\lambda_{max} = 605$ nm, toluene, r.t. (53)

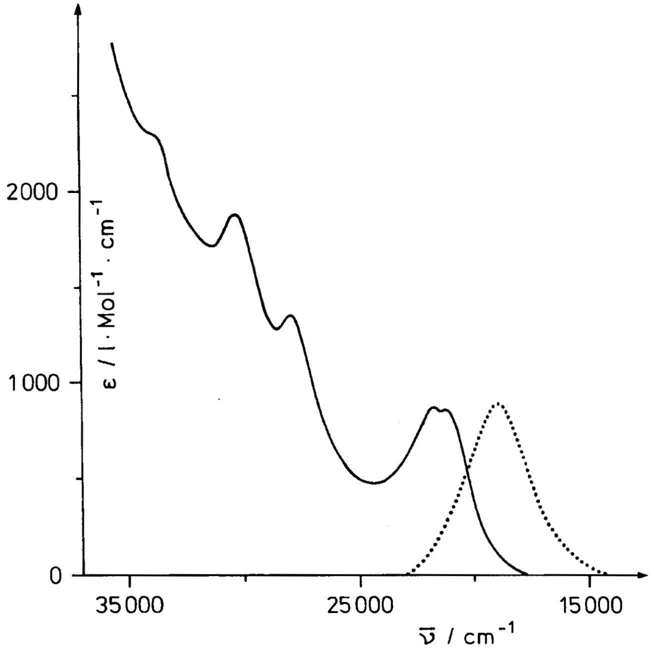

Fig. 6. Electronic absorption (*continuous line*) and emission (*dotted line*) spectra of $[NEt_4]_3[Ru(CN)_6]$ in EtOH; absorption at room temperature, emission excited at 366 nm and 77 K (intensity in arbitrary units)

$[Re^{II}(dmpe)_3]^{2+}$ fl. $\lambda_{max} = 600$ nm, CH_3CN, r.t.
dmpe = bis(dimethyl- $\phi = 0.65, \tau = 16$ ns (54)
phosphino)ethane

The ground states and the LMCT states of these complexes are spin-doublets. Accordingly, the emission is a fluorescence with a short lifetime.

3.3
d^{10} Metals

The lowest-energy transitions of metals with a rather stable and completely filled d-shell are of the LMCT type [6, 7]. Suitable examples are Zn(II), Cd(II), and Hg(II) compounds. However, simple mononuclear complexes of these d^{10} metal ions are apparently not luminescent. On the contrary, semiconductors such as ZnO or CdS are strongly luminescent. In the case of ZnO the valence and conduction band are derived from the filled p-orbitals of oxide and the empty 4s orbitals of Zn^{2+}, respectively [111]. It follows that the band gap emission of ZnO can be viewed as a luminescence from a LMCT state. Cluster compounds of Zn(II), Cd(II), and Hg(II) have been also observed to emit from LMCT states (Fig. 7) [112–116], e.g.,

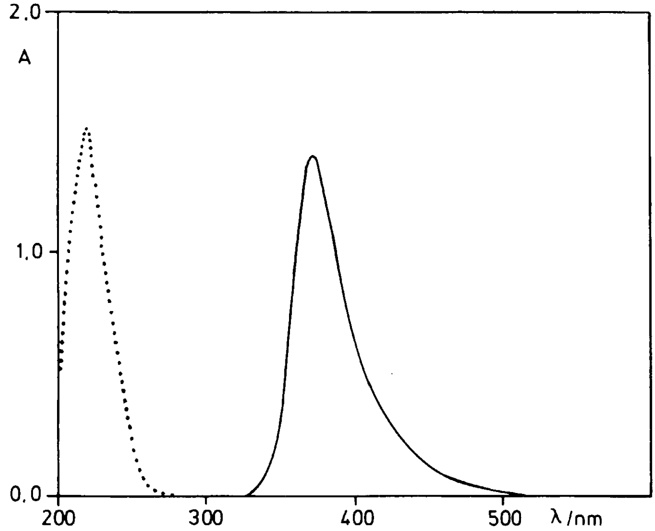

Fig. 7. Electronic absorption (*dotted line*) and emission (*continuous line*) spectra of $[\mathrm{Zn_4O}(\mathrm{acetate})_6]$ at r.t. 1-cm cell. Absorption: 2.43×10^{-4} mol $\mathrm{l^{-1}}$ in EtOH. Emission: 1.15×10^{-4} mol $\mathrm{l^{-1}}$ in $\mathrm{CH_2Cl_2}$, $\lambda_{\mathrm{exc}} = 300$ nm; intensity in arbitrary units

$$[\mathrm{Zn}_4^{\mathrm{II}}\mathrm{O}(\mathrm{acetate})_6] \qquad \begin{array}{l} \text{fl. } \lambda_{\mathrm{max}} = 372\ \mathrm{nm}, \mathrm{CH_2Cl_2}, \text{r.t.} \\ \phi = 0.15, \tau = 10\ \mathrm{ns} \end{array} \tag{55}$$

$$[\mathrm{Cd}_{10}^{\mathrm{II}}\mathrm{S}_4(\mathrm{SPh})_{16}]^{4-} \qquad \text{fl. } \lambda_{\mathrm{max}} = 545\ \mathrm{nm}, \mathrm{CH_3CN}, \text{r.t.}, \tau = 0.6\ \mathrm{ns} \tag{56}$$

$$[\mathrm{Hg}_4^{\mathrm{II}}(\mathrm{SPh})_6(\mathrm{PPh_3})_4]^{2+} \qquad \text{ph. } \lambda_{\mathrm{max}} = 690\ \mathrm{nm}, \mathrm{CH_2Cl_2}/\text{toluene}, 77\ \mathrm{K} \tag{57}$$

The rather low energies of the LMCT emission may be associated with the electronic interaction in the cluster moieties. It has been suggested that these clusters can serve as molecular models for the luminescence of semiconductors such as ZnO and CdS. Theoretical work has confirmed the conclusion that the cluster emission indeed originates from LMCT states. However, despite structural similarities the clusters cannot be considered to be real molecular models of the semiconductors [117].

Other candidates for emissions from LMCT states are complexes of the d^{10} metal ions Cu(I), Ag(I), and Au(I) with donor ligands. However, in these cases LMCT and MC ds transitions occur at comparable energies. These LMCT and MC states may even mix and clear distinctions are not possible. Such complications are frequently encountered. Suitable examples are tetranuclear Cu(I) clusters [86, 87, 118], e.g.,

$$[\mathrm{Cu^{I}I}(\mathrm{morpholine})]_4 \qquad \begin{array}{l} \text{ph. } \lambda_{\mathrm{max}} = 654\ \mathrm{nm}, \text{benzene}, \text{r.t.} \\ \phi = 0.004, \tau = 0.3\ \mu\mathrm{s} \end{array} \tag{58}$$

Originally, the emitting state has been assumed to be of the MC ds type [118], but was later corrected to have a considerable LMCT contribution [86, 87]. A si-

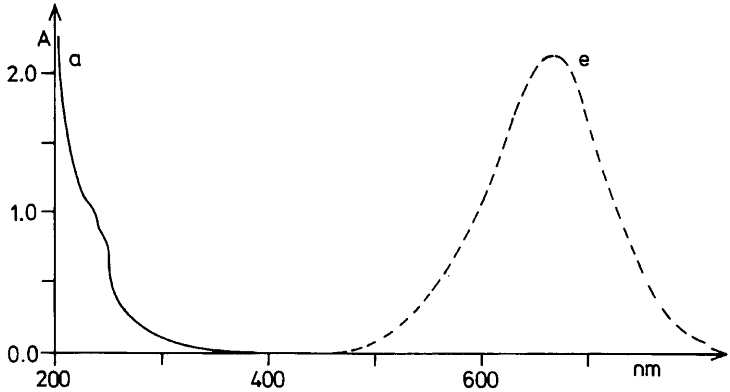

Fig. 8. Electronic absorption (a, *continuous line*) and emission (e, *dashed line*) spectra of $NBu_4[Au(SH)_2]$. Absorption: 3.75×10^{-4} mol l^{-1} in dry acetonitrile under argon at r.t., 1-cm cell. Emission: in toluene at 77 K, λ_{exc} = 300 nm; intensity in arbitrary units

milar situation exists for Au(I) complexes. For instance, the emissions of Au(I) complexes with certain sulfur-coordinating ligands have been attributed to mixed ds/LMCT excited states (Fig. 8) [119, 120], e.g.,

$$[Au^{I}(SH)_2]^- \qquad \text{ph. } \lambda_{max} = 665 \text{ nm, toluene, r.t.} \qquad (59)$$

However, there are also compounds with Au^I-S bonds which have been suggested to emit from rather pure LMCT states [121], e.g.,

$$\begin{array}{ll} Au^{I}_2(\text{p-tc})_2(\text{dppe}) & \text{ph. } \lambda_{max} = 495 \text{ nm, solid, r.t.} \\ \text{p-tc} = \text{p-thiocresolate;} & \\ \text{dppe} = \text{diphenylphosphinoethane} & \end{array} \qquad (60)$$

3.4
f^0 Metals

The best known example of an emitting LMCT state is the luminescence of the uranyl ion [122, 123]:

$$[U^{VI}O_2]^{2+} \qquad \begin{array}{l} \text{ph. } \lambda_{max} = 509 \text{ nm, } H_2O\text{, r.t.} \\ \phi = 0.23, \tau = 10\ \mu s \end{array} \qquad (61)$$

Since U(VI) has an empty valence shell with the electron configuration f^0 only low-energy LMCT transitions are feasible [123]. Accordingly, the $O^{2-} \rightarrow$ U(VI) LMCT assignment to the emitting state of UO_2^{2+} is unambiguous.

4
Metal-to-Ligand Charge Transfer Excited States

Low-energy MLCT transitions occur in complexes with reducing metals and acceptor ligands which provide π^* (or σ^*) orbitals at low energies. This situation is frequently encountered in organometallics [76, 124]. Although MLCT excited complexes may be quite reactive [125] they are often luminescent and not intrinsically reactive. Emissive MLCT states have mainly been observed for mononuclear complexes with d^6, d^8, and d^{10} electron configurations. The prototype acceptor ligands are polypyridines [126–129] such as 2,2′-bipyridyl (bipy) or 9,10-phenanthroline (*o*-phen) which have available delocalized π^* orbitals at rather low energies. In another terminology these ligands are known as 1,2-diimines. Of course, a variety of other acceptor ligands is also involved in MLCT emissions. Owing to the huge number of studies on luminescent MLCT states this subject has been discussed extensively. For details the reader is referred to various reviews and monographs [13, 126–129]. Only a few examples will be mentioned here.

4.1
d^6 Metals

Octahedral complexes with reducing d^6 metals of the second and third transition row including Mo^0, W^0, Re^I, Ru(II), Os(II), and Ir(III) constitute the majority of complexes with luminescent MLCT states. While the ground states are singlets the lowest excited states are triplets. Although the MLCT emissions are spin-forbidden processes they are relatively fast because they are facilitated by strong spin-orbit coupling. For this reason these emissions are observed under ambient conditions. Competing radiationless deactivations are apparently not rapid enough to quench the luminescence. On the contrary, complexes of first-row transition metals generally do not emit from MLCT states. In these cases the presence of low-energy LF excited states interferes with an MLCT emission. Moreover, spin-orbit coupling is smaller and radiative lifetimes of triplets longer. Facile radiationless deactivations can then prevent the appearance of an MLCT phosphorescence at r.t. although exceptions are known [130], e.g.,

$$Cr^0(CO)_4(bipy) \qquad \text{ph. } \lambda_{max} = 778\ \text{nm, benzene, r.t.} \tag{62}$$

A variety of complexes of the type $M^0(CO)_4(L\text{-}L)$ with M = Mo, W and L-L = polypyridyl have been observed to phosphoresce from MLCT states [124, 126, 131].

One of the largest groups of MLCT emitters is derived from Re(I) carbonyl complexes [76, 126, 132, 133], e.g.,

$$Re^I(\text{o-phen})(CO)_3Cl \qquad \text{ph. } \lambda_{max} = 577\ \text{nm}, CH_2Cl_2, \text{r.t.} \quad \phi = 0.036, \tau = 0.3\ \mu s \tag{63}$$

However, the importance of these Re(I) complexes is far surpassed by Ru(II) polypyridyl complexes [13, 126–129, 134]. Pioneering observations were reported by Crosby et. al. in 1965 and the following years [34, 135, 136]. In the meantime thousands of papers have been published on this subject. The homoleptic bipy complex can be considered as parent compound [126]:

$$[Ru(bipy)_3]^{2+} \qquad \text{ph. } \lambda_{max} = 602\ \text{nm}, H_2O, \text{r.t.} \quad \phi = 0.042, \tau = 0.6\ \mu s \tag{64}$$

While polypyridyl complexes of Mo^0, W^0, Re^I, Ru^{II}, Os^{II}, and Ir^{III} play an outstanding role as MLCT emitters, complexes of these metals with other acceptor ligands have also been shown to luminesce from MLCT states. In organometallic chemistry the aromatic 6π-electron ligands Cp^- ($C_5H_5^-$), C_6H_6, and $C_7H_7^+$ form a large family of compounds. The energies of their π^* orbitals decrease in this series [137]. Accordingly, MLCT energies become smaller in the same direction. While for $(C_6H_6)Mo^0(CO)_3$ the MLCT state lies above the lowest LF state [76, 124], an inversion of both states occurs in the case of $[(C_7H_7)Mo^0(CO)_3]^+$ which shows an MLCT emission under ambient conditions (Fig. 9) [138]:

$[(C_7H_7)Mo^0(CO)_3]^+$ ph. $\lambda_{max} = 578$ nm, CH_3CN, r.t., $\phi \sim 10^{-5}$ (65)

Arylisocyanides also provide low-energy π^* orbitals. Accordingly, suitable complexes with such ligands can display a luminescence from MLCT states [76, 124, 139], e.g.,

$[W^0(CNPh)_6]$ ph. $\lambda_{max} = 638$ nm, pyridine, r.t.
$\phi = 0.93$, (at 77 K, in Me-THF) (66)

Carbyne (or alkylidyne) complexes form another family of organometallics with emissive MLCT states [140, 141], e.g.,

$[W^0(CPh)(CO)_2(TMEDA)Br]$ ph. $\lambda_{max} = 640$ nm, toluene, r.t.
TMEDA = tetramethylethylenediamine $\phi = 5.3 \times 10^{-4}$, $\tau = 180$ ns (67)

These compounds are characterized by M≡CR triple bonds. The acceptor function of the carbyne ligand is associated with the presence of two degenerated π^* orbitals which are largely composed of p-orbitals of the coordinating carbon atom.

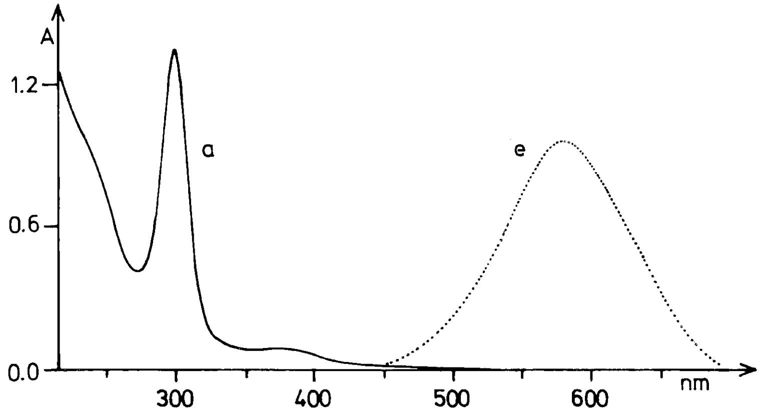

Fig. 9. Electronic absorption (*continuous line*) and emission (*dotted line*) spectra of $[(\eta\text{-}C_7H_7)Mo(CO)_3]PF_6$ at r.t. under argon. Absorption: 5.63×10^{-5} mol l^{-1} in EtOH, 1-cm cell. Emission: in MeCN, $\lambda_{exc} = 380$ nm, intensity in arbitrary units

Phosphines PR_3 are important π-acceptor ligands. Accordingly, phosphine complexes may have available emissive MLCT states [142], e.g.,

$[W^0(CO)_2(dppe)_2]$ ph. $\lambda_{max} = 568$ nm, Me-THF, 77 K
dppe = diphenyl- $\phi = 0.14$, $\tau = 0.14$ µs (68)
phosphinoethane

The origin of this emission is not quite clear. An IL assignment is also feasible. For another phosphine complex a luminescent MLCT state has been recently identified [143]:

$Re^I(binap)(CO)_3Cl$ ph. $\lambda_{max} = 570$ nm, ethanol, r.t., $\phi = 0.007$
binap = 2,2′-bis-(di-
phenylphosphino)-, (69)
1′-binaphthyl

In this case the binaphthyl moiety provides an extensive π-electron system. The binap ligand thus seems to be well suited as acceptor for a low-energy MLCT transition.

4.2
d^8 Metals

A variety of square planar complexes of reducing d^8 metals such as Rh^I, Ir^I, and Pt^{II} with acceptor ligands are characterized by low energy MLCT transitions. Olefin complexes belong to this category [76, 124, 144] and at least one compound of this type is known to emit from an M → olefin MLCT state [145]:

$[Ir^I(en)(cod)]^+$ ph. $\lambda_{max} = 488$ and 508 nm,
EtOH/MeOH, 77 K
en = ethylenediamine; (70)
cod = 1,5–cyclooctadiene

However, the MLCT state is apparently mixed with an MC d → p state in this case. When en is replaced by bipy the emission is shifted to longer wavelength and originates from an Ir^I → bipy MLCT state [145]:

$[Ir^I(bipy)(cod)]^+$ ph. $\lambda_{max} = 719$ nm, ethanol/methanol/
CH_2Cl_2, 77 K (71)
$\tau = 0.5$ µs

Rh(I) polypyridyl complexes also show emissions from such MLCT states [145]. Rh(I), Ir(I), and Pt(II) complexes with maleonitriledithiolate (mnt^{2-}) constitute another family of MLCT emitters [146], e.g.,

$(TBA)[Rh^I(CO)_2(mnt)]$ ph. $\lambda_{max} = 609$ nm, solid, 77 K
TBA^+ = tetrabutyl- $\tau = 238$ µs (72)
ammonium)

The vibrational structure of the luminescence spectra provides evidence for the assumption that the emission comes indeed from M → mnt^{2-} MLCT states.

Finally, some Pt(II) complexes with orthometalated ligands related to bipy display a luminescence from MLCT states [147], e.g.,

$[\mathrm{Pt^{II}(thpy)_2}]$ ph. $\lambda_{\mathrm{max}} = 585$ nm, methylcyclohexane, r.t.
$\mathrm{thpy^-}$ = deprotonated $\phi = 0.36$, $\tau = 3.2\ \mu\mathrm{s}$ (73)
2-(2-thienyl) pyridine

4.3
d^{10} Metals

Cu$^{\mathrm{I}}$ polypyridyl complexes are well known to emit from MLCT states [126, 148–150], e.g.,

$[\mathrm{Cu^I}$(2,9-diphenyl- ph. $\lambda_{\mathrm{max}} = 710$ nm, $\mathrm{CH_2Cl_2}$, r.t.
o-phen$)_2]^+$ $\phi = 1.1 \times 10^{-3}$, $\tau = 0.25\ \mu\mathrm{s}$ (74)

It is assumed that such tetrahedral complexes are distorted towards a planar structure in the MLCT state. In this planar geometry additional ligands may be attached. Since these exciplexes are not emissive the luminescence of Cu$^{\mathrm{I}}$ polypyridyl complexes can be quenched by a variety of nucleophiles. Recently, it has been shown that sterically demanding polypyridyl ligands restrict this exciplex formation and increase the emission quantum yields considerably [151].

Au(I) complexes may also show low-energy MLCT transitions. However, MC, ds, and dp transitions, as well as LMCT transitions, can occur in the same energy range [120]. Mixing of these transitions is possible, too. Accordingly, definite assignments are hampered by these complications. Nevertheless, a binuclear Au(I) complex was suggested to show low-energy MLCT transitions. This compound is also luminescent [152]:

$[\mathrm{Au_2^I(dmb)(CN)_2}]$ ph. $\lambda_{\mathrm{max}} = 468$ nm, $\mathrm{CH_2Cl_2}$, r.t.
dmb = 1,8-di-isocyano- $\tau = 0.13\ \mu\mathrm{s}$ (75)
p-menthane

Pt(0) complexes are also suitable candidates for the existence of low-energy MLCT transitions. Recently, the emission of a Pt(0) complex was attributed to a MLCT excited state [153]:

$[\mathrm{Pt^0(binap)_2}]$ ph. $\lambda_{\mathrm{max}} = 730$ nm, benzene, r.t.
binap = 2,2′-bis- $\phi = 0.024$, $\tau = 1.5\ \mu\mathrm{s}$ (76)
(diphenylphosphino)-,
1′-binaphthyl

The binap ligand is certainly able to provide π^* orbitals for a low-energy MLCT transition owing to the extended π-electron system of the binaphthyl substituent at the coordinating phosphorus atoms. However, the emission is suspiciously close to that of $[\mathrm{Pt^0(PPh_3)_4}]$ ($\lambda_{\mathrm{max}} = 740$ nm) [52] and $[\mathrm{Pt^0(PPh_3)_3}]$ ($\lambda_{\mathrm{max}} = 705$ nm) [51]. In these cases the luminescence was assigned to an MC dp excited state.

5
Ligand-to-Ligand Charge Transfer Excited States

Coordination compounds of the type L_{red}-M-L'_{ox} which simultaneously contain reducing and oxidizing ligands are frequently characterized by low-energy LLCT transitions [7, 154]. The metal mediates the electronic interaction between donor (L_{red}) and acceptor (L_{ox}) ligand. Suitable acceptor ligands include porphyrins and polypyridyls while anions such as halides, thiolates, and carbanions may serve as donor ligands. Some of these complexes have been observed to emit from LLCT states. Unfortunately, unambiguous assignments of LLCT transitions are frequently hampered by the presence of other transitions such as MC, LMCT, and MLCT in the same energy range. The identification of LLCT transitions is facilitated if MC, LMCT, and MLCT are absent or occur at rather high energies.

5.1
d^0 Metals

Complexes of d^0 metals which are only weakly oxidizing are well suited to detect emitting LLCT states [155], e.g.,

$[Cp_2Zr^{IV}biq]^{2+}$ ph. $\lambda_{max} = 518$ nm, THF, r.t. [155]
biq = 2,2′-biquinoline; $\phi = 0.01$ (77)
Cp = cyclopentadienyl

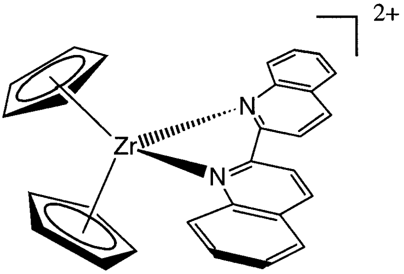

Structure 2

The luminescence originates from a $Cp^- \rightarrow$ biq LLCT triplet. The complex shares some remarkable features with the photosynthetic reaction center which is characterized by a pair of two bacteriochlorophyll molecules in close proximity but in an oblique orientation ("special pair"). In the primary photochemical step charge separation takes place by excited state electron transfer from this special pair to an acceptor. In the case of $[Cp_2Zr^{IV}biq]^{2+}$ the special pair is represented by both Cp^- ligands. However, in this complex charge separation takes place by a direct optical transition.

5.2
d^6 Metals

The lowest-energy excited state of Re^I(1,2-diimine)$(CO)_3X$ may switch from MLCT to $X^- \rightarrow$ diimine LLCT if X^- (e.g., alkyl anion) is a strong donor and provides the HOMO for the complex [156]. Unfortunately, such LLCT states are not emissive but reactive. However, a luminescent LLCT state can be observed by an appropriate choice of metal and ligands [157], e.g.,

$[Os^{II}(bipy)_2(CO)(DMABN)]^{2+}$ ph. $\lambda_{max} = 645$ nm, CH_2Cl_2, r.t.
DMABN = 4-(N,N-dimethylamino)benzonitrile $\phi = 6 \times 10^{-3}$ (78)

This DMABN → bipy LLCT state does not appear in absorption, but only in emission.

5.3
d^8 Metals

A variety of square planar complexes of the type M^{II}(1,2-diimine)(dithiolate) with M = Ni, Pd, and Pt are characterized by low-energy ($dithiolate^{2-} \rightarrow$ 1,2-diimine) LLCT transitions [7, 154, 158]. Such LLCT states may be luminescent (Fig. 10) [159], e.g.,

$[Pt^{II}(bipy)(tdt)]$ ph. $\lambda_{max} = 654$ nm, ethanol, 77 K
tdt^{2-} = 3,4-toluenedithiolate (79)

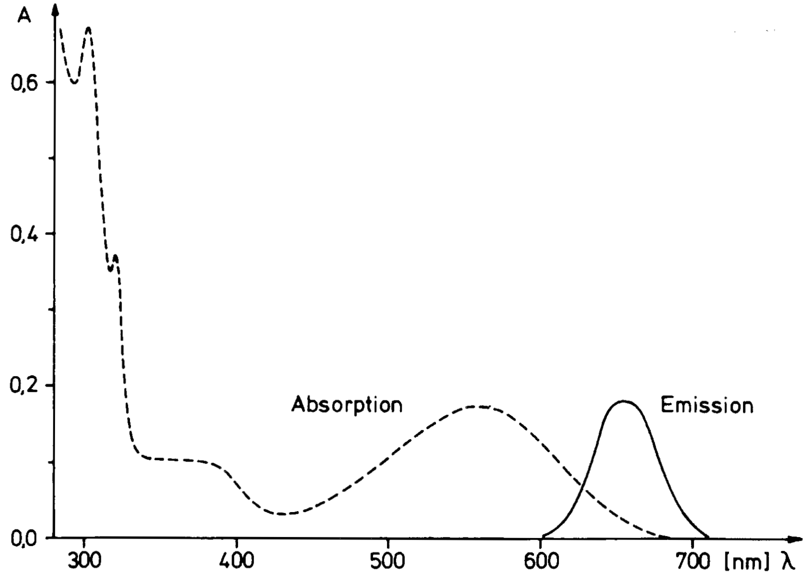

Fig. 10. Electronic absorption (*dashed line*) and emission (*continuous line*) spectrum of [(bipy)Pt(tdt)] in ethanol. Absorption: 4.9×10^{-5} mol l^{-1} at r.t., 1-cm cell. Emission: at 77 K, $\lambda_{exc} = 546$ nm; intensity in arbitrary units

In a later study it has been shown that this phosphorescence also occurs in CH_2Cl_2 at r.t. ($\lambda_{max} = 735$ nm, $\phi = 3.1 \times 10^{-4}$, $\tau = 0.29$ µs) [160]. Numerous other complexes of the type Pt^{II}(1,2-diimine)(dithiolate) have been also observed to be luminescent under ambient conditions [160].

5.4
d^{10} Metals

Pseudotetrahedral Zn(II) and Cd(II) complexes of the general composition [M (1,2-diimine)(S-aryl)$_2$] display also an emission from LLCT states [161–163], e.g.,

[Zn(o-phen) (4-Cl-Ph-S)$_2$] fl. $\lambda_{max} = 568$ nm, solid, 77 K
$\tau < 15$ ns (fl) and $\tau = 4.2$ µs (ph) (80)

The luminescence consists of a fluorescence and phosphorescence which were distinguished by their lifetimes.

Polynuclear complexes are also known to display emissions from LLCT states [86, 87, 164], e.g.,

$[Cu^I_4I_4(pyridine)_4]$ ph. $\lambda_{max} = 480$ nm, toluene, r.t.
$\phi = 3.4 \times 10^{-4}$, $\tau = 0.45$ µs (81)

In addition to this luminescence from a $I^- \rightarrow$ pyridine LLCT state a second more intense emission occurs at longer wavelength ($\lambda_{max} = 690$ nm) which comes from the cluster-centered excited state of $I^- \rightarrow Cu^I$ LMCT and MC ds parentage.

6
Metal-to-Metal Charge Transfer Excited States

MMCT transitions occur in polynuclear complexes with bridging ligands between oxidizing and reducing metal centers (M_{red}-L-M'_{ox}) [6, 7, 165, 166]. Mixed-valence (MV) compounds are typical examples [167–169]. MV complexes have not been observed to emit. This is not surprising since for symmetrical MV complexes there is no energy difference between the "ground state" (e.g., $[(NH_3)_5Ru_a^{II}\text{-µl-}Ru_b^{III}(NH_3)_5]^{5+}$) and the "MMCT state" ($[(NH_3)_5Ru^{III}_a\text{-µL-}Ru^{II}_b(NH_3)_5]^{5+}$) which are both equivalent. Even for non-symmetrical MV complexes (e.g., $[(NH_3)_5Ru^{III}\text{-µNC-}Ru^{II}(CN)_5\ ]^-$) [170] the small energy difference between ground and MMCT state prevents an emission (energy gap law). However, heteronuclear complexes with larger energy differences between ground and MMCT states are good candidates for luminescent MMCT states. Surprisingly, very little is known on MMCT emissions. Recently an interesting example was reported [171]:

$[Cu^I_3(dppm)_3W^{VI}S_4]^+$ ph. $\lambda_{max} = 615$ nm, solid, r.t.
dppm = bis(diphenylphosphino)methane $\tau = 2.8$ µs (82)

This tetranuclear d^{10}-d^0 complex contains reducing Cu(I) and oxidizing W(VI) which are bridged by sulfide ligands. Calculations led to the conclusion that the emission originates from a $Cu^I \rightarrow W^{VI}$ MMCT triplet.

Solid state systems which contain s^2 donors such as Pb^{2+} and Bi^{3+} and d^0 acceptors including Zr(IV), V(V), and W(VI) are characterized by low-energy $s^2 \rightarrow d^0$ MMCT transitions. These s^1d^1 MMCT states are emissive [61, 172, 173], e.g.,

$PbWO_4$ ph. $\lambda_{max} = 516$ nm, solid, r.t. (83)

Some luminescent materials are obtained by doping d^0 compounds with s^2 ions [61, 172, 174], e.g.,

$YVO_4{:}Bi^{3+}$ ph. $\lambda_{max} = 559$ nm, solid, r.t.
$\phi = 0.76$, $\tau = 4.5$ µs (84)

Although compounds with luminescent MMCT states are still a rarity it is anticipated that many more examples will be discovered in the future.

7
Ligand-Centered (or Intraligand) Excited States

There is a large number of complexes which luminesce from IL excited states. Any organic compound which emits in the coordinated state belongs to this category. Owing to the diversity of such luminophores it is difficult to treat this subject in a systematic manner. Only a few features of IL luminescence are outlined here.

The identification of an IL emission is rather simple if the luminescence of a free ligand does not change upon coordination. Generally, the electronic coupling between the emitting part of the ligand and the metal is quite weak in these cases. Frequently, the IL luminophore and the metal are separated by an electronically insulating bridge [175], e.g.,

$[\text{2-naphthyl-CONH–}(CH_2)_n\text{-COO-}Co^{III}(NH_3)_5]^{2+}$ (n = 1 – 5)
fl. $\lambda_{max} = 354$ nm, H_2O, r.t., $\tau \sim 10^{-8}$ s (85)

This complex shows the fluorescence of the naphthyl group which is protected from the metal by the saturated $\text{-}CH_2\text{-}$ chain of the bridging amino acid. However, there is a residual electronic interaction between the naphthyl group and the metal as indicated by a partial fluorescence quenching which is caused by excited state electron transfer from the naphthyl substituent to Co(III).

When the interaction between metal and ligand is much stronger the electronic structure of the ligand is modified. Accordingly, the emission of the free ligand changes upon coordination, but it still appears provided the emitting IL state is the lowest-energy excited state of the complex [176]. Since a variety of metals such as Mg^{2+}, Al^{3+}, Zn^{2+}, Th^{4+} do not participate in low-energy electronic transitions (MC, LMCT, MLCT, MMCT), any luminescence of complexes of these metals is of the IL type [177], e.g.,

$[Al^{III}(\text{oxinate})_3]$ fl. $\lambda_{max} = 540$ nm, DMF, r.t.
oxinate- = 8–quino- $\phi = 0.12$, $\tau = 10$ ns (86)
linolate (see below)

Even at low temperatures an IL phosphorescence is not observed because aluminum is a very light metal and apparently does not induce any intersystem crossing (ISC) in the ligand. In zinc complexes a moderate ISC takes place. In addition to an IL fluorescence at r.t., an IL phosphorescence appears, but only at low temperatures [178], e.g.,

$$[\mathrm{Zn^{II}(bipy)_3}]^{2+} \qquad \begin{array}{l} \text{fl. } \lambda_{max} = 328\text{ nm, methanol/water, 77 K,} \\ \quad \phi = 0.39 \\ \text{ph. } \lambda_{max} = 465\text{ nm, methanol/water, 77 K} \\ \quad \phi = 0.019, \tau = 1.75\text{ s} \end{array} \tag{87}$$

Generally, in complexes of heavy metals starting with elements of the second transition series, strong spin-orbit coupling facilitates spin-forbidden transitions (heavy atom effect). As a consequence the IL fluorescence is partially or completely quenched since the fluorescing IL singlet is rapidly deactivated to the lowest IL triplet. Owing to the reduced radiative lifetime of the IL triplet, the IL phosphorescence appears now at r.t. because competing radiationless deactivations are no longer fast enough to quench the IL phosphorescence (Fig. 11) [179], e.g.,

$$\begin{array}{ll} [\mathrm{Th^{IV}(Me\text{-}oxinate)_4}] & \text{fl. } \lambda_{max} = 510\text{ nm; ph. } \lambda_{max} = 775\text{ nm} \\ \text{Me-oxinate}^- = \text{2-methyl-} & \mathrm{CH_3CN}\text{, r.t.} \\ \text{8-quinolinolate} & \end{array} \tag{88}$$

Complexes of metals which can participate in low-energy electronic transitions are usually not observed to emit from IL states. This applies, for example, to complexes of open-shell metals of the first transition series such as iron and co-

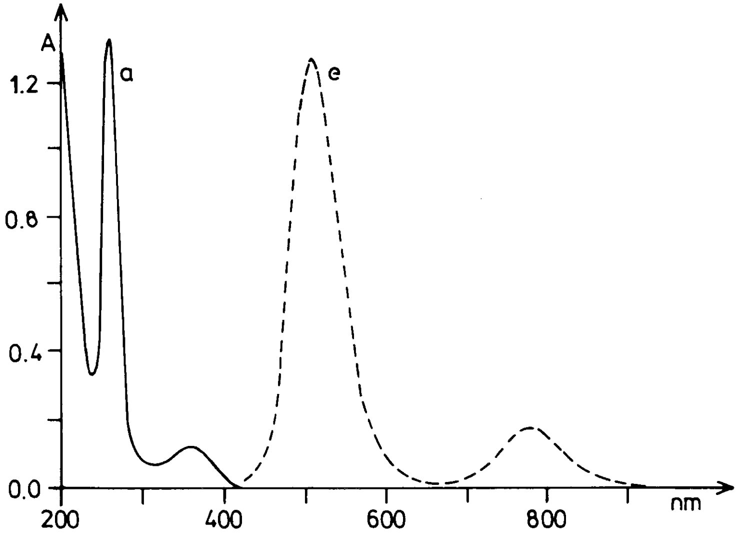

Fig. 11. Electronic absorption (a, *continuous line*) and emission (e, *dashed line*) spectra of 2.95 × 10^{-5} mol l^{-1} [Th(Me-oxinate)$_4$] in acetonitrile under argon at r.t., 1-cm cell. Emission: λ_{exc} = 360 nm, intensity in arbitrary units

balt which have available LF states at rather low energies. On the other hand, LF states of complexes with second- and third-row transition metals occur at much higher energies and are thus frequently located at energies well above those of IL states. Accordingly, an IL emission may be observed. Again, it is mostly a phosphorescence owing to the heavy atom effect [85, 180, 181], e.g.,

$[\mathrm{Pt^{II}(Ph_2\text{-}o\text{-}phen)(CN)_2}]$ ph. $\lambda_{max} = 530$ nm, polyethylene glycol, r.t.
$\mathrm{Ph_2\text{-}o\text{-}phen} = 4,7\text{-}$diphenyl-1, 10-phenanthroline $\tau = 0.1$ μs (89)

$[\mathrm{Pt^{IV}(bipy)(CH_3)_3I}]$ ph. $\lambda_{max} = 528$ nm, ethanol, r.t. (90)

$[\mathrm{Rh^{III}(bipy)_3}]^{3+}$ ph. $\lambda_{max} = 490$ nm, CH_3CN, r.t. $\tau < 15$ ns (91)

An IL assignment is frequently supported by the appearance of a vibrational structure of the low-temperature phosphorescence.

If the metals are reducing (e.g., Ru^{II}, Re^{I}) IL and MLCT states may occur at comparable energies. Moreover, IL and MLCT transitions can mix. Only a careful analysis then reveals the nature of the emitting state. However, this interference can be avoided by ligands which have low-energy IL states but are weak acceptors. In these cases IL states are located well below MLCT states and IL emissions are observed. Suitable are certain anionic ligands such as ortho-metallated phenylpyridine [126] and oxinate [177] (Fig. 12) [182, 183] (Struct. 3, 4) e.g.,

$\mathrm{Re^{I}(CO)_4(bzq)}$ ph. $\lambda_{max} = 540$ nm, benzene, r.t.
$\mathrm{bzq^-}$ = benzo[*h*]quinolin-10-yl $\tau = 6.4$ μs (92)

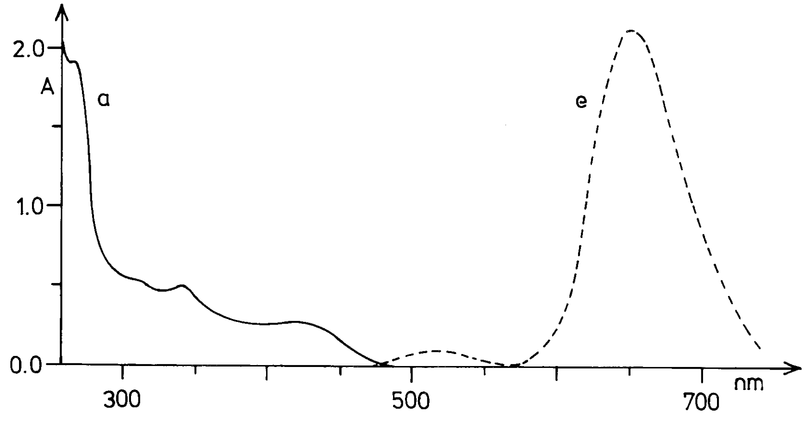

Fig. 12. Electronic absorption (a, *continuous line*) and emission (e, *dashed line*) spectra of 1.31×10^{-4} mol l^{-1} $[\mathrm{Re(CO)_4(oxinate)}]$ in acetonitrile under argon at r.t., 1-cm cell. Emission: $\lambda_{exc} = 440$ nm, intensity in arbitrary units

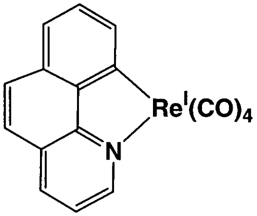

Structure 3

$Re^I(CO)_4$(oxinate) fl. (weak) $\lambda_{max} = 515$ nm, CH_3CN, r.t.
ph. (strong) $\lambda_{max} = 653$ nm, CH_3CN, r.t. (93)

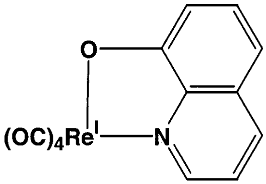

Structure 4

Metalloporphyrins constitute an important family of complexes which frequently emit from porphyrin IL states [13, 126, 184]. The characterization of emitting IL states outlined above also applies to metalloporphyrins and related complexes. For example, since zinc exerts only a moderate heavy atom effect, zinc porphyrins show an IL fluorescence at r.t. and a relatively long-lived phosphorescence at 77 K [185, 186], e.g.,

Zn^{II}TPP fl. $\lambda_{max} = 647$ nm, benzene
TPP = tetraphenyl- (methylcyclohexane), r.t.
porphyrin $\phi = 0.03, \tau = 2.7$ ns (94)
ph. $\lambda_{max} = 780$ nm, methylcyclohexane, 77 K
$\phi = 0.04, \tau = 0.04, \tau = 2.4$ ms

Iron porphyrins are not luminescent. In the case of Fe^{II}TPP (CO)(piperidine) the lowest excited state is a photoactive LF state [187]. If Fe(II) is replaced by Ru(II) [187] or Os(II) [188] the LF states are shifted above the porphyrin IL states. Accordingly, an IL emission appears [188]:

Os^{II}(TTP)(CO) ph. $\lambda_{max} = 653$ nm, CH_2Cl_2, r.t.
(CH_3OH) $\phi = 4 \times 10^{-3}, \tau = 0.01$ µs (95)
TTP = tetratolylporphyrin

Owing to the heavy-atom effect of osmium, the complex is only phosphorescent and this emission occurs even at r.t. Palladium and platinum porphyrins also display an IL phosphorescence under ambient conditions [3, 4, 126, 184, 189], e.g.,

Pt^{II}(Etio-P) ph. $\lambda_{max} = 641$ nm, NEt_3, r.t.
Etio-P = etioporphyrin $\phi \sim 0.3$ (in Me-THF), $\tau \sim 65$ µs (96)

Corrin is a ligand which is related to porphyrin. Vitamin B_{12} (cyanocobalamin) is a Co(III) corrin complex which is also not luminescent but photoactive owing to the presence of low-energy LF states [190] in analogy to $Fe^{II}TPP(CO)$(piperidine). Again, when Co(III) is replaced by Rh(III) the complex becomes luminescent because the photoactive LF state is then located above the emissive corrin IL excited state [190]:

$Rh^{III}(corrin)Cl_2$ λ_{max} = 632 nm, solid, r.t. or 77 K
corrin = 1,2,2,7,7,12,12- (97)
heptamethyl-15-cyanocorrin

8
Intraligand Charge Transfer Excited States

A ligand itself may consist of a reducing and oxidizing part. Accordingly, ILCT transitions can then exist [6, 7, 154] and an emission from ILCT states could appear. Indeed, such emissions have been observed.

The most common type of ILCT transition involves the promotion of an electron from a metal-ligand σ-bond to a π^* orbital of the same ligand [7]. Such ILCT transitions can occur at low energies if the M-L σ-bonding MO is located at rather high energies. Organometallics with aryl ligands might serve as simple examples.

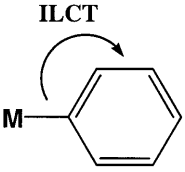

Structure 5

While ILCT states of phenyl complexes are unknown, a variety of other complexes with more elaborate ligands have been reported to emit from ILCT states of this type although other expressions such as SBLCT (σ-Bond-to-Ligand CT) [191, 192] or σ-a_π [148] have also been used to label these ILCT states.

A metal-silicon σ-bond may also provide the donor site for an emissive ILCT state [191], e.g.,

$[Ir^{III}(dmiprsiqn)_3$ ph. λ_{max} ~ 620 nm, toluene, r.t.
dmiprsiqn = 6-iso- $\phi = 0.01$, $\tau = 1$ µs (98)
propyl-8-quinolyl
dimethylsilyl

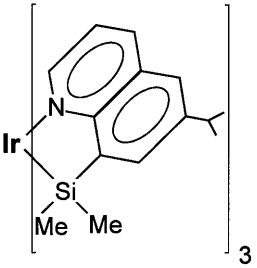

Structure 6

A variety of copper(I) arylphosphine complexes is characterized by emissive ILCT states [148, 193, 194], e.g.,

$[Cu^I(prophos)BH_4]$ prophos = 1,3-bis(diphenylphosphino) propane — ph. λ_{max} = 510 nm, benzene, r.t.; $\phi = 0.88$, $\tau = 4$ μs (99)

Structure 7

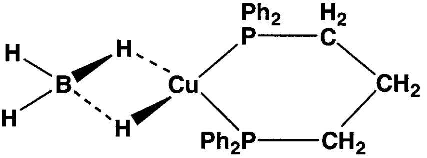

In this case ILCT involves a shift of electron density from Cu-P σ-bonds to the π^* orbitals of the phenyl substituents.

The emissive states of oxinate complexes which are described as IL states (see above) have apparently a considerable ILCT contribution [177, 183, 195]. Accordingly, such emissive states may be also termed ILCT [177], e.g.,

$[Pt^{II}(oxinate)_2]$ — ph. λ_{max} = 655 nm, DMF, r.t.; $\phi = 10^{-2}$, $\tau = 2.7$ μs (100)

ILCT in oxinate complexes is associated with the promotion of an electron from the Pt-O bond to the nitrogen atom of the heterocyclic ligand.

Recently, a different type of emissive ILCT state has been observed [196]:

$Pt^{II}(diphos)[S_2C_2(CH_2CH_2\text{-N-pyridinium})]^+$ — fl. λ_{max} = 677 nm, DMSO, r.t.; $\phi = 0.002$, $\tau = 0.2$ ns (101)
ph. λ_{max} = 732 nm, DMSO, r.t.; $\phi = 0.01$, $\tau = 8.3$ μs

Structure 8

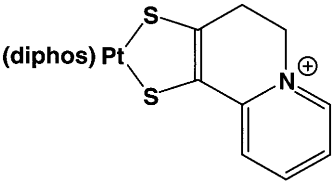

The pyridinium acceptor is covalently attached to the dithiolate donor which provides a π-electron for the ILCT transition.

Acknowledgment. We thank Professor Hans Güdel for providing valuable information.

9
References

1. Fleischauer PD, Fleischauer P (1970) Chem Rev 70:199
2. Demas JN, DeGraff BA (1991) Anal Chem 63:829A
3. Vinogradov SA, Wilson DF (1995) J Chem Soc Perkin Trans 2 103 and references cited therein
4. Wilson DF, Vinogradov SA, Lo L-W, Huang L (1996) Adv Exp Med Biol 388:101
5. Baldo MA, Lamansky S, Burrows PE, Thompson ME, Forrest SR (1999) Appl Phys Letters 75:4 and references cited therein
6. Vogler A, Kunkely H (1993) Charge transfer excitation of coordination compounds. Generation of reactive intermediates. In: Kalyanasundaram K, Grätzel M (eds) Photosensitization and photocatalysis using inorganic and organometallic compounds. Kluwer, Dordrecht, p 71
7. Vogler A, Kunkely H (1997) Comments Inorg Chem 19:283
8. Lever ABP (1984) Inorganic electronic spectroscopy. Elsevier, Amsterdam
9. Balzani V, Carassiti V (1970) Photochemistry of coordination compounds. Academic Press, New York
10. Adamson AW, Fleischauer PD (1975) Concepts of inorganic photochemistry. Wiley-Interscience, New York
11. Sykora J, Sima J (1990) Coord Chem Rev 107:1
12. Ferraudi GJ (1988) Elements of inorganic photochemistry. Wiley, New York
13. Roundhill DM (1994) Photochemistry and photophysics of metal complexes. Plenum Press, New York
14. Gächter BF, Konigstein JA (1974) J Chem Phys 60:2003
15. Moulton P (1982) Opt News 8:9
16. Albers P, Stark E, Huber G (1986) J Opt Soc Am B 3:134
17. Imbusch GF, Donegan JF, Bergin FJ (1987) In: DiBartolo B (ed) Spectroscopy of solid-state laser-type materials. New York, p 165
18. Huber G (1996) In: Miller A, Finlayson DM (eds) Laser sources and applications. Institute of Physics, Bristol, p 141
19. Mohammed AK, Maverick AW (1992) Inorg Chem 31:4441
20. Kunkely H, Vogler A (1999) Chem Phys Lett 302:583
21. Brunold T, Herren M, Oetliker U, Güdel H-U, Kesper U, Albrecht C, Reiner D (1994) J Lumin 60/61:138
22. Neyhart GA, Seward KJ, Boaz J, Sullivan BP (1991) Inorg Chem 30:4486
23. Yam VW-W, Che C-M (1990) Coord Chem Rev 97:93
24. Schläfer HL (1970) Z Chemie 10:9
25. Chatterjee KK, Forster LS (1964) Spectrochim Acta 20:1603
26. Porter GB, Schläfer HL (1963) Z Phys Chem (Frankfurt) 37:109
27. Porter GB (1975) In: Adamson AW, Fleischauer PD (eds) Concepts of inorganic photochemistry. Wiley-Interscience, New York, chap 2, p. 37
28. Kirk AD, Porter GB (1980) J Phys Chem 84:887
29. Wermuth M, Güdel HU (1997) Chem Phys Lett 281:81
30. Wrighton M, Ginley D (1974) Chem Physics 4:295
31. Wilson RB, Solomon EI (1980) J Am Chem Soc 102:4085
32. Mingardi M, Porter GB (1966) J Chem Phys 44:4354
33. Crosby GA (1967) J Chim Phys 64:160
34. Crosby GA (1975) Acc Chem Res 8:231
35. Wrighton MS, Pdungsap L, Morse DL (1975) J Phys Chem 79:66
36. Ford PC, Wink D, Dibenedetto J (1983) Progr Inorg Chem 30:213
37. Thomas TR, Crosby GA (1971) J Mol Spectros 38:118
38. Douglas IN, Nicholas JV, Wybourne BG (1968) J Chem Phys 48:1415
39. Zuloaga F, Kasha M (1968) Photochem Photobiol 7:549

40. Brunold TC, Güdel HU, Cavalli E (1996) Chem Phys Lett 252:112
41. Pelletier Y, Reber C (1997) Inorg Chem 36:721 and references cited therein
42. Yersin H, Otto H, Zink JI, Gliemann G (1980) J Am Chem Soc 102:951
43. Preston DM, Güntner W, Lechner A, Gliemann G, Zink JI (1988) J Am Chem Soc 110:5628
44. Broser I, Hoffmann A, Heitz R, Thurian P (1991) J Lumin 48/49:693
45. Broser I, Podlowski L, Thurian P, Heitz R, Hoffmann A (1994) J Lumin 60/61:588
46. Koutek ME, Mason WR (1980) Inorg Chem 19:648
47. Savas MM, Mason WR (1987) Inorg Chem 26:301
48. Kunkely H, Vogler A (1992) Inorg Chem 31:4539
49. Assefa Z, McBurnett BG, Staples RJ, Fackler JP Jr (1995) Inorg Chem 34:4965
50. Kunkely H, Vogler A (1997) J Organomet Chem 541:177
51. Harvey PD, Gray HB (1998) J Am Chem Soc 110:2145
52. Caspar JV (1985) J Am Chem Soc 107:6718
53. Geoffroy GL, Wrighton MS, Hammond GS, Gray HB (1974) J Am Chem Soc 96:3105
54. Andrews LJ (1978) Inorg Chem 17:3108
55. Fordyce WA, Crosby GA (1982) Inorg Chem 21:1455
56. Vogler A, Nikol H (1992) Pure Appl Chem 64:1311
57. Vogler A, Nikol H (1993) Comments Inorg Chem 14:245
58. Fukuda A, Inohara K, Onaka R (1964) J Phys Soc Japan 19:1274
59. Ranfangni A, Mugnai D, Bacci M, Viliani G, Fontane MP (1983) Adv Phys 32:823
60. Blasse G (1983) Rev Inorg Chem 5:319
61. Blasse G (1988) Progr Solid State Chem 18:79
62. Thompson LC (1979) In: Gschneider KA, Eyring L (eds) Handbook on the physics and chemistry of rare earths, vol 3. North-Holland, Amsterdam, p 209
63. Carnall WT (1979) In: Gschneider KA, Eyring L (eds) Handbook on the physics and chemistry of rare earths, vol 3. North-Holland, Amsterdam, p 171
64. Reisfeld R (1975) Struct Bonding (Berlin) 22:123
65. Reisfeld R, Jorgensen CK (1977) Lasers and excited states of rare earths. Inorg Chem Concepts 1:1
66. Blasse G (1979) In: Gschneider KA, Eyring L (eds) Handbook on the physics and chemistry of rare earths, vol 4. North-Holland, Amsterdam, p 237
67. Winston H, Marsh OJ, Suzuki CK, Telk CL (1963) J Chem Phys 39:267
68. Dawson WR, Kropp JL, Windsor MW (1966) J Chem Phys 45:2410
69. Szczurek T, Schlesinger M (1985) In: Jezowska-Trzebiatowska B, Legendziewicz J, Strek (eds) Rare earth spectroscopy. World Scientific, Singapore, p 309
70. Sabbatini N, Ciano M, Dellonte S, Bonazzi A, Balzani V (1984) J Phys Chem 88:1534
71. Blasse G, Dirksen GJ, Sabbatini N, Perathoner S (1987) Inorg Chim Acta 133:167
72. Roundhill DM, Gray HB, Che C-M (1989) Acc Chem Res 22:55
73. Fackler JP Jr, Assefa Z, Forward JM, Staples RJ (1994) Met-Based Drugs 1:459
74. King C, Wang J-C, Khan MNI, Fackler JP Jr (1989) Inorg Chem 28:2145
75. Sabin F, Vogler A (1992) Monatshefte Chem 123:705
76. Geoffroy GL, Wrighton MS (1979) Organometallic photochemistry. Academic Press, New York
77. Stiegman AE, Miskowski VM (1988) J Am Chem Soc 110:4053
78. Hopkins MD, Gray HB (1984) J Am Chem Soc 106:2468
79. Yam VW-W, Lai TF, Che C-M (1990) J Chem Soc Dalton Trans 3747
80. Balch AL (1994) Progr Inorg Chem 41:239
81. Kunkely H, Vogler A (1999) Chem Phys Lett 308:169
82. Kunkely H, Horvath O, Vogler A (1997) Coord Chem Rev 159:85
83. Kunkely H, Vogler A (1995) Chem Phys Lett 240:31
84. Kunkely H, Vogler A (1993) Chem Phys Lett 206:467
85. Kunkely H, Vogler A (1991) Coord Chem Rev 111:15
86. Ford PC, Vogler A (1993) Acc Chem Res 26:220
87. Ford PC, Cariati E, Bourassa J (1999) Chem Rev 99:3625
88. Kunkely H, Vogler A (1988) Chem Phys Lett 150:135

89. Kunkely H, Vogler A (1991) Inorg Chim Acta 186:155
90. Maverick AW, Najdzionek JS, MacKensie D, Nocera DG, Gray HB (1983) J Am Chem Soc 105:1878
91. Sabin F, Ryu CK, Ford PC, Vogler A (1992) Inorg Chem 31:1941
92. Kunkely H, Vogler A (1998) Transit Met Chem 23:207
93. Kunkely H, Vogler A (1991) Chem Phys Lett 187:609
94. Arnold FP, Burdett JK, Sita LR (1998) J Am Chem Soc 120:1637
95. Gliemann G, Yersin H (1985) Structure and Bonding 62:87
96. Schindler JW, Fukuda RC, Adamson AW (1982) J Am Chem Soc 104:3696
97. Pfennig BW, Thompson MW, Bocarsly AB (1989) J Am Chem Soc 111:8947
98. Paulson S, Sullivan BP, Caspar JV (1992) J Am Chem Soc 114:6905
99. Kenney JW III, Boone DR, Striplin DR, Chen Y-H, Hamar KB (1993) Organometallics 12:3671
100. Yam VW-W, Qi G-Z, Cheung K-K (1997) J Organomet Chem 548:289
101. Herrmann WA, Kühn FE, Fiedler DA, Mattner MR, Geisberger MR, Kunkely H, Vogler A, Steenken S (1995) Organometallics 14:5377
102. Kunkely H, Türk T, Teixeira C, de Bellefon CM, Herrmann WA, Vogler A (1991) Organometallics 10:2090
103. Pollagi TP, Stoner TC, Dallinger RF, Gilbert TM, Hopkins MD (1991) J Am Chem Soc 113:703
104. Thorn DL, Harlow RL (1992) Inorg Chem 31:3917
105. Heinselman KS, Hopkins MD (1995) J Am Chem Soc 117:12,340
106. Williams DS, Thompson DW, Korolev AV (1996) J Am Chem Soc 118:6526
107. Williams DS, Korolev AV (1998) Inorg Chem 37:3809
108. Vogler A, Kunkely H (1981) Inorg Chim Acta 53:L215
109. Bandy JA, Cloke FGN, Cooper G, Day JP, Girling RB, Graham RG, Green JC, Grinter R, Perutz RN (1988) J Am Chem Soc 110:5039
110. Lee YF, Kirchhoff JR (1994) J Am Chem Soc 116:3599
111. Bahnemann DW, Kormann C, Hoffmann MR (1987) J Phys Chem 91:3789
112. Türk T, Vogler A, Fox MA (1993) Advances in Chemistry Series 238:233
113. Kunkely H, Vogler A (1990) J Chem Soc Chem Commun 1205
114. Türk T, Resch U, Fox MA, Vogler A (1992) Inorg Chem 31:1854
115. Türk T, Resch U, Fox MA, Vogler A (1992) J Phys Chem 96:3818
116. Kunkely H, Vogler A (1989) Chem Phys Lett 164:621
117. Albinati A, Casarin M, Maccato C, Pandolfo L, Vittadini A (1999) Inorg Chem 38:1145
118. Vogler A, Kunkely H (1986) J Am Chem Soc 108:7211
119. Kunkely H, Vogler A (1997) J Photochem Photobiol A Chem 105:7
120. Kunkely H, Vogler A (1996) Z Naturforsch 51b:1067
121. Jones WB, Yuan J, Narayanaaswamy R, Young MA, Elder RC, Bruce AE, Bruce MRM (1995) Inorg Chem 34:1996
122. Bell JT, Biggers RE (1965) J Mol Spectrosc 18:247
123. Jorgensen CK, Reisfeld R (1982) Struct Bonding (Berlin) 50:136
124. Lees AJ (1987) Chem Rev 87:711
125. Vogler A, Kunkely H (1998) Coord Chem Rev 177:81
126. Kalyanasundaram K (1992) Photochemistry of polypyridine and porphyrin complexes. Academic Press, London
127. Yersin H, Vogler A (1987) Photochemistry and photophysics of coordination compounds, Springer, Berlin Heidelberg New York
128. Juris A, Balzani V, Barigelletti F, Campagna S, Belser P, von Zelewsky A (1988) Coord Chem Rev 84:85
129. Yersin H, Humbs W, Strasser J (1997) Electronic and vibronic spectra of transition metal complexes, vol. II. In: Yersin H (ed) Topics in Current Chemistry 191. Springer, Berlin Heidelberg New York, p 153
130. Manuta DM, Lees AJ (1986) Inorg Chem 25:1354
131. Stufkens DJ (1990) Coord Chem Rev 104:39

132. Stufkens DJ (1992) Comments Inorg Chem 13:359
133. Wrighton M, Morse DL (1974) J Am Chem Soc 96:998
134. Balzani V, Juris A, Venturi M, Campagna S, Serroni S (1996) Chem Rev 96:759
135. Crosby GA, Perkins WG, Klassen DM (1965) J Chem Phys 43:1498
136. Watts RJ (1983) J Chem Ed 60:834
137. Warren KD (1976) Struct Bonding 27:45
138. Kunkely H, Vogler A (1998) J Chem Soc Chem Commun 395
139. Mann KR, Gray HB, Hammond GS (1977) J Am Chem Soc 99:306
140. Cavalheiro CCS, Torraca KE, Schanze KS, McElwee-White L (1999) Inorg Chem 38:3254 and references cited therein
141. Bocarsly AB, Cameron RE, Rubin HD, McDermott GA, Wolff CR, Mayr A (1985) Inorg Chem 24:3976
142. Caruana A, Kisch H (1979) Angew Chem Int Ed Engl 18:328
143. Vogler A, Kunkely H (1999) Inorg Chem Commun 2:533
144. Vogler A, Kunkely H (1999) Comments Inorg Chem 21:149
145. Fordyce WA, Crosby GA (1982) Inorg Chem 21:1023
146. Johnson CE, Eisenberg R, Evans TR, Burberry MS (1983) J Am Chem Soc 105:1795
147. Maestri M, Sandrini D, Balzani V, Chassot L, Joliet P, von Zelewsky A (1985) Chem Phys Lett 122:375
148. Kutal C (1990) Coord Chem Rev 99:213
149. McMillin DR, McNett KM (1998) Chem Rev 98:1201
150. Gushurst AKI, McMillin DR, Dietrich-Buchecker CO, Sauvage J-P (1989) Inorg Chem 28:4070
151. Miller MT, Gantzel PK, Karpishin TB (1999) J Am Chem Soc 121:4292
152. Che C-M, Wong W-T, Lai T-F, Kwong H-L (1989) J Chem Soc Chem Commun 243
153. Tominaga H, Sakai K, Tsubomura T (1995) J Chem Soc Chem Commun 2273
154. Vogler A, Kunkely H (1990) Comments Inorg Chem 9:201
155. Kunkely H, Vogler A (1998) Eur J Inorg Chem 1863
156. Stufkens DJ, Vlcek A Jr (1996) The Spectrum 9:2
157. Perkins TA, Pourreau DB, Netzel TL, Schanze KS (1989) J Phys Chem 93:4511
158. Vogler A, Kunkely H, Hlavatsch J, Merz A (1984) Inorg Chem 23:506
159. Vogler A, Kunkely H (1981) J Am Chem Soc 103:1559
160. Cummings SC, Eisenberg R (1996) J Am Chem Soc 118:1949 and references cited therein
161. Truesdell KA, Crosby GA (1985) J Am Chem Soc 107:1787
162. Crosby GA, Highland RG, Truesdell KA (1985) Coord Chem Rev 64:41
163. Highland RG, Brummer JG, Crosby GA (1986) J Phys Chem 90:1593
164. Kyle KR, Ryu CK, Ford PC (1991) J Am Chem Soc 113:2954
165. Vogler A, Osman AH, Kunkely H (1985) Coord Chem Rev 64:159
166. Vogler A (1988) In: Fox MA, Chanon M (eds) Photoinduced electron transfer. Elsevier, part D, p 179
167. Brown D (1980) Mixed-valence compounds. Reidel, Dordrecht
168. Creutz C (1980) Inorg Chem 30:1
169. Hush NS (1967) Inorg Chem 8:391
170. Vogler A, Kisslinger J (1982) J Am Chem Soc 104:2311
171. Chan C-K, Guo C-X, Wang R-J, Mak TCW, Che C-M (1995) J Chem Soc Dalton Trans 753
172. Blasse G (1991) Struct Bonding 76:153
173. Groenink JA, Blasse G (1980) J Solid State Chem 32:9
174. Blasse G, Bril A (1968) J Chem Phys 48:217
175. Osman AH, Vogler A (1987) In: Yersin H, Vogler A (eds) Photochemistry and photophysics of coordination compounds. Springer, Berlin Heidelberg New York, p 197
176. Lytle FE (1970) Appl Spectrosc 24:319
177. Ballardini R, Varani G, Indelli MT, Scandola F (1986) Inorg Chem 25:3858
178. Ohno T, Kato S (1974) Bull Chem Soc Japan 47:2953
179. Kunkely H, Vogler A (1999) Chem Phys Lett 304:187
180. Kunkely H, Vogler A (1990) J Am Chem Soc 112:5625

181. Nishizawa M, Suzuki TM, Sprouce S, Watts RJ, Ford PC (1984) Inorg Chem 23:1837
182. Spellane P, Watts RJ, Vogler A (1993) Inorg Chem 32:5633
183. Kunkely H, Vogler A (1998) Inorg Chem Commun 1:398
184. Gouterman M (1978) In: Dolphin D (ed) The porphyrins, vol III. Academic Press, New York, part A, p 1
185. Quinby DJ, Longo FR (1975) J Am Chem Soc 97:5111
186. Harriman A (1981) J Chem Soc Faraday Trans 2 77:1281
187. Vogler A, Kunkely H (1976) Ber Bunsenges Phys Chem 80:425
188. Vogler A, Kisslinger J, Buchler JW (1985) In: Blauer G, Sund H (eds) Optical properties and structures of tetrapyrroles. de Gruyter, Berlin, p 107
189. Eastwood DL, Gouterman M (1970) J Mol Spectrosc 35:359
190. Vogler A, Hirschmann R, Otto H, Kunkely H (1976) Ber Bunsenges Phys Chem 80:420
191. Djurovich PJ, Watts RJ (1993) Inorg Chem 32:4681
192. Djurovich PJ, Watts RJ (1994) J Phys Chem 98:396
193. Segers DP, DeArmond MK, Grutsch PA, Kutal C (1985) Inorg Chem 23:2874
194. Liaw B, Orchard SW, Kutal C (1988) Inorg Chem 27:1311
195. Donges D, Nagle JK, Yersin H (1997) Inorg Chem 36:3040
196. Van Houten KA, Heath DC, Barringer CA, Rheingold AL, Pilato RS (1998) Inorg Chem 37:4647

Author Index Volume 201 - 213

Author Index Vols. 26 - 50 see Vol. 50
Author Index Vols. 51 - 100 see Vol. 100
Author Index Vols. 101 - 150 see Vol. 150
Author Index Vols. 151 - 200 see Vol. 200

The volume numbers are printed in italics

Astruc D, Blais J-C, Cloutet E, Djakovitch L, Rigaut S, Ruiz J, Sartor V, Valério C (2000) The First Organometallic Dendrimers: Design and Redox Functions. *210*:229 - 259
Augé J, see Lubineau A (1999) *206*:1 - 39
Baars MWPL, Meijer EW (2000) Host-Guest Chemistry of Dendritic Molecules. *210*:131 - 182
Ballauff M (2001) Structure of Dendrimers in Dilute Solution. *212*:177 - 194
Baltzer L (1999) Functionalization and Properties of Designed Folded Polypeptides. *202*:39 - 76
Bartlett RJ, see Sun J-Q (1999) *203*:121 - 145
Betzemeier B, Knochel P (1999) Perfluorinated Solvents - a Novel Reaction Medium in Organic Chemistry. *206*:61 - 78
Blais J-C, see Astruc D (2000) *210*:229 - 259
Bogár F, see Pipek J (1999) *203*:43 - 61
Brand SC, see Haley MM (1999) *201*:81 - 129
Bray KL (2001) High Pressure Probes of Electronic Structure and Luminescence Properties of Transition Metal and Lanthanide Systems. *213*:1 - 94
Bunz UHF (1999) Carbon-Rich Molecular Objects from Multiply Ethynylated π-Complexes. *201*:131 - 161
Chamberlin AR, see Gilmore MA (1999) *202*:77 - 99
Cloutet E, see Astruc D (2000) *210*:229 - 259
Cooper DL, see Raimondi M (1999) *203*:105 - 120
Cornils B (1999) Modern Solvent Systems in Industrial Homogeneous Catalysis. *206*:133 - 152
Crooks RM, Lemon III BI, Yeung LK, Zhao M (2001) Dendrimer-Encapsulated Metals and Semiconductors: Synthesis, Characterization, and Applications. *212*:81 - 135
Croteau R, see Davis EM (2000) *209*:53 - 95
Curran DP, see Maul JJ (1999) *206*:79 - 105
Davis EM, Croteau R (2000) Cyclization Enzymes in the Biosynthesis of Monoterpenes, Sesquiterpenes and Diterpenes. *209*:53 - 95
de la Plata BC, see Ruano JLG (1999) *204*:1 - 126
de Meijere A, Kozhushkov SI (1999) Macrocyclic Structurally Homoconjugated Oligoacetylenes: Acetylene- and Diacetylene-Expanded Cycloalkanes and Rotanes. *201*:1 - 42
de Meijere A, Kozhushkov SI, Khlebnikov AF (2000) Bicyclopropylidene - A Unique Tetrasubstituted Alkene and a Versatile C_6-Building Block. *207*:89 - 147
de Meijere A, Kozhushkov SI, Hadjiaraoglou LP (2000) Alkyl 2-Chloro-2-cyclopropylideneacetates - Remarkably Versatile Building Blocks for Organic Synthesis. *207*:149 - 227
Diederich F, Gobbi L (1999) Cyclic and Linear Acetylenic Molecular Scaffolding. *201*:43 - 79
Diederich F, see Smith DK (2000) *210*:183 - 227
Djakovitch L, see Astruc D (2000) *210*:229 - 259
Dormán G (2000) Photoaffinity Labeling in Biological Signal Transduction. *211*:169 - 225
Drabowicz J, Mikołajczyk M (2000) Selenium at Higher Oxidation States. *208*:143 - 176
Famulok M, Jenne A (1999) Catalysis Based on Nucleid Acid Structures. *202*:101 - 131
Frey H, Schlenk C (2000) Silicon-Based Dendrimers. *210*:69 - 129

Printing (Computer to Film): Saladruck, Berlin
Binding: Lüderitz & Bauer, Berlin